INVESTIGATION OF DYNAMIC BEHAVIOR OF GEOSYNTHETIC REINFORCED SOIL RETAINING STRUCTURES UNDER EARTHQUAKE LOADS

by

Ali Kasay Enünlü

B.S., in Civil Engineering, Kocaeli University, 1999

M.S., in Civil Engineering, Boğaziçi University, 2001

Submitted to the Institute for Graduate Studies in
Science and Engineering in partial fulfillment of
the requirements for the degree of
Doctor of Philosophy

Graduate Program in Civil Engineering

Boğaziçi University

2007

ACKNOWLEDGEMENTS

I would like to express my sincere gratitude to my thesis supervisor, Prof. Dr. Erol Güler, for his helpful suggestions, guidance, continuous support, encouragement, and understanding that he provided throughout this special project and the preparation of this thesis. And also I would wish to thank to Prof. Dr. Mustafa Erdik and Prof. Dr. Cem Avcı for their valuable suggestions throughout the preparation of this thesis. Additionally, thanks to my thesis defense committee members Assoc. Prof. Recep İyisan and Asst. Prof. Özer Çinicioğlu for their helpful suggestions.

I extend my gratitude to Dr. Waiel Mowrtage for his helps during the project at the laboratory and his suggestions for my PhD study.

Heartfelt thanks to my friends Öznur Selek, Tahir Erdem, Alper Okay, Onur Koç, Oktay Çırağ, Savaş Atmaca, Osman Kaya, Uğur Koçkal, Hasan Şenel, Ayşe Aydın, Fuat Aras, Aykut Erkal and Murat Hamderi, who helped me in my difficult times. I also extend my thanks to some of the persons that I encountered in my working environment as well. Around them special thanks to Mr. Özgün Dumrul for allowing me to complete my thesis' experiments.

I am grateful for the moral support that my family provided during my study. Additionally, the helping hand of an old civil engineer my father Nejat Enünlü when I needed contributed much to my study.

This thesis has been supported by Boğaziçi University Scientific Research Project BAP03A404 and TÜBİTAK Scientific Research Project MAG-103I005. Also, I have very much benefited from the Fahir İlkel PhD scholarship that I received during the period of 5 months. I thank them as well.

ABSTRACT

INVESTIGATION OF DYNAMIC BEHAVIOR OF GEOSYNTHETIC REINFORCED SOIL RETAINING STRUCTURES UNDER EARTHQUAKE LOADS

Due to their advantageous engineering properties and cost effectiveness large numbers of Geosynthetic-Reinforced Soil Retaining Walls (GRS-RWs) are being designed and constructed throughout the world and also in our country. In this thesis, in order to gain better insight into dynamic behavior of a GRS-RW under earthquake loads, two ½ reduced-scale shaking table tests were carried out using the shaking table facility at the Kandilli Observatory and Earthquake Research Institute (KOERI) of Boğaziçi University. The walls were 1.9 m tall, making them one of the tallest reduced-scale walls of its kind. By installing 8 linear displacement transducers to measure the strains of the geotextile members, 8 laser displacement sensors to measure the displacements of the facing blocks, an LVDT to measure the displacement of the shaking table and 11 accelerometers on several locations of the soil structure and onto the shaking table to evaluate the acceleration amplifications occurred, detailed displacement-time, average strain-time and acceleration-time histories of the components of the GRS-RW were obtained. In addition to the experimental tests, numerical analyses with the finite element (FEM) program Plaxis v 8.4 and the Newmark's displacement method were utilized.

The experimental test results showed that both experimental walls behaved rigidly and almost no residual displacements were observed on the front wall. While Newmark's analysis confirmed this phenomenon, Plaxis v8.4 simulated the dynamic behavior of the wall reasonably by demonstrating minor residual displacements at the top of the wall attaining to 5 mm and 6 mm for 1st and 2nd experiments, respectively. The general conclusion is that GRS-RWs designed according to the current specifications behave very successfully under earthquake loading conditions.

ÖZET

GEOSENTETİK DONATILI ZEMİN İSTİNAT YAPILARININ DEPREM YÜKLERİ ALTINDAKİ DAVRANIŞININ İNCELENMESİ

Gösterdikleri avantajlı mühendislik özellikleri ve maliyet düşüklükleri sebebi ile tüm dünyada ve ülkemizde çok miktarda Geosentetikler ile Donatılandırılmış Zemin İstinat Yapıları tasarlanmakta ve inşa edilmektedir. Bu projede, Geosentetik Donatılarla Güçlendirilmiş Zemin İstinat Yapıları'nın deprem yükleri altındaki dinamik davranışı hakkında daha iyi bir kavrayışa sahip olabilmek için Boğaziçi Üniversitesi, Kandilli Rasathanesi Deprem Araştırma Enstitüsü Sarsma Tablası Laboratuvarı'nda iki adet ½ oranında ölçeklendirilmiş İstinat Duvarı modelleri ile sarsma tablası deneyleri yapılmıştır. Zemin İstinat Duvarları 1.9 m yüksekliğinde olup, şu ana kadar yapılan çalışmalar içerisinde en yüksek küçük ölçekli duvar modellerinden birisi konumundadır. Geotekstillerin maruz kaldıkları deformasyonu ölçmek için 8 lineer deplasman cetveli, ön duvar yüzeyinin uğradığı yerdeğiştirmedikleri ölçmek için 8 lazer deplasman ölçme aleti, sarsma tablasının deplasmanını ölçmek için bir LVDT ve ivme büyültmelerini (amplifikasyonlarını) ölçmek için zemin yapısının çeşitli yerlerine ve sarsma tablası üzerine toplam 11 ivme-ölçer yerleştirilmek suretiyle yapının elemanlarına ait detaylı yerdeğiştirme-zaman, ortalama deformasyon-zaman ve ivme-zaman eğrileri elde edilmiştir. Deneysel çalışmalara ek olarak, Plaxis sonlu elemanlar programı kullanılarak nümerik analizler yapılmış ve Newmark Yerdeğiştirme Metodu tatbik edilmiştir.

Deney sonuçları göstermiştir ki iki deneyde de duvarımız rijit davranış göstermiş ve ön duvar yüzeyinde hemen hemen hiç kalıcı deformasyon gözlemlenmemiştir. Newmark analizi bu olguyu doğrularken, Plaxis v8.4 duvarın dinamik davranışını makul bir yaklaşıklıkla ön duvar yüzeyi tepe noktalarında 1. deneyde de 5 mm'ye 2. deneyde de 6 mm'ye varan küçük kalıcı deplasmanlar hesap ederek yansıtmıştır. Varılan genel sonuç günümüzde geçerli tasarım şartnamelerine uygun olarak tasarlanan Geosentetik Donatılı İstinat Duvarları'nın deprem yükleri altında son derece başarılı davranış gösterdiğidir.

TABLE OF CONTENTS

LIST OF FIGURES

LIST OF TABLES

LIST OF SYMBOLS

a_c	Critical horizontal acceleration of the sliding mass
a_{cs}	Minimum peak connection strength (N/m)
a_h	Horizontal acceleration
a_{max}	Maximum base acceleration
a_u	Minimum peak interface shear strength (N/m)
a_v	Vertical acceleration
A_i	Area of slice I
B	Linear elastic medium width
c	Viscous damping ratio
c_f	Cohesion of the foundation soil
c_s (c)	Cohesive strength of the soil
C	Damping matrix
C_c	Coefficient of curvature
C_{ds}	Coefficient of direct sliding
C_F	Dimensionless force coefficient
C_1	Coefficient for finding the critical failure surface inclination angle
$C_{1,}C_2$	Relaxation coefficients in Plaxis numerical analysis program
C_{1AE}	Coefficient for finding the dynamic active critical failure surface inclination angle in pseudo-static approach
C_2	Coefficient for finding the critical failure surface inclination angle
C_{2AE}	Coefficient for finding the dynamic active critical failure surface inclination angle in pseudo-static approach
C_3	Coefficient for finding the critical failure surface inclination angle
C_{3PE}	Coefficient for finding the dynamic passive critical failure surface inclination angle in pseudo-static approach
C_4	Coefficient for finding the critical failure surface inclination angle
C_{4PE}	Coefficient for finding the dynamic passive critical failure surface inclination angle in pseudo-static approach
C_u	Coefficient of uniformity
d	Grain diameter

e	Void ratio
E	Young's modulus
E_i	Initial stiffness
E_{50}	Confining stress dependent stiffness secant modulus for primary loading
E_{50}^{ref}	Reference stiffness modulus corresponding to the reference confining pressure p^{ref}
E_{ur}^{ref}	Reference Young's modulus for unloading and reloading corresponding to the reference confining pressure p^{ref}
E_{ur}	Stress-dependent stiffness modulus for unloading and reloading
E_{oed}	One-dimensional compression modulus
E_s	Elastic secant modulus (at 50 per cent σ_{max})
f	Frequency
F	Tensile strength of a strip in units force
$F_{dtyn\ i}$	Dynamic reinforcement load (component) in reinforcement layer i (N/m)
F_i	Total reinforcement load in reinforcement layer i (N/m)
$F_{sta\ i}$	Static reinforcement load (component) in reinforcement layer i (N/m)
FS	Factor of Safety (dimensionless)
FS_{cs}	Factor of safety against connection failure (dimensionless)
FS_{sc}	Factor of safety against interface shear failure (dimensionless)
FS_{sl}	Factor of Safety against base sliding (dimensionless)
FS_{sli}	Factor of safety against internal sliding (dimensionless)
g	Acceleration of gravity
G	Shear modulus
G_{ur}	Shear modulus for unloading, reloading
G_0	The initial or very small-strain shear modulus
G_{50}	Secant shear modulus
h	Height at back of reinforcement soil zone used in external stability calculations (m)
h_{IR}	Height from toe of wall to line of action of inertial force P_{IR} (m)
h_m	Depth in the model
h_p	Depth in the prototype

h_{zi}	Height of soil at back of reinforced soil zone used in internal sliding calculations (m)
h_{β}	Height from base of wall to center of gravity of wedge of soil above reinforced soil zone (m)
H	Wall height
H_w	Height of facing unit (m)
J	Elastic modulus of the reinforcement (Reinforcement stiffness)
J_o	Initial stiffness of the reinforcement
J_{tan}	Tangent stiffness of the reinforcement
k_b	Bond stiffness of the grout
k_c	Fraction of critical horizontal acceleration (critical horizontal inertial coefficient or seismic coefficient)
k_h	Fraction of horizontal acceleration (horizontal inertial coefficient or seismic coefficient)
k_v	Fraction of vertical acceleration (vertical inertial coefficient or seismic coefficient)
K	Stiffness matrix
K_a	Active earth pressure coefficient
K_0	Ratio of the horizontal and vertical effective stresses
K_{AE}	Dynamic active earth pressure coefficient
K_p	Coefficient of passive earth pressure
K_{PE}	Dynamic passive earth pressure coefficient
L	Reinforcement length
L_{min}	Minimum reinforcement length
L_w	Width of facing column
m	Symbol that refers to model
m	Stress dependency power
M	Mass matrix
MLTΘ	The four basic dimensions in fluid mechanics (Mass, Length, Time and Temperature)
M_o	Overturning moment
n	Scaling multiple
N	Multiple of earth's gravity

N_f	Centrifugal acceleration at failure in multiples of Earth's gravity
N_w	Total number of standard SRW units in facing column (dimensionless)
p	Symbol that refers to prototype
p^{ref}	Reference pressure
P_A	Active static earth pressure resultant
P_{AE}	Total dynamic active earth force
P_{iR}	Horizontal inertial force of the composite mass
P_p	Passive static earth pressure resultant
P_{PE}	Total dynamic passive earth force
PGA	Peak ground acceleration
q	Deviatoric stress
q_f	Ultimate deviatoric stress
r	Distance from the axis of the centrifuge
R	Radius of the failure of the failure circle
R_{inter}	Strength reduction factor for interfaces
Re	Dimensionless reynolds number
R_f	Failure ratio
R_S	Base sliding resisting force
s_b	Bond strength of the grout
S_i (z)	Out-of-balance horizontal shear force transmitted through facing unit interface at depth z below crest of wall (N/m)
S_v	Reinforcement vertical spacing
S_{vi}	Contributory area corresponding to reinforcement layer i (m^2/m)
t	Time
t_w	Reinforcing strip thickness
T	Tensile strength
T	Predominant period of the ground acceleration
T_f	Failure tensile load of the reinforcement
T_j	Tensile strength of the reinforcement j
T_g	Tensile strength of geotextile
T_p	Predominant period
T_y	Yield strength of the reinforcement
u_x	Prescribed displacements in Plaxis program

v_m	Peak ground velocity
V_p	Pressure wave velocity
V_s	Shear wave velocity
$V_u(z_i)$	Peak interface shear capacity at interface located at depth z below crest of wall (N/m)
w	Reinforcing strip width
w %	Water content
W	Weight of the soil wedge
W_w	Total weight of the facing column
W_i	Total wieght of the reinforced zone
W'_i	Reduced inertial zone weight of the reinforced zone
W_β	Weight of the contribution of the soil wedge in the infinite slope
W'_β	Reduced inertial zone weight of the soil infinite slope of the soil wedge
W_r	The overall total weight
y_j	Moment arm for reinforcement j
z	Depth from crest of wall (m)
z_i	Depth from crest of wall to reinforcement layer i (m)
z_{vi}	Distance from the crest of the wall to the mid-elevation of the contributory area S_{vi} (m)

α	The critical failure surface inclination angle to the horizontal (°)
α_{AE}	The dynamic critical active failure surface inclination angle to the horizontal in pseudo-static approach (°)
α_g	Scale factor for the acceleration
α_L	Scale factor for the linear dimensions
α_{PE}	The dynamic critical passive failure surface inclination angle to the horizontal in pseudo-static approach (°)
α_R	Rayleigh coefficient related to mass
α, β	Newmark scheme time integration parameters
β	Angle of the inclination of the backfill (backslope angle for the infinite slope) (°)
β_R	Rayleigh coefficient related to stiffness

β_1	Time integration coefficient of the generalized Newmark method
β_2	Time integration coefficient of the generalized Newmark method
δ	Interface friction angle (°)
δ_g	Interface friction angle of the grout (°)
δ_h	Horizontal spacings of the strips
δ_v	Vertical spacings of the strips
ε	Strain
ϕ_b	Peak friction angle of retained (backfill) soil (°)
ϕ_d	Peak friction angle of drainage (leveling pad) (°)
ϕ_f	Peak friction angle of foundation soil (°)
ϕ_i	Peak friction angle of the interface (°)
ϕ_{max}	Maximum angle of shear resistance of the soil (°)
ϕ_r	Peak friction angle of reinforced (infill) soil (°)
θ	Wall inclination (°)
θ_I	Angle from horizontal to tangent at center of slice I (°)
ψ	Seismic inertia angle (°)
ψ_i	Dilatancy angle of the interface (°)
ψ_s	Soil dilatancy angle (°)
ψ_{ws}	Index of wall safety against strip breakage
γ	Unit weight of the backfill
$\gamma_{0.7}$	Shear strain level at which secant shear modulus *G* is reduced to 70 per cent of G_0
$\gamma_{cut\text{-}off}$	The cut-off shear strain
γ_w	Unit weight of SRW units
λ	Failure ratio of the reinforcement
λ_{cs}	Slope of peak connection strength failure envelope (°)
λ_u	Slope of peak interface shear strength failure envelope for SRW units(°)
ω	Wall inclination angle (positive in a clockwise direction from the vertical) (°)
ω	Rotational speed
π_n	Dimensionless groups
μ	Fluid viscosity

υ	Poisson's ratio
υ_{ur}^{ref}	Poisson's ratio for unloading-reloading
ρ	Soil density
σ_h	Horizontal stress
σ_v	Vertical stress
σ^9_v	Vertical effective stress
σ_y	Vertical stress
τ_{max}	Shear stress at failure
$(\tau_{yx})_{max}$	Maximum overall shear stress provided by the soil
$(\tau_{yxr})_{max}$	Maximum overall shear stress of the reinforced soil
ΔK_{AE}	Incremental dynamic active earth pressure coefficient
ΔP_{AE}	Dynamic active earth pressure force increment
$\Delta P_{IR}(z_i)$	Internal force contribution
Δt	Time interval
ΔW_h (z)	Weight of the facing column above the sliding surface based on the hinge height taken at sliding surface at depth below crest of wall (N/m)
ΔW_i (z)	Weight of reinforced soil with constant height z acting on an internal sliding surface at depth below crest of wall (N/m)
$\Delta W'_i$ (z)	Reduced weight of the reinforced zone extending from the back of the facing column to length 0,5H beyond the face of the wall and having constant height z used to calculate inertial force P_{IR} (z) (N/m)
ΔW_w (z)	Total weight of the facing column above the sliding surface at depth z below the crest of the wall (N/m)
ΔW_{wi}	Weight of the facing falling with the contributory area S_{vi} of the corresponding reinforcement layer I (N/m)
$\sum$Mstage	Total multiplier parameter in staged construction in the Plaxis program
$\sum$Mdisp	Total multiplier used to control the magnitude of the prescribed displacements in the Plaxis program

ABBREVIATIONS

AASHTO	American Association of State Highway and Transportation Officials
GRS-RW	Geosynthetic Reinforced Soil Retaining Wall
FHWA	Federal Highway Administration
HSsmall	Hardening Soil Small Strain Stiffness Model
NCMA	National Concrete Masonry Association
M-O	Mononobe-Okabe (pseudo-static earth pressure theory)
RS-RW	Reinforced Soil Retaining Wall
SRW	Segmental Retaining Wall

1. INTRODUCTION

1.1. General

Turkey is confronted with major earthquakes and in the future will be confronted by many more. Thus, to resist the earthquakes in a more economical and efficient manner, new systems need to be investigated, further understood and developed. Likewise, in the geotechnical engineering domain, the reinforced earth structures are one of the promising solutions that need to be assessed deeply.

Nowadays, although the resistance and performance calculations of the geosynthetic reinforced soil-retaining structures under static loads can be done routinely and easily, there is not a general procedure that is adopted with respect to the strength and resistance criteria and design principles under earthquake loads. Generally, to investigate the dynamic behavior of these kinds of structures, the well-known procedures are the numerical methods (finite-element analysis), scale-model centrifuge tests, and scale-model shaking-table tests. Among these tests, much care must be shown to scale-model centrifuge tests and scale-model shaking-table tests, because they need a careful design strategy and planning to be able to be constructed.

Because examining the behavior of a full-scale prototype model of a soil retaining wall is not easy under dynamic conditions, scale-models of these prototypes of the soil retaining structures are constructed and the centrifuge tests and shaking table tests are applied to them. Deducting the full-scale behaviors from these small scale-models with these experiments is an important and complex matter that needs the usage of *Buckingham's π Theorem* and *similitude rules*. *Buckingham's π Theorem* is a compacting technique that allows reducing the number of dimensional variables into smaller number of dimensionless groups. The first benefit of this dimensional analysis is that with the help of these dimensionless groups, we do not need to do many experiments, which would otherwise cause us to spend very much money and time to it. Secondly, it suggests variables, which can be discarded, resulting to give us a great deal of insight into the form of the physical relationship we are trying to study. Finally, it provides *scaling laws*, which

can convert data from a cheap, small model into design information for an expensive, large prototype.

In addition to scale-model shaking table tests, finite element numerical analysis provides further information compared to traditional limit-equilibrium analysis, such as deformation, shear stress distribution in the soil and tensile load in the reinforcement layers that are necessary in order to estimate the performance of reinforced soil retaining walls.

1.2. Scope and Objective

In this study, firstly the Reinforced Soil Structures, their composition, history and their usage areas are explained briefly. Thereafter, the methods to investigate the behavior of these kinds of structures and conventional design methods are defined. Secondly, the Buckingham's Pi (π) Theorem, from which this scaled-model structure's π values are determined, and which is one of the most important supports that this study is based on is described in detail. A scaling factor of ½ was chosen according to our constraints and capabilities and some of the elements of the geosynthetic reinforced wall were produced according to this scaling factor. Thirdly, the characteristics of the rubber material as an absorbent material along with the soil characteristics are evaluated. Hereafter, the numerical modeling of the GRS-RW with the FEM program Plaxis v8.4 is described. Since to design a test structure of this kind is a delicate process under laboratory conditions, all the materials used for this study and the test setup are presented with their logical reasons. The instrumentation of all the electronic devices with their properties and capabilities were also a vital issue, so these are specified. Lastly, the results of the acceleration amplification study, geotextile-strain measurement study and front wall displacement evaluation study are presented in detail. Finally, the experimental results are compared with the favorite Finite Element (FEM) Geotechnical Engineering program Plaxis v8.4 and reached into a conclusion.

1.3. Organization of the Thesis

The study is presented in the thesis in the following order:

Chapter 1 Introduction to the subject, scope and objective of the study

Chapter 2 Literature review, description of the geosynthetic reinforced retaining walls and experimental and numerical methods

Chapter 3 Design of Geosynthetic Reinforced Segmental Retaining Walls, static and seismic earth pressures acting on retaining walls, Modes of failure

Chapter 4 Description of Dimensional analysis, Buckingham's π theorem, similitude (similarity) rules and scaling laws

Chapter 5 Tests for Investigation of Soil Properties and Evaluation of the Rubber as an Absorbent Material

Chapter 6 Numerical Modeling of The GRS-RW with the Plaxis Program, Calibrating the rubber fill with the Absorbent Boundary

Chapter 7 Design of test set-up, Instrumentation and reinforcement layout, Materials and Transducers selection, Dynamic Excitations, Shaking sequence, Evaluation of the test data

Chapter 8 Newmark's Displacement Method Analysis and Determination of the Inclination of the Failure Surface

Chapter 9 Evaluation of the Measurement Results

Chapter 10 Comparison of the results between experimental analysis and numerical analysis

Chapter 11 General Conclusions

2. DESCRIPTION AND LITERATURE REVIEW OF GEOSYNTHETIC-REINFORCED SOIL RETAINING WALLS

2.1. Geosynthetic Reinforced Soil Retaining Wall (GRS-RW)

2.1.1. Description of GRS-RWs

Reinforced soils are composite materials, which combine the typical resistance of two different materials in such a way to minimize the weakness of each one. The soil material, which is found cheaply and in large amounts, is a compression resistant material. On the other hand, the geosynthetic reinforcement is a relatively more expensive but highly tensile resistant material. As a result, the mutual combination of these two materials improves the global characteristics of this composite material, like the relationship between the one with concrete and steel. When a geosynthetic material is used as reinforcement in soil, this type retaining wall is called as Geosynthetic Reinforced Soil Retaining Wall (GRS-RW) (Figure 2.1).

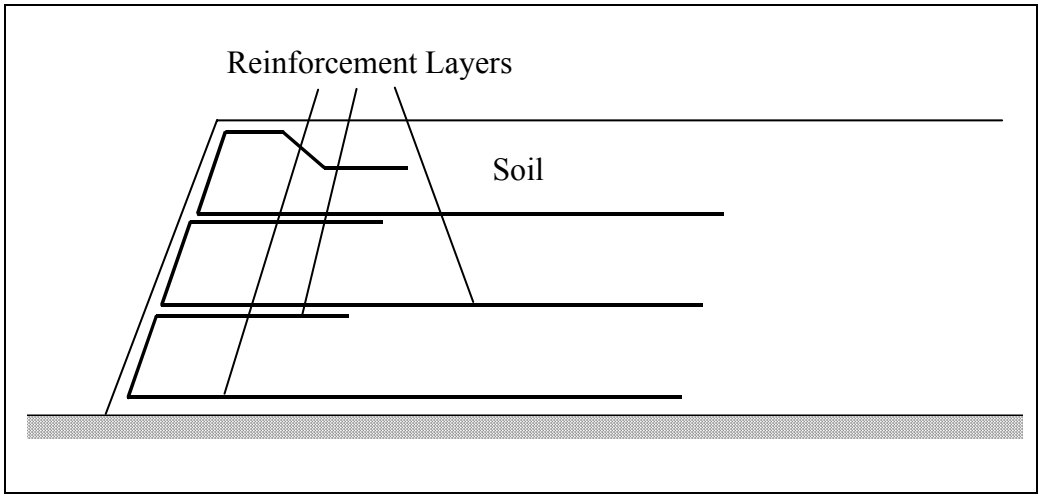

Figure 2.1. Typical view from a reinforced slope for embankment

By placing tensile reinforcing elements in the soil the strength of the soil can be improved significantly. Also by using a facing system, soil raveling between the reinforcing elements can be prevented. This allows very steep slopes and vertical walls to be safely constructed. A simple illustration of a segmental retaining wall with concrete

facing blocks can be seen from Figure 2.2. A further illustration in Figure 2.3 depicts a typical section drawing used by a company in the industry.

Figure 2.2. A simple illustration of a Geosynthetic-Reinforced Segmental retaining wall (Mirafi Construction Products)

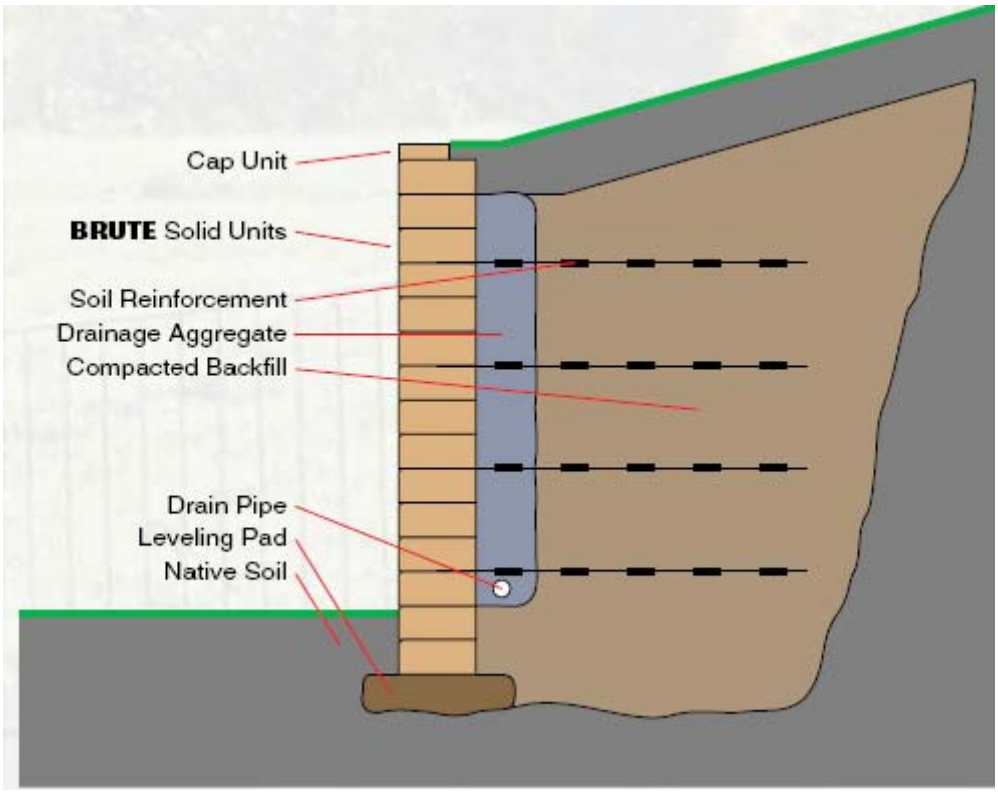

Figure 2.3. GRS-RW typical section drawing (BRUTE retaining wall system)

In conclusion, GRS-RWs are considered to be typically more ductile, more tolerable to differential settlements, more adaptable to low quality backfill, easier to construct, and more economical when compared to other types of retaining structures. An instance from a construction process of these types of structures can be seen from Figure 2.4.

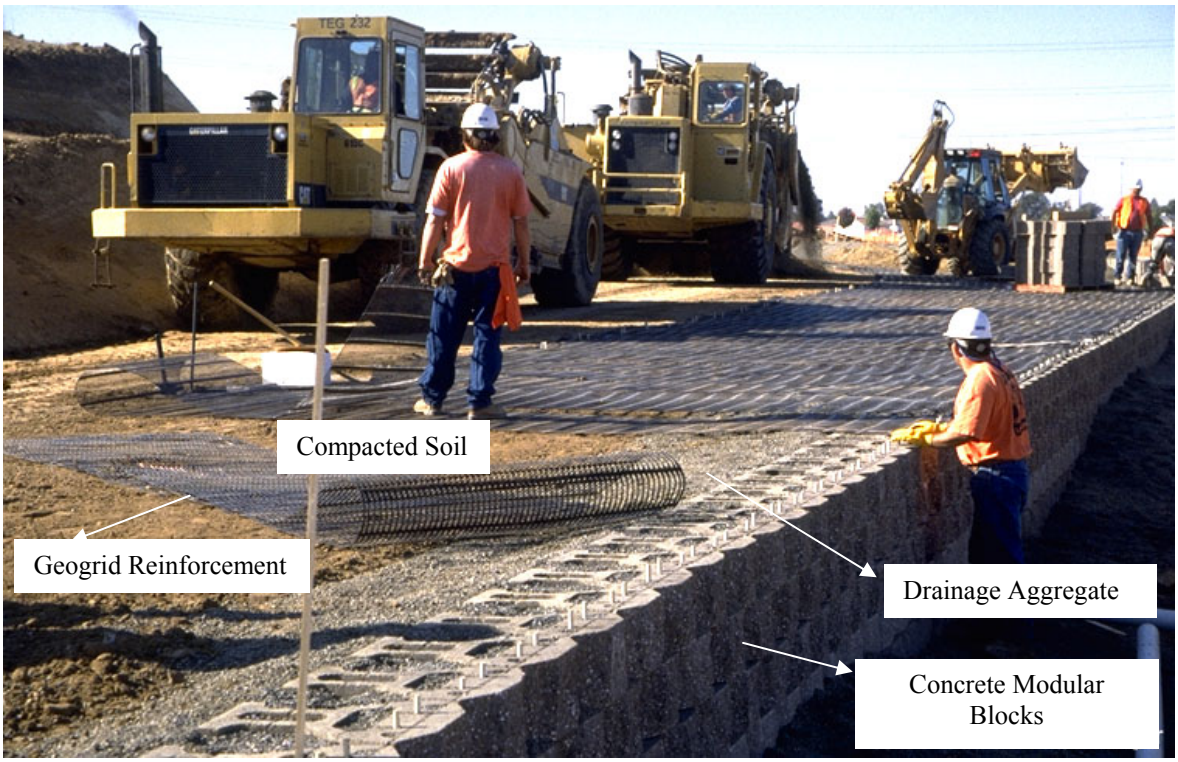

Figure 2.4. Construction process of a Geosynthetic-Reinforced Soil Structure

2.1.2. Terminology of GRS-RWs

A GRS-RW is composed of, mainly, 5 elements. They are named as; retained backfill soil, reinforcement, facing unit, mechanically stabilized soil mass and foundation soil. The demonstration of these components can be seen in Figure 2.5.

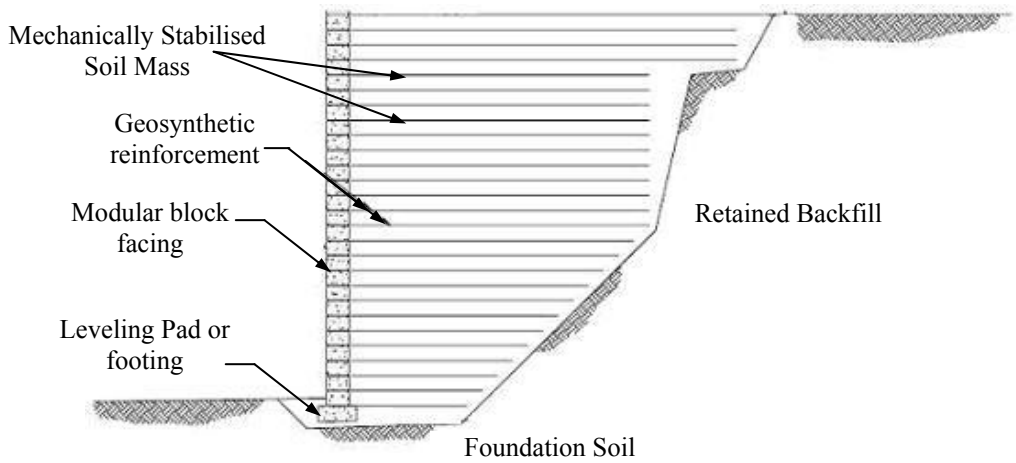

Figure 2.5. The principal elements of a GRS-RW

Retained backfill is the fill material located between the mechanically stabilized soil mass and the natural soil. The backfill material is selected to satisfy the following requirements: 1. Friction strength: friction angle should be high enough to ensure the necessary soil reinforcement interaction. 2. Susceptibility to creep should be sufficiently low to prevent excessive deformation. 3. Maximum grain size should not be so large as to adversely affect placement of reinforcements or compaction. 4. Moisture content may have to be limited to avoid difficulties during compaction. 5. Corrosiveness should not be excessive. In addition, all backfill material should be free from organic and other deleterious materials.

Reinforcement is an inclusion where soil-inclusion stress transfer occurs continuously along itself. Among the most used reinforcements, we can count the steel strips and geotextile or geosynthetic sheets. Geosynthetics is a generic term that encompasses flexible synthetic materials used in geotechnical engineering such as geotextiles, geomembranes, geonets and geogrids.

Facing unit is a component of the reinforced soil system used to prevent the soil from raveling out between the rows of reinforcement. The most common facings are the precast concrete modular blocks, concrete panels, metal sheets and plates, gabions, welded wire mesh, shotcrete, wood lagging and panels and wrapped sheets of geosynthetics. For example, in GRS-RWs, the modular blocks, which are used to retain the backfill, contributes to the integration and stabilization of the system through the interaction between the blocks, blocks and backfill, as well as between the blocks and geosynthetic layers. Modular-block units are typically connected to geosynthetic reinforcement layers using mechanical and/or frictional connection devices such as polymeric pins, inserts, clips, concrete shear keys. Additionally, the dead weight of the modular blocks increases the performance of the global stability of GRS-RWs.

Mechanically stabilized soil mass is a generic term that encompasses reinforced fill or sometimes called reinforced earth and multi-anchored soil mass. Reinforced fill is a term used when multiple layers of inclusions act as reinforcements in soils placed as fill, whereas multi-anchored soil mass is a term used when multiple layers of inclusions act as

anchored tendons in soils placed as fill. “Reinforced Earth” is a trademark for a specific reinforced soil system.

Foundation soil is the soil beneath the mechanically stabilized soil mass and the retained backfill, which carries this overall system. Surely, it is important that the foundation soil satisfies the criteria of the design manuals. The bearing capacity, settlement potential and position of ground water levels are some of the important factors that need to be investigated before the implementation of the reinforced earth structures. As a result, before the application, weak foundation soil characteristics may be improved to satisfy the adequate bearing capacity and/or limiting total and/or differential settlements (FHWA, 1996) [1].

2.1.3. Basic Principles

If we consider the soil element in Figure 2.6a, which is part of an infinite mass of soil, the application of a vertical stress σ_v causes a deformation in the element and also causes consequently an σ_h lateral compression from the adjacent soil. Horizontally the soil element undergoes a “tensile deformation” ε_h, which is one of the principal causes of local failure.

On the other hand, when a geosynthetic material, i.e. a geotextile, a geogrid,etc. is put into the soil as in Figure 2.6b, after the application of a vertical stress, not only the soil element deforms but also the geosynthetic material itself undergoes extensions, tensile deformations.

This extension of the material creates a tensile strength T in the reinforcement, which in turn produces a horizontal stress σ_h^*. This stress provides a confinement action on the soil granules and greatly contributes to resist the horizontal forces and to reduce horizontal deformations.

As a result, it can be concluded that the inclusion of the geosynthetic material to the soil greatly reduces the stresses and strains applied to the soil, and the vertical stress

applied to the composite soil material can be increased compared to the unreinforced soil, at equal deformations.

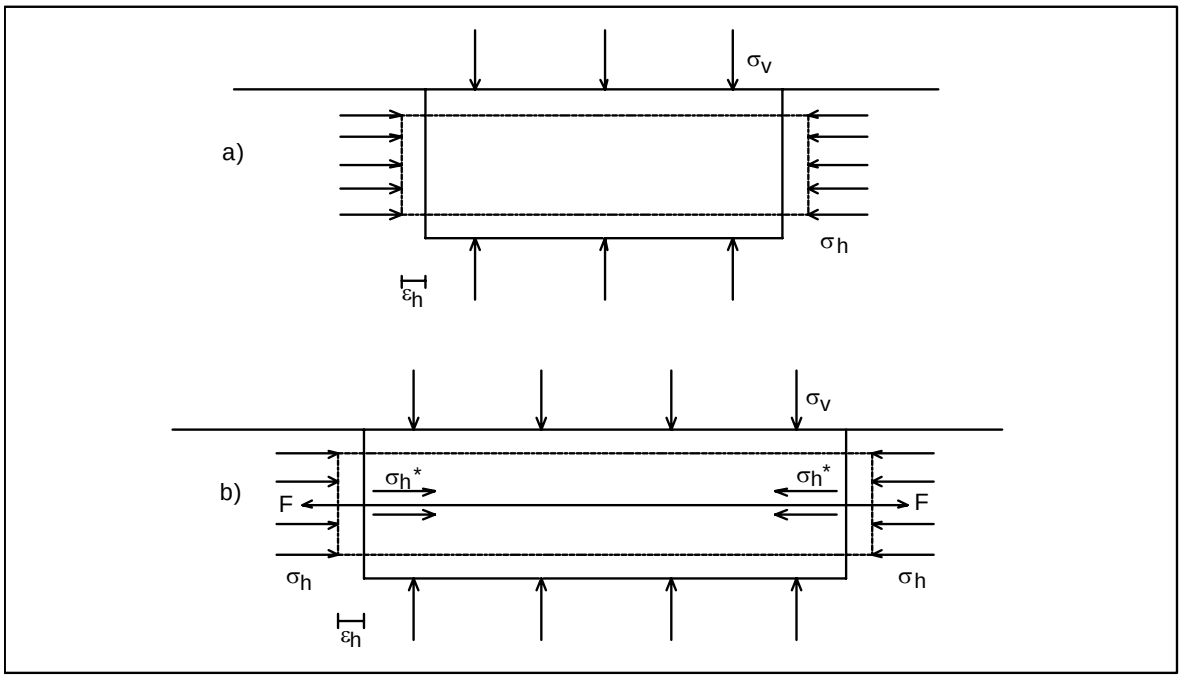

Figure 2.6. Stresses and strains in an unreinforced and reinforced soil element[2]

Additionally, with respect to the shear stresses in the soil, if we look at Figure 2.7, we can see the natural shear stress distribution in the soil when a vertical stress is applied. The maximum shear stress provided by the soil can be found with the formula:

$$\left(\tau_{yx}\right)_{\max} = \sigma_y . \tan\phi_{\max} \tag{2.1}$$

where ϕ_{max}= maximum angle of shear resistance of the soil;

$(\tau_{yx})_{max}$= maximum overall shear stress provided by the soil.

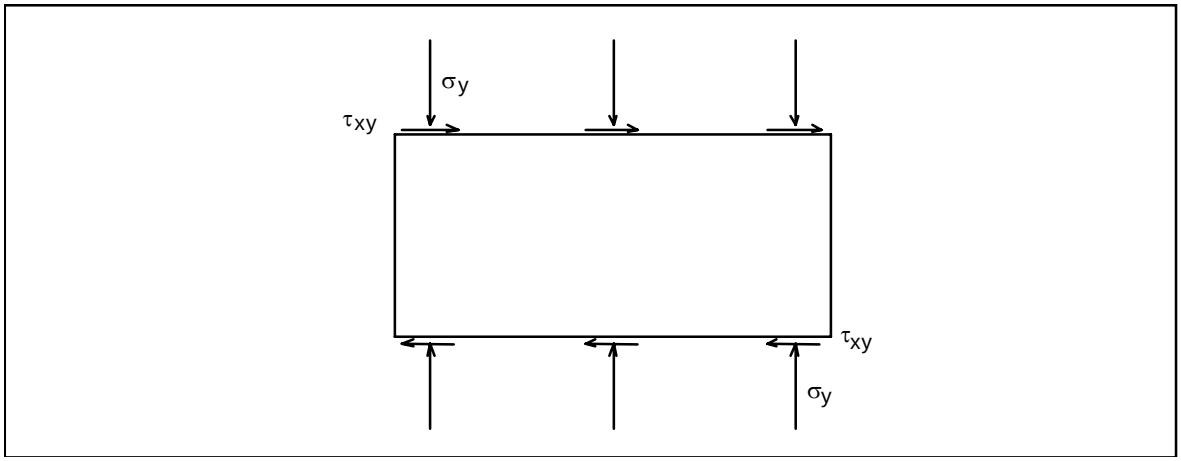

Figure 2.7. Shear stresses in an unreinforced soil element [2]

When the soil element is crossed by a reinforcement element which makes a θ angle with the shearing direction (Figure 2.8), the state stress is modified because the tension T generates a shear stress produced by the tangential component T.sinθ, meanwhile the normal component T.cosθ generates another τ_{yx} caused by the friction angle ϕ_{max} in the soil (Jewell,1980) [2].

Therefore:

$$\left(\tau_{yxr}\right)_{\max} = \sigma_{yr}.\tan\phi_{\max} + \left(T/A_s\right).\cos\theta.\tan\phi_{\max} + \left(T/A_s\right).\sin\theta \qquad (2.2)$$

Total Shear Resistance	=	Shear Resistance of soil alone	+	Shear Stress caused by the normal component of T	+	Shear Stress caused by the tangential component of T

where A_s = area of the soil element

$(\tau_{yxr})_{max}$ = maximum overall shear stress of the reinforced soil

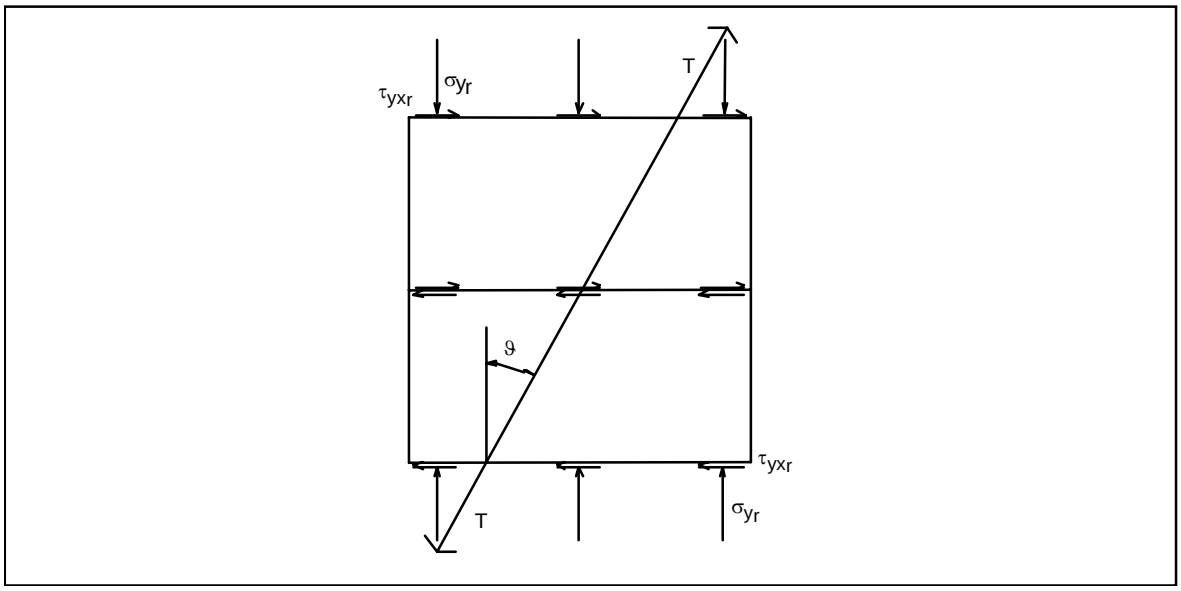

Figure 2.8. Shear stresses in a reinforced soil element [2]

The variation of the tensile forces along the reinforcement and the location of the maximum force has been established both experimentally, through instrumented models and full-scale structures, and theoretically, using numerical analysis.

As shown in Figure 2.9a, the maximum tensile force in the reinforcement is generally located some distance behind the facing. In order to create a maximum force at that location, the shear stresses exerted by the fill on the reinforcement must be in opposite directions on the two sides of the peak force as shown.

The locus of the points of maximum tensile force, called the maximum tensile forces line, thus separates the reinforced fill into two zones:

- An active zone between the facing and the maximum tensile forces line, where the shear stresses on the reinforcements are directed towards the wall face.
- A resistant zone behind the maximum tensile forces line, where the shear stresses on the reinforcement are directed away from the wall face.

The global effect is that the tensile force generated in the reinforcement by the soil in the active zone is transferred through the reinforcement back to the soil in the resistant zone.

The location of the maximum tensile forces line is influenced by the extensibility of the reinforcement as well as the overall stiffness of the facing. Figures 2.9b and 2.9c show the limiting locations of the maximum tensile forces line in walls with inextensible and extensible reinforcements:

- With inextensible reinforcements (Figure 2.9b), the maximum tensile forces line can be modeled by a bilinear failure surface which is vertical in the upper part of the wall. The state of stress is assumed to be at rest at the top and decreases to the active state in the lower part of the wall (the at rest state at the top of the wall has been attributed to both construction stresses and the restraint provided by the reinforcements against lateral yielding).

- With extensible reinforcements (Figure 2.9c), the maximum tensile forces line coincides with the Coulomb or Rankine active failure plane, and the stresses in the fill correspond to the active earth pressure condition.

The location of the maximum tensile forces line may also vary due to external factors such as the shape of the structure and surcharge conditions [1].

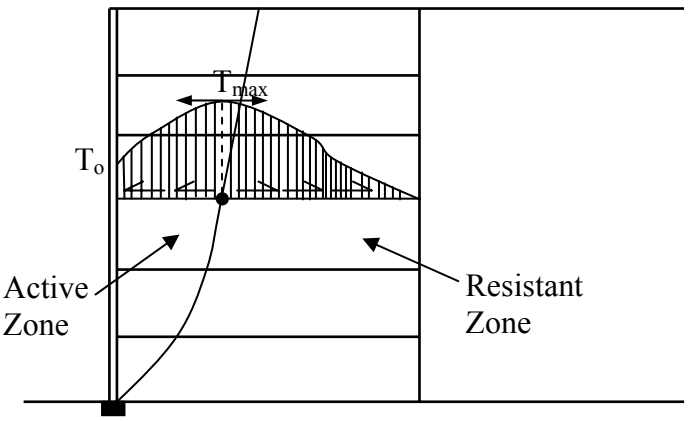

a) General case

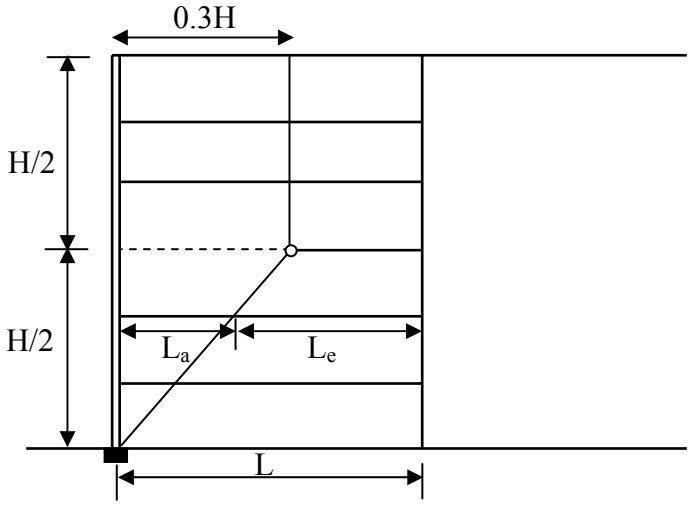

b) Inextensible reinforcements

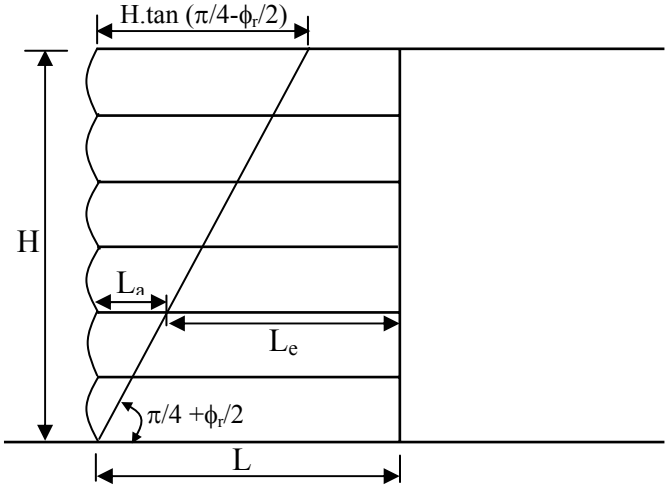

c) Extensible reinforcements

Figure 2.9. Tensile forces in the reinforcements and schematic maximum tensile force line [1]

2.1.4. History of the Development of Reinforced Soil Structures

The earliest remaining examples of soil reinforcement are the ziggurat of the ancient city of Dur-Kurigatzu, now known as Agar-Quf, and the Great Wall of China. The Agar-Quf ziggurat, which stands five kilometers north of Baghdad was constructed of clay bricks varying in thickness between 130-400 mm, reinforced with woven mats of reed laid horizontally on a layer of sand and gravel at vertical spacing varying between 0.5 and 2.0 m. Reeds were also used to form plaited ropes approximately 100 mm in diameter which pass through the structure and act as reinforcement (Bagir, 1944). The Agar-Quf structure is now 45 m tall, originally it is believed to have been over 80 m high; it is thought to be over 3000 years old. The Great Wall of China, parts of which were completed circa 200 B.C., contains examples of reinforced soil; in this case use was made of mixtures of clay and gravel reinforced with tamarisk branches (Dept. of Transport, 1977).

A significant development to modern concept of reinforced soil structures was made in United States in 1925 by Munster. He produced an earth retaining wall using an array of wooden members and a light facing. Munster minimized the problem associated with the settling of the backfill by using sliding attachments between the reinforcing members and the facing. Although the materials and details suggested by Munster would not find favor in modern construction, the techniques inherent in this system are valid and form the core of one of the construction techniques used today.

The modern concept of earth reinforcement and soil structures was proposed by Casagrande who idealized the problems in the form of a weak soil reinforced by high-strength membranes laid horizontally in layers (Westergaard, 1978). The modern form of earth reinforcement was introduced by French architect and engineer Henry Vidal in the 1960s. Vidal's concept was for a composite material formed from flat reinforcing strips laid horizontally in a frictional soil, the interaction between the soil and the reinforcing members being solely by friction generated by gravity. This material he described as "Reinforced Earth", a term that has become generic in many countries, being used to describe all forms of earth reinforcement or soil structures. In some countries, including the United States and Canada, the term is a trademark. The first major retaining walls using the Vidal concept were built near Menton in the South of France in 1968.

The use of textiles for reinforcement could not be contemplated until the development of synthetic polymer-based materials. Synthetic fabrics were known prior to 1940 but it was not until the late 1960s and early 1970s that the advances in synthetic fabric and geotextile developments led to the construction of reinforced soil structures. In the 1960s the grid reinforcement was used to reclaim land for Nyeta Airport, Tokyo and to improve the bearing capacity of weak subsoil (Yamanouchi, 1967). Following the example of the California Highway Authority, high strength geogrid reinforcement is now used for concrete faced structures. The first geotextile-reinforced wall was constructed in France in 1971, and in U.S. in 1974. After 1980s, the usage of geotextile reinforcement in reinforced soil has increased significantly. Geogrids for the reinforcement of soils were developed in 1980 and used as earth reinforcement in 1981. Since then, the use of geogrid products spreaded in United States. Nowadays, the utilization of modular block dry cast facing units is adopted throughout the world due to their lower cost and higher availability. Generally, these small concrete units are used with grid reinforcement, and such a wall system is named as modular block wall (MBW). According to the last reports, more than 200 such structures were constructed in the U.S., for highway applications [3].

2.1.5. The Use and Performance of Reinforced Soil Structures

Reinforced soil structures are cost-effective alternatives for all applications where reinforced concrete or gravity types of walls have traditionally been used to retain the soil. These include bridge abutments and wing walls as well as areas where right-of-way is restricted, such that an embankment or excavation with stable side slopes cannot be constructed. They are particularly suited to economical construction in steep sided terrain, in ground subject to slope instability, or in areas where foundation soils are poor.

As a coherent yet flexible gravity mass, Reinforced Earth is particularly well suited for construction in seismically active regions. The structures provide the high degree of structural damping needed to absorb large energy releases associated with earthquakes. For this same reasons, Reinforced Earth has proven effective is supporting high-speed railway lines.

Reinforced soil walls offer significant technical advantage over conventional reinforced concrete retaining structures at sites with poor foundation conditions. When compared to conventional reinforced concrete retaining walls, they can undergo larger displacements due to their flexible behavior. Additionally, in such cases, the reduced cost of reinforced soil versus conventional construction, plus the elimination of costs for foundation improvements, such as piles and pile caps that may be required for support of conventional structures have resulted in cost savings. In situations where a steep reinforced slope can replace a conventional wall, cost savings can be 70 percent or more.

The advantages of reinforced soil structures can be stated as follows:

1) Without using large equipment they can be constructed simply and rapidly.
2) Even ordinary craftsmen without special skills can construct these types of structures.
3) Need little site preparation.
4) Require little space in front of the structure for construction operations.
5) Reduce right-of-way acquisition by constructing or excavating steeper slopes.
6) Do not require rigid, unyielding foundation support, because reinforced structures are tolerant to deformations. It is possible build on low-bearing capacity of soils with the reinforcement on the base that would otherwise normally request a preliminary consolidation and great caution during construction.
7) It is possible to use less valuable and cheaper materials and with the possibility to build with steeper slopes the quantity of the material needed for an embankment reduces. Thus, it is cheap and cost-effective.
8) It provides improved stability as the reinforcement guarantees an improvement in the factor of safety, even in seismic areas.

Whereas the disadvantages are:

1) Require a relatively large space behind the wall face to obtain enough wall width for internal and external stability.
2) Need granular fill mostly at the present time.

3) Usually require a drainage system for ground nailing which may be difficult to construct and maintain [1].

The observed performances of reinforced soil and geosynthetic reinforced soil retaining structures during recent earthquakes are very satisfactory. According to the surveys conducted by Sandri (1994) immediately after the Northridge Earthquake of 17 January 1994, the 9 reinforced segmental retaining wall structures located within 23 to 113 km of the earthquake epicenter, which are greater than 4.5 m in height, showed no evidence of visual damage. Only 2 structures (Valencia and Gould Walls) showed tension cracks within and behind the reinforced soil mass. All the facing columns for all walls were intact eventhough peak horizontal ground accelerations as great as 0.5g were estimated at one site.

A similar survey of three geosynthetic reinforced walls and four geosynthetic reinforced slopes by White and Holtz (1996) after the same earthquake revealed no visual indications of distress. Stewart et al. (1994) reported that slope indicator measurements at the toe of a 24 m high geogrid reinforced slope which was estimated to have sustained peak horizontal ground accelerations of 0.2g showed no movement. But, some unreinforced crib walls and unreinforced segmental walls were observed to have developed cracks in the backfill due to the limited flexible characteristic of concrete crib walls. Similar good performance of several geosynthetic reinforced soil walls and slopes during the 1989 Loma Prieta earthquake (Richter magnitude=7.1) was reported by Eliahu and Watt (1991) and Collin et al. (1992).

Additionally, after the 1995 Great Hanshin Earthquake, in Kobe, Japan, reports from Tatsuoka et al. (1995, 1996) shows that the 6.2 m high geosynthetic reinforced soil retaining wall with a full height rigid facing construction have moved 260 mm at the top and 100 mm at ground level but no damage was observed, although the peak ground acceleration at the site have been as great as 0.7g. This phenomenon of tilting of the wall is attributed to the shortening of the reinforcement lengths due to site constraints.

Nishimura et al. (1996), after the same earthquake in Japan, surveyed 10 geogrid reinforced soil walls and steepened slopes after the same event. All structures survived the

earthquake even though peak ground accelerations were estimated to be in the rage of 0.3 to 0.7g. Nishimura et al. determined critical accelerations for these structures using GRB (1990) and PWRI (1992) methods of analysis and found that predicted critical acceleration coefficient (k_h) values were as low as 0.1. Results of stability calculations using these methods led them to conclude that the length of reinforcement layers at the top of the reinforced soil structures should be increased in order to capture critical failure volumes generated under even modest horizontal seismic accelerations [4].

2.2. Centrifuge Tests of RS-RWs

2.2.1. Centrifuge Tests

In geotechnical engineering, self-weight forces are the dominant loads and the generated confining pressures by them govern the behavior of the soil mass. In order to replicate gravity-induced stresses of a prototype in a *1/n* scaled model, it is necessary to test the model in gravitational field n types larger than that of the prototype. So, in centrifuge tests, by artificially creating a gravitational field, the behavior of the in-situ structures under various load conditions can be simulated and examined.

In a centrifuge device, soil models placed at the end of a centrifuge arm, which is located at a distance *r* from the axis of the centrifuge, can be rotated at a rotational speed, $\omega = \sqrt{ng/r}$, so that they are subjected to an inertial radial acceleration field, which, as far as the model is concerned, feels like a gravitational acceleration field but *N* times stronger than Earth's gravity. Soil held in a model container has a free unstressed surface and within the soil body the magnitude of stress increases with depth at a rate related to the soil density and the strength of the acceleration field. If the same soil is used in the model as in the prototype and if a careful model preparation procedure is adopted whereby the model is subjected to a similar stress history ensuring that the packing of the soil particles is replicated, then for the centrifuge model subjected to an inertial acceleration field of *n* times Earth's gravity the vertical stress at depth h_m will be identical to that in the corresponding prototype at depth hp where $h_p = nh_m$. This is the basic scaling law of centrifuge modeling, that stress similarity is achieved at homologous points by accelerating a model of scale *n* to *n* times Earth's gravity. The illustration of this modeling can be seen

in Figure 2.10. Additionally, an example centrifuge test device is shown in Figure 2.11 and a cross-section is depicted in Figure 2.12.

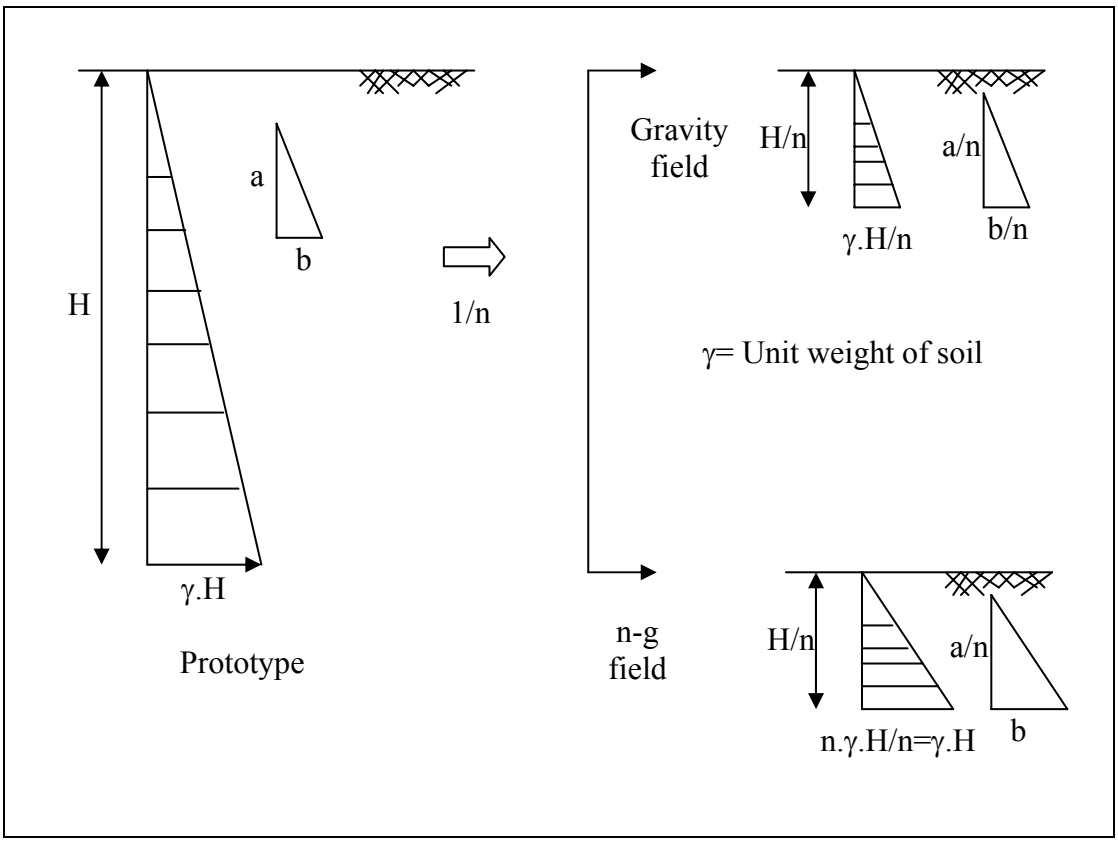

Figure 2.10. Modeling under artificial gravity field

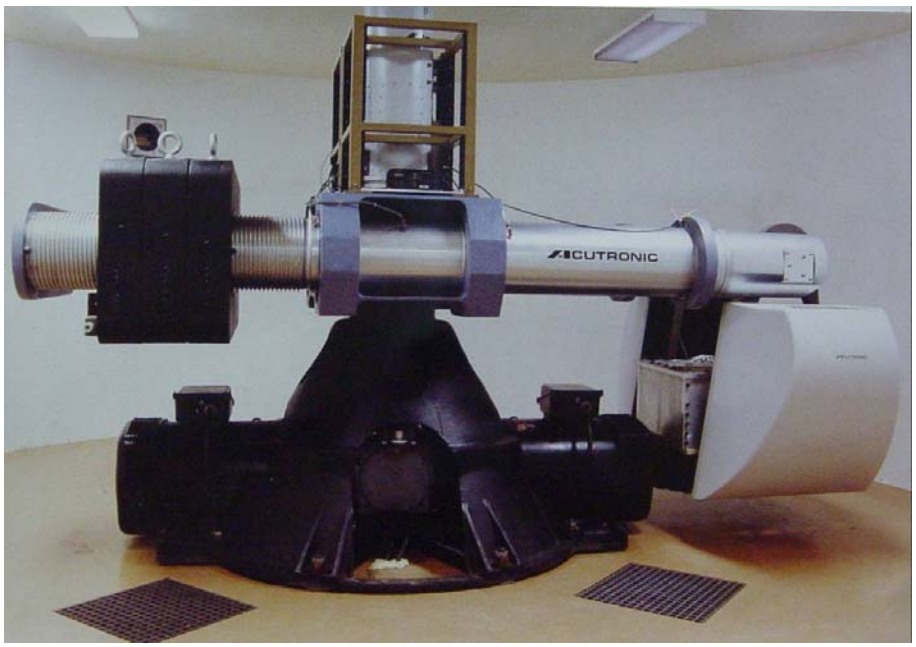

Figure 2.11. Centrifuge test device

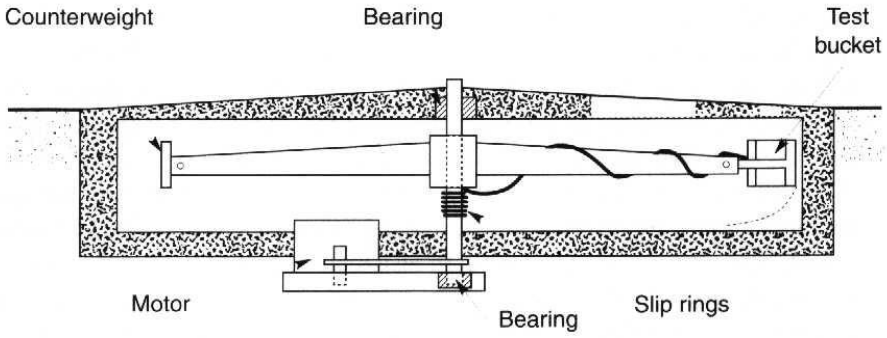

Figure 2.12. Cross-section through a geotechnical centrifuge. [5]

While the centrifuge is spinning, a shaking table can be mounted on the end of the arm and it can be vibrated, sending pressure and shear waves up through the model mounted on the shaking table. This emulates a real earthquake and the waves propagated up through the soil and by the help of this procedure not only static behavior but also the dynamic behavior of reinforced soil structures can be investigated.

2.2.2. Previous Studies on Centrifuge Tests of RS-RWs

By Goodings and Santamarina (1987), several reinforced soil retaining wall models were tested centrifugically and the effect of the retained fill and the foundation on the performance of walls was studied. In their studies, they adopted the π groups; w/d, $\delta h/\delta v$, $\delta v/H$, $t_w/(\delta h.\delta v)$, where w is the reinforcing strip width, d is the grain diameter, δh and δv are the horizontal and vertical spacing of the strips, H is the wall height and t_w is the reinforcing strip thickness. A certain dimensionless ratio ψ_{ws}, the index of wall safety against strip breakage, was adopted and defined as $\psi_{ws}=(N_f\gamma HK_a\delta h\delta v)/F$, where F is the tensile strength of a strip in units force, N_f is the centrifugal acceleration at failure in multiples of Earth's gravity, γ is the unit weight of the backfill, and K_a is the active earth pressure coefficient for the backfill. If ψ_{ws} =1 when a wall collapses due to strip breakage, then it is accurate portrayal of the forces in the wall; if it is greater than one, then the forces causing failure are less than those considered and a design based on ψ_{ws} would be conservative. Aluminum foil for the reinforcing strips and the skin was selected and acceleration was increased slowly on a 1.2-m-radius 10-g-ton Genisco centrifuge until

catastrophic failure of the retaining wall occurred at N_f gravities. Two series of models, the tall model (L/H=0.76) and the short model (L/H=1.36) were tested. In tall models, the height of the walls H is taken to be 144 mm; δv=16mm; δh=30mm; and w=8mm, whereas in short models H=80mm; δv=16mm; δh=50mm; and w=8mm. In conclusion, for tall models, which are similar to prototype walls, the effect of the retained fill on the overall internal stability of the wall was found to be small. Short models were more sensitive to changes in retained fill, possibly due to a distribution of reinforcing strips that did not lead to efficient reinforcing of the soil. The influence of vertical shear from the retained fill acting on the back of the wall was highlighted. In both tall and short models, the foundation was found to have greater effect than typically assumed and soft foundations led to superior wall performance [6].

Centrifuge model tests, by Porboha and Goodings (1995) were performed to study the behavior of soil retaining walls reinforced with a nonwoven geotextile stimulant and backfilled with cohesive soil. Models were constructed on either firm or rigid foundations reinforced with different lengths of reinforcement, and loaded to failure under increasing self weight in the geotechnical centrifuge. Since the failure mechanisms and the prototype equivalent heights at failure are interconnected functions of reinforcement length, they tested the models against the overturning failure and rotational sliding failure types. They constructed a 152 mm high model. Unreinforced vertical models on firm foundations failed by overturning at prototype equivalent height of 5.3m. In this mode of failure a block of soil at the front of the model toppled forward, rotating around the toe of the wall. When the wall was reinforced with geotextile length equal to 0.5H, the prototype equivalent height increased to 6.1m and failure occurred not by toppling but by rotational sliding, in which a block of soil mass slipped along a concave upwards surface. In conclusion, results showed that when backfill is cohesive soil, to derive maximum benefit from the presence of the geotextiles, the length of the reinforcement for vertical walls should be at least 75% of the height to contain the failure surface within the reinforced zone. Regarding the foundation rigidity, the reinforced models on firm foundations showed higher prototype equivalent heights at failure when compared to the identical models with rigid foundations [7].

A centrifuge testing program was undertaken to investigate the failure mechanism of geosynthetic reinforced soil slopes and to evaluate the assumptions in their design by

Zornberg et al. (1998). Scaling laws were established so that factors of safety in the models would be identical to those in the prototype structures. Their adopted scaling laws are described briefly as in the following:

For simplicity, the Ordinary Method of Slices (Fellenius, 1936), which only satisfies equilibrium of moments for a circular failure surface, is considered in the limit equilibrium expressions stated below. The Factor of Safety (FS) of the prototype is calculated as the division of the sum of the Moments resisting slope failure by the sum of the Moments driving slope failure, which is

$$FS_p = \frac{\sum (A_i.\rho.g).\cos\theta_i.\tan\phi.R + \sum T_j y_j}{\sum (A_i.\rho.g).\sin\theta_i.R} \tag{2.3}$$

where (A_i.ρ.g) = weight of slice I per unit length of slope; A_i = area of slice I; ρ = soil density; g = acceleration due to gravity; θ_I = angle from horizontal to tangent at center of slice I; R= radius of the failure of the failure circle; ϕ= soil friction angle; T_j= tensile strength of the reinforcement j; and y_j= moment arm for reinforcement j. Similarly, Factor of Safety of the model FS_m is described as

$$FS_m = \frac{\sum (A_{im}.\rho_m.g_m).\cos\theta_i.\tan\phi_m.R_m + \sum T_{jm} y_{jm}}{\sum (A_{im}.\rho_m.g_m).\sin\theta_i.R_m} \tag{2.4}$$

where the variables with subscript m refer to the model. The following relations between the model and the prototype are:

$$A_{im} = (\alpha_L)^2.A_i \tag{2.5}$$

$$g_m = \alpha_g.g \tag{2.6}$$

$$R_m = \alpha_L.R \tag{2.7}$$

$$y_{jm} = \alpha_L.y_j \tag{2.8}$$

where α_L = scale factor for the linear dimensions; and α_g = scale factor for the acceleration. It is noted that a model built with a scale α_L = 1/N requires that the acceleration caused by the gravity be scaled by α_g = N in order to bring the model to prototype stress levels. Incorporating Equations 2.5, 2.6, 2.7, 2.8 into Equation 2.4, the Factor of the Safety for the model can be given as

$$FS_m = \frac{\sum (A_i.\rho_m.g).\cos\theta_i.\tan\phi.R + \sum \left[\frac{T_{jm}}{(\alpha_L)^2.\alpha_g} \right].y_j}{\sum (A_i.\rho_m.g).\sin\theta_i.R} \tag{2.9}$$

Since similarity between the failure responses of model and prototype requires that

$$FS_m = FS_p \tag{2.10}$$

the scaling relationships for the analysis of cohesionless reinforced slopes can be established by comparing Equation 2.3 and Equation 2.4. This comparison shows that the following similitude requirements should be satisfied:

$$\rho_m = \rho \tag{2.11}$$

$$\tan\phi_m = \tan\phi \tag{2.12}$$

$$T_{jm} = (\alpha_L)^2.\alpha_g.T_j = (1/N)^2.N.T_j = (1/N).T_j \tag{2.13}$$

From the condition at Equation 2.13, it is understood that, for an *N*th-scale reinforced slope model a planar reinforcement having 1/N the strength of the prototype reinforcement should be used.

By using these similitude rules and scaling laws, they constructed their models with a total height of 254 mm. Each model was a 228 mm high geotextile reinforced slope built over a 25.4 mm thick foundation layer and the slope face in all models was 1H:2V. The number and spacing of the reinforcements varied and all reinforcements had the same

length. They used two different relative sand densities to understand the importance of the soil shear strength on the behavior of the failure of the geotextile reinforced soil slope.

Their conclusions were as follows:

- Failure in the models was characterized by well-defined shear surfaces through the toe of the slope, which is in good agreement with current design methods for reinforced slopes based on limit equilibrium.
- Failure initiated at mid-height of the slopes, contradicting the assumptions in current design methods that failure should develop from the toe of the reinforced slopes.
- The location of the critical failure surfaces was found to be approximately the same for all models, which were built with different reinforcement spacing, reinforcement tensile strengths, and soil densities.
- Settlements on top of the structure during centrifuge testing were observed to depend on the properties of the backfill soil, but to be essentially independent of the tensile strength and spacing of the reinforcements.
- Important contribution to the stability of the models was provided by the overlapping layers, which failed by breakage instead of by pullout when intersected by the failure surfaces.
- The test results indicate that the stability of the reinforced slopes is governed by the peak shear strength and not by the critical state shear strength of the backfill soil. Because higher g-level at failure was observed in the models where higher relative density of the same soil were used. This was attributed to the late mobilization of the maximum shear strength along the failure surface in the model where soil having higher shear strength was used.
- Unlike the conventional triangular distribution of reinforcement tension with a maximum tension at the base of the slope, a new distribution of reinforcement forces with depth, consistent with the failure mechanism observed in the slope models, is proposed for the design of geosynthetic reinforced soil slopes, where the location of the maximum reinforcement tension in the proposed distribution depends on the inclination of the reinforced slope [8].

2.3. Shaking-Table Tests of RS-RWs

2.3.1. Shaking-Table Tests

Shaking table tests are the tests where earthquake motion can be simulated. The simulator can reproduce historical and artificial earthquakes and blasting activity. Also, cyclic and fatigue tests can be performed on the simulator. Most shaking tables utilize a single horizontal translation degree of freedom, but shaking tables with multiple degrees of freedom have also been developed. Shaking tables are usually displaced by servohydraulic actuators (Figure 2.13); their dynamic loading capacities are controlled by the capacity of the hydraulic pumps that serve the actuators. Large pumps and large actuators are required to produce large displacements of heavy models at moderate or high frequencies.

Shaking tables of many sizes have been used for geotechnical earthquake engineering research. Some are quite large, allowing models with dimensions of several meters to be tested. Thus shaking tables can often utilize actual, prototype soils rather than resorting to the smaller particle sizes often required for smaller scale model tests. For these large models, soils can be placed, compacted relatively easily, and instrumented relatively easily.

On the other hand, high gravitational stresses cannot be produced in a shaking table test. Though the contractive behavior associated with high normal stresses at significant depths can be simulated by placing soil very loosely during model preparation, the process of preparing such models is quite difficult. Because of the low normal stress levels, the contribution of factors that produce cohesive component of strength will be greater in the model than in the prototype [5].

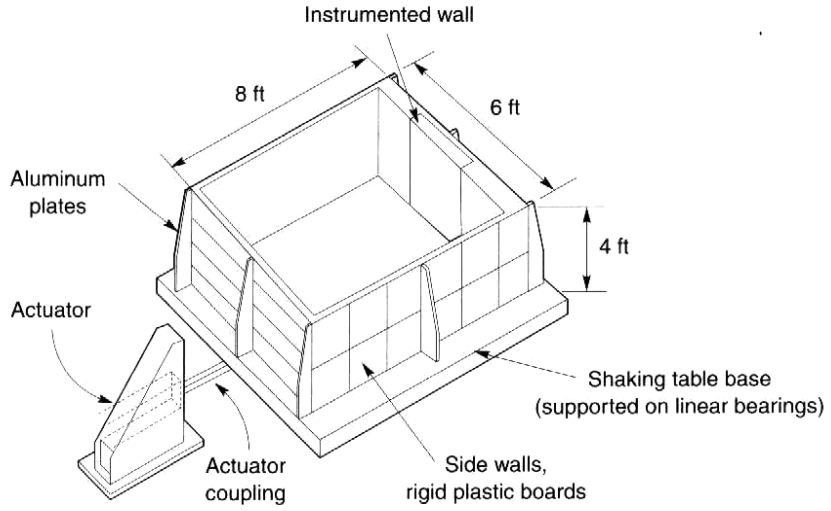

Figure 2.13. Shaking table with soil bin used for dynamic earth pressure research. [5]

2.3.2. Previous Studies on Shaking Table Tests of RS-RWs

Chida et al. (1985) performed series of shaking table tests of a half-scale model of a metal strip-reinforced soil wall. The physical model was constructed with four equal height incremental concrete panels for a total height of 3 m. A 1.4 m high-unreinforced slope fill was placed over the reinforced section that incorporated eight 4 m long steel strip reinforcement layers. The physical model was 5.2 m from the toe to the back of the shaking table container. Hence, the width of model to height of facing ratio was approximately 1.7 with only a 1.2 m column of unreinforced soil between the back of the reinforced soil zone and the back of the shaking table container. The back vertical boundary of the experiment comprised rigid wall attached directly to the shaking table. The toe of the wall was constrained horizontally. The model base was excited in a series of experiments using a sinusoidal input acceleration with different frequencies ranging from f = 2 to 7 Hz and peak base accelerations ranging from approximately a_{max} = 0.1g to 0.4g. Resulting maximum reinforcement loads were approximately the same magnitude in all layers and were observed to increase linearly with increasing peak base acceleration for frequencies less than approximately 0.4g. A maximum frequency of 7 Hz for a half-scale corresponds to approximately 5 Hz at prototype scale. They adopted a scale model frequency of $\sqrt{2}$ times the frequency of the prototype ($f_{scaled} = f_{prototype} \times \sqrt{2}$). For tests carried out with an estimated base acceleration of a_{max} = 0.4g at f = 2 Hz, and a_{max} = 0.17g

at f = 7 Hz, there was a non-uniform distribution of the dynamic load increment in the reinforcement layers with large values developed in the layers at the top of the structure. Here, the dynamic load increment in a reinforcement layer is the difference between the maximum tensile load under seismic loading and the maximum tensile load under static loading. Peak acceleration amplification between the base of the wall and the top of the wall was observed to increase by a factor of two at a frequency f = 5 Hz (f = 3 Hz at prototype scale).

Murata et al. (1994) reported the results of shaking table tests carried out on a reinforced embankment model with a crest width of 3.45 m and contained by two 2.5 m high walls constructed with gabion baskets and an outer continuous concrete panel. The model was subjected to harmonic motion and actual earthquake records. The harmonic record was observed to generate larger deformations than the earthquake record.

Sakaguchi (1996) performed shaking table tests on a 1.5 m high model test of a reinforced wall. The tests were constructed with lightweight blocks and five layers of geogrid reinforcement. The tests showed that wall displacements and permanent strains in the reinforcement accumulated with time during a 4 Hz sinusoidal base acceleration record applied for 7 seconds (peak accelerations up to approximately 0.5g were applied to the model). The reinforced zone was observed to act as a monolithic body with no evidence of a yield surface propagating across the reinforcement layers even after large wall displacements developed [9].

Matsuo et al. (1998) carried out shaking table tests on six geosynthetic-reinforced soil retaining wall (GRS-RWs) models. In their models, the geogrid reinforcement length, wall height, wall facing type, wall slope, and input acceleration waveform were varied in order to observe the behavior and the reinforcement mechanisms that occur in GRS-RWs. They tested 3 different models of GRS-RWs. Case 1 was the 1.00 m high and 1.64 m wide panel with vertical facings. The wall facings consisted of five discrete wooden facing panels that were each 40 mm thick and 200 mm high, and the geogrid reinforcement layers were 400 mm long with a vertical spacing of 200 mm. In case 2, longer geogrid layers were used (700 mm long). In case 3, the wall height, number of discrete facing panels, and length of the geogrid were %40 larger than in Case 1. Case 5 had a continuous facing

panel; the discrete panels were connected using two rigid steel bars. Case 6 had inclined facing panels (1V:0.2H). Each model was constructed in a rigid steel container with transparent acrylic plates on one side to enable visual observation. The container was 4 m wide, 2 m high and 1 m long. First, the firm, 200 mm thick foundation layer was prepared at the bottom of the container by compacting sandy silt with a water content of %16. The wall was built by compacting air-dried sand in 100 mm thick layers. The geogrid reinforcements were connected to the facing panels at mid-height using metal fittings, and the facing panels were interlocked with an overlap. The model walls were subjected to sinusoidal records with a frequency of 5 Hz and 20 cycles. Linear Variable Differential Transducers (LVDTs) were used to measure the front wall displacements and the strain gauges measured the strains of the geogrids, whereas the accelerometers and earth pressure cells were embedded in the wall and the foundation soil and were also attached to the facing panels. The pressure cells were positioned to measure the vertical earth pressures in the foundation soil, the horizontal earth pressures at the rear face of the reinforced soil, and the horizontal earth pressures acting on the facing panels. The results they obtained are as follows:

- For the model walls with vertical discrete panels, the reinforced soil mass moved forward due to shaking, the greatest displacement occurred at the mid-height area, and the bottom-facing panel inclined forward. A slip surface ran down into the backfill soil and into the lowest layer of the reinforced soil. The magnitude of the input acceleration at which the slip surface first appeared was the greatest for the model wall with the longest reinforcement.
- For the model wall with a continuous facing, the reinforced soil mass tilted forward with its deformation mode restricted by the rigidity of the continuous facing. A slip surface formed that was similar in shape to the slip surfaces in the walls with vertical discrete facings. The wall displacement was larger than that of the model walls with discrete facings.
- For the model walls with inclined facings, the slip surface was circular and the movement of the entire sliding block appeared to be rotational.
- When comparing the input acceleration amplitude required causing the same wall displacement, the acceleration of the wall subjected to an earthquake record was approximately %20 larger than that of the wall subjected to a sinusoidal record. But,

surely one must not forget that the predominant frequency of the input motions has a significant effect on the induced displacements.

- When the model was vibrated at an input acceleration large enough to induce plastic deformation, the amplitude of the response acceleration within the potential sliding block in the direction toward the back side of the wall was smaller than that of the input acceleration.
- For the models walls with discrete facings, the increase in both the earth pressure acting on the wall and the tensile force in the geogrid reinforcement was significant at the bottom of the wall. In contrast, for the model wall with a continuous facing, the increase was constant with depth.
- For the models walls with discrete facings, the earth pressure acting on the back of the reinforced soil mass responded with double the frequency of the input acceleration, when the input acceleration was large.
- The results were compared with the results of the pseudo-static seismic stability analyses that are adopted in the current Public Works Research Institute design manual. The results of this comparison demonstrated that, while the current design method provides a certain margin of safety against the failure of reinforced soil walls, it is important to determine the factors of safety with which reinforced walls do not suffer any detrimental deformation.
- Using the cumulative damage method to calculate permanent deformation, the displacement of the model wall subjected to an earthquake record was predicted from test data of the model subjected to a sinusoidal record: the predicted wall displacement was only approximately one fifth of the measured displacement. The cumulative damage method does not consider the difference in frequency of the input wave, which may explain why a smaller displacement value was calculated for the wall subjected to an earthquake record [10].

M.M. El-Emam et al. (2001) investigated the behavior of reinforced soil walls under seismic loading using shaking table tests and numerical simulation, giving particular emphasis on wall footing toe restraint conditions. Two different facing toe arrangements were used. It was either hinged (restrained in the vertical and horizontal directions, while free to rotate) or sliding (restrained in the vertical direction only and free to rotate and slide horizontally). Mainly, their investigation was focused on the influence of the toe boundary

condition on lateral displacements, reinforcement loads, toe loads and acceleration amplification in the backfill. They performed a series of shaking table tests to fourteen 1-m high 1/6 reduced-scale reinforced soil retaining wall models. In order to predict the behavior of equivalent (prototype) models at full scale, the model walls were designed according to the simulation rules proposed by Iai (1989). The reinforcement (knitted geogrid polyster) vertical spacing for the models was S_v = 0.23 m and the reinforcement length, L, was chosen to give L/H = 0.6, where H is the height of the model. The model walls were constructed with different toe boundary conditions and loaded to failure using a stepped-amplitude harmonic excitation record of 5 Hz. The actuator stroke was increased at 5 second intervals to generate an equivalent incremental base acceleration of 0.05g until excessive model deformation occurred. The facing panel was constructed using rectangular hollow steel sections with cross section dimensions 75 mm by 38 mm. A total of 26 sections were bolted together to form a 1 m-high rigid facing with a thickness of 75 mm and length of 1.4 m. Many instruments were installed in each test wall to monitor: a) facing horizontal movements; b) reinforcement displacements and strains; c) horizontal and vertical toe loads; and, d) facing and backfill acceleration response at different elevations. The cable-extension position transducers (extensometers), the strain gauges and accelerometers were the principal measuring devices attached and placed to several locations of the retaining wall. Extensometers were used to measure facing displacements during base shaking, whereas the strain gauges and accelerometers were utilized to measure strains of geosynthetics and accelerations at the facing, in the backfill and at the table, respectively. The conclusions reached were as follows:

- The displacement response for the model wall with a sliding toe was greater than the response of the model with a hinged toe when base acceleration amplitude exceeded 0.3g.
- The vertical toe load was found to be greater than the facing self-weight throughout each experiment, due to downdrag forces, and increased as the input base acceleration increased. Downdrag forces are the forces that occur from the frictional shear forces developed between the soil and the facing column as well as the vertical component of forces at the connections due to settlement of the soil behind the facing.

- The type of toe boundary condition did not influence the magnitude of vertical toe loads generated at end of construction (static) and under dynamic loading.
- The footing for models with a restrained toe attracted approximately 50% of the static and dynamic horizontal earth force acting at the back of the facing panel. Also, reinforcement load in the bottom reinforcement layer was greater for the unrestrained toe case compared to the hinged toe case.
- Input base acceleration was amplified towards the backfill surface. The amplification factor was found to be 1.2 for input accelerations lower than 0.3g and increased sharply to about 2.2 for greater input base acceleration amplitudes. The trend of increasing amplification factor with increasing base acceleration is reversed from the trend reported in the literature for reduced-scale reinforced soil walls constructed with relatively in-extensible reinforcement layers.
- Overall, the shaking table model test results of the model walls were found to be in close agreement with the measured data of the numerical analysis calculations done with the FEM program Flac [11].

Large scale shaking table tests were reported by Hoe I. Ling et al (2005). The large-scale shaking table facility at the Japan National Research Institute of Agricultural Engineering was used. The tested three walls were 2.8 m high, constructed on a soil foundation 20 cm thick. The foundation was of the same type of sand as the backfill. The steel container, which was designed to accommodate the wall, was 2 m in width and 4 m in depth. To prevent waves reflecting from the steel walls during shaking, expanded polystyrene boards 10 cm thick were placed at the front and back ends of the steel container. Three large scale 2.8 m high modular-block geosynthetic-reinforced soil walls were subjected to significant shaking using the Kobe earthquake motions. Each wall was excited with a one-dimensional horizontal maximum acceleration of 0.4g followed by 0.86g. The summary and conclusions were:

- The reinforced soil retaining walls showed negligible deformation under simulated moderate earthquake (peak acceleration of 0.4g). Under very strong shaking of 0.86g, the walls performed well. The third wall that had a longer top geogrid layer of 90 per cent the wall height, which was grouted in between top two courses of blocks, gave the best performance eventhough its overall reinforcement length was

only 60 per cent the wall height. Thus, the wall performance under earthquake shaking could be improved by increasing the length of the top reinforcement layer, reducing vertical reinforcement spacing, and grouting the top blocks to ensure firm connection to the reinforcement. Longer reinforcement layer inhibits the formation of tension cracks with in the reinforced mass. The optimal reinforcement length and spacing may be determined through parametric studies upon validation of numerical procedures.

- Under earthquake loading, the lateral displacement was largest at the top of the wall. A larger settlement occurred in the unreinforced zone of the backfill, very likely to slight lateral slide of the reinforced (coherent) mass. The amplification ratio of the walls was less than 1.35 under a peak acceleration of 0.86g. The facing blocks and reinforced soil zone gave similar response without showing phase lag.
- The vertical motions of Kobe earthquake did not much affect the wall deflection and acceleration, but increased the vertical stress under the backfill and blocks, the reinforcement load, and the connection load [12].

2.4. The Finite Element Method (FEM) Analysis of RS-RWs

2.4.1. FEM Method

The finite element method (FEM) has been utilized to analyze different types of geotechnical structures, such as earth dams, embankments, shallow and deep foundations, slopes and retaining walls. However, still the application of the finite element method to RS-RWs is relatively recent. Because reinforced soil systems are complex systems that involve determining the interaction between different structural components and soil, determining these parameters is sophisticated and design is rare. However, finite element analysis renders additional information compared to traditional limit-equilibrium analysis, such as deformation and tensile load in the reinforcement layers that are necessary for understanding the performance of reinforced soil structures. The results obtained from finite element analysis can be used to guide the development of more accurate limit-equilibrium design procedures.

Finite element analysis of reinforced soil structures can be conducted using computer programs that simulate soil-structure interaction, i.e. programs that have the relevant soil and structural elements and material models. The program should be able to simulate the construction sequences, such as backfilling and the installation of reinforcement layers and wall facings. Modern FEM methods use a discrete approach because computing costs have significantly reduced. In a discrete analysis, the reinforcement, soil and facing, and their interactions are modeled separately.

2.4.2. Previous Studies on Seismic Analysis of RS-RWs with FEM

Bathurst and Hatami (1998) carried out numerical experiments on a reinforced soil wall using the two-dimensional, explicit dynamic finite difference program Fast Lagrangian Analysis of Continua (FLAC). The reference continuous panel wall is 6.0 m high with six uniformly spaced reinforcement layers. The wall facing was modeled as a continuous concrete panel with a thickness of 0.14 m. The panel was either hinged at its base or free to slide horizontally. The soil was modeled as a purely frictional, elastic-plastic material with a Mohr-Coulomb failure criterion and non-associated flow rule. The friction angle of the soil was $\phi = 35°$ and dilatancy angle $\psi_s = 6°$, and unit weight $\gamma = 20$ kN/m^3. For simplicity and reduction of computation time, the elastic modulus was held constant for the duration of numerical experiment including construction. The reinforcement layers were modeled using linear, elastic-plastic cable elements with negligible compressive strength and an equivalent cross-sectional area of 0.002 m^2. The interface between the reinforcement and the soil was modeled by a grout material of negligible thickness with an interface friction angle $\delta_g = 35°$. The bond stiffness and bond strength of the grout were taken as $k_b = 2\times10^6$ MN/m/m and $s_b = 10^3$ kN/m, respectively. The interface and grout properties were selected to simulate a perfect bond between the soil and reinforcement layers. The wall-soil interface was modeled using a thin soil column, 0.05 m thick, directly behind the facing panel. The soil-wall interface column material was assigned a friction angle $\phi_i = 20°$, and a dilatancy angle $\psi_i = 0$. A similar thin soil layer was introduced at the base of the soil region but was assigned the same properties as the reinforced and retained soil materials. Because FLAC does not allow assigning zero-thickness interfaces in combination with intersecting free-field boundaries used in dynamic modeling, this procedure was adopted. Either a typical minimum reinforcement ratio of L/H = 0.7 for static design of reinforced soil walls

(e.g. FHWA 1996) or L/H = 1 was applied to the model. The yield strength of the reinforcement was kept constant at T_y = 200 kN/m, but the Elastic Modulus *J*, varied from 500 kN/m to 69000 kN/m. After static equilibrium was reached, the full width of the foundation was subjected to the variable-amplitude harmonic ground motion record. This acceleration record was applied horizontally to all nodes at the bottom of the soil zone at equal time intervals of Δt = 0.05 sec. The accelogram has both increasing and decaying peak acceleration portions and is expressed as:

$$\ddot{U}(t) = \sqrt{\beta.e^{-\alpha.t}.t^{\xi}}.\sin(2.\pi.f.t) \tag{2.14}$$

where: α=5.5, β= 55, ξ= are constant coefficients and *f* is frequency and *t* is the time. The peak amplitude is 0.2 g and the frequency is f = 3 Hz. This was a typical predominant frequency of medium to high frequency content earthquakes. A frequency of 3 Hz was chosen to give stable numerical results in all simulations while generating large displacements and large reinforcement loads within a relatively short simulation time (6 seconds). Elgamal et al. (1996) have proposed that for conventional reinforced cantilever wall-backfill systems less than 10 m in height, and subject to typical situations of seismic excitation, a viscous damping ratio of c = 5% is conservative. So, a damping ratio of c = 5% was chosen for the reference case but several analyses with damping ratios of %10 and %20 were also carried out. The conclusions and the results reported are as follows:

- Wall displacements and reinforcement loads accumulated during base shaking.
- The magnitude of total wall displacement at the wall crest and relative wall displacement with respect to the wall toe at the end of the base excitation were less for a reinforced wall that was free to slide at the base than for a wall that could only rotate about the toe.
- With increasing reinforcement stiffness and length the magnitude of permanent wall displacement diminished and the greatest influence on the magnitude of the wall displacement was the foundation condition (hinged or free to slide condition).
- Wall-Soil interface soil column worked well by satisfying the maximum reinforcement loads being generated at the connections.

- The harmonic input motion resulted in additional tensile loads being generated in reinforcement layers that were significantly larger than values resulting from static loading alone. The magnitude of additional dynamic loads in reinforcement layers was observed to increase with increasing stiffness of the reinforcement.
- For walls with sliding base, dynamic load increments increased in generally linear fashion with depth below the crest of the wall regardless of reinforcement stiffness. For walls with a fixed base, the dynamic load increments did not increase with depth and were attenuated in the lower layers for walls with reinforcement stiffness J≤ 2000 kN/m. For stiffer reinforcements, a linear trend of the dynamic reinforcement loads similar to that noted for sliding-base cases was observed.
- Horizontal ground acceleration was amplified with height above the base foundation. The amplification factor ranged from 2 to 2.8 for models with a damping ratio of 5%.
- The soil in the retained zone was observed to yield during shaking and the inclination of the failure surface in this region was reasonably well predicted by Mononobe-Okabe theory.
- There was no evidence of an interior shear surface propagating from the heel of the facing panel and intersecting all reinforcement layers as is assumed in conventional pseudo-static methods of analysis [9].

Additionally, briefly it can be noted that the reference harmonic base input acceleration record are strongly influenced by the magnitude of the damping ratio of the soil and the type of far-end boundary condition adopted. However, the greatest influences on wall response are the choice of base ground motion record and the difference between the frequency of the base excitation record and the fundamental frequency of the model. The applied frequency of base excitation is close to the fundamental frequency of the model, so large displacements and reinforcement loads were reported in this paper.

Ling et al. (2000) used the finite element program M-CANDE to conduct finite element analysis of the full-scale geosynthetic reinforced retaining wall that was built at the Public Works Research Institute (PWRI), Ministry of Construction, in Japan. The wall was 6 m high and 5 m wide and was constructed in a concrete test pit with a concrete floor.

The sidewalls of the test facility were lubricated grease and polymer sheets. Silty sand was used as the backfill. A uniaxial geogrid manufactured from the extruded high-density polymer is used as the soil reinforcement. The geogrid reinforcements were bolted to the concrete blocks by using bolts and metal frames. Each block was 50 cm high and 35 cm wide. Several strain gages were mounted to measure the strains of the geogrids and LVDTs were placed onto several locations of the wall face and lateral displacements were measured. The vertical and horizontal loads acting at the toe of the facing were also measured using load cells. The M-CANDE program is capable of performing out of plane strain analyses under static load conditions. The program can simulate the construction sequence and inclusion of the reinforcement and interface elements in each solution increment. In each increment of analysis, the solution is iterated to a user-selected convergence criterion at the element level. The foundation, backfill, and facing blocks were modeled by quadrilateral elements. The backfill was modeled using a nonlinear elastic soil model (Duncan et al. 1980) with a variable Young's modulus and a constant Poisson's ratio. A linear elastic model was used for the concrete foundation and concrete blocks. Poisson's ratio was taken as 0.17. The geosynthetic reinforcement was simulated using one-dimensional elements having non-linear material properties. The tangent stiffness of the geosynthetic element, J_{tan}, is obtained from the following expression, which is based on the hyperbolic load-strain, T-ε, relationship (Ling et al. 1995):

$$J_{\tan} = j_o\left(1-\lambda\frac{T}{T_f}\right)^2 \tag{2.15}$$

where: J_o=initial stiffness; T=reinforcement tensile load; T_f = failure tensile load; and λ = failure ratio. Three node interface elements were used to model the interactions at the concrete block-concrete block and concrete block-backfill soil interfaces. The slippage or debonding of an interface element is based on the Coulomb failure criterion. The model requires two property values: the interface friction angle, δ, and the tensile strength normal to the interface, T_c. The concrete block-concrete block and concrete block-backfill soil interactions were studied using a large direct shear device. The soil-geogrid interaction was not used because the geogrids were assumed to be fully bonded to the soil. After the FEM analysis was performed and the results were compared, they reached to a conclusion that

the finite element model was able to give satisfactory agreement between the measured and predicted results and the simulations of additional well-instrumented walls should be attempted [13].

Ling et al. (2004) conducted Finite Element Analysis for both PWRI (Public Works Research Institute Wall in Japan) and centrifuge walls under two-dimensional using a modified version of Diana-Swandyne-II (Chan 1993;Zienkiewicz et al. 1998). They opted a generalized plasticity model for granular soil and the geosynthetic model for expressing the monotonic and cyclic behavior of soil and reinforcement. For the soil, the generalized plasticity model required 15 parameters for simulating cyclic loading, whereas 11 of these parameters could be obtained from static tests. For the geogrid reinforcements, Ling et al. (2001b) formulated a bounding surface model to simulate the uniaxial cyclic behavior of geogrids. A total of nine parameters required for cyclic loading, whereas in the case of monotonic loading five parameters were sufficient. The dynamic analysis was initiated using the input motion at the base of the mesh. In the dynamic analysis, the time integration was performed using the generalized Newmark method (Katona and Zienkiewicz 1985) with coefficients $\beta_1 = 0.6$ and $\beta_2 = 0.605$. In addition to material damping that is simulated by the constitutive models, system viscous damping (Rayleigh damping) was considered in the analyses for the sand and interface (5%), rubber (%10), and aluminum (%5), where the values were determined based on the fundamental frequency of reinforced soil walls. No system damping was assigned to the geogrid. The analysis was iterated to convergence with a tolerance of 0.05 using the norm of relative displacements. As a result, the comparison of numerical and experimental results showed that the finite element procedure was able to simulate the construction behavior as well as dynamic behavior favorably. The results of analyses confirmed that the length and spacing of reinforcement played an important role in minimizing wall deformations and strains in the reinforcements [14].

3. DESIGN OF GEOSYNTHTIC REINFORCED SEGMENTAL RETAINING WALLS

3.1. Static and Seismic Earth Pressures acting on Retaining Walls

The earth pressure theories describe about the condition to develop a state of limit equilibrium in the soil. The forces and pressures acting on a wall are in fact highly indeterminate. Static equilibrium equations are insufficient to obtain a solution for lateral forces; additional assumptions must be incorporated in the analysis. For nonlinear materials such as soils, this is commonly and conveniently done by assuming that a "limit" or failure state exists along some surface and that the shear force along the surface corresponds to the shear strength of the material. With these assumptions, equilibrium equations can be solved. Hence, this approach is commonly called "limit-equilibrium analysis." To assure that the assumed failure does not in fact occur, a factor (safety factor or strength mobilization factor) is applied to the material strength. It should be noted that this solution approach differs significantly from that commonly used for indeterminate structural analysis, where stress-strain properties and deformations are employed. This limit-equilibrium approach provides no direct information regarding deformations; it is implied that deformations are sufficient to induce the failure condition. Deformations are indirectly limited to tolerable values by judicious choice of a safety factor.

The seismic behavior of retaining walls depends on the total lateral earth pressure that develops during earthquake motion. These total pressures include both the static gravitational pressure that exist before the earthquake and transient dynamic pressures induced by the earthquake as well.

3.1.1. Static Earth Pressures acting on Retaining Walls

Static earth pressures on retaining structures are influenced by wall and soil movements. The two types of static pressures, active and passive develop according to the movement of the wall. The minimum horizontal pressure condition, or active earth pressure, develops when a wall rotates about its base and away from the backfill an amount

on the order of 0.001 to 0.003 radian (a top deflection of 0.001 to 0.003h, where h is the wall height). As the wall moves, horizontal stresses in the soil are reduced and vertical stresses due to backfill weight are carried by increasing shear stresses until shear failure is imminent. If a wall is moved toward the backfill, horizontal stresses increase and shear stresses reverse direction, first decreasing and then increasing to a maximum at failure. Because the horizontal stress component along the shear planes is resisted by both shear stress and vertical stress components, higher horizontal stresses can be developed than for the active pressure case. Development of the maximum possible horizontal stress, or passive pressure, requires much larger wall rotations than for the active case, as much as 0.02 to 0.2 radians.

The approaches of Rankine (1857) and Coulomb (1776) are widely used in most of the practices.

3.1.1.1. Rankine's Theory. If the vertical wall is frictionless and the retained earth materials are level, homogeneous, isotropic (similar stress-strain properties in all directions or in practical terms, not reinforced), semi-infinite and characterized by the Mohr–Coulomb strength criterion (i.e.,$\tau = c+\sigma\tan\phi$), the limiting states of stress can be estimated using Rankine [1857] earth pressure theory. The minimum active earth pressure is:

$$P_a = K_A\sigma_v^{'} - 2c\sqrt{K_A} \tag{3.1}$$

where K_A is the coefficient of minimum active earth pressure; $\sigma^9{}_v$ is the vertical effective stress at the point of interest, and c is the cohesive strength of the soil.

When the principal stress planes are vertical and horizontal (as in the case of a smooth vertical wall retaining a horizontal backfill), the coefficient of minimum active earth pressure is given by:

$$K_A = \frac{1-\sin\phi}{1+\sin\phi} = \tan^2\left(45^\circ - \frac{\phi}{2}\right) \tag{3.2}$$

In the case of cohesionless backfill inclined at an angle β with the horizontal, infinite slope solutions can be used to compute K_A as:

$$K_A = \cos\beta \frac{\cos\beta - \sqrt{\cos^2\beta - \cos^2\phi}}{\cos\beta + \sqrt{\cos^2\beta - \cos^2\phi}} \text{ for } \beta \leq \phi \tag{3.3}$$

For dry homogenous cohesionless backfill, Rankine's theory predicts a triangular active pressure distribution oriented parallel to the backfill surface (Figure 3.1). The active earth pressure resultant, P_A, acts at a point located H/3 above the base of a wall of height, H, with magnitude of:

$$P_A = \frac{1}{2} K_A \gamma H^2 \tag{3.4}$$

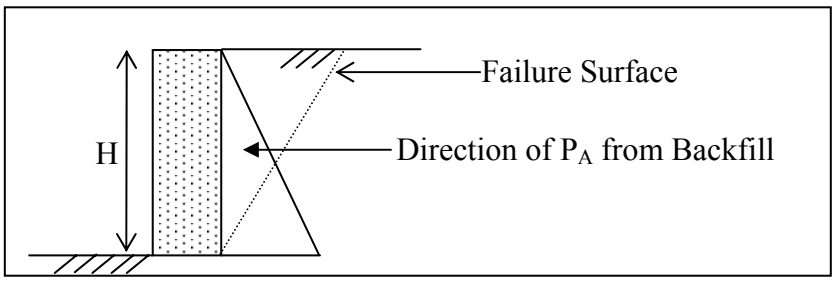

Figure 3.1. Active earth pressure by Rankine

The angle of the shear plane with respect to horizontal is (45 + ϕ/2), measured from the heel of the wall.

Under maximum passive conditions, Rankine theory predicts wall pressure given by:

$$P_P = K_p \sigma'_v + 2c\sqrt{K_p} \tag{3.5}$$

where K_p is the coefficient of maximum passive earth pressure and c is the cohesion.

For smooth, vertical walls retaining horizontal backfills,

$$K_p = \frac{1+\sin\phi}{1-\sin\phi} = \tan^2\left(45° + \frac{\phi}{2}\right) \tag{3.6}$$

and for backfills inclined at β with the horizontal,

$$K_p = \cos\beta \frac{\cos\beta + \sqrt{\cos^2\beta - \cos^2\phi}}{\cos\beta - \sqrt{\cos^2\beta - \cos^2\phi}} \tag{3.7}$$

For dry homogenous backfill, Rankine's theory predicts a triangular passive pressure distribution oriented parallel to the backfill surface. The passive earth pressure resultant, or passive thrust, P_p, acts at a point located H/3 above the base of a wall of height, H, with magnitude of:

$$P_p = \frac{1}{2} K_P \gamma H^2 \tag{3.8}$$

In this case, the angle of the shearing plane measured from the heel with respect to horizontal is (45 - ϕ/2).

3.1.1.2. Coulomb's Theory. Coulomb [1776] solved the lateral earth pressure problem assuming a homogeneous, isotropic material, rough wall, planar failure surface, and Mohr–Coulomb strength criterion. The Coulomb theory provides a method of analysis that gives the resultant horizontal force on a retaining system for any slope of wall, wall friction, and slope of backfill provided β≤ϕ. A wide range of earth pressure problems can be solved using the force polygon technique implied in Coulomb's method. The closed-form solution for the minimum active earth force for a general case including dry, cohesionless material, inclined rough wall, and sloping backfill is presented in Figure 3.2.

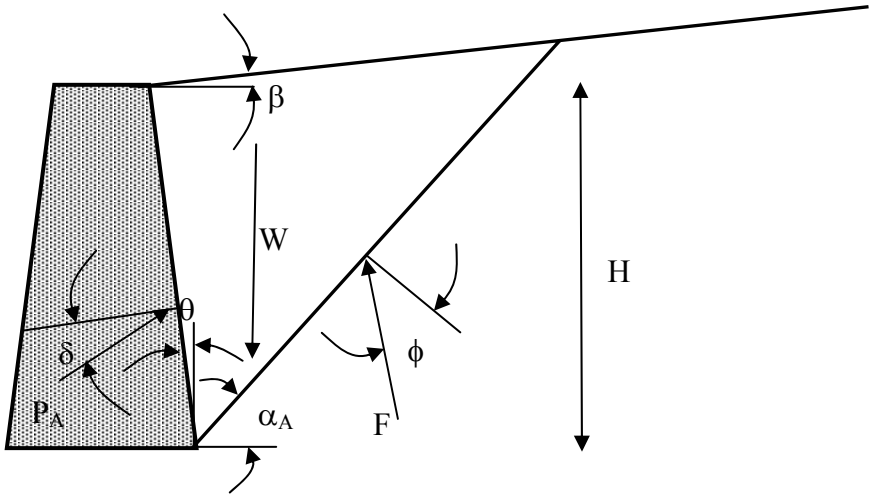

Figure 3.2. Diagram showing earth pressure acting on the wall

Under the minimum active earth pressure conditions, the active thrust on a wall with the geometry as shown in the previous Figure 3.2 is obtained from force equilibrium. For the critical failure surface, the active thrust on a wall retaining cohesionless soil can be expressed as:

$$P_A = \frac{1}{2} K_A \gamma H^2 \tag{3.9}$$

where $K_A = \dfrac{\cos^2(\phi - \theta)}{\cos^2\theta \cos(\delta + \theta)\left[1 + \sqrt{\dfrac{\sin(\delta + \phi)\sin(\phi - \beta)}{\cos(\delta + \theta)\cos(\beta - \theta)}}\right]^2}$ (3.10)

in which δ is the angle of interface friction between the wall and the soil; β is the backslope angle (from horizontal) and θ is the wall inclination. The critical failure surface is inclined at an angle to the horizontal by:

$$\alpha_A = \phi + \tan^{-1}\left[\frac{\tan(\phi - \beta) + C_1}{C_2}\right] \tag{3.11}$$

where:

$$C_1 = \sqrt{\tan(\phi - \beta)\left[\tan(\phi - \beta) + \cot(\phi - \theta)\right]\left[1 + \tan(\delta + \theta)\cot(\phi - \theta)\right]} \tag{3.12}$$

$$C_2 = 1 + \{\tan(\delta + \theta)[\tan(\phi - \beta) + \cot(\phi - \theta)]\} \tag{3.13}$$

P_A acts at a point located H/3 above the base of the wall of height H.

For maximum passive conditions in cohesionless backfills, Coulomb theory predicts a passive thrust:

$$P_p = \frac{1}{2} K_P \gamma H^2 \tag{3.14}$$

where:

$$K_p = \frac{\cos^2(\phi + \theta)}{\cos^2\theta \cos(\delta - \theta)\left[1 + \sqrt{\frac{\sin(\delta + \phi)\sin(\phi + \beta)}{\cos(\delta - \theta)\cos(\beta - \theta)}}\right]^2} \tag{3.15}$$

The critical failure surface for maximum passive earth pressure conditions is inclined to the horizontal at:

$$\alpha_P = -\phi + \tan^{-1}\left[\frac{\tan(\phi + \beta) + C_3}{C_4}\right] \tag{3.16}$$

where:

$$C_3 = \sqrt{\tan(\phi + \beta)[\tan(\phi + \beta) + \cot(\phi + \theta)][1 + \tan(\delta - \theta)\cot(\phi + \theta)]} \tag{3.17}$$

$$C_4 = 1 + \{\tan(\delta - \theta)[\tan(\phi + \beta) + \cot(\phi + \theta)]\} \tag{3.18}$$

In contrast to Rankine theory, Coulomb theory can be used to predict soil thrust on walls with irregular backfill slopes, concentrated loads on the backfill surface, and seepage forces. Coulomb wedge theory calculates less earth pressure than Rankine theory for a level backslope whereas the values converge under backslope conditions when $\delta = \beta$. Coulomb theory calculates a unique failure angle for every design condition whereas application of Rankine theory to reinforced soil structures fixes the internal failure plane at

45 + ϕ/2. If the shoring system is vertical and the backfill slope and wall friction angles are zero, Coulomb's equation will be the same as Rankine's for a level ground motion [15].

3.1.2. Mononobe-Okabe Pseudo-Static Approach for Seismic Earth Pressures acting on Retaining Walls

Okabe (1926) and Mononobe and Matsuo (1929) extended Coulomb's theory of static active and passive earth pressures to include the effects of dynamic earth pressures on retaining walls. The Mononobe-Okabe theory incorporates the effect of earthquakes through the use of a constant horizontal acceleration in units of g, $a_h = k_h.g$, and a constant vertical acceleration in units of g, $a_v = k_v.g$, acting on the soil mass comprising Coulomb's active wedge (or passive wedge) within the backfill as shown in Figures 3.3 and 3.4. The term k_h is the fraction of horizontal acceleration (horizontal inertial coefficient or seismic coefficient), k_v is the fraction of vertical acceleration (vertical inertial coefficient or seismic coefficient), and g is the acceleration of gravity. In the following figures, positive a_v values act downward, and positive a_h values act to the left. The acceleration of the mass in the directions of positive horizontal and positive vertical accelerations result in the inertial forces $k_h.W$ and $k_v.W$ as shown in the following figures, where W is the weight of soil wedge. These inertial forces act opposite to the direction in which the mass is accelerating. This type of analysis is described as a pseudostatic method of analysis, where the effect of the earthquake is modeled by an additional set of static forces, $k_h.W$ and $k_v.W$.

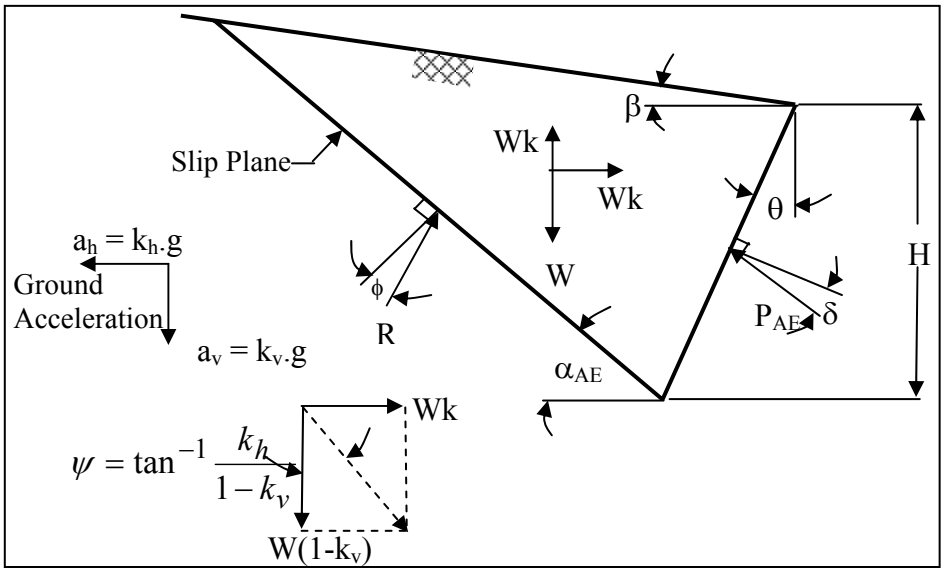

Figure 3.3. Mononobe-Okabe active wedge

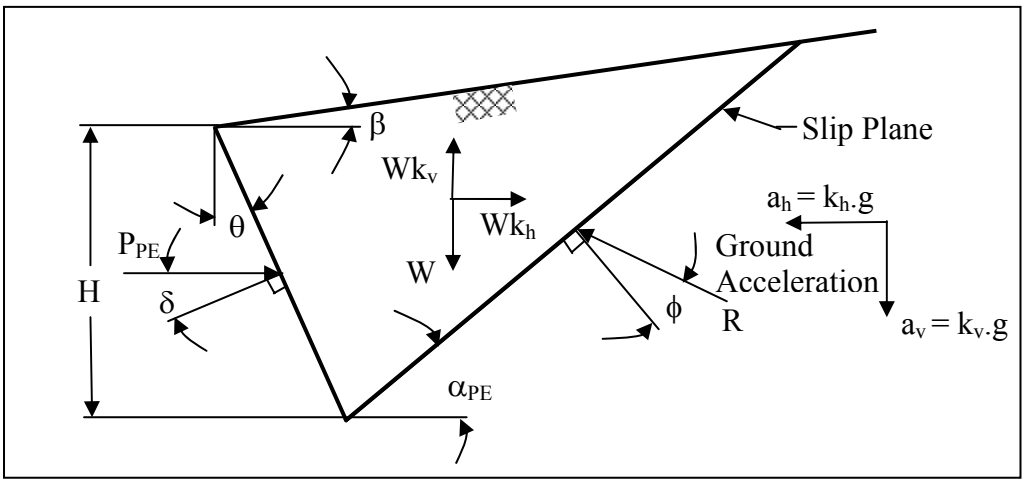

Figure 3.4. Mononobe-Okabe passive wedge

The Mononobe-Okabe theory gives the net static and dynamic force. For positive $k_h>0$, P_{AE} is larger than the static P_A, and P_{PE} is less than the static P_P.

The Mononobe-Okabe relationship for P_{AE} for dry backfills, given by Whitman and Christian (1990) is equal to:

$$P_{AE} = \frac{1}{2} K_{AE} [\gamma_t (1 - k_v)] H^2 \tag{3.19}$$

and acts at an angle δ from the normal to the back of the wall of height H. The dynamic active earth pressure coefficient, K_{AE}, is equal to:

$$K_{AE} = \frac{\cos^2(\phi - \psi - \theta)}{\cos\psi \cos^2\theta \cos(\psi + \theta + \delta)\left[1 + \sqrt{\frac{\sin(\phi + \delta)\sin(\phi - \psi - \beta)}{\cos(\delta + \psi + \theta)\cos(\beta - \theta)}}\right]^2} \tag{3.20}$$

and the seismic inertia angle, ψ, is equal to:

$$\psi = \tan^{-1}\left[\frac{k_h}{(1 - k_v)}\right] \tag{3.21}$$

The seismic inertia angle represents the angle through which the resultant of the gravity force and inertial forces rotated from the vertical.

The planar slip surface extends upwards from the heel of the wall through the backfill and is inclined at an angle α_{AE} from the horizontal. α_{AE} is given by Zarrabi (1978) to be equal to:

$$\alpha_{AE} = \phi - \psi + \tan^{-1}\left[\frac{-\tan(\phi-\psi-\beta)+C_{1AE}}{C_{2AE}}\right] \tag{3.22}$$

where

$$C_{1AE} = \sqrt{\tan(\phi-\psi-\beta)[\tan(\phi-\psi-\beta)+\cot(\phi-\psi-\theta)][1+\tan(\delta+\psi+\theta)\cot(\phi-\psi-\theta)]} \tag{3.23}$$

$$C_{2AE} = 1+[[\tan(\delta+\psi+\theta)][\tan(\phi-\psi-\beta)+\cot(\phi-\psi-\theta)]] \tag{3.24}$$

In the calculation of earth pressure using Equation 3.19, the vertical component was neglected as suggested by Seedman and Whitman (1970). Then the equation can be simplified as:

$$P_{AE} = \frac{1}{2}K_{AE}\gamma H^2 \tag{3.25}$$

The Mononobe-Okabe relationship for P_{PE} for dry backfill, given by Whitman and Christian (1990), is equal to:

$$P_{PE} = \frac{1}{2}K_{PE}[\gamma_t(1-k_v)]H^2 \tag{3.26}$$

and acts at an angle δ from the normal to the back of the wall of height H. The dynamic passive earth pressure coefficient, K_{PE}, is equal to:

$$K_{PE} = \frac{\cos^2(\phi - \psi + \theta)}{\cos\psi \cos^2\theta \cos(\psi - \theta + \delta)\left[1 - \sqrt{\frac{\sin(\phi + \delta)\sin(\phi - \psi + \beta)}{\cos(\delta + \psi - \theta)\cos(\beta - \theta)}}\right]^2} \quad (3.27)$$

The planar slip surface extends upwards from the heel of the wall through the backfill and is inclined at an angle α_{PE} from the horizontal. α_{PE} is equal to

$$\alpha_{PE} = \psi - \phi + \tan^{-1}\left[\frac{\tan(\phi + \beta - \psi) + C_{3PE}}{C_{4PE}}\right] \quad (3.28)$$

where

$$C_{3PE} = \sqrt{\tan(\phi + \beta - \psi)[\tan(\phi + \beta - \psi) + \cot(\phi + \theta - \psi)][1 + \tan(\delta + \psi - \theta)\cot(\phi - \psi + \theta)]} \quad (3.29)$$

$$C_{4PE} = 1 + [[\tan(\delta + \psi - \theta)][\tan(\phi - \psi + \beta) + \cot(\phi - \psi + \theta)]] \quad (3.30)$$

Seed and Whitman (1970) presented a simplified procedure for computing the dynamic active earth pressure on a vertical wall retaining dry backfill. They considered the group of structures consisting of a vertical wall ($\theta = 0$) retaining a granular horizontal backfill ($\beta = 0$) with ϕ equal to 35 degrees, $\delta = \phi/2$ and k_v equal to zero. P_{AE} is defined as the sum of the initial static active earth pressure force and the dynamic active earth pressure force increment,

$$P_{AE} = P_A + \Delta P_{AE} \quad (3.31)$$

where

$$\Delta P_{AE} = \Delta K_{AE} \frac{1}{2} \gamma_t H^2 \quad (3.32)$$

The dynamic active earth pressure coefficient is equal to

$$K_{AE} = K_A + \Delta K_{AE} \tag{3.33}$$

and

$$\Delta K_{AE} = \frac{3}{4} k_h \tag{3.34}$$

Using this simplified procedure, K_A is computed using Equation 3.10, and ΔK_{AE} is computed using Equation 3.34. All forces act an angle δ from the normal to the back of a wall, as shown in Figure 3.5. Also in Figure 3.6, the earth pressure distributions acting on the wall are depicted in detail. P_A acts at a height equal to H/3 to 0.6H, depending upon the value of k_h. The acting point of the earth pressure above the base of the wall can be found as:

$$Y = \frac{P_A \frac{H}{3} + \Delta P_{AE}(0.6H)}{P_{AE}} \tag{3.35}$$

The results of instrumented shake table tests conducted on model walls retaining dense sands show Δ_{PAE} acts at a height of between 0.43H and 0.58H, depending upon the mode of wall movement that occurs during shaking. The height of the model walls used in the shake table tests, as summarized in Matsuzawa, Ishibashi, and Kawamura (1985), were 2.5 feet and 4 feet.

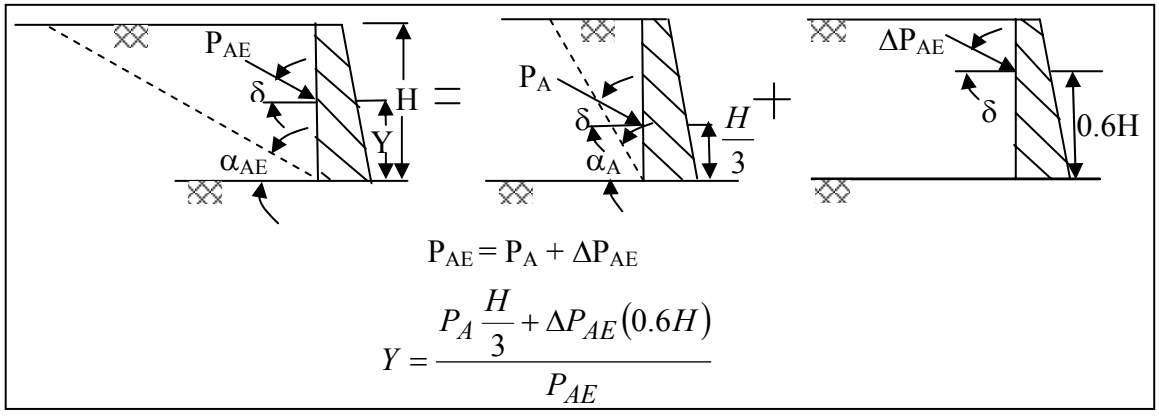

Figure 3.5. The acting locations of the static active and incremental dynamic active earth pressure forces

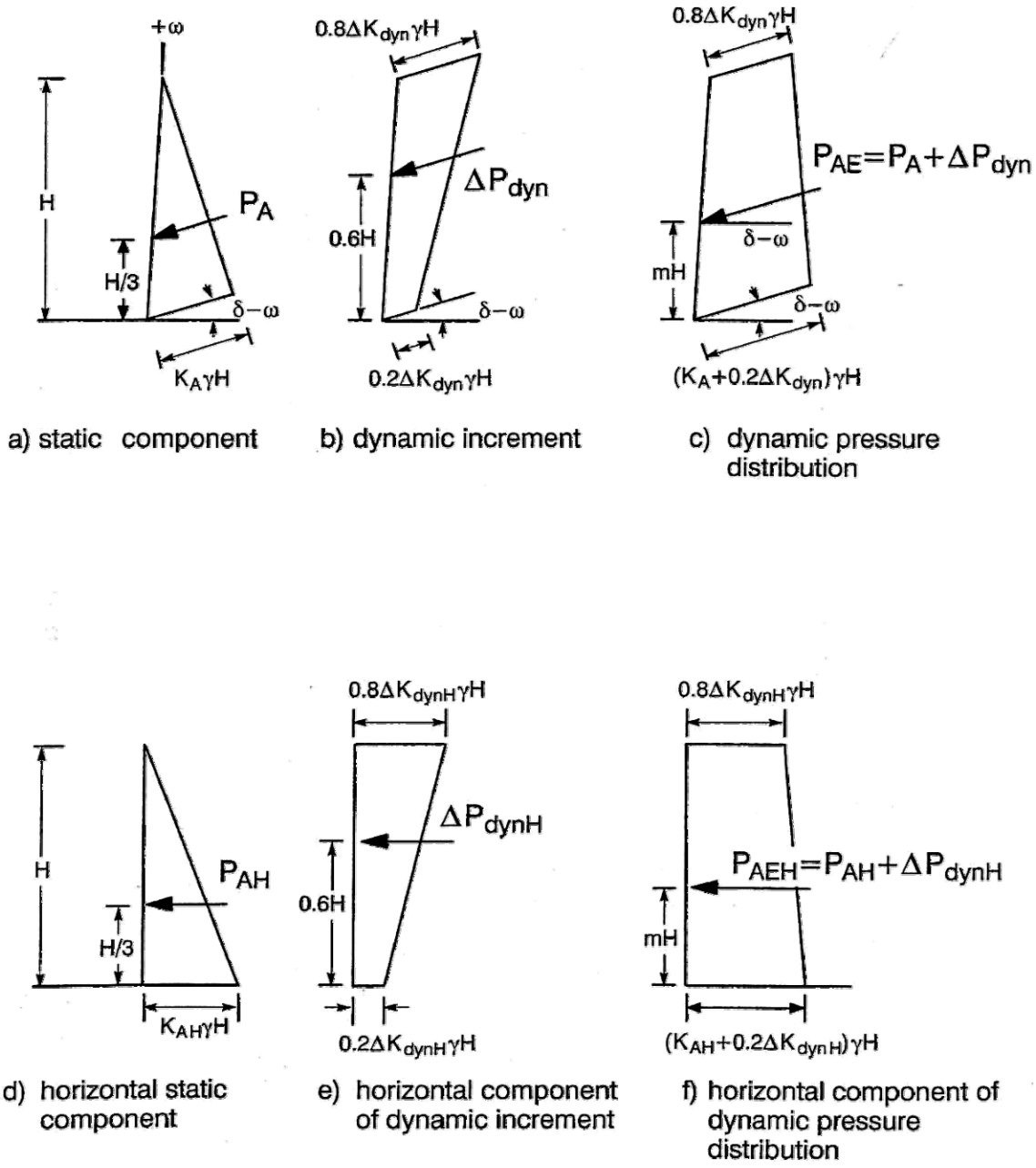

Figure 3.6. The earth pressure distributions during dynamic loading with pseudo-static approach [17]

Current AASHTO/FHWA guidelines use an equation proposed by Segrestin and Bastick (1988) that relates k_h to a_{max} (a_m) according to

$$k_h = \frac{\left(1.45 - \frac{a_{\max}}{g}\right) a_{\max}}{g} \tag{3.36}$$

where a_{max} is the peak base acceleration. This formula results in $k_h > a_m/g$ for $a_m < 0.45g$. In some practices, it is also advised to take k_h = PGA/g in which PGA represents the peak ground acceleration. Generally, the selection of k_h for design is based on engineering judgment, experience and in some instances local regulations. As the value of the horizontal pseudo-static coefficient increases, the inclination of the failure surface decreases resulting smaller values of α_{AE}.

As given by Kramer (1996), a reinforced wall is treated like a gravity wall for the evaluation of external stability. The earthquake loading is represented pseudostatically by the dynamic thrust, ΔP_{AE}. The external stability can be evaluated by the following procedure for a particular wall design.

Peak ground acceleration, a_c, at the centroid of the reinforced zone can be calculated from the equation

$$a_c = \left(1.45 - \frac{a_{\max}}{g}\right) a_{\max} \tag{3.37}$$

and dynamic thrust from

$$\Delta P_{AE} = 0.375 \frac{a_c \gamma_b H^2}{g} \tag{3.38}$$

where γ_b is unit weight of the backfill soil. The overturning moment can be calculated by

$$M_o = \left(P_{AE}\right)_y Y \tag{3.39}$$

where $(P_{AE})_y$ = dynamic load at height y and Y = the acting point of the dynamic load [16], [17].

For all external and facing stability calculations for conventional SRW structures and for all external stability and internal stability for GR-SRW structures, k_h recommended is calculated from (NCMA):

$$k_h = \frac{PGA}{2g} \tag{3.40}$$

3.2. Modes of Failure

Stability analyses for geosynthetic reinforced segmental retaining wall systems under static and seismic loading conditions involve separate calculations to establish factors of safety against external, internal and facing modes of failure (Figure 3.7).

External stability calculations consider the reinforced soil zone and the facing column as a monolithic gravity structure. The evaluation of factors of safety against base sliding, overturning about the toe and foundation bearing capacity is similar to that used for conventional reinforced concrete gravity structures.

Internal stability analyses for geosynthetic reinforced soil walls are carried out to ensure that the structural integrity of the reinforced zone is preserved with respect to reinforcement over-stressing within the reinforced zone, pullout of geosynthetic reinforcement layers from the anchorage zone and internal sliding along a reinforcement layer.

Facing stability analyses are carried out to ensure that the facing column is stable at all elevations above the toe of the wall and connections between the facing units and reinforcement layers are not over-stressed.

Minimum recommended factors of safety for static and seismic design of Geosynthetic Reinforced Segmental Retaining Wall (SRW) structures are given in Table 3.1.

In general, minimum recommended factors of safety for seismic design are taken as 75% of the values recommended for statically loaded structures following AASHTO/ FHWA practice.

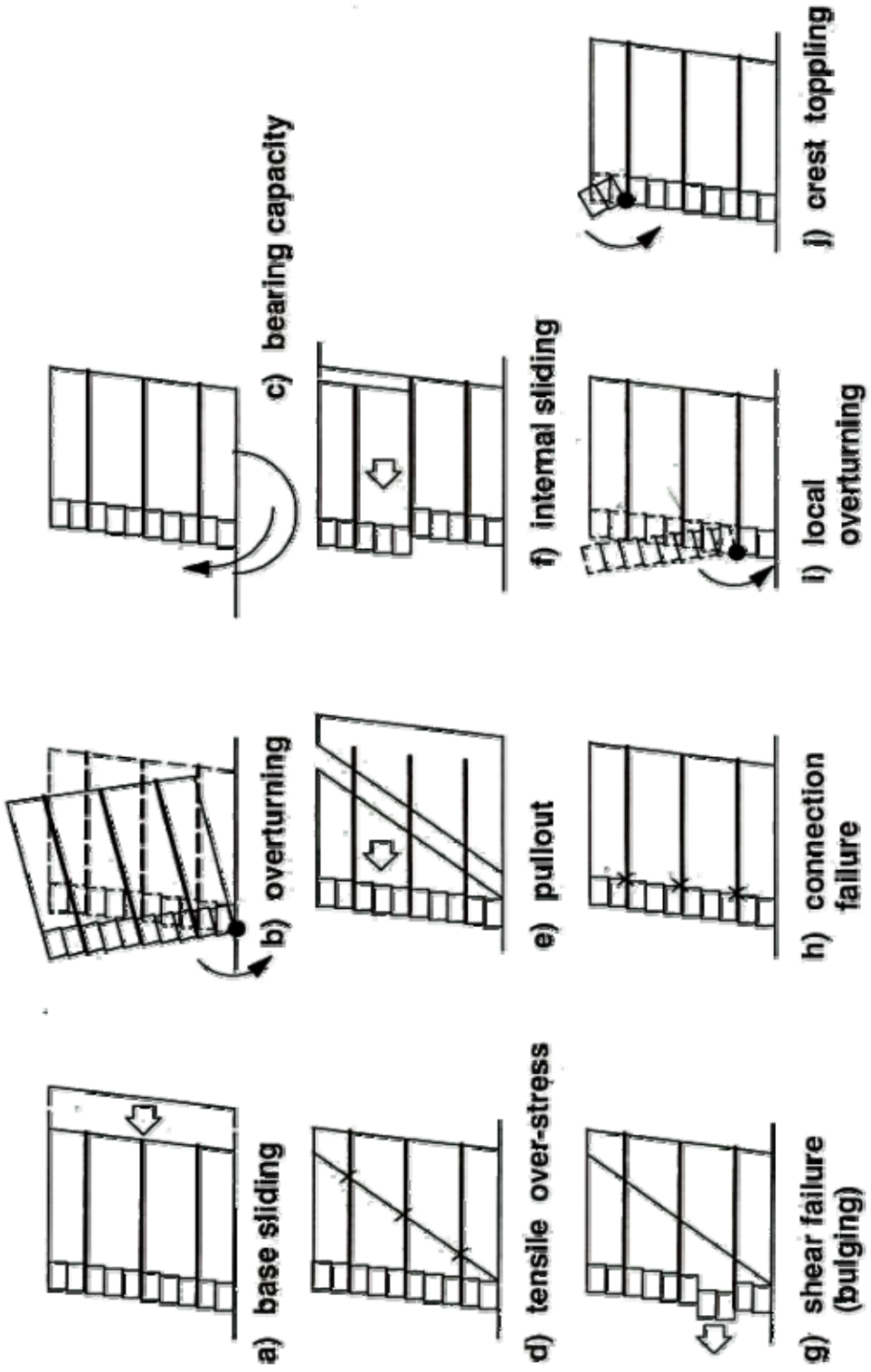

Figure 3.7. Modes of failure for reinforced SRW structures: external (a, b, c); internal (d, e, f); and facing (g, h, i, j) (after Bathurst and Cai 1995) [17]

Table 3.1. Recommended minimum factors of safety for design of Geosynthetic Reinforced SRW Structures [17]

Failure Mode		Static	Seismic
a) Base Sliding	FS_{sl}	1.5	1.1
b) Overturning	FS_{ot}	1.5*	1.1
c) Bearing Capacity	FS_{bc}	2.0	1.5
Global Stability	FS_{gl}	1.3 – 1.5	1.1
d) Tensile over-stress	FS_{os}	1.0	1.0
e) Pullout	FS_{po}	1.5	1.1
f) Internal sliding	FS_{sli}	1.5	1.1
g) Shear (bulging)	FS_{sc}	1.5	1.1
h) Connection	FS_{cs}	1.5	1.1
i) Local Overturning**	FS_{otl}	1.5	1.1
j) Crest Toppling	FS_{otc}	1.5	1.1

In this study, the criteria of the NCMA's Segmental Retaining Walls - Seismic Design Manual [17] is used as a guide. For the seismic design of conventional gravity structures and external stability of reinforced segmental retaining walls the peak horizontal ground acceleration may be reduced by 50 per cent as recommended by AASHTO (1996) guidelines for the free-standing conventional SRW structures and reinforced SRW structures, which are typically able to tolerate lateral deformations of this magnitude provided they are not seated on piles and/or constrained from moving laterally by connected structures. Hence, using the AASHTO approach, the horizontal seismic coefficient for all external stability and internal sliding stability calculations for GR-SRW structures (NCMA) is estimated according to Equation 3.40, i.e. (k_h(ext) = PGA/2).

Whereas, for facing and internal stability calculations of reinforced SRW structures the k_h(int) is based on the equation proposed by Segrestin and Bastick (1998) stated previously in Equation 3.36.

In this study for the experimented retaining wall, base sliding, internal sliding and column shear failure mechanisms, which are the most governing modes corresponding to external, internal and facing types respectively, are presented.

3.2.1. External Stability

External stability calculations for factors of safety against base sliding of a geosynthetic reinforced segmental retaining wall are similar to those carried out for conventional gravity structures. For reinforced structures, the gravity mass is taken as the composite mass formed by the reinforced soil zone and the facing column. The earth pressure distribution proposed by Bathurst and Cai (1995) to calculate the destabilizing forces for factor of safety against sliding along the foundation surface and the simplified geometry and body forces assumed in these calculations are illustrated in Figure 3.8.

$k_h = a_c/2g$ is used to calculate the magnitude of the uniformly applied horizontal seismic coefficient value k_h, in all external stability calculations (i.e. $k_h = k_h(ext)$). The peak friction angle is taken as $\phi = \phi_b$ in earth pressure and force calculations in which ϕ_b denotes the peak friction angle of retained (backfill) soil. The calculation of force components P_{AH} and ΔP_{dynH} assumes full mobilization of interface friction between the reinforced soil zone and the retained soil (i.e. $\delta = \phi$ with ϕ equal to lesser of ϕ_r and ϕ_b values, where ϕ_r represents peak friction angle of reinforced (infill) soil).

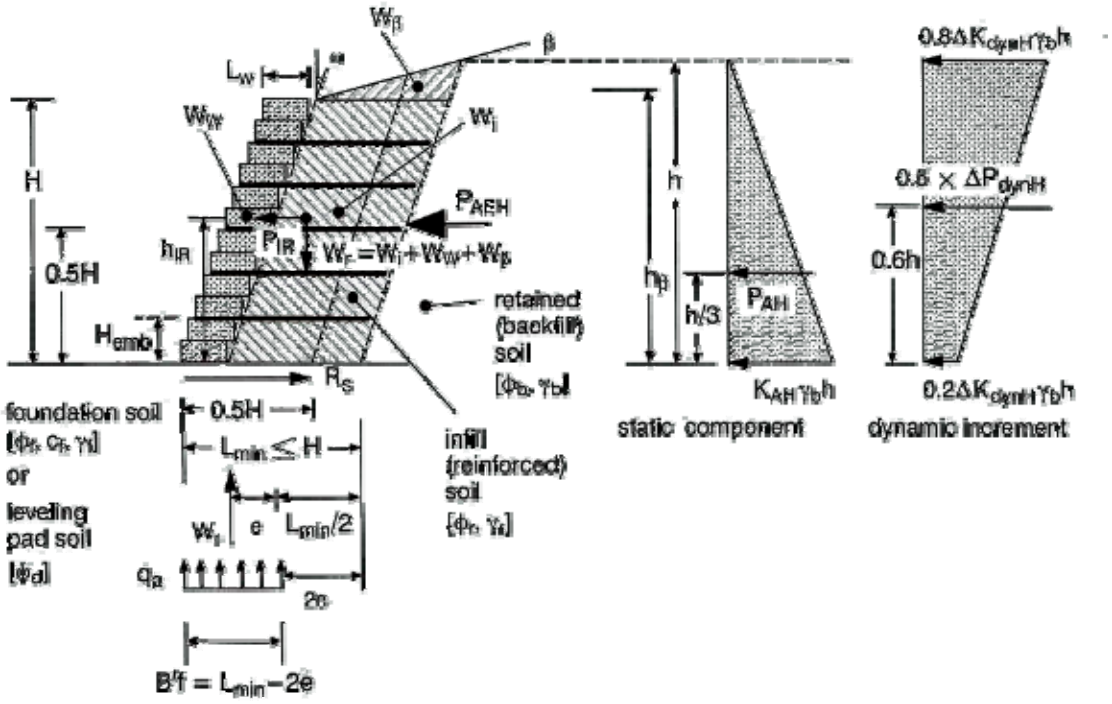

Figure 3.8. Geometry and forces in external stability calculations for GRS-RW structures [17]

The total weight W_r is used to calculate resisting terms in factor of safety expressions for base sliding and overturning and the applied load in bearing capacity calculations. This term is calculated by adding the total weight of the facing column (W_w), the total weight of the reinforced zone (W_i) and the contribution of the wedge of soil (W_β). The formulations are as follows:

$$W_r = W_w + W_i + W_\beta \tag{3.41}$$

$$W_w = N_w L_w H_w \gamma_w = L_w H \gamma_w \tag{3.42}$$

$$W_i = \left(L_{min} - L_w\right) H \gamma_r \tag{3.43}$$

$$W_\beta = \frac{1}{2}\gamma_r \left(L_{min} - L_w\right)^2 \left(\frac{\tan\beta}{1 - \tan\beta \tan\omega}\right) \tag{3.44}$$

Definitions of terms are defined as:

W_i = total weight of the reinforced zone extending from the back of the facing column to length L_{min} beyond the face of the wall and having constant height H;

W_β = contribution of the wedge of soil in the slope above the crest of the wall at height H;

W_w = total weight of the facing column.

L_w = width of facing column (toe to heel dimension of SRW unit) (m)

N_w = total number of standard SRW units in facing column (dimensionless)

γ_w = unit weight of SRW units (N/m^3).

L_{min} = minimum reinforcement length

The results of parametric analyses reported by Bathurst and Cai (1995) have illustrated that as the backslope angle β for the infinite slope case increases, the factors of safety against external stability modes of failure diminish rapidly and reasonable solutions even for modest values of ground acceleration are not possible. This result is due in part to the formulation of earth forces calculated using the M-O method and the conservative estimates of soil strength parameters that are routinely used for the design and analysis of geosynthetic reinforced wall systems. In order to prevent this problem from developing the following empirical rule is proposed in this design guideline: Regardless of the wall geometry and reinforcement lengths the maximum value of the reinforced zone width L_{min} (Figure 3.8) is restricted to the height of the wall H. Hence $L_{min} \leq H$. This approach has been adopted by the Reinforced Earth Company (RECO 1990) for the design of steel strip reinforced soil wails for the same reasons given above.

The quantity P_{IR} in Figure 3.8 represents the horizontal inertial force of the composite mass used in external stability factor of safety calculations. Different strategies have been proposed in North America to compute $P_{IR} < k_h W_r$ to ensure reasonable designs (Bathurst and Alfaro 1996). The basis of this assumption is to account for the transient nature of peak accelerations in the gravity mass and retained soil and the expectation that horizontal inertial forces induced in the reinforced mass and the retained (backfill) soil zone will not reach peak values at the same time during a seismic event.

The method adopted here uses the AASHTO/FHWA approach and assumes that the horizontal inertial force P_{IR} is due to an equivalent mass comprising the facing column and a portion of the reinforced soil zone extending to a distance 0.5 H beyond the face of the wall. The general approach is illustrated in Figure 3.8 and applies to any infinite backfill slope condition (i.e. $\beta > 0$). The inertial force P_{IR} is calculated using:

$$P_{IR} = k_h \, (ext) \, (W_w + W'_i + W'_\beta) \tag{3.45}$$

where the reduced inertial zone weights W'_i and W'_β are calculated by substituting L_{min} = 0.5 H in equations 3.43 and 3.44. Hence:

$$W'_i = \left(0.5H - L_w\right) H \gamma_r \tag{3.46}$$

$$W'_{\beta} = \frac{1}{2}\gamma_r (0.5H - L_w)^2 \left(\frac{\tan\beta}{1 - \tan\beta \tan\omega} \right) \tag{3.47}$$

The dynamic earth force P_{AE} is applied at the back of the reinforced mass described by the minimum reinforcement length L_{min} and height h. The quantity h can be calculated as:

$$h = H + (L_{min} - L_w) \left(\frac{\tan\beta}{1 - \tan\beta \tan\omega} \right) \tag{3.48}$$

For structures with a horizontal backslope ($\beta = 0$) the problem geometry is simplified since h = H.

The horizontal component of dynamic earth force P_{AEH} acting over depth at the back of the reinforced zone is calculated using the following expression:

$$P_{AEH} = P_{AH} + 0.5 \times \Delta P_{dynH} = \frac{K_{AH}\gamma_b h^2}{2} + 0.5 \times \frac{\Delta K_{dynH}\gamma_b h^2}{2} \tag{3.49}$$

Note that only 50% of the dynamic earth force increment, ΔP_{dynH}, acting over height h is considered in external stability calculations.

The application of the dynamic increment of backfill soil force ΔP_{dynH} differs from the method used by AASHTO/FHWA. AASHTO/FHWA applies ΔP_{dynH} to the back of the inertial zone identified by the dashed line at distance 0.5H behind the wall face in Figure 3.8. For sloped backfills the method used in this document is slightly more conservative but greatly simplifies calculations. For horizontal backfills there is no difference between methods with respect to location of the dynamic force increment. However, AASHTO/FHWA guidelines assume that the interface friction angle at the boundary between the reinforced zone and backfill soil is equal in magnitude to the angle of the constant slope behind the wall crest (i.e. $\delta = \beta$). However, there is no justification for linking interface friction angle to slope angle. The magnitude of earth pressures for external stability

calculations in this document will almost always be less than AASHTO/FHWA values since $\delta = \phi \geq \beta$. In addition, AASHTO/FHWA assumes that $\omega = 0$ for walls with $\omega < 10°$ and this leads to higher earth pressures and hence more conservative static and seismic designs for reinforced SRW structures using their method. The interpretation of Coulomb and M-O earth pressure theory used in NCMA document provides a seamless transition between the analysis and design of statically loaded structures described in the DMSRW and the methodology for seismic loaded SRW structures.

3.2.1.1. Base Sliding (Figure 3.7 (a)). The factor of safety against base sliding FS_{sl} at the bottom of the reinforced mass (i.e. bottom of the lowermost facing unit and reinforced soil zone) can be expressed as:

$$FS_{sl} = \frac{R_S}{P_{IR} + P_{AH} + 0.5 \times \Delta P_{dynH}} \tag{3.50}$$

The base sliding resistance force, R_S, (Figure 3.8) is calculated as follows:

a) If the reinforced soil (infill) or drainage fill controls:

$$R_S = C_{ds}\, W_r \tan\phi \tag{3.51}$$

with $\phi = \phi_d$ or ϕ_r whichever value has the least magnitude where ϕ_d is the peak friction angle of drainage (leveling pad) soil (°) .

b) If the foundation soil controls:

$$R_S = C_{ds}\, [c_f\, L_{min} + Wr \tan\phi_f] \tag{3.52}$$

Here the quantity C_{ds} is the coefficient of direct sliding and cannot exceed unity. For soil to soil interfaces the value for this parameter can be assumed to be equal to one. For the case of a geosynthetic layer placed at the base of the reinforced soil zone, $C_{ds} < 1$ maybe appropriate.

The calculated value of FS_{sl} should not be less than 1.1.

3.2.2. Internal Stability

3.2.2.1. Reinforcement Loads. The contributory area approach used for the static stability analysis of segmental retaining walls is extended to the dynamic loading case. In this method the reinforcement layers are modeled as tie-backs with the tensile force, F_i, in layer i equal to the earth pressure integrated over the contributory area, S_{vi}, at the back of the facing column plus the corresponding wall inertial force increment. Hence:

$$F_i = k_h(\text{int})\Delta W_{wi} + F_{stai} + F_{dyni} \tag{3.53}$$

where: $k_h(\text{int})\Delta W_{wi}$ = wall inertial force increment; F_{stai} = static component of reinforcement load; and F_{dyni} = dynamic component of reinforcement load. The quantity ΔW_{wi} is the weight of the facing falling with the contributory area S_{vi} of the corresponding reinforcement layer and hence can be calculated as follows:

$$\Delta W_{wi} = S_{vi} L_w \gamma_w \tag{3.54}$$

referring to Figure 3.9:

$$F_{stai} = K_{AH} \gamma_r z_{vi} S_{vi} \tag{3.55}$$

$$F_{dyni} = \left[0.8 - 0.6\frac{z_{vi}}{H}\right]\Delta K_{dynH} \gamma_r H S_{vi} \tag{3.56}$$

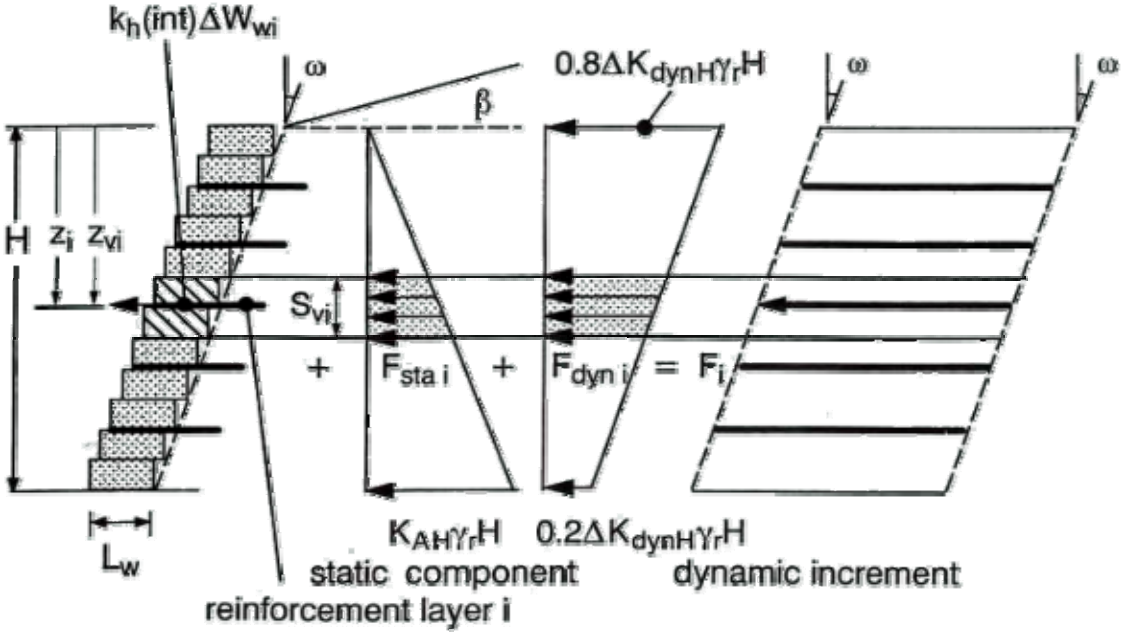

Figure 3.9. Geometry and forces used to calculate reinforcement loads for reinforced SRW structures [17]

The quantity z_{vi} is the distance from the crest of the wall to the mid-elevation of the contributory area S_{vi}. For constant reinforcement spacing $z_{vi} = z_i$. For non-uniform spacing $z_{vi} \neq z_i$. The contributory area for the topmost reinforcement layer is taken from the wall crest to mid-elevation between the first and second reinforcement layers from the crest. The contributory area for the bottommost layer is taken from the mid-elevation between the bottom layer and the layer immediately above, and the base elevation of the reinforced soil mass. The value of horizontal seismic coefficient ($k_h = k_h(int)$) used to calculate the wall inertial force increment ($k_h(int)\ \Delta W_{wi}$ in Equation 3.53) and dynamic component of reinforcement load (i.e. ΔK_{dynH} term in Equation 3.56) is determined from Equation 3.36 (Segrestin and Bastick)**.**

3.2.2.2. Internal Sliding (Figure 3.7 (f)). The factor of safety against internal sliding FS_{sli} along a reinforcement layer located at depth z below the crest of the wall can be expressed as:

$$FS_{sli} = \frac{R_S(z_i)}{\Delta P_{IR}(z_i) + P_{AEH}(z_i)} \tag{3.57}$$

The internal force contribution $\Delta P_{IR}(z_i)$ is calculated as:

$$\Delta P_{IR}(z_i) = k_h(\text{ext})\left(\Delta W_w(z_i) + \Delta W_i'(z_i) + \Delta W_\beta'\right) \tag{3.58}$$

The value of k_h (ext) used to calculate the inertial force contribution is determined from k_h = PGA/2g (Equation 3.40). Quantity $\Delta W_w(z_i)$ is the total weight of the facing column above the sliding surface located at depth z_i. Similar to the approach adopted for base sliding, the reduced reinforced zone weight $\Delta W_i'(z_i)$ is calculated using:

$$\Delta W_i'(z_i) = (0.5H - L_w)z_i\gamma_r \tag{3.59}$$

The geometry and forces used to calculate internal sliding of reinforcement layers can be seen in Figure 3.10.

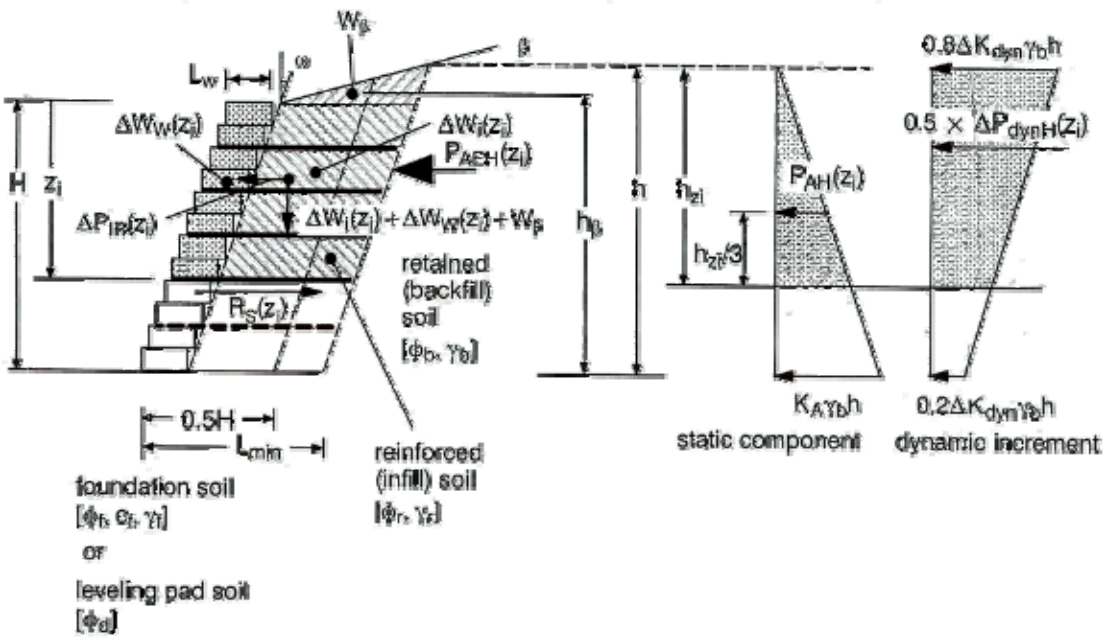

Figure 3.10. Geometry and forces used to calculate internal sliding of reinforcement layers in reinforced SRW structures [17]

Finally, the reduced reinforced zone weight in the slope above the reinforced mass, W'_β, is calculated using Equation 3.47.

The horizontal component of dynamic earth force $P_{AEH}(z_i)$ acting over the depth h_{zi} at the back of the reinforced zone is calculated using the following expression;

$$P_{AEH}(z_i) = P_{AH}(z_i) + 0.5 \times \Delta P_{dynH}(z_i) = \frac{K_{AH}\gamma_b h_{zi}^2}{2} + \left[0.8h_{zi} - 0.3\frac{h_{zi}^2}{h}\right]\Delta K_{dynH}\gamma_b h \qquad (3.60)$$

The value of k_h, used to calculate the horizontal component of the dynamic force increment ($\Delta P_{dynH}(z_i)$) is determined from k_h = PGA/2g from Equation 3.40 (i.e. $k_h = k_h(ext)$. The quantity h_{zi} can be calculated as:

$$h_{zi} = z_i + (L_{min} - L_w)\left(\frac{\tan\beta}{1 - \tan\beta\tan\omega}\right) \qquad (3.61)$$

For structures with a horizontal backslope ($\beta = 0$) the problem geometry is simplified since $h_{zi} = z_i$. The sliding resistance $R_S(z_i)$ corresponding to interface i is calculated using:

$$R_S(z_i) = V_u(z_i) + C_{ds}\left(\Delta W_i(z_i) + W_\beta\right)\tan\phi_r \qquad (3.62)$$

The quantity $V_u(z_i)$ is the peak interface shear capacity between facing column units calculated using:

$$V_u(z_i) = a_u + \Delta W_h(z_i)\tan\lambda_u \qquad (3.63)$$

where a_u is the minimum available interface shear strength in (kN/m) and λ_u is the apparent peak interface friction angle between facing units (degrees) corresponding to the appropriate normal load range on the interface shear strength envelope.

The quantity C_{ds} in Equation 3.62 is the coefficient of direct sliding for the soil-geosynthetic interface and cannot exceed unity. Quantity $\Delta W_i(z_i)$ is calculated as:

$$\Delta W_i(z_i) = (L_{min} - L_w)z_i\gamma_r \qquad (3.64)$$

and W_β is calculated using Equation 3.44.

Only 50% of the external dynamic earth force increment, $\Delta Pd_{ynH}(z_i)$, acting over the height h_{zi} is considered for internal sliding stability calculations. The calculation of force components $P_{AH}(z_i)$ and $\Delta P_{dynH}(z_i)$ assumes full mobilization of interface friction between the reinforced soil zone and the retained soil (i.e. $\delta = \phi$ with ϕ equal to the lesser of ϕ_r and ϕ_b).

The calculated value of FS_{sli} should not be less than 1.1.

3.2.3. Facing Stability

3.2.3.1. Interface Shear (Figure 3.7 (g)). The influence of interface shear transmission on facing column stability can be analyzed by treating the facing column as a beam in which the integrated lateral pressure (i.e. distributed load) must equal the sum of the reactions (forces in reinforcement layers). The calculation of interface shear force under dynamic loading must include the effect of wall facing inertia. The general approach is illustrated in Figure 3.11. The locally maximum interface shear forces will occur at reinforcement elevations.

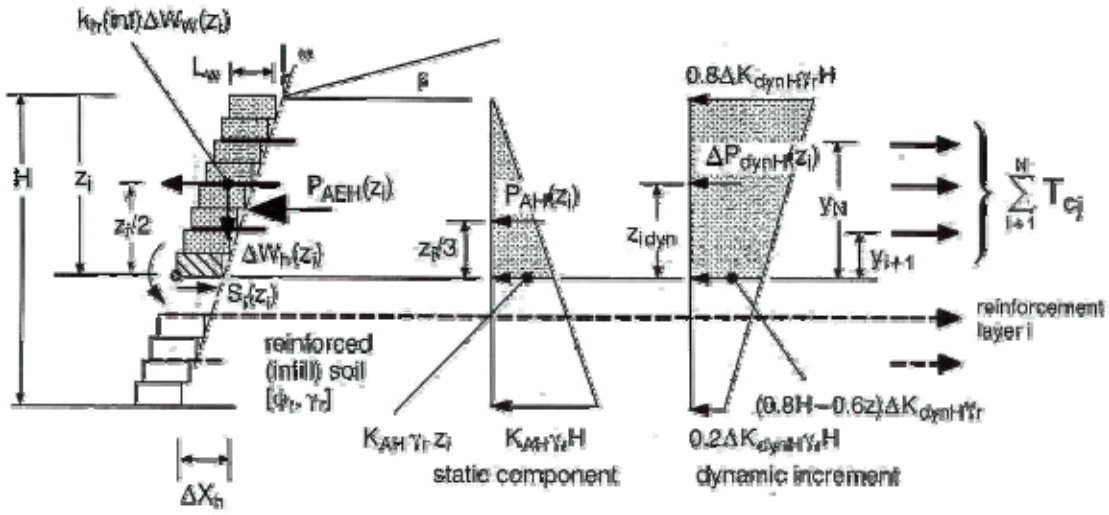

Figure 3.11. Geometry and forces used to calculate interface shear (bulging) and overturning of the facing column for reinforced SRW structures [17]

The out-of-balance horizontal force S_i transmitted to an interface at depth z_i (corresponding to reinforcement layer i) is the difference in magnitude between the horizontal

component of dynamic earth force plus facing column inertia force and the sum of the horizontal loads carried by the reinforcement layers above the target interface. Hence:

$$S_i(z_i) = k_h(\text{int})\Delta W_w(z_i) + P_{AEH}(z_i) - \sum_{i+1}^{N} F_j \qquad (3.65)$$

Here N is the number of reinforcement layers. The horizontal component of dynamic earth force $P_{AEH}(z_i)$ acting over the depth z_i at the back of the facing column is calculated using the following expression;

$$P_{AEH}(z_i) = P_{AH}(z_i) + \Delta P_{dynH}(z_i) = \frac{K_{AH}\gamma_r z_i^2}{2} + \left[0.8z_i - 0.3\frac{z_i^2}{H}\right]\Delta K_{dynH}\gamma_r H \qquad (3.66)$$

Coefficients of earth pressure (K_{AH} and ΔK_{dynH}) are calculated using $\phi = \phi_r$ and $0 \leq \delta \leq \phi_r$. Typically δ is taken as $2\phi_r/3$ for facing stability calculations. Quantity ΔK_{dynH} in Equation 3.66 is calculated using $k_h=k_h(\text{int})$ (Equation 3.36)**.** The summation of reinforcement reactions can be calculated using Equation 3.53. The factor of safety against interface shear failure (FS_{sc}) at a reinforcement layer is:

$$FS_{sc} = \frac{V_u(z_i)}{S_i(z_i)} \qquad (3.67)$$

where $V_u(z_i)$ is the peak shear capacity of the interface calculated using Equation 3.63. The selection of interface shear strength parameters should be based on the results of laboratory interface shear data simulating the geosynthetic-modular block interface.

The calculated value of FS_{sc} should not be less than 1.1.

3.2.3.2. Connection Failure (Figure 3.8 (h)). The dynamic factor of safety, FS_{cs}, against connection failure of the reinforcement layer with the facing column can be expressed as:

$$FS_{cs} = \frac{T_{ci}}{F_i} \qquad (3.68)$$

Here, F_i is the tensile load in the reinforcement layer i calculated using Equation 3.53 and T_{ci} is the peak connection capacity for that layer calculated as:

$$T_{ci} = a_{cs} + \Delta W_h(z_i)\tan\lambda_{cs} \tag{3.69}$$

The quantity a_{cs} is the minimum available peak connection strength in kN/m and λ_{cs} is the apparent peak interface friction angle describing the connection failure envelope (degrees) corresponding to the range of normal weight over which $\Delta W_h(z_i)$ applies.

The calculated value of FS_{cs} should not be less than 1.1.

4. DIMENSIONAL ANALYSIS AND SIMILARITY

4.1. Introduction

Dimensional analysis is a method for reducing the number and complexity of experimental variables, which affect a given physical phenomenon, using a sort of compacting technique. Usually, a phenomenon depends upon n dimensional variables, and dimensional analysis helps us to reduce the problem to only k *dimensionless* variables, where the reduction $n\text{-}k = 1$, 2, 3 or 4, depending upon the problem complexity. Generally, $n\text{-}k$ equals the number of different dimensions (sometimes called basic or primary or fundamental dimensions), which govern the problem. In fluid mechanics, the four basic dimensions are usually taken to be mass M, length L, time T, and temperature Θ, or an $MLT\Theta$ system for short. Sometimes an $FLT\Theta$ system can be used, with force F replacing mass.

Although its purpose is to reduce variables and group them in dimensionless form, dimensional analysis has several side benefits. The first is an enormous saving in time and money by running the experiments to evaluate the values for the single-group of variables, rather than running many experiments for every variable that constitutes the group.

A second benefit of dimensional analysis is that it helps our thinking and planning for an experiment or theory. It suggests dimensionless ways of writing equations before much money is wasted on computer time to find solutions. It suggests variables, which can be discarded; sometimes dimensional analysis will immediately reject variables, and sometimes it groups them off to the side, where a few simple tests will show them to be unimportant. Finally, dimensional analysis will often give a great deal of insight into the form of the physical relationship we are trying to study.

Thirdly, dimensional analysis provides *scaling laws* which can convert data from a cheap, small *model* into design information for an expensive, large *prototype.* When the scaling law is valid, it is said that a condition of *similarity* exists between model and prototype.

4.2. Dimensional Analysis

In reducing variables and grouping them in dimensionless form a self-evident axiom in physics is exploited. This rule is called the "*principle of dimensional homogeneity* (PDH)" and it can be stated as:

"If an equation truly expresses a proper relationship between variables in a physical process, it is *dimensionally homogeneous*; i.e., each of its additive terms will have the same dimensions."

All the equations which are derived from the theory of mechanics are of this form. For example, if we consider the relation which expresses the displacement of a falling body:

$$S = S_0 + V_0 t + \frac{1}{2} g t^2 \tag{4.1}$$

Each term in this equation is a displacement, or length, and has dimensions $\{L\}$. The equation is dimensionally homogenous. Equation 4.1 also illustrates some other factors that often enter into a dimensional analysis. These are:

1-) *Dimensional variables* are the quantities which actually vary during a given case and would be plotted against each other to show the data. In Eq. 4.1, these are S and t. All have dimensions, and all can be nondimensionalized as a dimensional-analysis technique.
2-) *Dimensional constants* may vary from case to case but are held constant during a given run. In Eq. 4.1, these are S_0, V_0 and g. They all have dimensions and conceivably could be nondimensionalized, but they are normally used to help nondimensionalize the variables in the problem.
3-) *Pure constants* have no dimensions and never did. They arise from mathematical manipulations. In Equation 4.1 it is ½ which came from an integration: $\int t\, dt = ½\, t^2$.

The motive behind dimensional analysis is that any dimensionally homogenous equation can be written in an entirely equivalent nondimensional form which is more

compact. The exact process of this theorem is explained in detail in the following topic named as the "The π Theorem".

4.3. The π(Pi) Theorem

Although there are several methods of reducing a number of dimensional variables into a smaller number of dimensionless groups, the most popular one is proposed in 1914 by Buckingham and is now called the *Buckingham's π theorem*. The name π comes from the mathematical notation π, meaning a product of variables. The dimensionless groups found from the theorem are power products denoted by π_1, π_2, π_3, etc. The method allows the πs to be found in sequential order without resorting to free exponents. The first part of the π theorem explains what reduction in variables to expect:

If a physical process satisfies the principle of dimensional homogeneity and involves *n* dimensional variables, it can be reduced to a relation between only *k* dimensionless variables or π's. The reduction j = n-k equals the maximum number of variables which do not form a π among themselves and is always less than or equal to the number of dimensions describing the variables.

The second part of the theorem shows how to find the π's one at a time:

Find the reduction *j*, then select *j* variables which do not form a π among themselves. Each desired π group will be a power product of these *j* variables plus one additional variable which is assigned any convenient nonzero exponent. Each π group thus found is independent.

To be brief, typically, there are six steps involved:

1-) List and count the *n* variables involved in the problem. If any important variables are missing, dimensional analysis will fail.
2-) List the dimensions of each variable according to *MLT*Θ or *FLT*Θ.

3-) Find *j*. Initially guess *j* equal to the number of different dimensions present and look for *j* variables which do not form a π product. If no luck, reduce *j* by 1 and look again. With practice, the *j* will be found rapidly.

4-) Select *j* variables, which do not form a π product. Make sure they please you and have some generality if possible, because they will then appear in every one of your π groups. For example, pick density or velocity or length.

5-) Add one dimensional variable to your *j* variables and form a power product. Algebraically find the exponents, which make the product dimensionless. Try to arrange for your output or *dependent* variables (force, pressure drop, torque, power) to appear in the numerator and your plots will look better. Do this sequentially, adding one new variable each time, and you find all $n-j = k$ desired π products.

6-) Write the final dimensionless function and check your work to make sure all π groups are dimensionless.

4.4. The Determination of the π Values of the Geosynthetic Reinforced Soil Retaining Wall

A ½ model of the soil retaining wall will be experimented according to the scaling law theory and the π theorem. The π values of the Geosynthetic Soil Retaining Wall are deducted according to the steps explained previously. This step by step procedure will be adopted to explain the determination of the π values.

Step 1 & *Step 2*: List and count the *n* variables and list dimensions of each variable:

13 variables are considered in the analysis. These scaling law parameters that are thought to affect the system response, with their dimensions, are defined in Table 4.1.

Table 4.1. Most common parameters considered for dimensional analysis in this study

PARAMETERS		SI UNIT	DIMENSION
H	Height of the wall	[m]	(L)
L	Length of Geotextiles	[m]	(L)
S_v	Vertical spacing between strips	[m]	(L)
w	Block of width	[m]	(L)
T_g	Tensile strength of the geotextiles	[N/m^2]	($ML^{-1}T^{-2}$)
γ	Density of the backfill	[kg/m^3]	(ML^{-3})
f	Frequency of the Dynamic Excitation	[sec^{-1}]	(T^{-1})
c	Cohesion of the backfill	[N/m^2]	($ML^{-1}T^{-2}$)
γ_w	Density of the block	[kg/m^3]	(ML^{-3})
a	Acceleration	[m/sec^{-2}]	(LT^{-2})
h	Block Height	[m]	(L)
g	Acceleration of gravity	[m/sec^{-2}]	(LT^{-2})
τ_b	Compression strength of the block	[N/m^2]	($ML^{-1}T^{-2}$)

Note that the Rankine active coefficient, K_a, the angle of friction of the soil, ϕ_{soil}, and the strain, ε, are already dimensionless parameters and dimensional analysis can not provide information regarding them.

Step 3 & Step 4: Find *j*. No variable contains the dimension Θ, and so *j* is less than or equal to 3 (*MLT*). We inspect the list and select 3 variables arbitrarily, they are *H, g, γ*. There are 13 dimensioned variables and the number of π values will be *n-j* = *k*, which is 13-3=10.

Step 5: Combine *H, g, γ* with one additional variable, in sequence, to find the 10 π products [18].

As a result, the π values can be obtained from the following equations:

$$\pi_1 = M^0 L^0 T^0 = H^x g^y \gamma_w{}^z L^1 = L^{x+y-3z+1} M^z T^{-2y} \quad (4.2)$$

$$\pi_2 = M^0 L^0 T^0 = H^x g^y \gamma_w{}^z S_v{}^1 = L^{x+y-3z+1} M^z T^{-2y} \quad (4.3)$$

$$\pi_3 = M^0 L^0 T^0 = H^x g^y \gamma_w{}^z w^1 = L^{x+y-3z+1} M^z T^{-2y} \quad (4.4)$$

$$\pi_4= M^0\ L^0\ T^0 = H^x\ g^y\ \gamma_w{}^z\ T_g{}^1 = L^{x+y-3z-1}\ M^{z+1}\ T^{-2y-2} \quad (4.5)$$

$$\pi_5= M^0\ L^0\ T^0 = H^x\ g^y\ \gamma_w{}^z\ f^1 = L^{x+y-3z}\ M^z\ T^{-2y-1} \quad (4.6)$$

$$\pi_6= M^0\ L^0\ T^0 = H^x\ g^y\ \gamma_w{}^z\ c^1 = L^{x+y-3z-1}\ M^{z+1}\ T^{-2y-2} \quad (4.7)$$

$$\pi_7= M^0\ L^0\ T^0 = H^x\ g^y\ \gamma_w{}^z\ a^1 = L^{x+y-3z+1} M^z\ T^{-2y} \quad (4.8)$$

$$\pi_8= M^0\ L^0\ T^0 = H^x\ g^y\ \gamma_w{}^z\ h^1 = L^{x+y-3z+1}\ M^z\ T^{-2y} \quad (4.9)$$

$$\pi_9= M^0\ L^0\ T^0 = H^x\ g^y\ \gamma_w{}^z\ \tau_b{}^1 = L^{x+y-3z-1}\ M^{z+1}\ T^{-2y-2} \quad (4.10)$$

$$\pi_{10}= M^0\ L^0\ T^0 = H^x\ g^y\ \gamma_w{}^z\ \gamma^1 = L^{x+y-3z-3}\ M^{z+1}\ T^{-2y} \quad (4.11)$$

In conclusion the π values obtained are as follows:

$$\pi_1 = \frac{L}{H} \quad (4.12)$$

$$\pi_2 = \frac{S_v}{H} \quad (4.13)$$

$$\pi_3 = \frac{w}{H} \quad (4.14)$$

$$\pi_4 = \frac{T_g}{Hg\gamma_w} \quad (4.15)$$

$$\pi_5 = f\sqrt{\frac{H}{g}} \quad (4.16)$$

$$\pi_6 = \frac{c}{Hg\gamma} \quad (4.17)$$

$$\pi_7 = \frac{a}{g} \tag{4.18}$$

$$\pi_8 = \frac{h}{H} \tag{4.19}$$

$$\pi_9 = \frac{\tau_b}{Hg\gamma_w} \tag{4.20}$$

$$\pi_{10} = \frac{\gamma}{\gamma_w} \tag{4.21}$$

Presented in Table 4.2 are the most common scaling factors of this study.

Table 4.2. Most common scaling factors used in this study

Quantity	Theoretical Ratio (Prototype/Model)	Study
Length	n	2
Density	1	1
Stress	n	2
Strain	1	1
Acceleration	1	1
Frequency	$n^{-0.5}$	$1/\sqrt{2}$
Time	$n^{0.5}$	$\sqrt{2}$

4.5. Scale Effects

Usually it is impossible to satisfy in a model all the requirements of the similarity at the same time. So, it becomes necessary to determine which parameters affect the system and the phenomenon the least and to devote effort to satisfy others. Errors in the results because of these parameters that are not correctly satisfied are called *scale effects*. These also include any new and unwanted phenomenon that takes place in the model due to the change in size. Such effects need to be determined and known in order to achieve correct application of model results to the prototype.

In geotechnical models, scale effects may include, among others, problems related to:

a. Strength: A small specimen sampled from a natural deposit, or remolded, which has fissures, cracks, layers, inclusions or other such structural features, may not have these characteristics in a distribution representative of that occurring in the prototype. In most cases, this would cause the tester using small specimens to conclude that the material of the prototype is stronger than it actually is.
b. Shear at interfaces or edges: Since the effect of an interface has a constant distance of influence then it will have a proportionally different effect depending on the size of the model, that is, its effect will be large in a small model, and small in a large model.
c. Continuum: The assumption that a soil or rock mass acts as a continuum is only valid if a minimum quantity of particles is involved in an event; if the model is not large enough to include this minimum number of particles, the model will behave differently than the prototype in which the continuum assumption is correct [19].

4.6. Boundary Similarity

The theory of similarity establishes that similarity must also be satisfied on the boundaries of the system. This requirement is usually difficult to achieve.

Three-dimensional soil or rock structures with one-dimension considerably greater than the other two, which are analyzed based on plane strain conditions on a transverse section, are usually modeled by examining a characteristic “thin slice” of the prototype. The boundaries of these model slices become the walls of the box in which the model is contained, rather than the adjacent soil in the prototype.

If x_3 is the direction of the longest dimension, boundary similarity requires that strain in the x_3 direction, ε_{33}, must equal to zero, which can be achieved by using a rigid box. Normal stress in the x_3 direction, σ_{33}, must be the same in the model as in the prototype, and shear stress in the other two directions, ξ_{31} and ξ_{32}, must be zero. These two conditions require that the friction between the material of the model and the box of the containing

wall must be zero. Since this condition is impossible to satisfy, the state of stresses existing in the model will differ from that in the prototype.

In order to minimize side effect in soil models, Terzaghi recommended that the ratio of the width of the model (b) to its height (H) should be greater than two and that any measurements should be made at the center of the model. Lyndon and Schofield (1978) cite research by Fuglsang's (1971). In his centrifugal model tests of slopes in boulder clay fills, he found that a b/H ratio between 3 and 4 was necessary to reduce the boundary effects to a minimum. Terzaghi's criterion, however, has been adopted by most researchers who were concerned about side effect [19].

In examining side effects, Vargin (1967) studied the influences of the position of the side walls of an experimental box on the measured soil pressures. He filled the box with sand, measured the soil pressure and then moved the box wall which he referred to as a retaining wall. He found that:

a. before the retaining wall is moved, the soil pressure measured is not affected by the position of the side walls;
b. when the retaining wall is moved, a reduction in pressure arises, and the b/H ratio is found to influence that reduction;
c. when there is a continuous uniform load on the soil surface this side effect is reduced; and
d. after a retaining wall displacement of H/200, the effect becomes constant.

Lazabnik and Chernysheva (1968) also presented an analysis to quantify the influence of side effect. It consisted of defining the percentages of decrease of pressure on the wall (F/E%) as a function of the b/H ratio, where F is the friction against walls and E is the earth pressure on the retaining wall. They found identical correlation between this theoretical analysis and Virgin's experimental results.

These studies suggest that to reduce undesirable side wall effects, since the box used to contain the model has in general fixed dimensions, the height of the model must be limited. This means that to model a tall soil structure, the scaling ratio will be large and

scale effects are likely to increase. An alternative would be to decrease side friction to a minimum [19].

4.7. The Scaling Factors Used in a Previous Study

Warrasak Jakrapiyanun et al. (2003) carried out shaking table tests to evaluate the soil-foundation-structure-interaction (SFSI). The test was $1/9^{th}$ scale, the aluminum foundation was portrayed by a pile group of 3 by 3. The pile group was made from aluminum, with the fixed head condition. Reinforced concrete column was inserted into hollow pile cap. The reinforced concrete superstructure was firmly fixed to the pile group. A laminar container having dimensions of 2m × 4m × 2m was designed to fit the requirements of these tests, scaling factors, size of soil and structure model and the shaking table capacity. The test structure was excited different motions. The results of this experiment is not in the scope of this thesis, so only the scaling factors used in this previous study is presented in Table 4.3 [20]. These scaling factors were proposed by Iai and Sugano (1999) [21].

Table 4.3. Scaling factors used in a previous study [20]

Quantity	Theoretical Ratio (Prototype/Model)	Study
Length	λ	9
Density	1	1
Stiffness	λ	9
Force	λ^3	729
Mass	λ^3	729
Acceleration	1	1
Velocity	$\lambda^{0.5}$	3
Frequency	$\lambda^{-0.5}$	1/3
Time	$\lambda^{0.5}$	3

As it can be seen, the scaling factors are same with the values derived in Chapter 4.4.

5. TESTS FOR INVESTIGATION OF SOIL PROPERTIES AND EVALUATION OF THE RUBBER AS AN ABSORBENT MATERIAL

5.1. Soil

A uniform sandy soil which had some gravel particles in it and obtained from Kilyos region was used in this study. To classify our soil, sieve analysis was conducted and grain size distribution curve was obtained to be as the one in Figure 5.1.

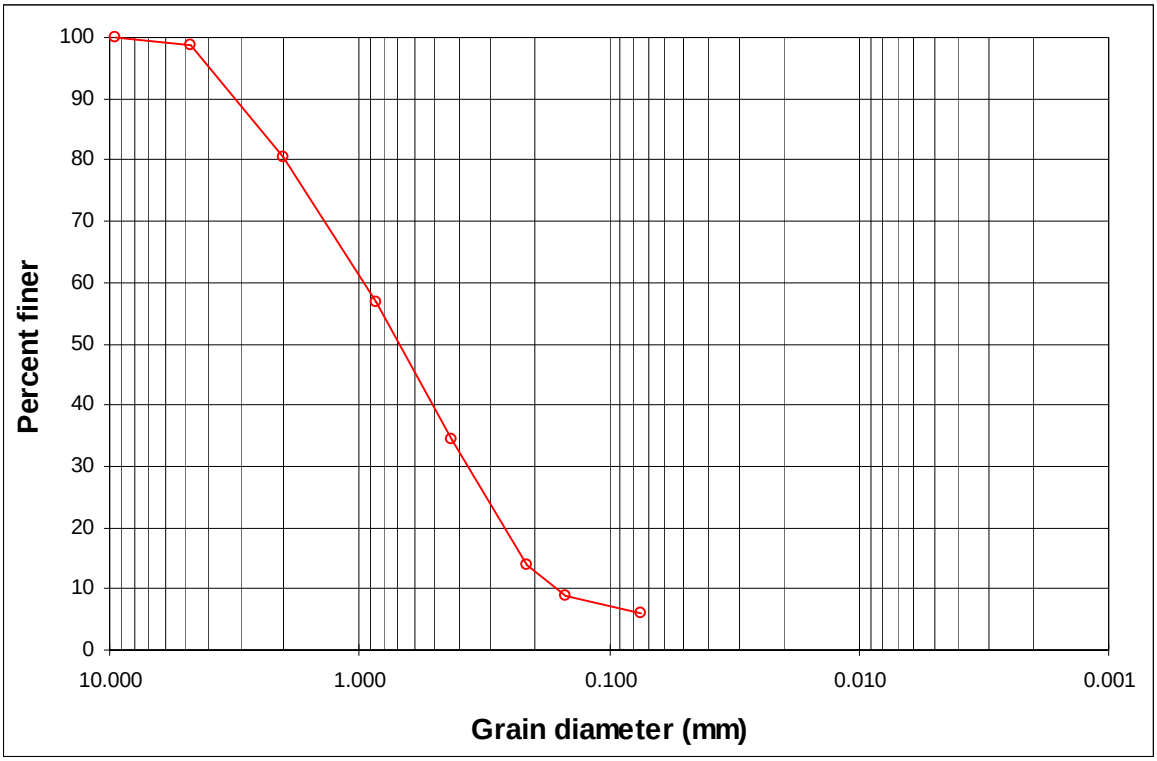

Figure 5.1. Grain size distribution of the soil

The related parameters, the coefficient of uniformity C_u and the coefficient of curvature C_c were calculated to be 9.13 and 1.17, respectively. Since almost 6 per cent of the soil passed from the Sieve No: 200, Casagrande liquid limit analysis was performed to those that passed from the Sieve No: 40. No matter how much water the soil comprises after every one or two blows the soil closed the groove and showed a non-plastic behavior indicating that the soil is in fact a SW-SM (well graded-silty sand) type of soil.

The triaxial CD tests were performed to evaluate the properties of the soil. Figures 5.2 through 5.4 show the triaxial test results and the evaluated Elastic secant modulus (E_s at 50 per cent σ_{max}). In Figure 5.5, internal friction angle (ϕ) and cohesion (c) determination specific to the soil are shown.

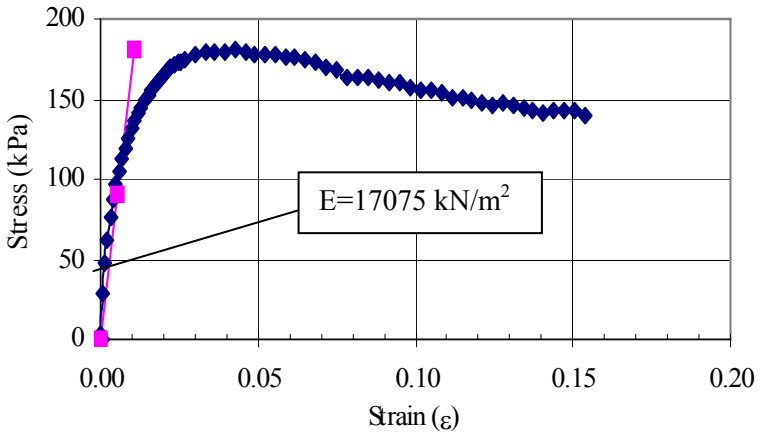

Figure 5.2. Triaxial test of S3 soil specimen where σ_3=50 kPa

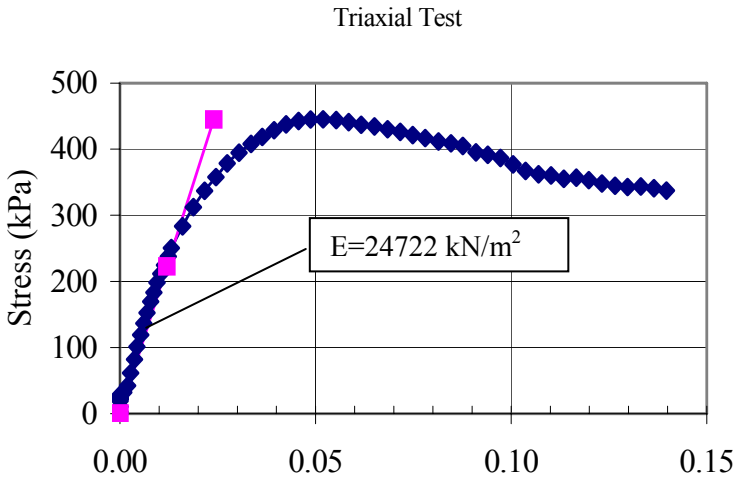

Figure 5.3. Triaxial test of S6 soil specimen where σ_3=100 kPa

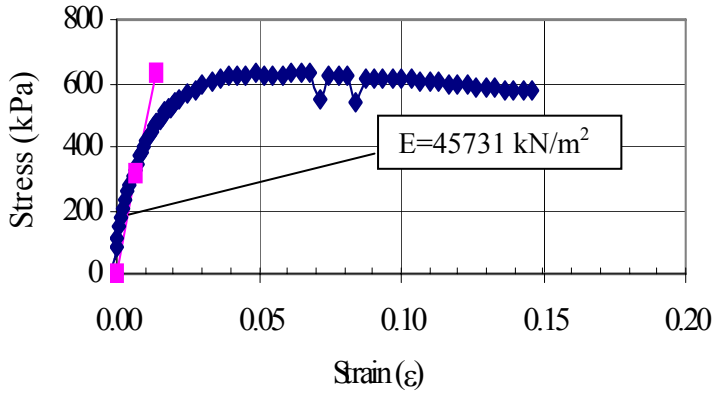

Figure 5.4. Triaxial test of S4 soil specimen where σ_3=150 kPa

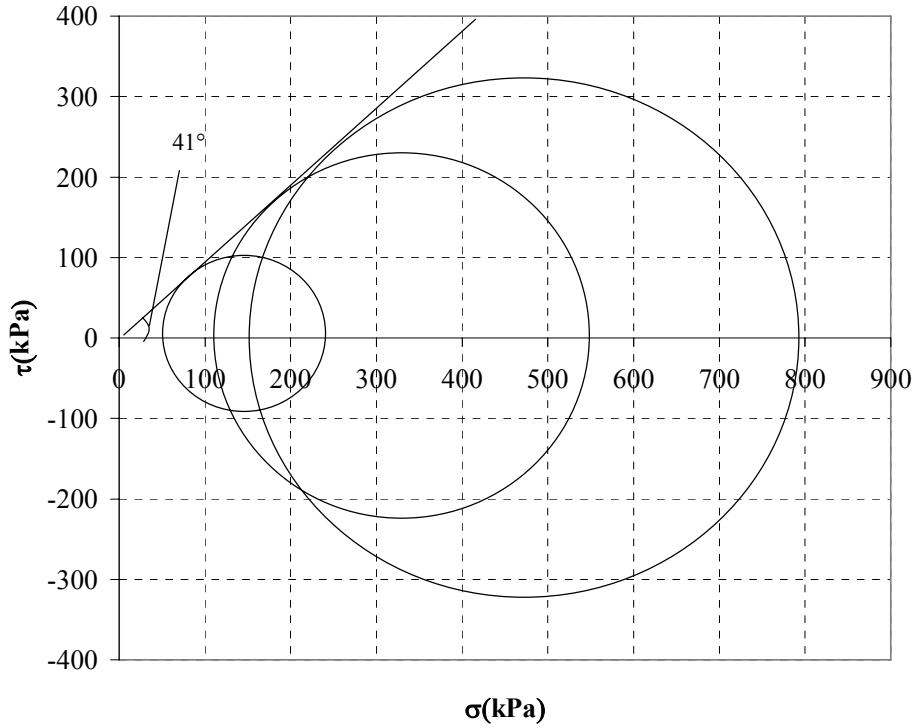

Figure 5.5. Internal friction angle determination

As seen in Figure 5.5 the internal friction angle (ϕ) and cohesion of the soil are found to be 41° and 1 kN/m^2, respectively. E_s can be assumed to be approximately 29180 kN/m^2 by taking the arithmetic average of the three values. Presented in Table 5.1 are the specimen parameters during the tests and soil parameters evaluated.

Table 5.1. Specimen parameters and soil properties

Specimen	Diameter (cm)	Height (cm)	Area (cm^2)	Mass (gr)	γ (kN/m^3)	e (void ratio)	σ_3 (kPa)	$\sigma_{fail.}$ (kPa)	E (kPa)	E_s (kPa)	φ (°)
S3	3.79	7.66	11.28	148.5	17.2	0.51	50	181	17075	29180	41
S4	3.64	7.7	10.4	144.55	17.71	0.47	150	632	45731		
S6	3.77	7.74	11.16	150.31	17.08	0.52	100	445	24722		

However, the results of the sand cone tests conducted after the completion of shaking table experiments demonstrate that in fact the average unit weights of the sand were 15 kN/m^3 and 16 kN/m^3 for the 1st and 2nd experiments, respectively (see section 7.2.3). With the observation of these results, actual internal friction angles of the sand were correlated with the determined internal friction angle of the sand (41°). By taking into account the values of 14 kN/m^3 and 20 kN/m^3 as typical minimum and maximum dry unit weights of silty sand type of soils and the correlation chart between relative density and internal

friction angle (Figure 5.6), one can evaluate relative density with the well-known equation below and find the related approximate angle of internal friction.

$$D_r = \frac{\gamma_{k\max}}{\gamma_k} \frac{\gamma_k - \gamma_{k\min}}{\gamma_{k\max} - \gamma_{k\min}} \tag{5.1}$$

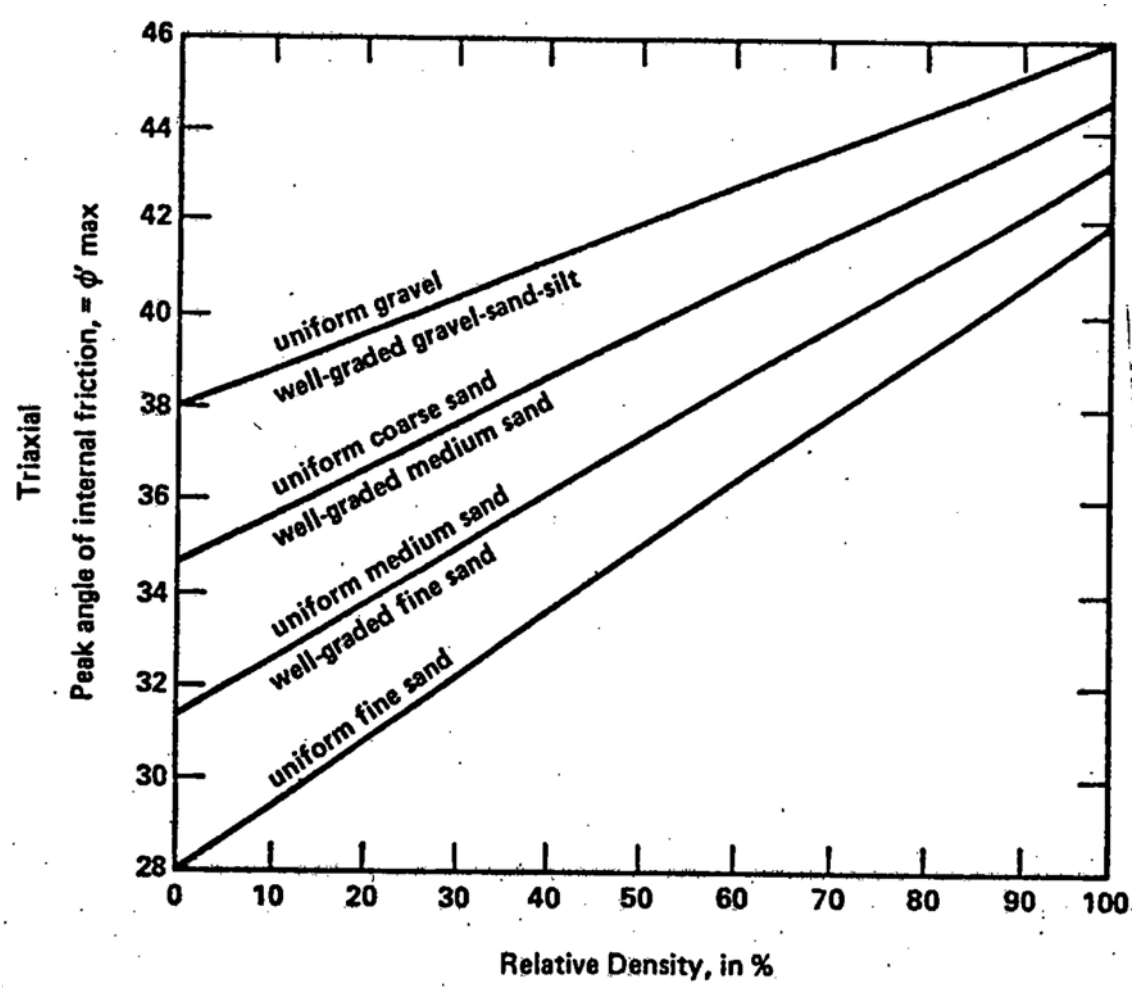

Figure 5.6. Chart for the approximate evaluation of the peak internal friction angles (Report to FHWA, Schmertmann, 1978)

By determining the relative densities for γ_d=17 kN/m^3, γ_d=16 kN/m^3 and γ_d=15 kN/m^3 as D_r=0.6, D_r=0.43 and D_r=0.24 (for uniform coarse sand, well-graded medium sand), the angle of internal friction values are evaluated to be 41°, 38° and 36°, respectively.

5.2. Soil-Granular Rubber Mixtures and Granular Rubber

The rubber that was used was a granular material and can be seen in the following Figure 5.7.

Figure 5.7. Granular rubber material

To satisfy the need of absorbing the possible returning earthquake waves from the back of the boundary, the properties of the soil-rubber mixtures and granular rubber material alone were investigated. The stress-strain curves of the soil-rubber mixtures and of the rubber material alone can be seen in Figure 5.8 through 5.16. While K1, K2 and K3 types of mixtures and K4, K5 and K6 types represent a mixture of 75 per cent of soil plus 25 per cent of granular rubber and a mixture of 50 per cent of soil and 50 per cent of granular rubber respectively, K7, K8 and K9 types denote for the granular rubber material alone.

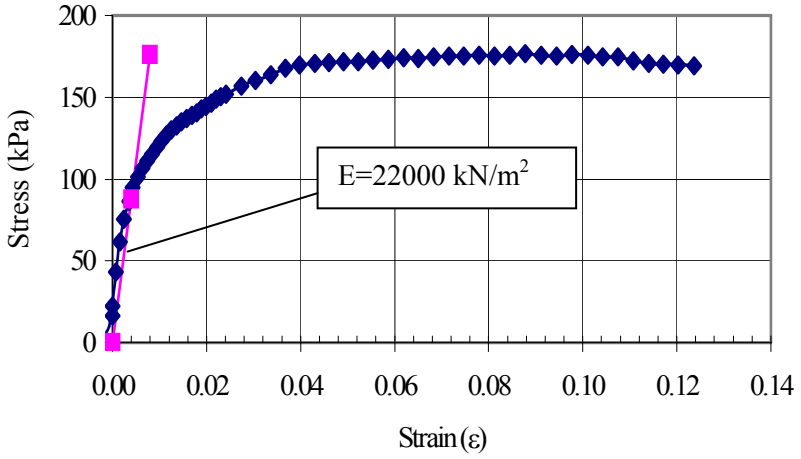

Figure 5.8. Triaxial test of K1 soil-rubber mixture specimen where σ_3=50 kPa

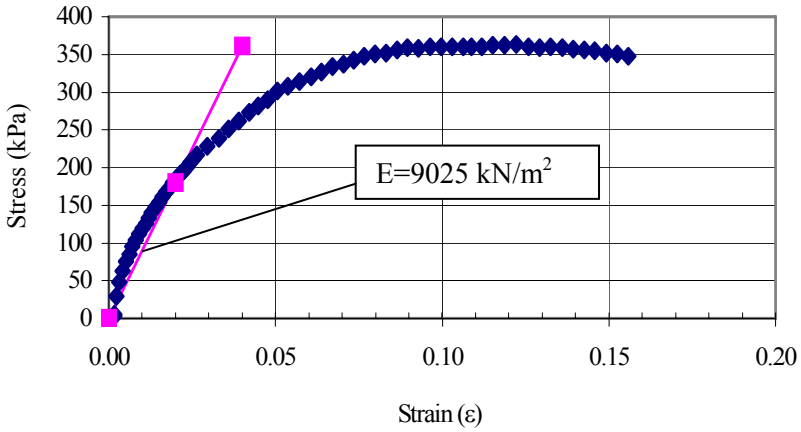

Figure 5.9. Triaxial test of K2 soil-rubber mixture specimen where σ_3=100 kPa

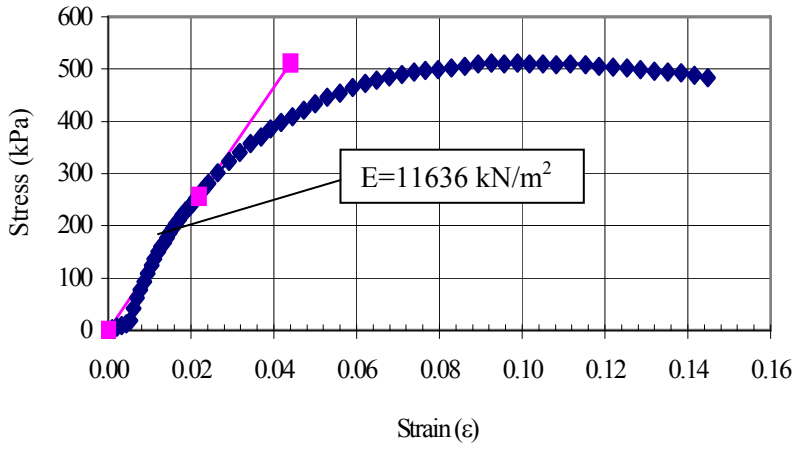

Figure 5.10. Triaxial test of K3 soil-rubber mixture specimen where σ_3=150 kPa

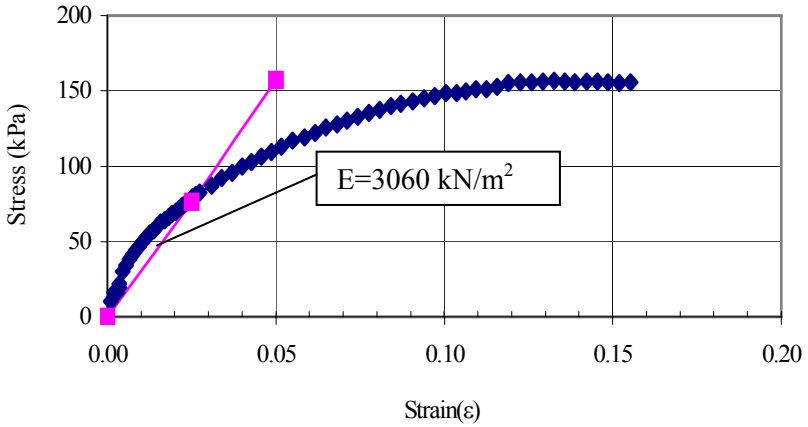

Figure 5.11. Triaxial test of K4 soil-rubber mixture specimen where σ_3=50 kPa

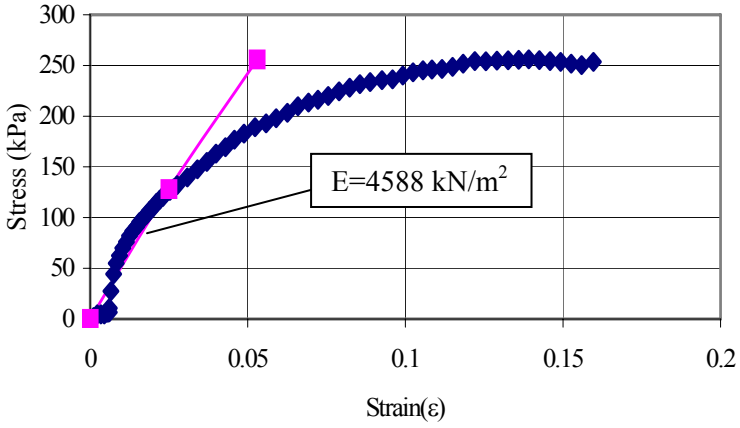

Figure 5.12. Triaxial test of K5 soil-rubber mixture specimen where σ_3=100 kPa

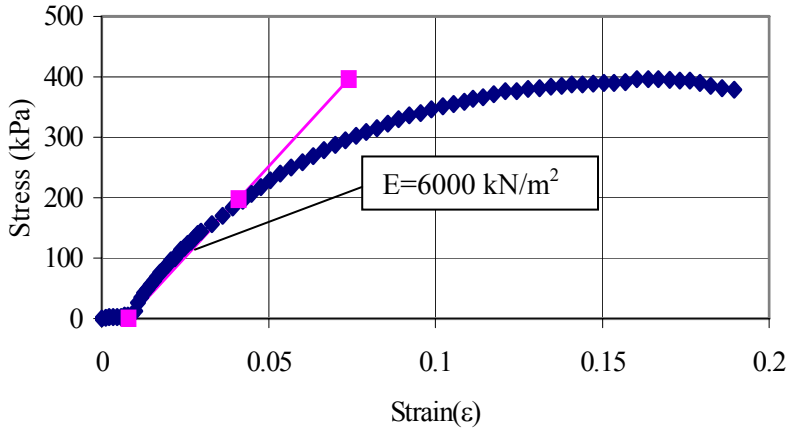

Figure 5.13. Triaxial test of K6 soil-rubber mixture specimen where σ_3=150 kPa

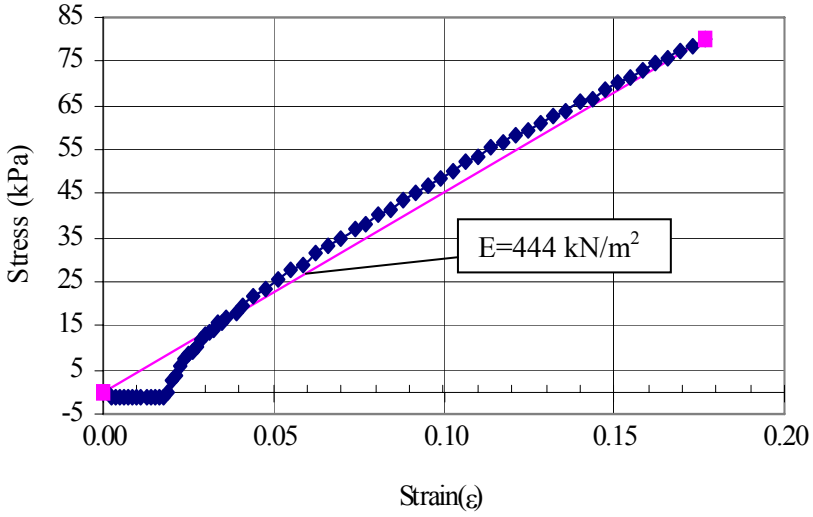

Figure 5.14. Triaxial test of K7 rubber specimen where σ_3=50 kPa

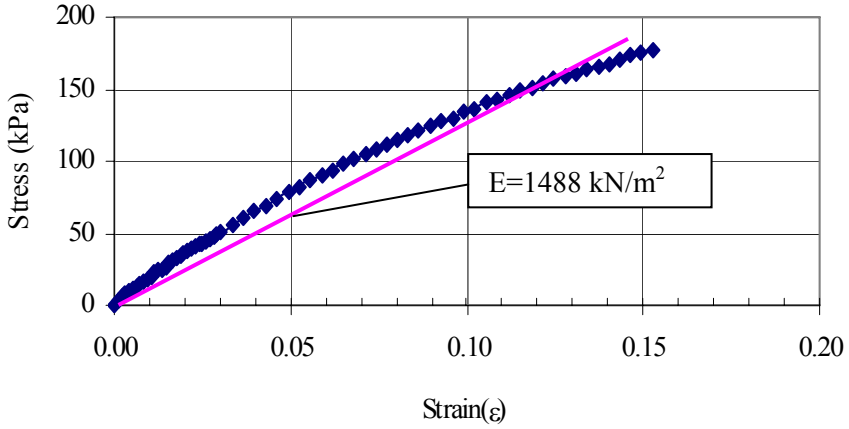

Figure 5.15. Triaxial test of K8 rubber specimen where σ_3=100 kPa

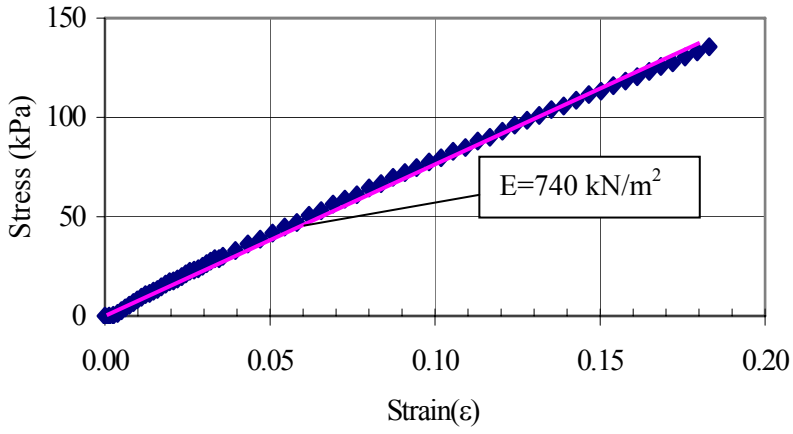

Figure 5.16. Triaxial test of K9 rubber specimen where σ_3=150 kPa

Presented in Table 5.2 are the specimen parameters and the evaluated properties of soil-rubber mixtures and rubber material alone.

Table 5.2. Specimen parameters and soil-rubber mixture and rubber properties

Specimen		**Diameter (cm)**	**Height (cm)**	**Area (cm^2)**	**Mass (gr)**	**γ (kN/m^3)**	**σ_3 (kPa)**	**$\sigma_{fail.}$ (kPa)**	**E (kPa)**	**$E_{assum.}$ (kPa)**	**ϕ (°)**
% 75 Soil + %25 Rubber Mix.	K1	3.81	7.69	11.4	134.42	15.05	50	176	22000	14220	40
	K2	3.58	7.52	10.06	118.15	15.32	100	361	9025		
	K3	3.74	7.61	10.98	128.78	15.12	150	512	11636		
%50 Soil + % 50 Rubber Mix.	K4	3.71	7.69	10.8	113.47	13.4	50	157	3060	4549	33
	K5	3.64	7.38	10.4	108.57	13.88	100	256	4588		
	K6	3.64	7.55	10.4	106.07	13.25	150	396	6000		
Rubber itself	K7	3.43	6.7	9.24	50	7.93	50	-	444	891	-
	K8	3.39	6.67	9.02	50	8.15	100	-	1488		
	K9	3.41	6.68	9.13	50	8.04	150	-	740		

6. NUMERICAL MODELING OF THE GRS-RW WITH THE PLAXIS PROGRAM

6.1. Plaxis FEM Program

Because in the beginnings of this study the newest version of Plaxis program (Plaxis v8.4) had not yet been published, many of the preliminary analyses of the GRS-RW under static and dynamic loading were performed by Plaxis v7.2 program, i.e. Calibrating the Rubber Fill with the Absorbent Boundary in Section 6.6 and Evaluation of the Fundamental Frequency of the Wall in Section 9.3. The Plaxis v8.4 program was only utilized in the stage of "Comparison of the Experiment Results with the Numerical Analysis Results", which is explained in detail in Section 10.

The Plaxis program was established by the researches conducted at Delft University of Technology in the late 1970's on the use of finite element methods for geotechnical design. It is a finite element code for 2D plane strain and axi-symmetric modeling of soil and rock behavior for use on fast personal-computers. The code uses automatic calculation procedures, and interactive menus combined with direct graphical output. The module provides elastic model, Mohr-Coulomb and modified Cam-Clay constitutive models. All models can deal with drained/undrained and non-porous material behavior. Higher order 15-noded or 6-noded elements are used to model the geometry. A variety of structural elements exist to model walls, plates, anchors and geotextiles. Interface elements provide a proper soil-structure interaction. Staged construction enables a realistic simulation of the building process. Iterative procedures are used in combination with automatic load stepping. This provides efficient solutions as the user does not need to select suitable load increments.

6.2. Modeling of the Elements of GRS-RW

To construct the geometric model of a GRS-RW in Plaxis program; points, lines, clusters, geotextile elements, interface elements, horizontal and vertical fixities, absorbent boundaries and prescribed displacements are utilized. Start and end points form the lines.

Lines are used to define the physical boundaries of the geometry. Also, lines enclose the areas to form clusters. The Plaxis program automatically recognizes the clusters after an enclosed area is formed. After composing the material properties of the soils or modular blocks in the material database, the materials are assigned to their related clusters. The soil in the clusters is always homogenous. In Figure 6.1, the model constructed in Plaxis program is shown to give a brief opinion.

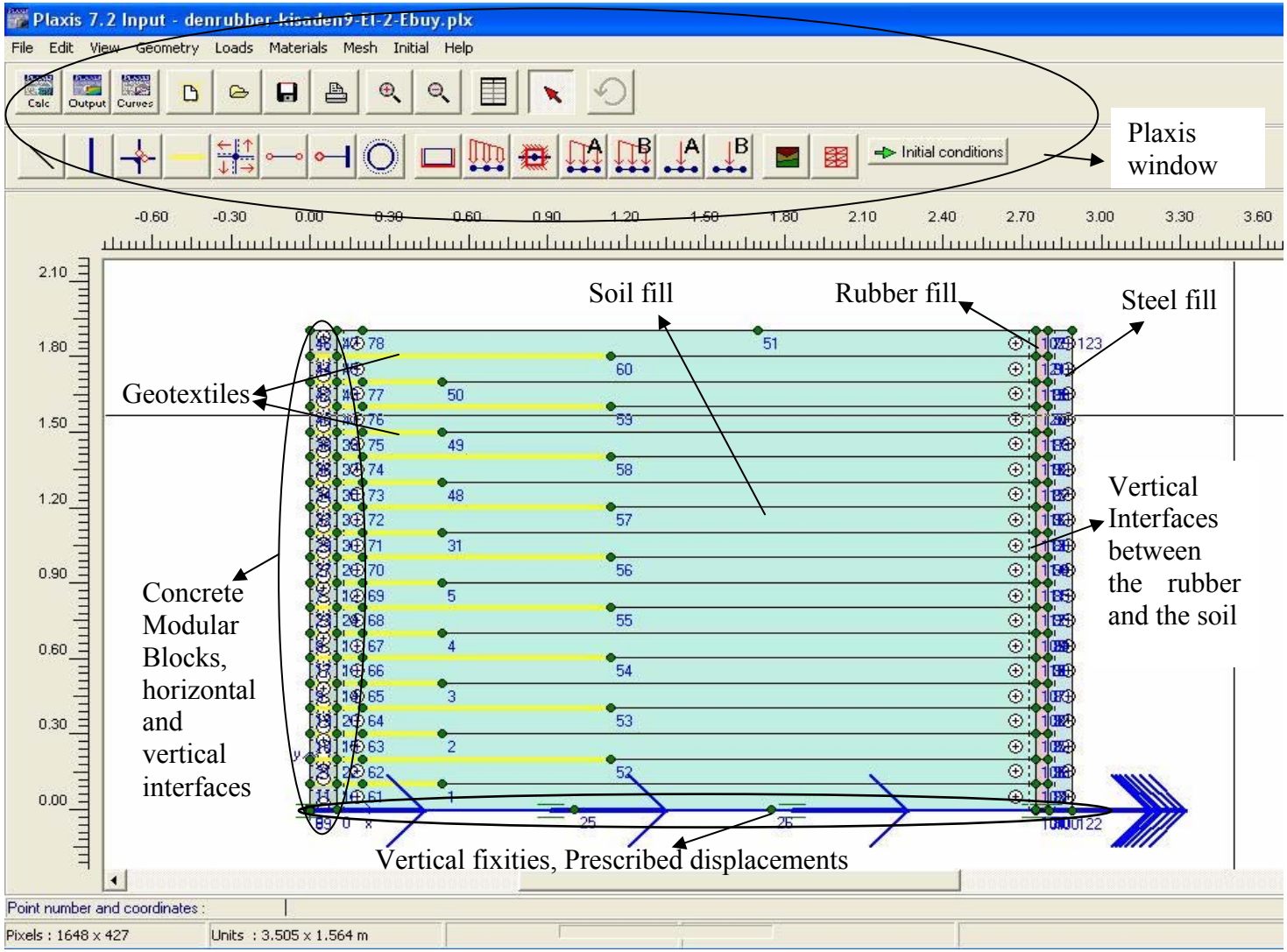

Figure 6.1. Plaxis window and an example of the representation of the GRS-RW model in Plaxis

6.2.1. Modeling of the Soil

Soil and rock tend to behave in a highly non-linear way under load. This non-linear stress-strain behavior can be modeled at several levels of sophistication. Clearly, the number of model parameters increases with the level of sophistication. The well-known Mohr-Coulomb model can be considered as a first order approximation of real soil behavior. This elastic perfectly-plastic model requires five basic input parameters, namely a Young's modulus, E, a Poisson's ratio, ν, a cohesion, c, a friction angle, ϕ, and a dilatancy angle, ψ.

The material properties and model parameters for soil clusters are entered in material data sets. The material properties of interfaces are related to the soil properties and are entered in the same data sets as the soil properties. A data set for soil and interfaces generally represents a certain soil layer and can be assigned to the corresponding cluster(s) in the geometry model. By default, the interfaces in that cluster obtain the same data set. This is indicated in the interface properties window as cluster material. To form a cluster, it is simply needed to construct a closed area by the help of line element.

Plaxis supports various models to simulate the behavior of soil and other continua. Out of these models, Mohr-Coulomb model and Hardening Soil Model with Small-Strain Stiffness are opted for the analyses.

6.2.1.1. Mohr-Coulomb model. This well known model is an elastic perfectly plastic model used as a first approximation of soil behavior in general. The model involves five parameters, Young's modulus, E, Poisson's ratio, ν, cohesion, c, friction angle, ϕ, and dilatancy angle, ψ.

In the analyses with Plaxis v7.2, this model was adopted for the soil material. The Elastic modulus of the soil was selected to be 3 times the $E_{average,soil}$, which is 87540 kN/m^2, the friction angle $\phi_{soil} = 41°$, cohesion $c_{soil} = 1$ kN/m^2, Poisson's ratio $\nu = 0.3$, unit weight $\gamma_{soil} = 16.5$ kN/m^3 and $\psi_{soil} = 11$, from $\psi = \varphi - 30°$.

6.2.1.2. Hardening Soil model. In contrast to an elastic perfectly-plastic model, the yield surface of a hardening plasticity model is not fixed in principal stress space, but it can expand due to plastic straining. Distinction can be made between two main types of hardening, namely shear hardening and compression hardening. Shear hardening is used to model irreversible strains due to primary deviatoric loading. Compression hardening is used to model irreversible plastic strains due to primary compression in oedometer loading and isotropic loading. Both types of hardening are contained in the present model.

The Hardening Soil model is an advanced model for simulating the behavior of different types of soil, both soft soils and stiff soils, Schanz (1998). When subjected to primary deviatoric loading, soil shows a decreasing stiffness and simultaneously irreversible plastic strains develop. In the special case of a drained triaxial test, the observed relationship between the axial strain and the deviatoric stress can be well approximated by a hyperbola. Such a relationship was first formulated by Kondner (1963) and later used in the well-known hyperbolic model (Duncan & Chang, 1970). The Hardening-Soil model, however, supersedes the hyperbolic model by far. Firstly by using the theory of plasticity rather than the theory of elasticity. Secondly by including soil dilatancy and thirdly by introducing a yield cap.

A basic feature of the present Hardening-Soil model is the stress dependency of soil stiffness. For oedometer conditions of stress and strain, the model implies for example the relationship:

$$E_{oed} = E_{oed}^{ref}\left(\frac{-\sigma'_1}{p^{ref}}\right)^m \tag{6.1}$$

where p^{ref} is a reference pressure and m is the stress dependency parameter. For hard and soft soils, m is selected to be 0.5 and 1, respectively.

A basic idea for the formulation of the Hardening-Soil model is the hyperbolic relationship between the vertical strain, ε_1, and deviatoric stress, q, in primary triaxial loading. Here standard drained triaxial tests tend to yield curves that can be described by:

$$-\varepsilon_1 = \frac{1}{E_i}\frac{q}{1-\frac{q}{q_a}} \quad \text{for : } q < q_f \tag{6.2}$$

where q_a is the asymptotic value of the shear strength and E_i the initial stiffness, which is equal to:

$$E_i = \frac{2E_{50}}{2-R_f} \tag{6.3}$$

This relation is plotted in Figure 6.2. The parameter E_{50} is the confining stress dependent stiffness modulus for primary loading and is given by the equation:

$$E_{50} = E_{50}^{ref}\left(\frac{c\cos\varphi - \sigma_3^{'}\sin\varphi}{c\cos\varphi + p^{ref}\sin\varphi}\right)^m \tag{6.4}$$

where E_{50}^{ref} is a reference stiffness modulus corresponding to the reference confining pressure p^{ref}. In PLAXIS, a default setting p^{ref}=100 stress units is used. The actual stiffness depends on the minor principal stress, $\sigma_3^{'}$, which is the confining pressure in a triaxial test. Please note that $\sigma_3^{'}$ is negative for compression. The amount of stress dependency is given by the power *m*. For hard and soft soils, *m* is selected to be 0.5 and 1, respectively [22].

The ultimate deviatoric stress, q_f, and the quantity q_a in Eq. 6.2 are defined as:

$$q_f = \left(c\cot\varphi - \sigma_3^{'}\right)\frac{2\sin\varphi}{1-\sin\varphi} \text{ and } q_a = \frac{q_f}{R_f} \tag{6.5}$$

Again it is remarked that $\sigma_3^{'}$ is usually negative. The relationship for q_f is derived from the Mohr-Coulomb failure criterion, which involves the strength parameters *c* and φ. As soon as $q = q_f$, the failure criterion is satisfied and perfectly plastic yielding occurs as described by the Mohr-Coulomb model [22].

The ratio between q_f and q_a is given by the failure ratio R_f, which should obviously be smaller than 1. In PLAXIS, R_f= 0.9 is chosen as a suitable default setting.

For unloading and reloading stress paths, another stress-dependent stiffness modulus is used:

$$E_{ur} = E_{ur}^{ref}\left(\frac{c\cos\varphi - \sigma_3^{'}\sin\varphi}{c\cos\varphi + p^{ref}\sin\varphi}\right)^{m} \tag{6.6}$$

where E_{ur}^{ref} is the reference Young's modulus for unloading and reloading, corresponding to the reference pressure p^{ref}. In many practical cases it is appropriate to set E_{ur}^{ref} equal to 3 E_{50}^{ref} ; this is the default setting used in PLAXIS [22].

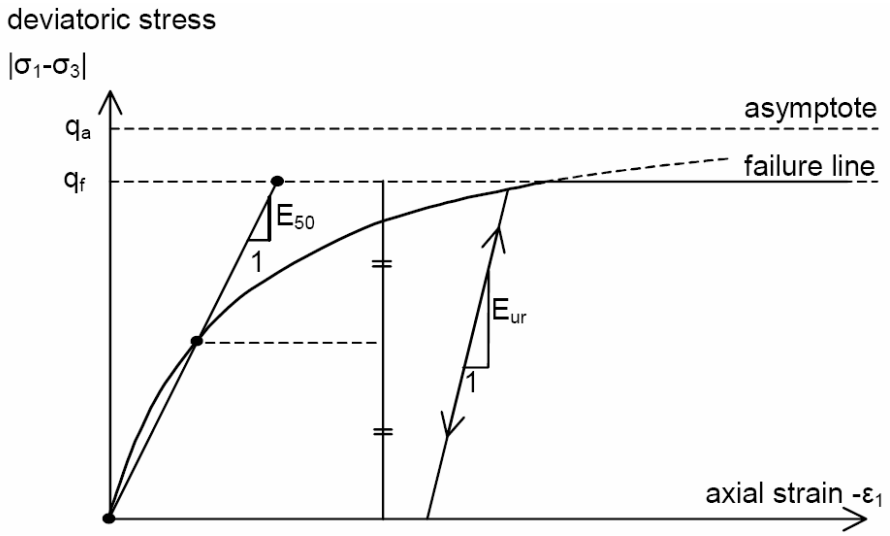

Figure 6.2. Hyperbolic stress-strain relation in primary loading for a standard drained triaxial test [22]

The advantage of the Hardening Soil model over the Mohr-Coulomb model is not only the use of a hyperbolic stress-strain curve instead of a bi-linear curve, but also the control of stress level dependency. When using the Mohr-Coulomb model, the user has to select a fixed value of Young's modulus whereas for real soils this stiffness depends on the stress level. It is therefore necessary to estimate the stress levels within the soil and use these to obtain suitable values of stiffness. With the Hardening Soil model, however, this

cumbersome selection of input parameters is not required. Instead, a stiffness modulus E_{50}^{ref} is defined for a reference minor principal stress of $-\sigma_3^{'} = p^{ref}$. As a default value, the program uses p^{ref} = 100 stress units.

Within Hooke's law of isotropic elasticity conversion between *E* and *G* goes by the equation *E = 2 (1+υ) G*. As E_{ur} is a real elastic stiffness, one may thus write E_{ur} *= 2 (1+υ)* G_{ur}, where G_{ur} is an elastic shear modulus. Please note that PLAXIS allows for the input of E_{ur} and υ_{ur} but not for a direct input of G_{ur}. In contrast to E_{ur}, the secant modulus E_{50} is not used within a concept of elasticity. As a consequence, there is no simple conversion from E_{50} to G_{50}.

In contrast to elasticity based models, the elastoplastic Hardening Soil model does not involve a fixed relationship between the (drained) triaxial stiffness E_{50} and the oedometer stiffness E_{oed} for one-dimensional compression. Instead, these stiffnesses can be inputted independently. The oedometer stiffness is defined by:

$$E_{oed} = E_{oed}^{ref}\left(\frac{c\cos\varphi - \sigma_1^{'}\sin\varphi}{c\cos\varphi + p^{ref}\sin\varphi}\right)^m \tag{6.7}$$

where E_{oed} is a tangent stiffness modulus as indicated in Figure 6.3. Hence, E_{oed}^{ref} is a tangent stiffness at a major principal stress of $-\sigma_1^{'} = p^{ref}$. σ_1 is used rather than σ_3 and primary loading is considered.

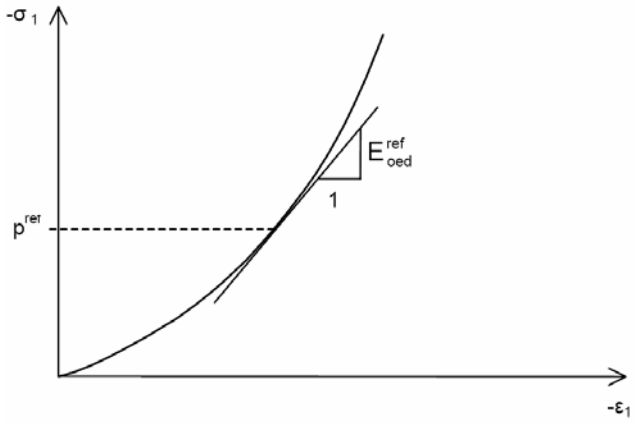

Figure 6.3. Definition of E_{oed}^{ref} in oedometer test results [22]

In conclusion, the input parameters of the model are:

- m : Stress dependent stiffness according to a power law (Power for stress-level dependency of stiffness).
- E_{50}^{ref} : Plastic straining due to primary deviatoric loading (Secant stiffness in standard drained triaxial test).
- E_{oed}^{ref} : Plastic straining due to primary compression (Tangent stiffness for primary oedometer loading).
- E_{ur}^{ref} : Unloading/reload. stiffness at engineering strains ($\varepsilon \approx 10^{-3}$~$10^{-2}$).
- υ_{ur}^{ref} : Poisson's ratio for unloading-reloading
- Failure according to the Mohr-Coulomb model. Parameters c, φ and ψ [22].

6.2.1.3. Hardening Soil Model with Small-Strain Stiffness (HSsmall). The original Hardening Soil model assumes elastic material behaviour during unloading and reloading. However, the strain range in which soils can be considered truly elastic, i.e. where they recover from applied straining almost completely, is very small. With increasing strain amplitude, soil stiffness decays nonlinearly. Plotting soil stiffness against log (strain) yields characteristic S-shaped stiffness reduction curves. Figure 6.4 gives an example of such a stiffness reduction curve. It outlines also the characteristic shear strains that can be measured near geotechnical structures and the applicable strain ranges of laboratory tests. It turns out that at the minimum strain which can be reliably measured in classical laboratory tests, i.e. triaxial tests and oedometer tests without special instrumentation, soil stiffness is often decreased to less than half its initial value.

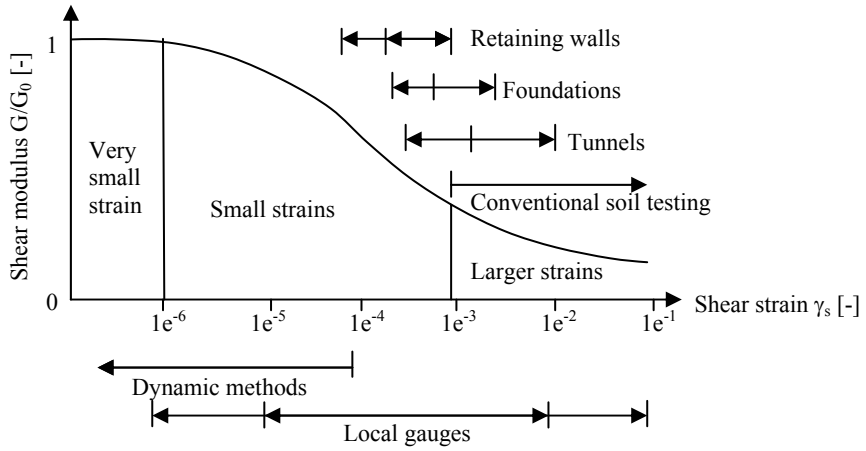

Figure 6.4. Characteristic stiffness-strain behavior of soil with typical strain ranges for laboratory tests and structures (after Atkinson & Sallfors) [22]

The soil stiffness that should be used in the analysis of geotechnical structures is not the one that relates to the strain range at the end of construction according Figure 6.4. Instead, very small-strain soil stiffness and its non-linear dependency on strain amplitude should be properly taken into account. In addition to all features of the Hardening Soil model, the HSsmall model offers the possibility to do so.

The HSsmall model implemented in PLAXIS is based on the Hardening Soil model and uses almost entirely the same parameters (see Section 6.2.1.2). In fact, only two additional parameters are needed to describe the stiffness behavior at small strains:

• the initial or very small-strain shear modulus G_0

• the shear strain level $\gamma_{0.7}$ at which the secant shear modulus G is reduced to 70 per cent of G_0

In soil dynamics, small-strain stiffness has been a well known phenomenon for a long time. In static analysis, the findings from soil dynamics have long been considered not to be applicable.

Seeming differences between static and dynamic soil stiffness have been attributed to the nature of loading (e.g. inertia forces and strain rate effects) rather than to the magnitude of applied strain which is generally small in dynamic conditions (earthquakes excluded). As inertia forces and strain rate have only little influence on the initial soil stiffness, dynamic soil stiffness and small-strain stiffness can in fact be considered as synonyms.

The probably most frequently used model in soil dynamics is the Hardin-Drnevich relationship. From test data, sufficient agreement is found that the stress-strain curve for small strains can be adequately described by a simple hyperbolic law. The following analogy to the hyperbolic law for larger strains by Kondner was proposed by Hardin & Drnevich:

$$\frac{G}{G_0} = \frac{1}{1 + \left| \frac{\gamma}{\gamma_r} \right|} \tag{6.8}$$

where the threshold shear strain γ_r is quantified as:

$$\gamma_r = \frac{\tau_{\max}}{G_0} \tag{6.9}$$

with τ_{max} being the shear stress at failure. Essentially, Eq. 6.8 and Eq. 6.9 relate large (failure) strains to small-strain properties which often work well.

More straightforward and less prone to error is the use of a smaller threshold shear strain. Santos & Correia, for example suggest to use the shear strain $\gamma_r = \gamma_{0.7}$ at which the shear modulus G_0 is reduced to 70 % of its initial value. Eq. 6.8 can then be rewritten as:

$$\frac{G}{G_0} = \frac{1}{1 + a\left|\frac{\gamma}{\gamma_{0.7}}\right|} \text{ where a = 3/7} \tag{6.10}$$

. Figure 6.5 shows the fit of the modified Hardin-Drnevich relationship (Eq. 6.10) to normalized test data.

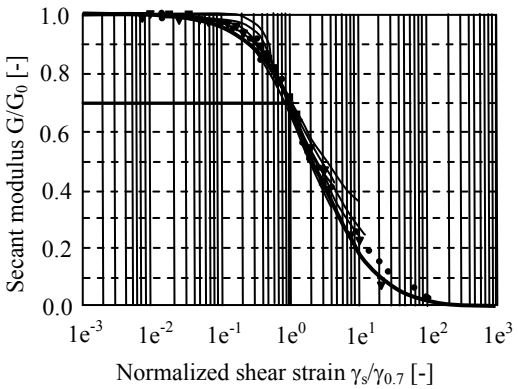

Figure 6.5. Results from Hardin-Drenevich relationship compared to test data by Santos & Correia [22]

The decay of soil stiffness at small strains can be associated with loss of intermolecular and surface forces within the soil skeleton. Once the direction of loading is reversed, the stiffness regains a maximum recoverable value which is in the order of the

initial soil stiffness. Then, while loading in the reversed direction is continued, the stiffness decreases again.

The stiffness reduction curve defined in Eq. 6.10 reaches far into the plastic material domain. In the Hardening Soil and HSsmall model, stiffness degradation due to plastic straining is simulated with strain hardening. In the HSsmall model, the small-strain stiffness reduction curve is therefore bounded by a certain lower limit, determined by conventional laboratory tests:

• The lower cut-off is introduced at the unloading reloading stiffness G_{ur} which is defined by the material parameters E_{ur} and ν_{ur}.

• The cut-off shear strain $\gamma_{cut\text{-}off}$ calculates as:

$$\gamma_{cut-off} = \frac{7}{3}\left(\frac{G_0}{G_{ur}} - 1\right)\gamma_{0.7} \text{ where } G_{ur} = \frac{E_{ur}}{2(1+\upsilon_{ur})} \tag{6.11}$$

Within the HSsmall model, the actual quasi-elastic tangent shear modulus is calculated by integrating the secant stiffness modulus reduction curve over the actual shear strain increment. An example of a stiffness reduction curve used in the HSsmall model is shown in Figure 6.6.

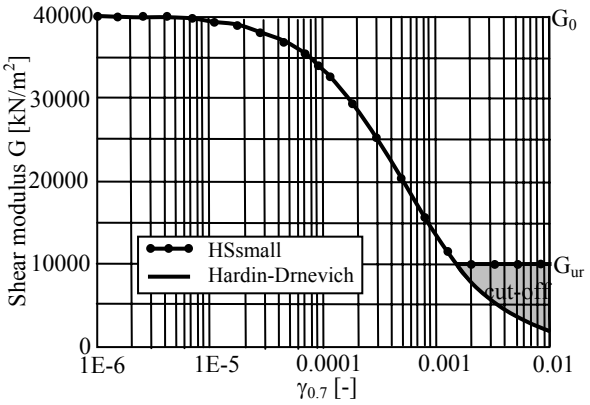

Figure 6.6. Cut-off of the small-strain degradation curve as used in the HS-Small model [22]

Masing described the hysteretic behavior of materials in unloading / reloading cycles in the form of the following rules:

- The shear modulus in unloading is equal to the initial tangent modulus for the initial loading curve.
- The shape of the unloading and reloading curves is equal to the initial loading curve, but twice its size. In terms of the introduced threshold shear strain $\gamma_{0.7}$, Masing's rule can be fulfilled by the following setting in the Hardin-Drnevich relation:

$$\gamma_{0.7re-loading} = 2\gamma_{0.7virgin-loading} \tag{6.12}$$

The HSsmall model consequently adopts Masing's rule by doubling the threshold shear strain provided by the user for virgin loading. If hardening plasticity readily accounts for more rapidly decaying small-strain stiffness during virgin loading, the user defined threshold shear strain is always doubled. Next, the hardening laws of the HSsmall model are fitted such, that the small-strain stiffness reduction curve is reasonably well approximated. Figure 6.7 illustrates Masing's rule and the secant stiffness reduction in virgin loading and unloading / reloading.

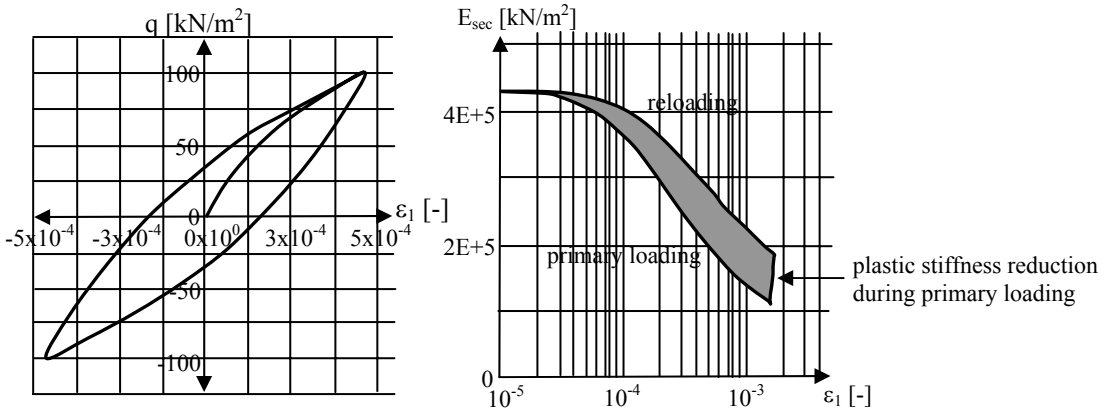

Figure 6.7. Left: Hysteretic material behavior. Right: HSsmall stiffness reduction in initial – or primary loading and in unloading/reloading [22]

Compared to the standard HS model, the HSsmall model requires two additional stiffness parameters as input: G_0^{ref} and $\gamma_{0.7}$. All other parameters remain the same as in the standard HS model. G_0^{ref} defines the shear modulus at very small strains e.g. $\varepsilon < 10^{-6}$ at a reference minor principal stress of $-\sigma_3^{'} = p^{ref}$.

Poisson's ratio ν_{ur} is assumed a constant, as everywhere in Plaxis, so that the shear modulus G_0^{ref} can also be calculated from the very small strain Young's modulus as $G_0^{ref} = E_0^{ref} / \left(2\left(1+\upsilon_{ur}\right)\right)$. The threshold shear strain $\gamma_{0.7}$ is the shear strain at which the secant shear modulus is decayed to $0.7\,G_0^{ref}$. The threshold shear strain $\gamma_{0.7}$ is to be supplied for virgin loading.

A number of factors influence the small-strain parameters G_0 and $\gamma_{0.7}$. Most importantly they are influenced by the material's actual state of stress and void ratio e. In the HSsmall model, the stress dependency of the shear modulus G_0 is taken into account with the power law:

$$G_0 = G_0^{ref}\left(\frac{c\cos\varphi - \sigma_1^{'}\sin\varphi}{c\cos\varphi + p^{ref}\sin\varphi}\right)^m \tag{6.13}$$

which resembles the ones used for the other stiffness parameters. The threshold shear strain $\gamma_{0.7}$ is taken independently of mean stress.

Assuming that within a HSsmall (or HS) computation void ratio changes are rather small, the material parameters are not updated for changes in the void ratio. Knowledge of a material's initial void ratio can nevertheless be very helpful in deriving its small-strain shear stiffness G_0. Many correlations are offered in the literature. A good estimation for many soils is for example the relation given by Hardin & Black:

$$G_0^{ref} = \frac{(2.97-e)^2}{1+e}33[MPa] \tag{6.14}$$

In the absence of test data, one can refer to the previous studies implemented by several researchers in this field. Most of these studies have shown that when test data are plotted to show the variation with shear strain of the ratio of shear modulus at strain γ to shear modulus at a shear strain of 10^{-4} per cent of the results fall within the relatively narrow band shown in Figure 6.8. Thus a close approximation to the modulus versus shear strain relationship for any sand can be obtained by determining the modulus at a very low strain level, e.g. wave propagation methods in the field, and then reducing this value for other strain levels in accordance with the results indicated by the average (dashed) line in Figure 6.8 [23]. Using the original Hardin-Drnevich relationship, the threshold shear strain $\gamma_{0.7}$ might be also related to the model's failure parameters. Applying the Mohr-Coulomb failure criterion in Eq. 6.9 and Eq. 6.10 yields:

$$\gamma_{0.7} \approx \frac{1}{9G_0}\left[2c'\left(1+\cos\left(2\varphi'\right)\right)-\sigma_1'\left(1+K_0\right)\sin\left(2\varphi'\right)\right] \tag{6.15}$$

where K_0 is the earth pressure coefficient at rest and σ' is the effective vertical stress (pressure negative) [22].

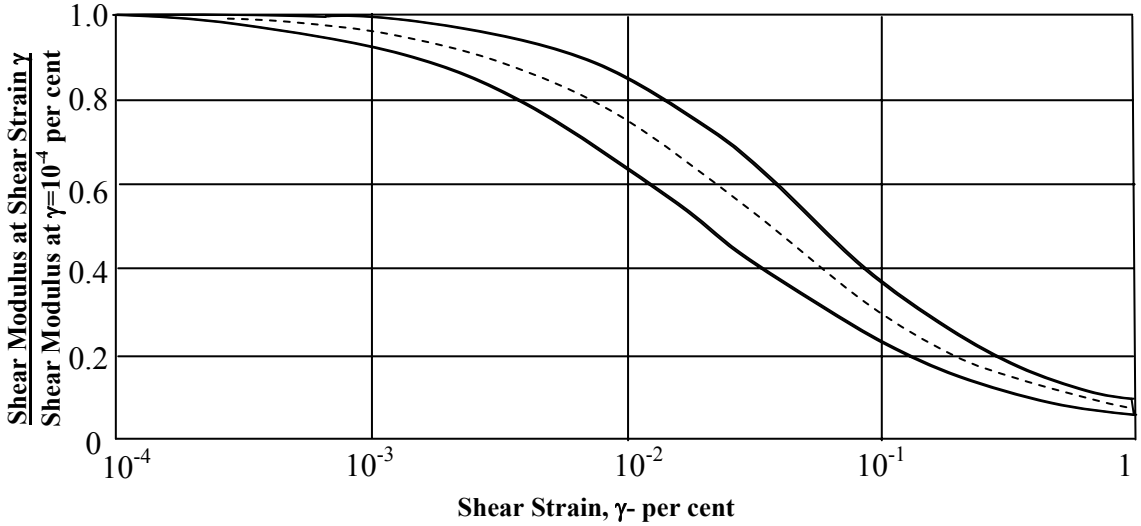

Figure 6.8. Variation of shear modulus with shear strain for sands (after Seed and Idriss, 1970) [23]

In the analyses with Plaxis v8.4, the required parameters of the soil for this model were selected to be as in Table 6.1.

Table 6.1. Parameter selection for HSsmall model in Plaxis v8.4

Parameter	Value	Comments
γ_{soil}	15, 16 kN/m^3	For 1st and 2nd experiments, respectively
E_{50}^{ref}	24720 kN/m^2	$E_{sec.}$ at 100 kN/m^2 confining pressure
E_{oed}^{ref}	24720 kN/m^2	In the absence of test data $E_{50}^{ref} = E_{oed}^{ref}$ is advised in Plaxis manual
E_{ur}^{ref}	74170 kN/m^2	E_{ur}^{ref} =3 E_{50}^{ref} is advised in Plaxis manual
Power	0.5	Hard soil
c	1 kN/m^2	Mohr-Coulomb parameter
φ	36°, 38°	Mohr-Coulomb parameter, For 1st and 2nd experiments, respectively
ψ	6°, 8°	Mohr-Coulomb parameter, For 1st and 2nd experiments, respectively
$\gamma_{0.7}$	0.0001	Approximate value by the help of dashed line in Figure 6.8
G_0^{ref}	134000 kN/m^2	by Eq. 6.14 for e=0.5
ν_{ur}	0.2	default value
p^{ref}	100 kN/m^2	default value
K_0^{nc}	0.412, 0.384	from K_0^{nc} = 1-sinφ, For 1st and 2nd experiments, respectively
Rf	0.9	default value

6.2.2. Modeling of the Reinforcement

Geotextiles are composed of geotextile elements. When 6-node soil elements are employed then each geotextile element is defined by 3 nodes, whereas 5-node geotextile elements are used in combination with 15-node soil elements. Axial forces are evaluated at the Newton-Cotes stress points.

The reinforcement material used in Plaxis is the geotextile material. In Plaxis, geotextiles are defined as slender objects with a normal stiffness but with no bending stiffness. Geotextiles can only sustain tensile forces but no compression. These objects are mostly used to model soil reinforcements for example geogrids or fabric wovens. Finite element methods have been used extensively to study the performance of this type of structures.

Geotextiles can be selected from the geometry sub-menu or by clicking on the corresponding button in the tool bar. The creation of geotextiles in the geometry model is

similar to the creation of geometry lines. When creating geotextiles, corresponding geometry lines are created simultaneously. The only material property of a geotextile is an elastic normal (axial) stiffness EA, which can be specified in the material data base.

In this study, the stiffness of the reinforcement was taken as J = 364 kN/m for the tensile yield strength of T_y = 40 kN/m at 11 per cent of yield strain.

6.2.3. Modeling of the Facing Element

The facing elements were of concrete modular block type and they were modeled with line elements by forming clusters of 10 cm × 10 cm. The linear elastic model was opted for the facing elements. The Elastic Modulus of the concrete modular block was chosen to be $E_{mod.}$ = 4.4E+06 kN/m^2, Poisson's ratio ν = 0.17 and unit weight $\gamma_{mod.}$ = 21 kN/m^3.

6.2.4. Modeling of the Interface

Interfaces, which are composed of interface elements, are used to model the interaction between structures and the soil. When using 6-node soil elements, the corresponding interface elements are defined by three pairs of nodes, whereas for 15-node soil elements the interface elements are defined by five pairs of nodes. In Figure 6.9, the interface elements are shown to have a finite thickness, but in the finite element formulation the coordinates of each node pair coincides with each other so that zero thickness element condition is satisfied.

Each interface has assigned to itself a "virtual thickness" which is an imaginary dimension used to obtain the material properties of the interface. The virtual thickness is defined as the virtual thickness factor times the average element size. The average element size is determined by the global coarseness setting for the mesh generation. The default value of the virtual thickness factor is 0.1.

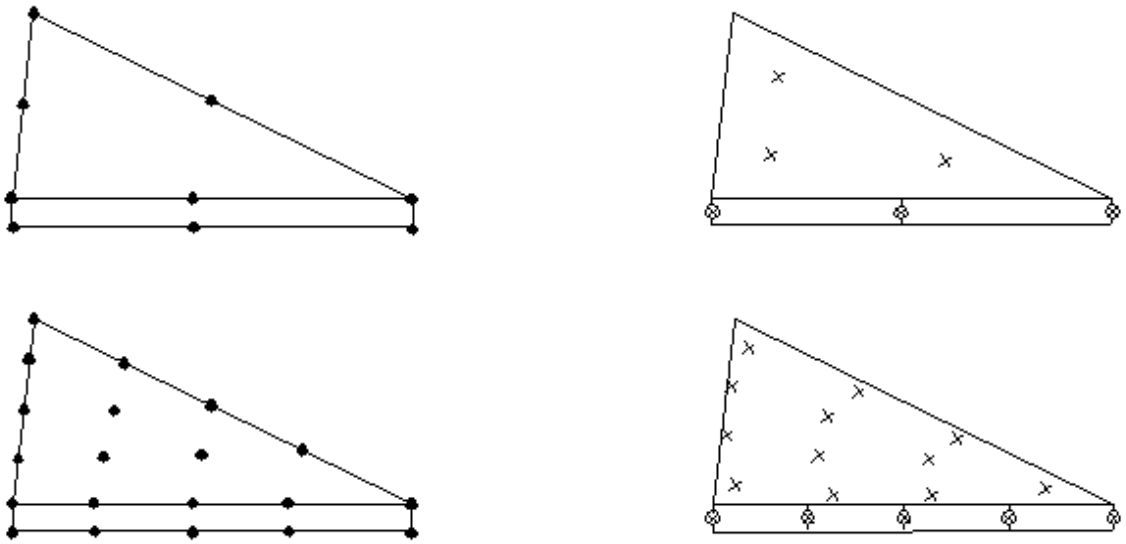

Figure 6.9. Distribution of nodes and stress points in interface elements and connection with soil elements

The stiffness matrix for interface elements is obtained using Newton-Cotes integration points. The position of these integration points (or stress points) coincides with the position of the node pairs. Hence, for the 6-node interface elements a 3-point Newton-Cotes integration is used, whereas the 10-node interface elements use 5-point integration.

The roughness of the interaction between the structure and the soil is modeled by choosing a suitable value for the strength reduction factor (R_{inter}) in the interface. This factor relates the interface strength (friction and adhesion) to the soil strength (friction angle and cohesion).

An elastic-plastic model is used to describe the behavior of interfaces for the modeling of soil-structure interaction. The Coulomb criterion is used to distinguish between elastic behavior, where small displacements can occur within the interface, and plastic interface behavior (slip).

For the interface to remain elastic the shear stress τ is given by:

$$|\tau| < \sigma_n . \tan \varphi_i + c_i \tag{6.16}$$

and for plastic behavior τ is given by:

$$|\tau| = \sigma_n . \tan \varphi_i + c_i \tag{6.17}$$

where φ_i and c_i are the friction angle and cohesion of the interface and σ_n and τ are the normal stress and shear stress acting in the interface. The strength properties of interfaces are linked to the strength properties of a soil layer. Each data set has an associated strength reduction factor for interfaces (R_{inter}). The interface properties are calculated from the soil properties in the associated data set and the strength reduction factor by applying the following rules:

$$c_i = R_{\text{int } er} . c_{soil} \tag{6.18}$$

$$\tan \varphi_i = R_{\text{int } er} . \tan \varphi_{soil} \leq \tan \varphi_{soil} \tag{6.19}$$

$$\psi_i = 0° \text{ for } R_{inter} < 1, \text{ otherwise } \psi_i = \psi_{soil} \tag{6.20}$$

As a default value R_{inter} is rigid and equal to 1, but it can be modified after it is turned to manual option. If R_{inter} is rigid, then this means that the interface should not influence the strength of the surrounding soil. In general, for real soil-structure interaction the interface is weaker and more flexible than the associated soil layer, which means that R_{inter} should be less than 1.

In this study, interfaces were defined between the modular blocks and the soil, between the soil and rubber fill and between the modular blocks and geotextile elements.

The interface between the modular blocks and the soil and the interface between the soil and rubber fill were modeled with the Mohr-Coulomb material model. All the properties specific to this model were the same as in the Mohr-Coulomb soil model for the analyses with Plaxis v7.2. The only exception was when selecting the interface properties. The interface strength reduction factor is recommended to be taken as 2/3 in the Plaxis manual. Therefore a value of $R_{inter} = 0.7$ was selected. On the other hand, in the analyses

with Plaxis v8.4 for these kinds of interfaces, the elastic modulus of the soil was selected to be 3 times the $E_{average,soil}$, which is 87540 kN/m^2, the friction angle ϕ_{soil} = 36° and 38° (for 1st and 2nd experiments respectively), cohesion c_{soil} = 1 kN/m^2, poisson's ratio ν = 0.3, unit weight γ_{soil} = 15 and 16 kN/m^3 (for 1st and 2nd experiments respectively), ψ_{soil} = 6° and 8° (for 1st and 2nd experiments respectively), from $\psi = \varphi - 30°$ and R_{inter} = 0.7.

The interface between the modular blocks and the geotextile elements were also modeled with the Mohr-Coulomb material model. All the properties specific to this model were the same as in the facing elements, except that cohesion was taken to be c = 2 kN/m^2 and internal friction angle φ = 30° as a common value. Since, the voids of the two uppermost levels of modular blocks were concreted and steel bars were placed before the concretion, internal friction angle was taken to be φ = 30° and a very high cohesion value was assigned (c=100 kN/m^2) to the interface between them or no interface element was put. Both solutions satisfied the rigidity and high cohesion at the uppermost two levels.

6.2.5. Modeling of the Rubber Fill

Rubber fill was used on the back of the fill to absorb earthquake induced vibrations. For the rubber fill the clusters were formed and property of the rubber material was assigned to the clusters. The rubber fill was modeled to be a linear elastic material. The properties assigned were based on the laboratory measurements summarized in Section 5.2. The Elastic Modulus of the material was taken to be E_{rubber} = 891 kN/m^2, Poisson's ratio ν = 0.2 and unit weight γ_{rubber} = 5.3 kN/m^3.

6.2.6. Modeling of the Absorbent Boundary Element

In opting for absorbent boundaries, a damper is used instead of applying fixities in a certain direction. The damper ensures that an increase in stress on the boundary is absorbed without rebounding. The boundary then starts to move.

The normal and shear stress components absorbed by a damper in x-direction are:

$$\sigma_n = -c_1 \rho V_p \dot{u}_x \tag{6.21}$$

$$\tau = -c_2 \rho V_s \dot{u}_y \tag{6.22}$$

where ρ is the density of the materials; V_p and V_s are the pressure wave velocity and the shear wave velocity, respectively; C_1 and C_2 are relaxation coefficients that have been introduced in order to improve the effect of the absorption. When pressure waves strike the boundary perpendicular, relaxation is redundant (C_1=C_2=1). In the presence of shear waves, the damping effect of the absorbent boundaries is not sufficient without relaxation. The effect can be improved by adapting the second coefficient in particular. The experience gained until now shows that the use of C_1=1 and C_2=0.25 results in a reasonable absorption of waves at the boundary. However, it is not possible to state that shear waves are fully absorbed so that in the presence of shear waves a (limited) boundary effect is noticeable. Additional research is therefore necessary on this point, but the method described is sufficient for practical applications.

V_p and V_s are determined using below equations:

$$V_p = \sqrt{\frac{E_{oed}}{\rho}} \text{ where } E_{oed} = \frac{(1-\upsilon)E}{(1+\upsilon)(1-2\upsilon)} \text{ and } \rho = \frac{\gamma}{g} \tag{6.23}$$

$$V_s = \sqrt{\frac{G}{\rho}} \text{ where } G = \frac{E}{2(1+\upsilon)} \tag{6.24}$$

in which E = Young's modulus, ν = Poisson's ration, γ = total unit weight, E_{oed}= One dimensional compression modulus, G =Shear Modulus and g is the gravity acceleration (9.8 m/s^2) [22].

In this study, the absorbent boundary element was put at the very back of the backfill whose related parameters were taken as C_1=1 and C_2=0.25 like it is advised.

6.2.7. Modeling of the Steel Container

The steel container's bottom plate needed to be modeled in every model of Plaxis in order to get satisfactory and consistent results. Otherwise, at the end of the dynamic analyses, large residual displacements were observed on the front wall caused by the sliding of the whole reinforced mass in the external failure mode. So, the 8 mm thick bottom plate of the steel container was modeled in all of the models and with a rigid base like this one, the failure of the structure was prevented and more accurate results close to the experiments were obtained.

At the back boundary the steel container's retention of the structure was satisfied by modeling a 90 mm thick steel plate only for the Plaxis model with the rubber fill. Because the total fixities had priority over prescribed displacements, this solution was adopted.

The steel material was modeled by creating clusters and assigning steel material properties inside it as a fill. Linear elastic model was adopted and γ_{steel} = 76.8 kN/m^3, E_{steel} = 2.00E+08 kN/m^2, ν = 0.3.

6.2.8. Modeling of the Fixities

Fixities are prescribed displacements equal to zero. These conditions can be applied to geometry lines as well as to geometry points. There are two kinds of fixities; horizontal fixities where $u_x = 0$ and vertical fixities where $u_y = 0$. In addition, one can select total fixity, which is a combination of both ($u_x = u_y = 0$). On a geometry where fixities are used as a condition, the fixities have priority over other types of loading conditions (prescribed displacements or traction loads) during the calculations.

The vertical fixities were modeled at the very bottom of the structure in both of the Plaxis models to prevent the system not to move vertically. However, the horizontal fixities were put at the very back of the structure only in the absorbent boundary model. The horizontal fixities prevented the soil not to move horizontally only in the plastic calculation-staged construction type of loading phase since in the dynamic analysis phase

the absorbent boundary moved and absorbed the waves for not to rebound back to the soil fill.

6.2.9. Modeling of the Prescribed Displacements

A special method to introduce dynamic loads in a model is the use of prescribed displacements. Earthquakes can be modeled by means of prescribed displacements with a dominant horizontal component. Prescribed displacements are special conditions that can be imposed on geometry lines to control the displacements of these lines. Prescribed displacements are controlled by the load multipliers Mdispl and ∑Mdispl. During calculations the reaction forces corresponding to prescribed displacements in x- and y-direction are calculated and stored as output parameters.

Plaxis allows the use of earthquake records in SMC-format as input data for earthquake loading. The SMC-files use centimeters as unit of length. So to have corresponding input values in Plaxis, when the unit length in Plaxis is set to meters [m], it is needed to scale the prescribed displacements by changing $u_x = 1$ into $u_x = 0.01$. The SMC (Strong Motion CD-ROM) format is currently used by the U.S. Geological Survey National Strong-motion Program to record data of earthquakes and other strong vibrations.

However, in this study ASCII file type of input data was used in the analyses. Since it was a simple process to create any kind of data with any text editor for this type of file, the experimentally measured base displacements (shaking table's displacement) were created as input data. In this type of file, in every line a pair of values (actual time and corresponding multiplier) is defined, leaving at least one space between them. The time should increase in each new line. It is not necessary to use constant time intervals.

6.3. Generation of the Meshes

After the geometry model is created, a finite element mesh will be generated according to the composition and position of the clusters and lines. The meshes are needed in order to perform finite element calculations. The generation of the mesh is based on a robust triangulation procedure, which results in "unstructured" meshes. These meshes look

disorderly, but the numerical performance of such meshes is usually better than for regular (structured) meshes. The meshes are composed of triangular elements, nodes and stress points.

For a 2D analysis (plane strain or axisymmetry), the meshes are generated by either 6-node or 15-node triangular elements. The 6-node triangle is the default element for a 2D analysis. It provides a second order interpolation for displacements. The element stiffness matrix is evaluated by numerical integration using a total of three Gauss points (stress points). For the 15-node triangle the order of interpolation is four and the integration involves twelve stress points.

For a 3D analysis (3D axisymmetry) only one element type is available, the 15-node wedge element. This element gives a second order interpolation for displacements and the integration involves six stress points.

The 15-node triangle is a very accurate 2D element, which has been shown to produce high quality stress results for difficult problems, as for example in collapse calculations for incompressible soils. However, using 15-node triangles leads to relatively high memory consumption and slow calculation and operation performance. In order to avoid long calculation times and slow performance, usually the default element of 6-node triangle is chosen. This element type performs well for most types of calculations. However, the accuracy of the results will in most cases be less than would be obtained using the same number of 15-node triangles.

The accuracy of the 15-node wedge for a 3D analysis is comparable to the 6-node triangle in a 2D analysis. Higher order element types are not considered for a 3D analysis because this will lead to large memory consumption and unacceptable calculation times (Figure 6.10.).

In the analysis, very fine types of meshes are generated by 6-node triangular elements.

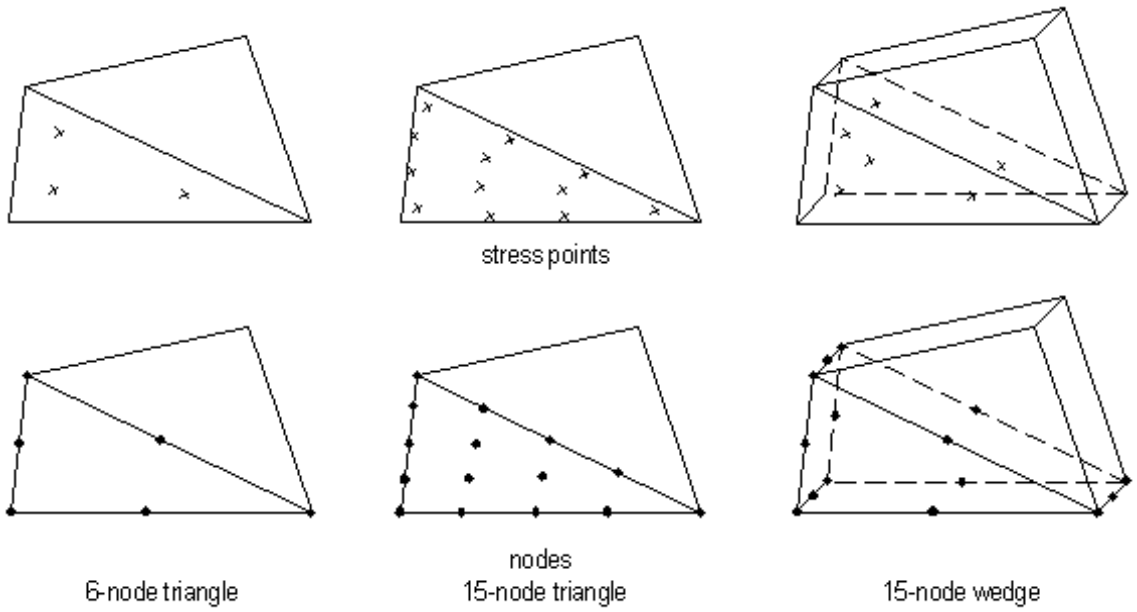

Figure 6.10. Position of nodes and stress points in soil elements (Brinkgreve and Vermeer, 1998)

6.4. Determination of the Initial Conditions

In this stage, the initial stress state and the initial situation are specified. There are two modes for these purposes: the mode for the generation of initial water pressures and the mode for the specification of the initial geometry configuration and the generation of initial effective stress field.

The initial stresses in a soil body are influenced by the weight of the material and the history of its formation. In a PLAXIS analysis two possibilities exist for the specification of these stresses. These are the *K_0-procedure* and *Gravity loading*. The *K_0-procedure* should only be used with a horizontal surface and with any soil layers and phreatic lines parallel to the surface. Otherwise, the *Gravity loading* should be adopted.

The coefficient K_0, represents the ratio of the horizontal and vertical effective stresses:

$$K_0 = \sigma'_{xx} / \sigma'_{yy} \tag{6.25}$$

In practice, the value of K_0 for a normally consolidated soil is often assumed to be related to the friction angle by the empirical formula:

$$K_0 = 1 - \sin\varphi \tag{6.26}$$

In an over-consolidated soil, K_0 would be expected to be larger than the value given by this formula.

When the K_0 procedure is adopted, Plaxis generates the vertical stresses that are in equilibrium with the self-weight of the soil. However, horizontal stresses are calculated from the specified value of K_0.

All the analysis in this study is done according to the K_0 procedure.

Once the initial stresses are generated, the initial phase is constructed and it can be proceeded to the calculations phase.

6.5. Calculations Phase

Four types of different calculations can be performed according to the needs in the calculations phase. These are: Plastic calculation, Consolidation analysis, Phi-c reduction (safety analysis) and Dynamic calculation.

A plastic calculation is selected to carry out an elastic-plastic deformation analysis in which it is not necessary to take the decay of excess pore pressures with time into account and to include effects of large deformations. The stiffness matrix in a plastic calculation is based on the original undeformed geometry. In general, a plastic calculation does not take time effects into account.

A consolidation analysis is selected when it is necessary to analyze the development or dissipation of excess pore pressures in water-saturated clay-type soils as a function of time.

Phi-c reduction (safety analysis) is selected when it is desired to calculate a global safety factor for the situation at hand. This process reduces the strength parameters of the soil.

A dynamic analysis is performed when it is desired to apply dynamic loads to the structure. A dynamic analysis can only be carried out after a series of plastic calculations.

6.5.1. Plastic Calculation-Staged Construction Type Loading Input Analysis

In the analysis of the numerical models conducted in this study, this type of calculation and loading was adopted till to the dynamic analysis phase. The staged construction is the most important type of loading input where it is possible to change the geometry and load configuration by deactivating or reactivating loads, volume clusters or structural objects as created in the geometry input. In this case, the total level to be reached at the end of the construction phase is defined by specifying a new geometry and load configuration, and/or pore pressure distribution. Staged construction is performed using the *Load advancement ultimate level procedure*, which terminates the calculation when the specified state or load level is reached or when soil failure is detected. The ultimate load level is controlled by a total multiplier parameter ($\sum Mstage$). This multiplier generally starts at zero and it is expected to reach the ultimate level of 1.0 at the end of the calculation phase.

6.5.2. Dynamic Analysis

During a deformation analysis it is necessary to control the magnitude of all types of loading. In the dynamic analysis, dynamic loads are defined by means of dynamic Multipliers. The loadings to be applied are calculated from the product of the input value of the load, as entered in the Input program, and the corresponding multiplier. Distinction is made between Incremental multipliers, Total multipliers and Dynamic multipliers. Incremental multipliers represent the increment of load for a particular calculation step, whereas total multipliers represent the total level of the load in that step. For example, $\sum Mdisp$ is a total multiplier that is used in this study to control the magnitude of the

prescribed displacements as entered in the Input program. Prescribed displacements are imposed on the model to control the displacements of certain points.

According to the preferences, there are two dynamic loading options: “Harmonic load multiplier” and “Load multiplier from data file” type of loading. Both of these types of loading were implemented in this study.

6.5.2.1. Harmonic Loading. In the Plaxis analysis, harmonic loading was only used when calibrating the rubber fill with the absorbent boundary. This process is described in section 6.6 in detail.

6.5.2.2. Earthquake Input Record. Even with a very advanced shaking table, it is impossible to simulate exactly the scaled El-Centro acceleration-time history record. So rather than the input scaled-El Centro acceleration-time history record, the shaking table’s measured displacement-time history record was used in the numerical analyses with PLAXIS v7.2 and PLAXIS v8.4 program. An example plot of the simulated El Centro earthquake displacement-time history record measured from the shaking table can be seen in Figure 6.11.

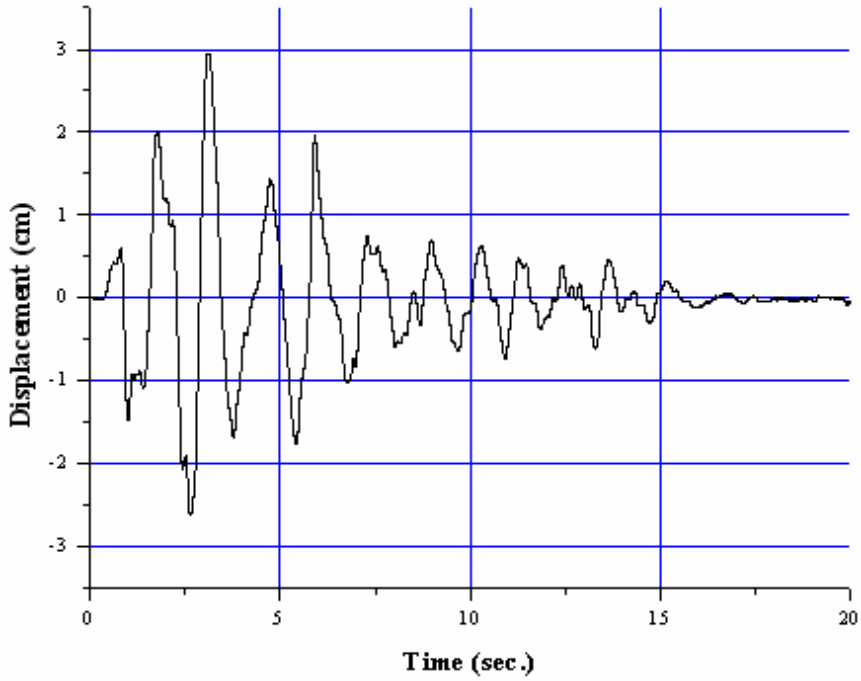

Figure 6.11. Simulated 2nd experiment 1st El Centro excitation record

6.5.2.3. Equation of the Dynamic Behavior. The basic equation for the time-dependent movement of a volume under the influence of a dynamic load is:

$$\underline{\underline{M}}\,\ddot{\underline{u}} + \underline{\underline{C}}\,\dot{\underline{u}} + \underline{\underline{K}}\,\underline{u} = \underline{F} \tag{6.27}$$

where M is the stiffness matrix; u is the displacement vector; C is the damping matrix; K is the stiffness matrix and F is the load vector. The displacement, u, the velocity, $\dot{u}$, and the acceleration, $\ddot{u}$, can vary with time. The last two terms in the equation ($Ku = F$) correspond to the static deformation.

Here the theory is described on the bases of linear elasticity. However, in principle, all models in Plaxis can be used for dynamic analysis. The soil behavior can be both drained and undrained. In the latter case, the bulk stiffness of the groundwater is added to the stiffness matrix, K, as is the case for the static calculation.

In the matrix M, the mass of materials (soil + water + any constructions) is taken into account. In Plaxis the mass matrix is implemented as lump matrix.

The matrix C represents the material damping of the materials. In reality, material damping is caused by friction or by irreversible deformations (plasticity or viscosity). With more viscosity or more plasticity, more vibration energy can be dissipated. If elasticity is assumed, damping can still be taken into account using the matrix C. To determine the damping matrix, extra parameters are required, which are difficult to determine from tests. In finite element formulations, C is often formulated as a function of the mass and stiffness matrices (Rayleigh damping) as:

$$\underline{\underline{C}} = \alpha_R \underline{\underline{M}} + \beta_R \underline{\underline{K}} \tag{6.28}$$

where α_R and β_R are Rayleigh coefficients. Here, when the contribution of M is dominant (for example, $\alpha_R = 10^{-2}$ and $\beta_R = 10^{-3}$) more of low frequency vibrations are damped, and when the contribution of K is dominant (for example, $\alpha_R = 10^{-3}$ and $\beta_R = 10^{-2}$) more of the high-frequency vibrations are damped. In the standard settings of Plaxis, $\alpha_R = \beta_R = 0$ [24].

In this study, since wave propagation was not of concern α_R (mass proportional) was taken to be zero, as reported by other researchers (e.g. Liu, 2004) and the other coefficient β_R (stiffness proportional) was obtained from the following equation (Dewoolkar, 1996):

$$\xi = \frac{\beta\omega}{2} = \pi f\beta \tag{6.29}$$

The damping ratio and natural frequency was chosen to be ξ=0.05 and f = 12.5 Hz, respectively. Thus, β_R = 0.0013 was obtained as a global damping parameter [25].

In Plaxis v8.4 Rayleigh damping parameters are needed to be assigned to each element of GRS-RW separately. So, while for the sand, modular block, interfaces 5 per cent damping (α_R =0, β_R = 0.0013) was opted, for the rubber material 10 per cent damping was assigned (α_R =0, β_R = 0.0026).

6.5.2.4. Time Integration Scheme. In the numerical integration of dynamics, the formulation of the time integration constitutes an important factor for the stability and accuracy of the calculation process. Explicit and implicit integration are the two commonly used time integration schemes. The advantage of explicit integration is that it is relatively simple to formulate. However, the disadvantage is that the calculation process is not as robust and it imposes serious limitations on the time step. The implicit method is more complicated, but it produces a more reliable (more stable) calculation process and usually a more accurate solution.

The implicit time integration scheme of Newmark is a frequently used method. With this method, the displacement and the velocity at the point in time $t+\Delta t$ are expressed respectively as:

$$u^{t+\Delta t} = u^{t} + \dot{u}^{t}\Delta t + \left(\left(\frac{1}{2} - \alpha\right)\ddot{u}^{t} + \alpha\ddot{u}^{t+\Delta t}\right)\Delta t^{2} \tag{6.30}$$

$$\dot{u}^{t+\Delta t} = \dot{u}^{t} + \left((1-\beta)\ddot{u}^{t} + \beta \ddot{u}^{t+\Delta t} \right) \Delta t \tag{6.31}$$

In the above equations, Δt is the time step. The coefficients α and β determine the accuracy of the numerical time integration. They are not equal to the α and β for the Rayleigh damping. In order to obtain a stable solution, the following condition must apply:

$$\beta \geq 0.5,\ \alpha \geq \frac{1}{4}\left(\frac{1}{2} + \beta\right)^2 \tag{6.32}$$

It is advised to use the standard setting of Plaxis, in which the damped Newmark scheme with the parameters of α = 0.3025 and β = 0.60 are utilized.

In this study these advised parameters were used.

6.6. Calibrating the Rubber Fill with the Absorbent Boundary

To determine the amount of rubber fill needed in the experiments at the back of the backfill in order to satisfy the conditions of an absorbent boundary, rubber-filled models were created, where the rubber fill width varied. The obtained results of the dynamic analysis were compared with the absorbent boundary model in Plaxis, where absorbent boundary element was put at the back of the backfill. For the dynamic analysis, the harmonic motion used by the researchers Bathurst and Hatami in their studies (1998), was adopted.

6.6.1. Absorbent Boundary Model

Because the absorbent boundary element has a dominant character over fixities and it absorbs earthquake waves and prevents them not to be reflected at the back by moving, the fill length for the model in which the absorbent boundary element was put needed to be prolonged to be 25 m. As the absorbent boundary element moves, the verticality of the back surface changed between 5 and 10 cm. Since this would cause inaccurate results if it

were put right at the back where the soil fill finishes (to the end of L =2.8 m), such a solution was adopted. In Figure 6.12 the absorbent boundary model and its modeled details can be seen.

6.6.2. Rubber-Filled Back Model

Rubber was filled at the very back of the structure before the 10 cm long steel fill, which was modeled to satisfy the steel container's retention at the back. In Figure 6.13, the rubber-filled back model and its modeled details can be seen.

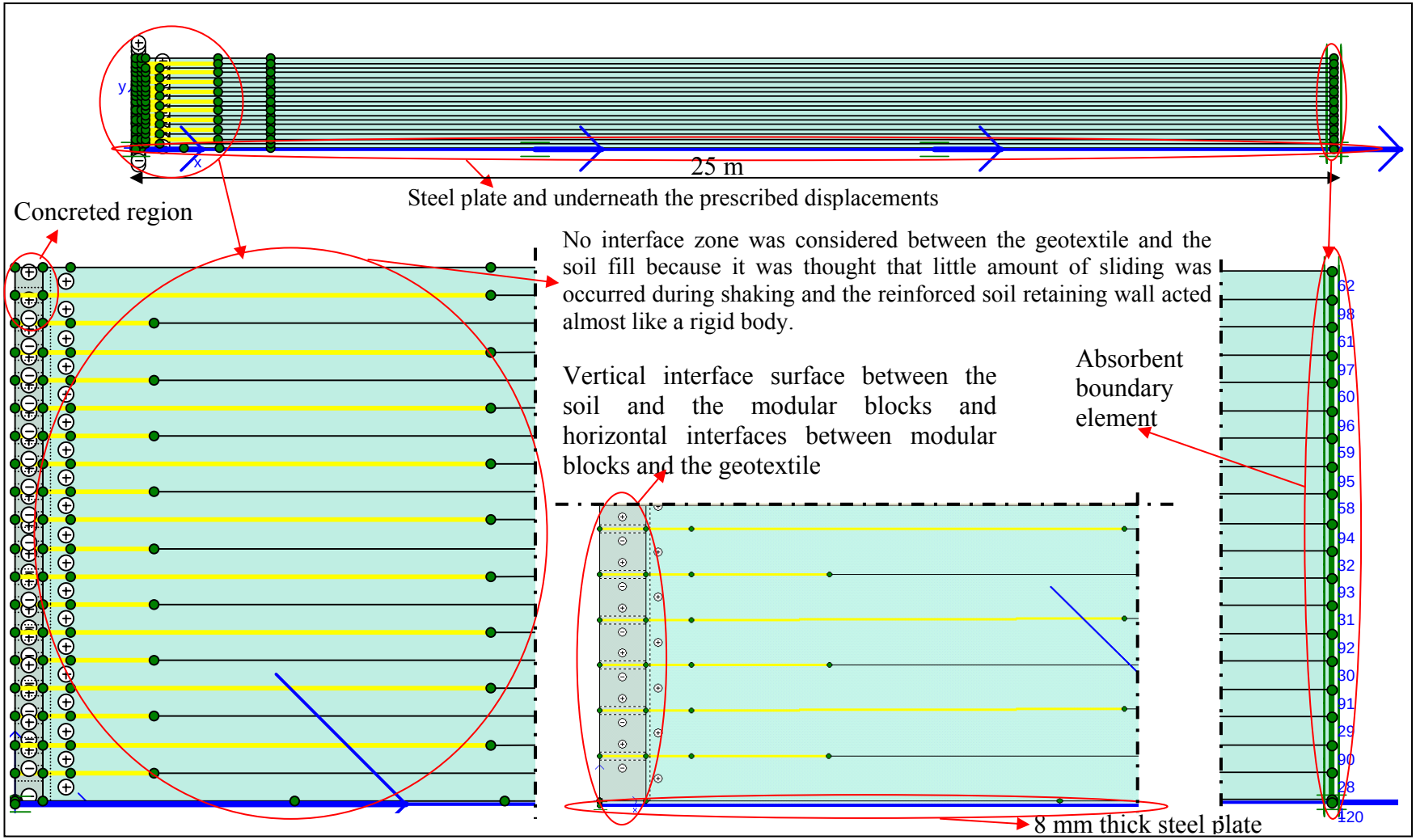

Figure 6.12. Absorbent boundary model

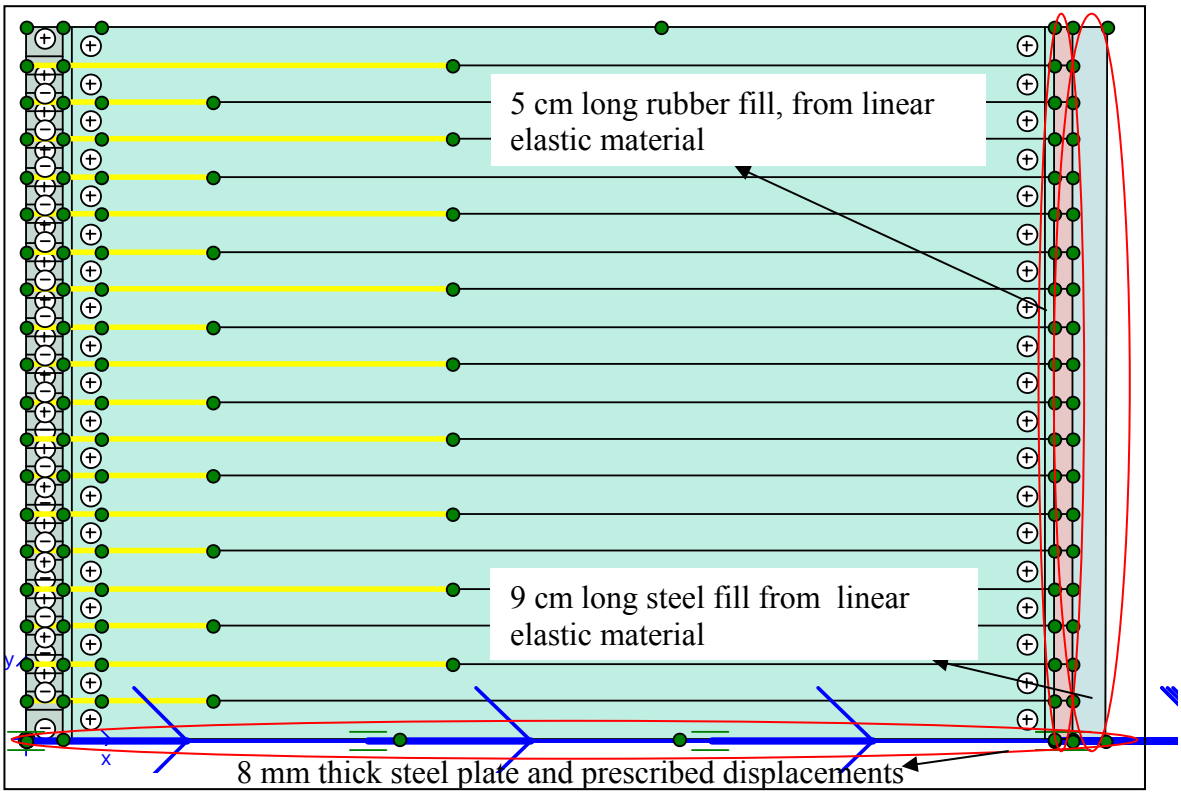

Figure 6.13. Rubber-filled back model

6.6.3. Harmonic Motion

The harmonic motion used by the researchers Bathurst and Hatami in their studies, 1998 was opted. This acceleration record after it was scaled, was applied horizontally to all nodes at the bottom of the soil zone at equal time intervals of $\Delta t = 0.05$ sec. The accelogram has both increasing and decaying peak acceleration portions and is expressed with the formula stated previously in Equation 2.14. This original harmonic motion and its scaled version can be seen in Figures 6.14 and 6.15, respectively.

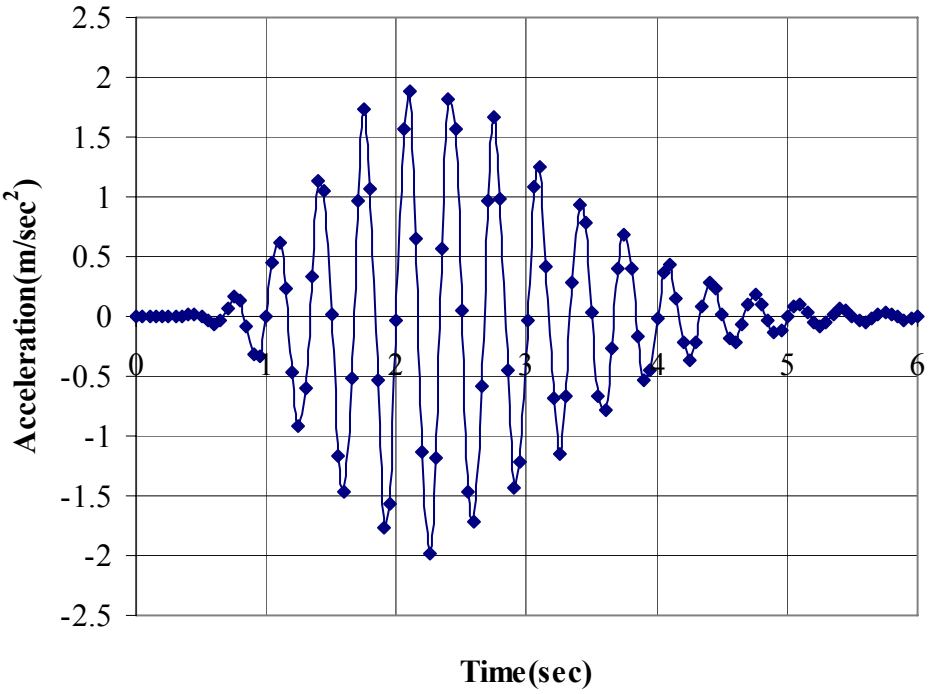

Figure 6.14. Original record of the harmonic motion

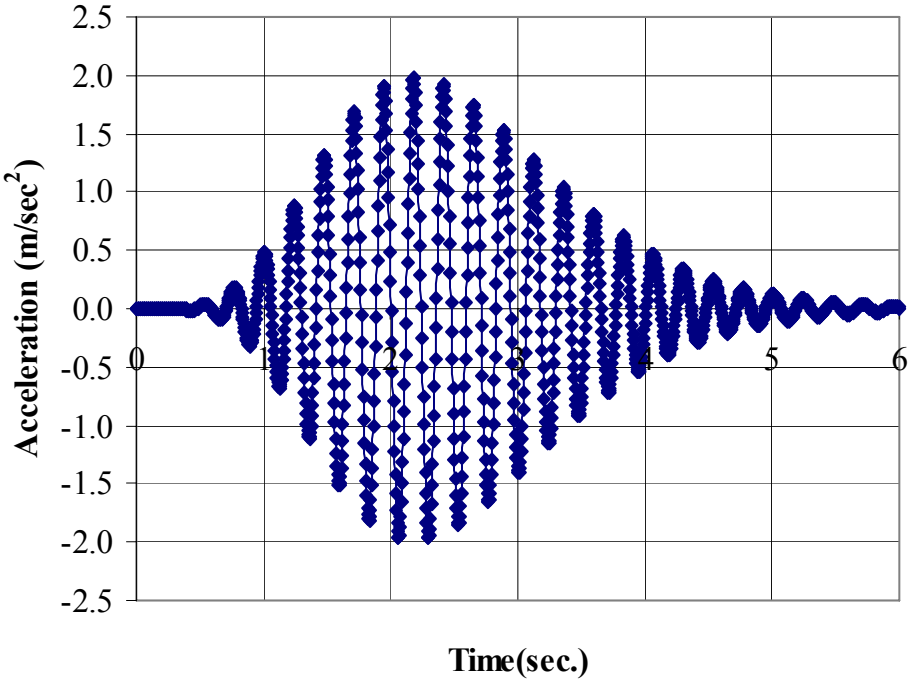

Figure 6.15. Scaled harmonic motion

6.6.4. Obtained Results

In conclusion, 5 cm long rubber fill satisfied the needs of the absorbent boundary region by giving a similar top displacement-time history curve as it is shown in Figure 6.16.

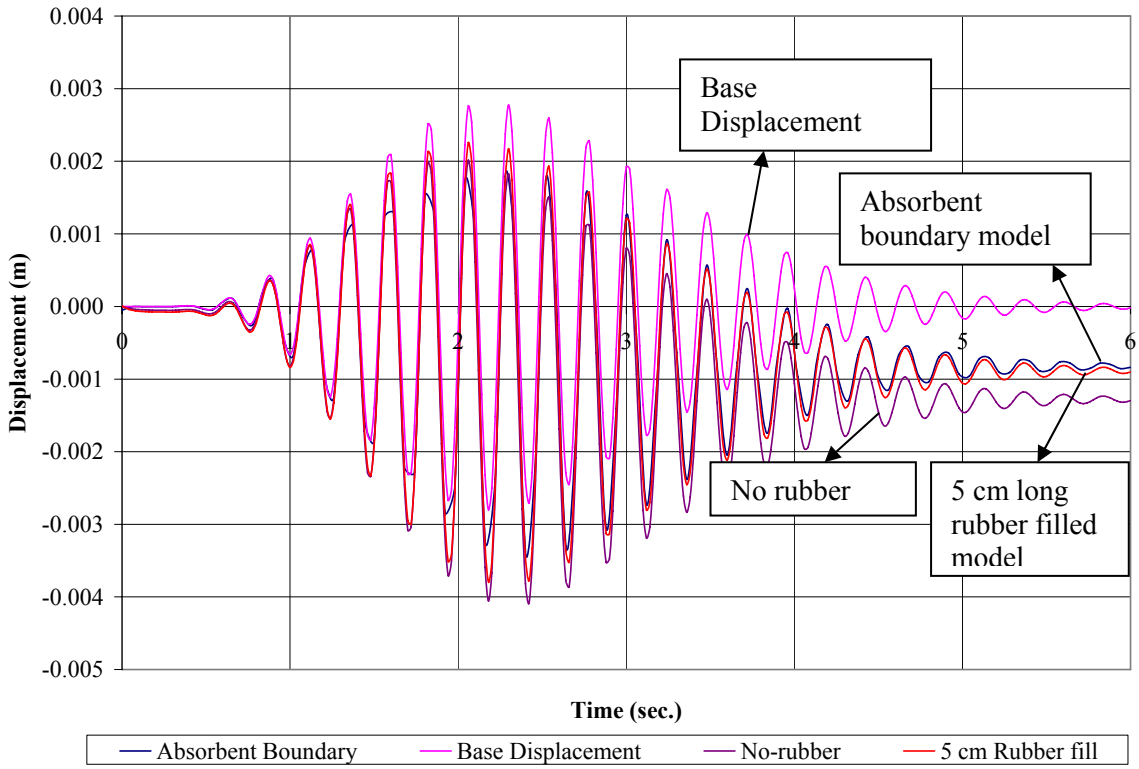

Figure 6.16. Comparisons of obtained top displacement-time history results

Table 6.2 lists the input values of the parameters used in Plaxis v7.2. The only differences in Plaxis v8.4 models when compared to Plaxis v7.2 models are the soil model adopted (HSsmall in Plaxis v8.4) and separate assignment of Rayleigh damping coefficients to each element of GRS-RW (in Plaxis v8.4). Also, in modeling with Plaxis v8.4, real unit weight values of the soil measured at the end of the shaking table experiments and corresponding correlated internal friction angle values were used.

Table 6.2. The overall summary of the parameters used to construct the numerical analysis models in Plaxis v7.2

THE NUMERICAL ANALYSIS WITH PLAXIS							
Elements	**Material Model**	**γdry (kN/m^3)**	**Eref (kN/m^2)**	**ν**	**c (kN/m^2)**	**φ**	**Interface**
Modular Blocks	Linear Elastic	21	4.4E+06	0.17	-	-	Rigid
Soil	Mohr-Coulomb	16.5	8.7540E+04	0.3	1	41	Rigid
The interface between the Modular Blocks and Geotextile	Mohr-Coulomb	21	4.4E+06	0.17	2	30	Rigid
Interface between the modular Blocks and the Soil and Interface between the Soil and Rubber fill	Mohr-Coulomb	16.5	8.7540E+04	0.3	1	41	Rinter=0.7 (as advised in the plaxis manual with the value of 2/3)
Rubber	Linear Elastic	5.3	8.91E+02	0.2	-	-	Rinter=0.7 (as advised in the plaxis manual with the value of 2/3)
Steel	Linear Elastic	76.82	2.00E+08	0.3	-	-	Rinter=0.7 (as advised in the plaxis manual with the value of 2/3)
Geotextile Element	Linear Elastic	EA=364 kN/m for 40 kN/m at %11 strain					
	Dynamic Analysis Parameters						
Absorbent Boundary	Boundary C_1 = 1			Boundary C_2 = 0.25			
Damping (ξ=0.05)	Rayleigh alpha = 0			Rayleigh beta = 0.0013			
Time integration	Newmark alpha = 0.3025			Newmark beta = 0.6			

7. TEST SETUP

7.1. Shaking Table

7.1.1. Shaking Table Facilities

In this study, the large uniaxial shaking table facility at the Shaking Table Laboratory of Kandilli Observatory and Earthquake Research Institute (KOERI) in Kandilli was used. The ANCO R-148 uniaxial shaking table (3x3 m) was manufactured by ANCO Engineers, Inc. It is driven by a servo-hydraulic actuator. Test objects up to 10 tons force (100 kN) can be accommodated over a frequency range of 0-50 Hz. The R-148 tabletop is of welded steel construction and has tapped holes for attaching test items to the table. The table has precision ground rails, which engage eleven roller linear bearings on the base to allow for the desired linear horizontal motion.

The actuator has a ± 12 cm stroke and has dual 3-stage Moog servo-valve rated at 200 GPM each. The Moog servo-valve and GS actuator are controlled by a GS2000 analog control servo-loop, servo-controller. The servo-controller accepts the displacement table program signals from the digital control system and seeks to control the actuator to match this signal.

Table motion and data acquisition are provided by a Data Physics 550 WIN digital data control and acquisition system. This system allows for a feedback accelerometer on the moving table, a PC-based (COMPAQ) digital control system reading this acceleration, and this same PC system producing an analog drive signal to the actuator servo-controller. The data acquisition and control system for the R-148 is a 16 channel Data Physics 550 WIN Compaq PC-based system. The system is composed of, 16 channel digital control system (1 output, 16 inputs) which includes anti-aliasing filters, amplifier, a UPS for safe operation, the COMPAQ control PC and Monitor, the Gardner System servo-controller, and the emergency hydraulic power supply/dump valve e-stops.

The achievable motion and 5 per cent Response Spectrum for R-148 table with 10 tons of test specimen is shown in Figure 7.1. The table has a peak nominal table motion (input to test specimens) of, 24 cm peak-to-peak displacement, peak velocity of approximately ±1.2 m/s, and peak acceleration (with a 10-ton payload) of approximately, ±2.0g.

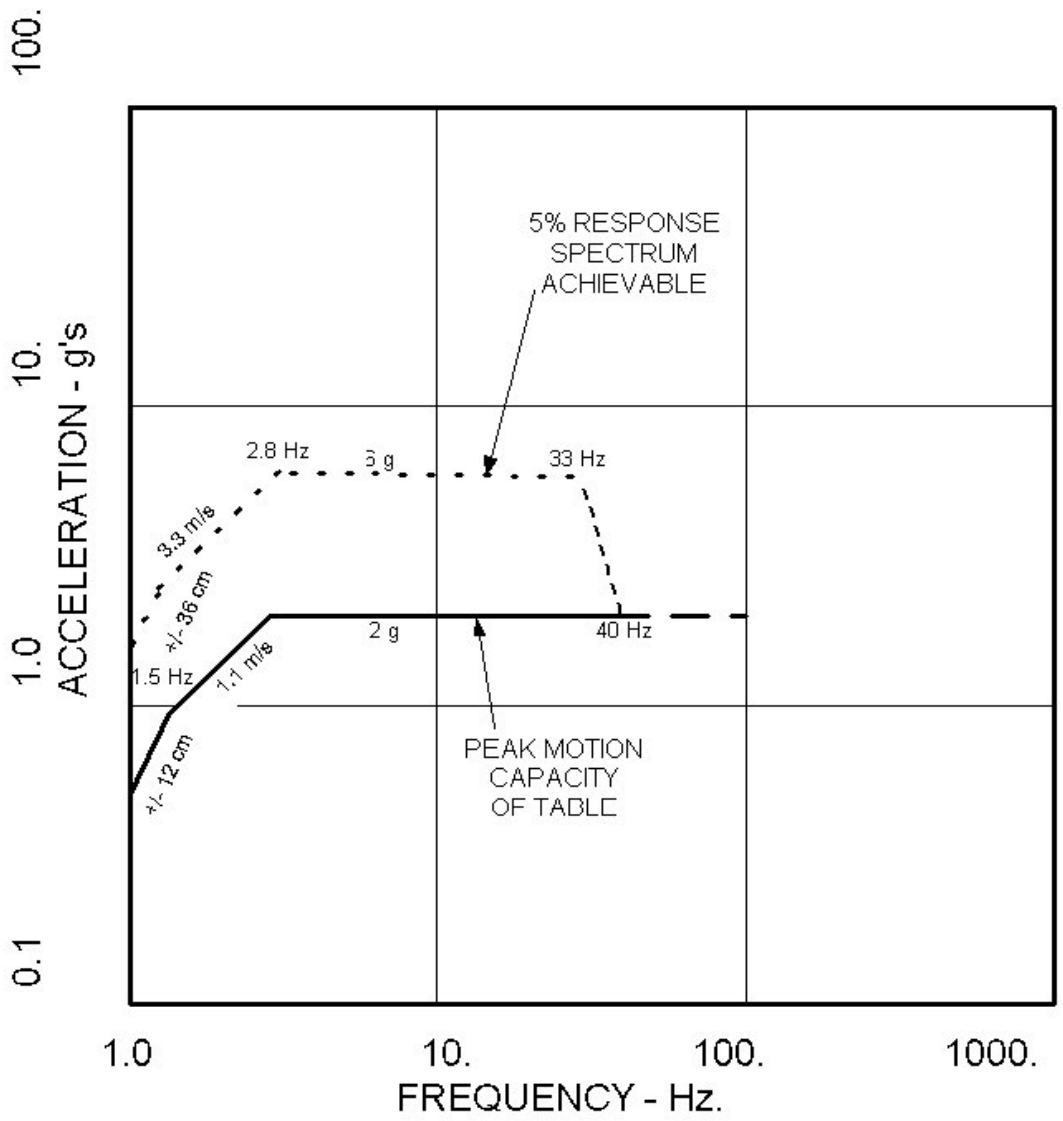

Figure 7.1. The achievable motion and 5 per cent Response Spectrum with 10 tons of load

7.1.2. Shaking Table Response to El Centro Earthquake Motion

Figures 7.2 and 7.3 shows the measured table response to the El Centro earthquake motion.

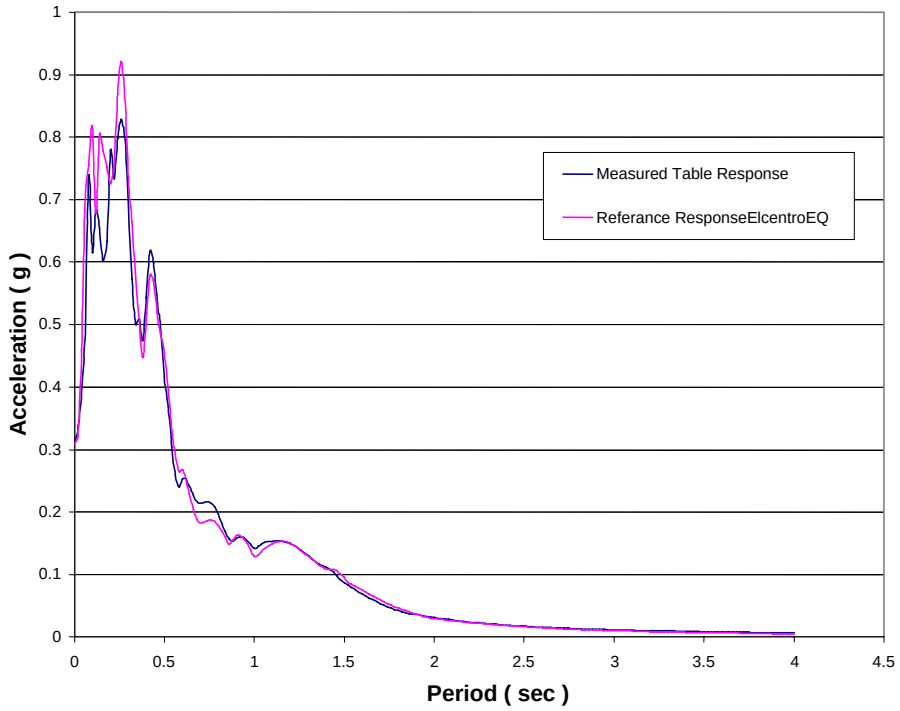

Figure 7.2. Measured table Response Spectrum to El Centro earthquake record

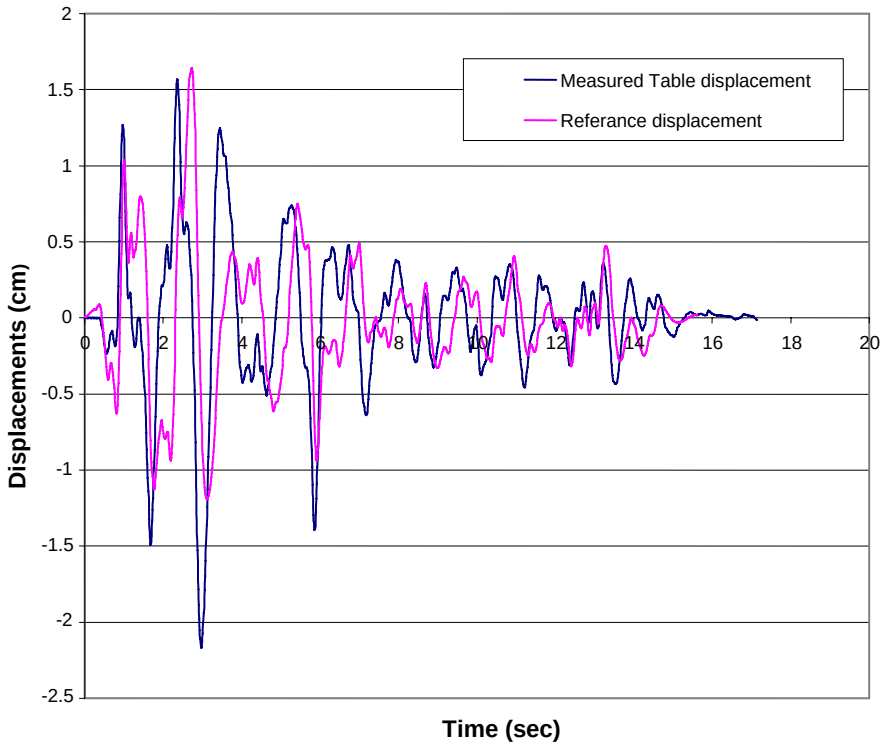

Figure 7.3. Measured table displacement response to El Centro earthquake record

7.2. Materials and Transducers

7.2.1. Steel Container

A steel container was fabricated to accommodate the geotextile-reinforced soil retaining wall. The steel container ought to be designed to fit onto the shaking table according to the carrying capacity needs and dimensional constraints of the shaking table, which had a maximum of 10 tons of carrying capacity and dimensions of 3 x 3 m of width and length. As a result of these limits, the steel container was designed to weigh approximately 4 tons, and soil it accommodates to weigh 5 tons. Thus, this container allowed us to construct a Geotextile Reinforced Soil Retaining Wall (GRS-RW), which had 1.9 m of height, 2.8 m of length and 0.53 m of width (Figure 7.4.).

Figure 7.4. Steel container on the shaking table

7.2.2. Rubber Sheets

6 mm thick rubber sheets were placed along the steel container's side surfaces excluding the back boundary in order to satisfy frictionless sliding between the greased surfaces of the steel container and the sand fill (Figure 7.5).

Figure 7.5. Rubber sheets used in this study

7.2.3. Sand

After the experiments were completed the sand cone tests were performed to determine the density of the soil and water contents were determined**.** Layers 19, 11 and 6 were chosen for this purpose in which the layers 19, 11 and 6 coincide to the sand layers between 1.90 m – 1.80 m, 1.10 m – 1.00 m and 0.60 m – 0.50 m, respectively. The sand cone test is a simple test in which the fine sand is used to determine the volume occupied by certain amount of soil mass in the specified layer or region. Some certain amount of soil mass is extracted from the region and later a certain type of fine sand from a coned-container is made fill the soil-extracted region in order to determine the volume of this soil-extracted space. The weights of 1000 m^3 of the fine sand and the fine sand that stays in the cone are 1428 gr and 1670 gr, respectively. For an example, in the 19^{th} layer the soil

extracted from the region was 1072 gr and 1100 gr of fine sand put to the region which occupied 770 cm^3 of space. As a result, the density of the sand with a 3.68 per cent water content equaled to:

$$d_{19} = \frac{1072}{770} = 1.39 gr/cm^3$$

All the parameters of the sand cone test, calculated dry unit weights and water contents for the 1st and 2nd experiments can be seen in Tables 7.1 and 7.2.

Table 7.1. Test parameters of the sand for the 1st Experiment

Test Parameters	**Layer No**		
	19	**11**	**6**
Weight of replaced soil (gr):	1072	2265	1908
Average w (%):	3.68		
Weight of fine sand used (gr):	1100	1931	1704
Volume (cm3):	770	1352	1193
Dry unit weight of soil (kN/m3):	13.16	15.84	15.13
Average Dry Unit weight (kN/m3):	14.71		

Table 7.2. Test parameters of the sand for the 2nd Experiment

Test Parameters	**Layer No**		
	19	**11**	**6**
Weight of replaced soil (gr):	1875.5	1268	945.5
Average w (%):	3.91		
Weight of fine sand (gr):	1419	1145	851
Volume (cm3):	993.70	801.82	595.94
Dry Unit weight of soil (kN/m3):	17.82	14.93	14.97
Average Dry Unit weight(kN/m3):	15.91		

7.2.4. Rubber

The rubber material presented previously in Chapter 5.2 placed as a 5 cm wide fill at the back of the structure.

7.2.5. Geotextile

The geosynthetic material was of a polyester-woven type of geotextile material having a tensile strength of T_{ult} = 40 kN/m at ultimate strain of ε_{ult} = 11 per cent (Figure 7.6).

Figure 7.6. One of the geotextile layers used in the experiments.

7.2.6. Concrete Modular Blocks

In many segmental retaining wall systems the blocks are hollow: the hollow concrete blocks are filled with soil during installation, thus increasing the weight of the blocks and providing the anchorage for the geosynthetics. The blocks are self stable through gravity without soil pressure; therefore the blocks themselves act as formwork for the construction of the geosynthetic reinforced soil block.

The real dimensions of the modular-blocks used in the field have a size of 40 cm × 20 cm × 20 cm. So, for a ½ scaled system, the dimensions of the modular blocks were manufactured specially to be 20 cm × 10 cm × 10 cm by casting the concrete into specially designed steel molds. Since these blocks are hollow, the certain thickness of the concrete block was found to be 3 cm, by mathematically equating the unit weight of the scaled modular block to the non-scaled modular blocks used in the field (Figure 7.7).

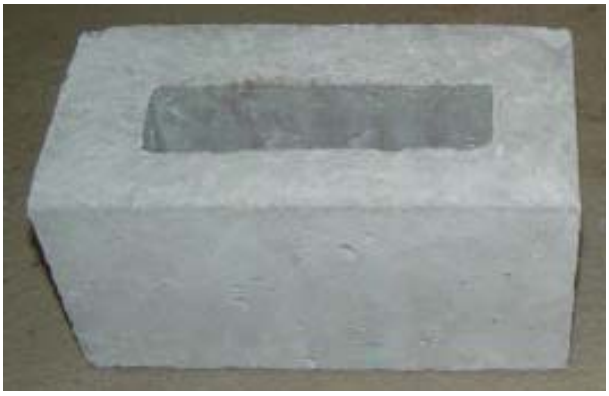

Figure 7.7. Wet-cast concrete modular block used in this study

Compression tests applied to a concrete modular block specimen and regarding stress-strain diagram was obtained as in Figure 7.8. An E_{secant} value of $4.4x10^6$ kN/m^2 was evaluated and used in the numerical analyses.

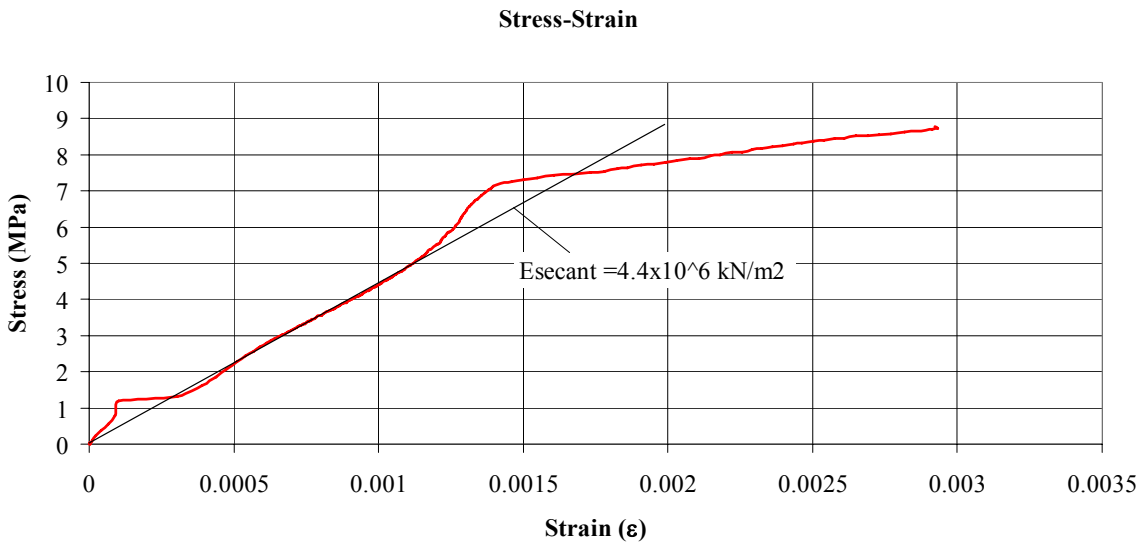

Figure 7.8. Stress-strain diagram of a concrete modular block

7.2.7. Compactor

The soil was compacted using Dynapac compactors of LF82 and LF72 (Figure 7.9). The specifications on the compactor LF82 are as follows:

Net Weight: 80 kg

Plate Dimensions: W460 mm x L540 mm

Frequency: 90 Hz

Amplitude: 1.1 mm

Centrifugal Force: 18 kN

Engine: Honda GX160

Engine output: 4.1 kW / 3600 rpm

Figure 7.9. Dynapac LF82 type of compactor (LF72 has the same appearance)

Whereas the specifications on the compactor LF72 are:

Net Weight: 62 kg

Plate Dimensions: W400 mm x L510 mm

Frequency: 92 Hz

Amplitude: 0.8 mm

Centrifugal Force: 10 kN

Engine: Honda GX120

Engine output: 2.9 kW / 3600 rpm

7.2.8. Laser Sensors

The Laser Displacement Sensors were of type ODSL8-V/4-400-S-12 from Leuze Electronic. They have a displacement measurement range from 2 to 40 cm with 0.1 mm of precision measurement ability. It has a measurement time of 5 ms (200 Hz) and a response time of up to 20 ms (Figure 7.10).

Figure 7.10. Laser sensor

7.2.9. Displacement Transducers

The transducers were of non-contact type having a measurement range of 20 cm of distance. They have a ≤10µm of resolution capacity and 1 kHz of sampling rate. The transducer measures the data when its special magnet operates at a distance of 4 to 8 mm from the top of its profile's surface and moves parallel along it. Its product name is "Balluff Micropulse AT type of Transducer" (Balluff BTL6 A11-M0200-A1-S115) from Balluff (Figure 7.11).

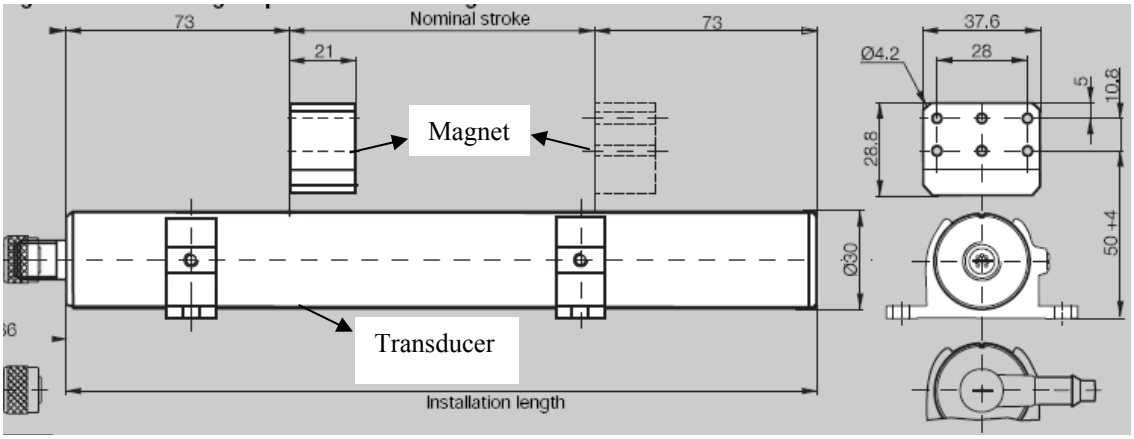

Figure 7.11. The operating principle of the transducer in the measurement process.

7.2.10. LVDT

The LVDT that was used to measure the shaking table's displacements was of type "High Accuracy DC Long Stroke Displacement Transducer LD600-100" manufactured by "Omega Engineering Inc.", which could sense the distances up to 100 mm. It has a 10 V input voltage having an output (sensitivity) of 200 mV/cm. Its response time is 100 Hz and its linearity is 0.25% Fs (%0.25 deviation can occur) (Figure 7.12).

Figure 7.12. The LVDT used in the experiment

7.2.11. Accelerometers

Accelerometers were of capacitive type, which have +/- 3g acceleration measurement capacity, an average of 1000mV/g sensitivity and a frequency range of 0 to 100 Hz. The manufacturer of this accelerometer is "PCB Piezotronics Inc." and the model is "Model 3801G3FB3G" (Figure 7.13).

Figure 7.13. The accelerometer used in the experiment

7.2.12. Data Acquisition (DAQ) System

National Instruments' PCI-6229 M series of DAQ device was used in the experiments. It allows working with 32 analog input channels which have 16-bit of resolution and 250 kS/s (250000 samples per second) of sampling rate. The VI Logger DAQ software, SCB-68 noise-shielded connector blocks and SHC68-68-EPM cables were the other accessories used in this DAQ system (Figure 7.14).

Figure 7.14. A view from the computer room where the DAQ system was installed.

7.3. Dynamic Excitations

7.3.1. Harmonic Motion

Harmonic loadings are preferred by researchers in order to understand the behavior of the GRS-RWs under specific typical predominant frequencies (i.e. 3 Hz.) of earthquakes as well as under resonant frequencies. Additionally, when compared to earthquake records they present simplicity to the proposed work and allow to understand the components of the systems within a relatively short simulation time.

In this study, sine motions were created during the experiments as in the example time history curve in Figure 7.15, which had peak amplitudes close to 0.23 g and the frequencies ranged approximately from 4.2 Hz to 4.8 Hz. These frequencies being close to the ½ scaled frequency of 3 Hz, which is 4.24 Hz ($3\sqrt{2}$ Hz.), represents the typical predominant frequency of medium-to high-frequency content of earthquakes.

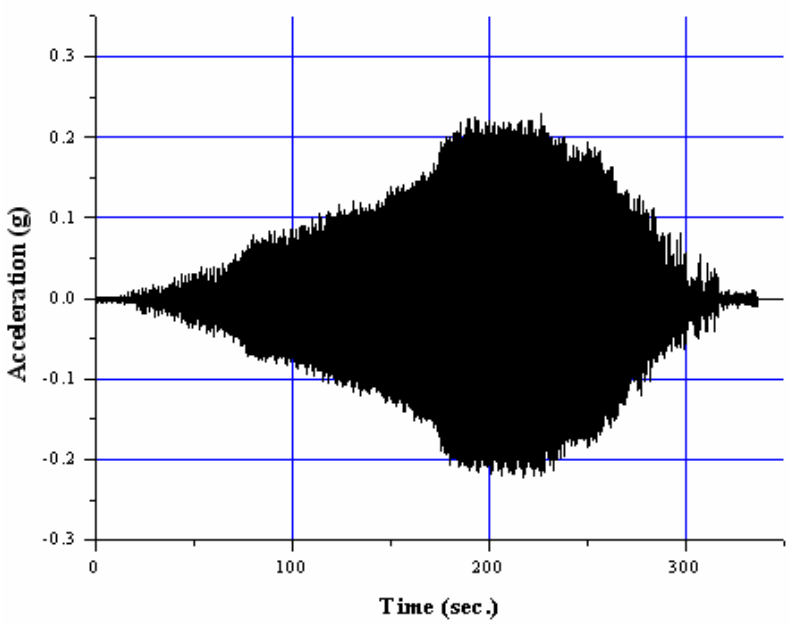

Figure 7.15. 2nd experiment sine wave time history record

7.3.2. El Centro Earthquake Motion

Since our model was a ½ scaled reduced model of the prototype not only the dimensions of the wall but also the frequency of the dynamic excitations should be scaled. According to the scaling laws derived in Chapter 4.4 the original El Centro earthquake record was scaled by incrementing the excitation frequency by $\sqrt{2}$. The original record and the scaled versions of the North-South component of the El Centro Earthquake (1940) can be seen in Figures 7.16 and 7.17. (nisee.berkeley.edu/data/strong_motion/a.k.chopra/ el_centro_data)

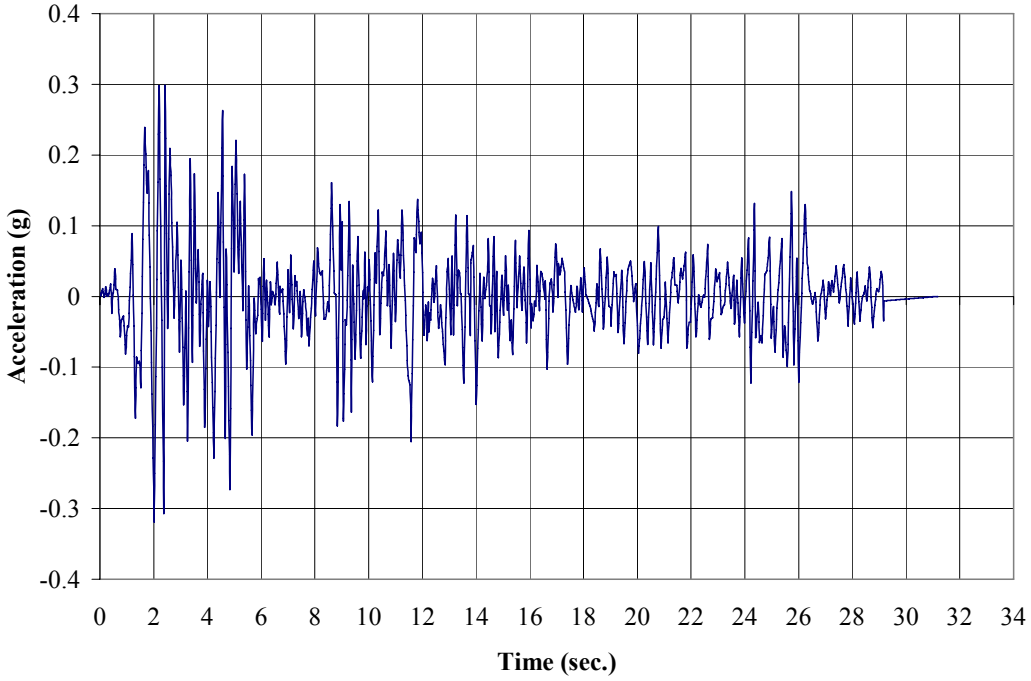

Figure 7.16. Original record of the North-South component of El Centro earthquake

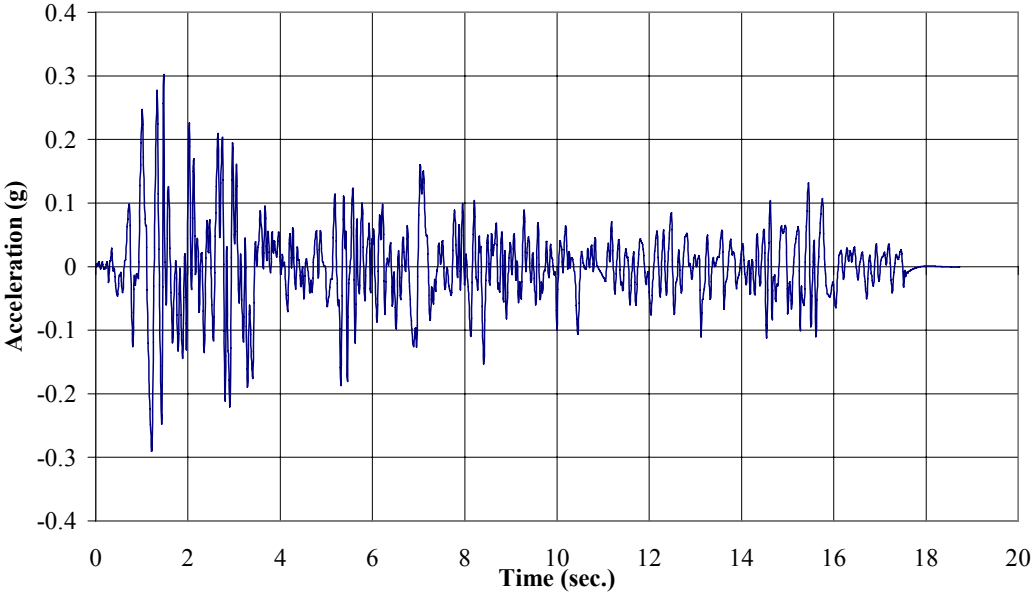

Figure 7.17. Scaled record of the North-South component of El Centro earthquake

7.4. Design of the Test Set-Up

Firstly, the steel container was bolted onto the shaking table satisfying a very tight connection with the table as shown in Figure 7.18. Then, the inside two lateral surfaces of the steel container was lubricated by grease oil and 6 mm thick rubber sheets were temporarily taped onto it by the so-called strong “Duct-tapes”. This is shown in Figure

7.19. These duct tapes were unfixed as the step by step staged construction of the sand fill progressed and sand mass supported the rubber sheets from falling down. The aim of this system was to satisfy frictionless sliding of the retaining wall during shaking.

Figure 7.18. 3 of the 8 bolted connections on one side of the steel container. There were 8 connections on the other side as well.

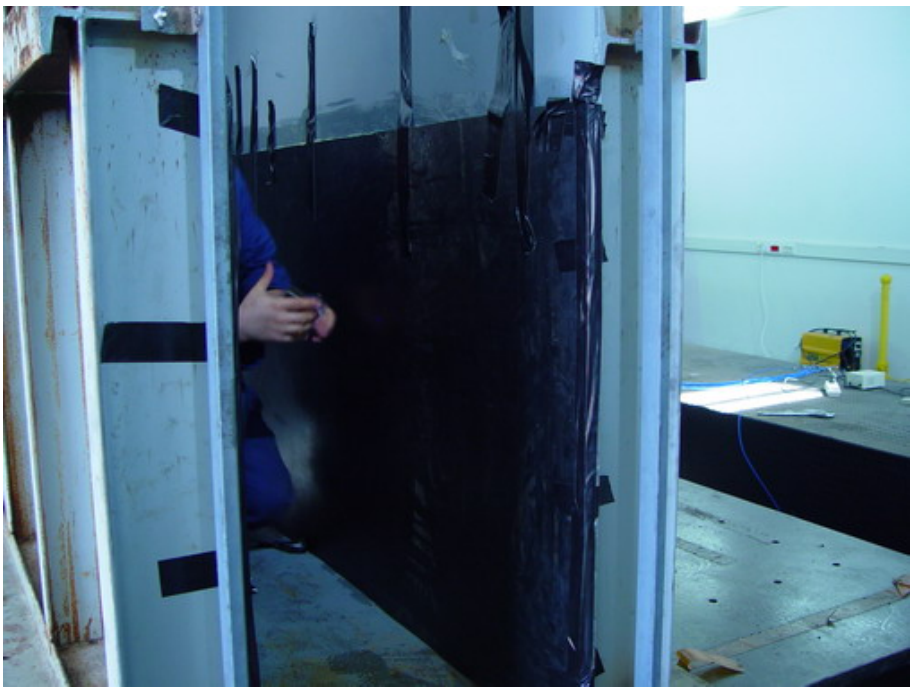

Figure 7.19. Rubber sheets were placed after the lubrication of the side surfaces.

After one level of rubber sheets were installed on the sides of the wall, the filling of the sand fill was commenced. As the filling inside with the sand fill by 10 cm of lifts progressed, the sand fill was compacted at every stage by a Dynapac site-model compactor. This compactor was operated close to the highest operating level on the place where the modular blocks start and advanced to the end of the wall where the granular rubber material was placed. Only one advancement in one direction was considered to be enough for compaction. After this operation was finished, a little swelling of the sand at the sides of the surfaces of the steel container was observed and these regions were compacted with a hammer. Figure 7.20 shows the compaction process and the compacted layer.

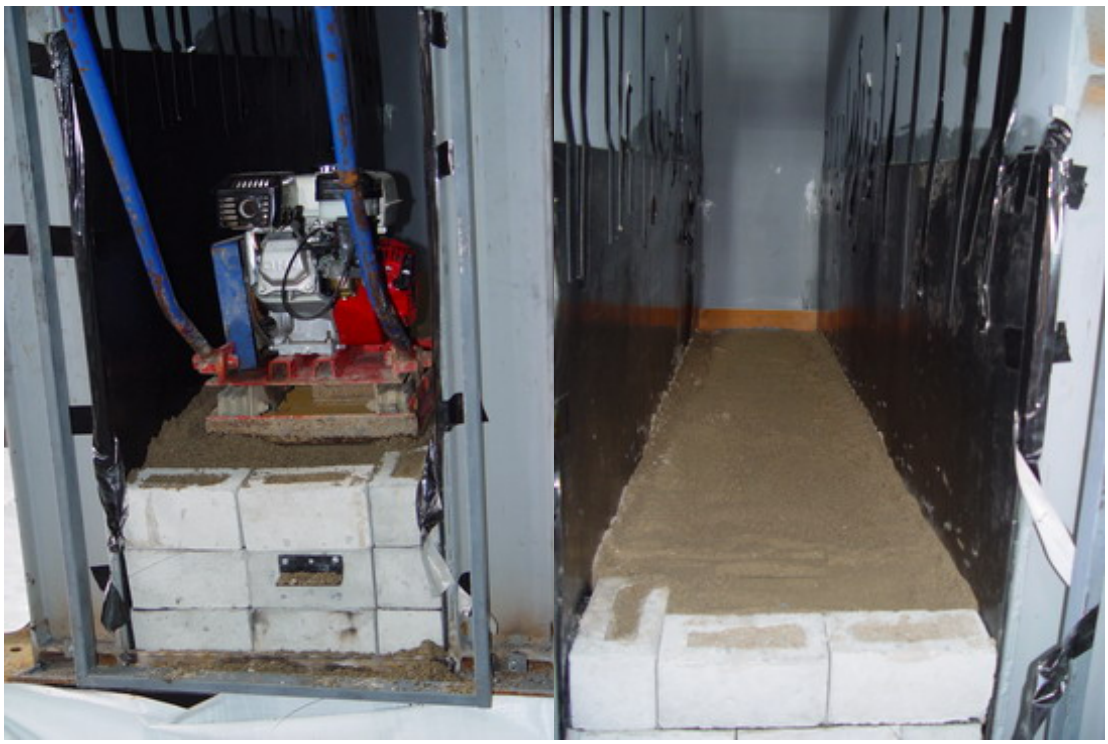

Figure 7.20. The compaction process and the resultant compacted layer.

As soon as the compaction finishes, the geotextile materials were laid down onto the sand. The vertical spacing of both the primary and the secondary layers of geotextiles were taken to be 20 cm, which made a total of 9 quantities from each type of layer forming a vertical shift pattern arrangement between each other. The primary reinforcement lengths were designed according to L/H=0.9 criteria for the first experiment and L/H=0.6 for the second experiment. For secondary reinforcement lengths, a previous research undertaken at

the Public Works Research Institute (PWRI), Ministry of Construction in Japan was adopted (Ling et al., 2000). In that full-scale experiment, these intermediate layers were modeled as 1.0 m so in this ½ scale model study 0.50 m of reinforcement length was chosen. These intermediate layers provide better surficial stability and a better platform for compaction equipment and ensures uniform soil density to the face of the slope.

The primary geotextiles, which coincide to the layers at H=40 cm and H=160 cm from the bottom of the GRS-RW were selected to be the ones whose behaviors were to be investigated. Four locations on the surface of the geotextile reinforcement were determined and thin nails were passed under and above several longitudinal fibres in the similar manner of sewing as shown in Figures 7.21 and 7.22. The nylon monofilament line (fishing line), which was made of a single strand, was simply passed around the nail and no other connection or any kind of knot was adopted. After all of the monofilament lines were passed around the nails on the geotextile, they were passed through strong flexible polymer pipes that are usually used in medical industry. The places that correspond to the concrete blocks were previously drilled and holes were created so that the monofilament lines were allowed to be connected with the strain measurement setup (Figure 7.23). Besides, the facing wall toe was restricted by welding a piece of steel plate at the bottom part of the container. As a result, a fixed toe was formed (Figures 7.23 and 7.24). After the connections were performed onto the geotextile in this way, the connected areas were covered with a patch of geotextile in order to prevent the penetration of soil particles through the strong flexible polymer pipe and the resultant possible blockage of the path of the monofilament line (Figure 7.25). These patches were attached to the main reinforcement with a sticky tape.

Figure 7.21. The geotextile layer and the regions where the monofilament lines were attached.

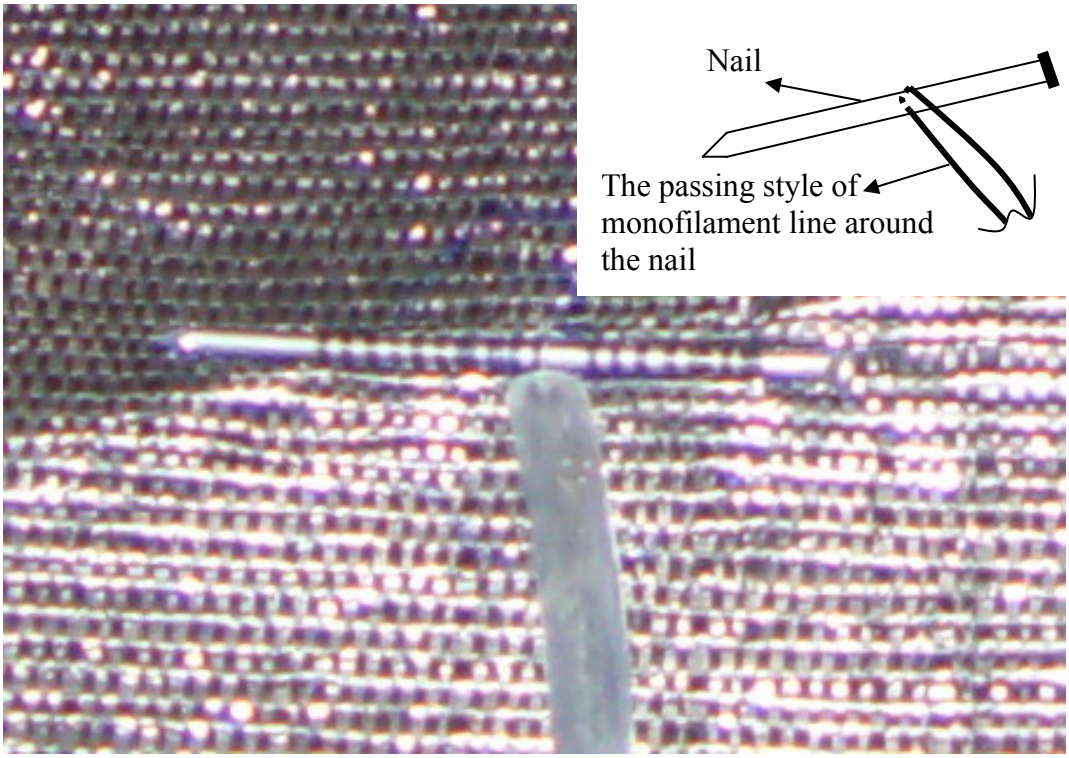

Figure 7.22. The enlarged view of the connection of the monofilament line around the nail.

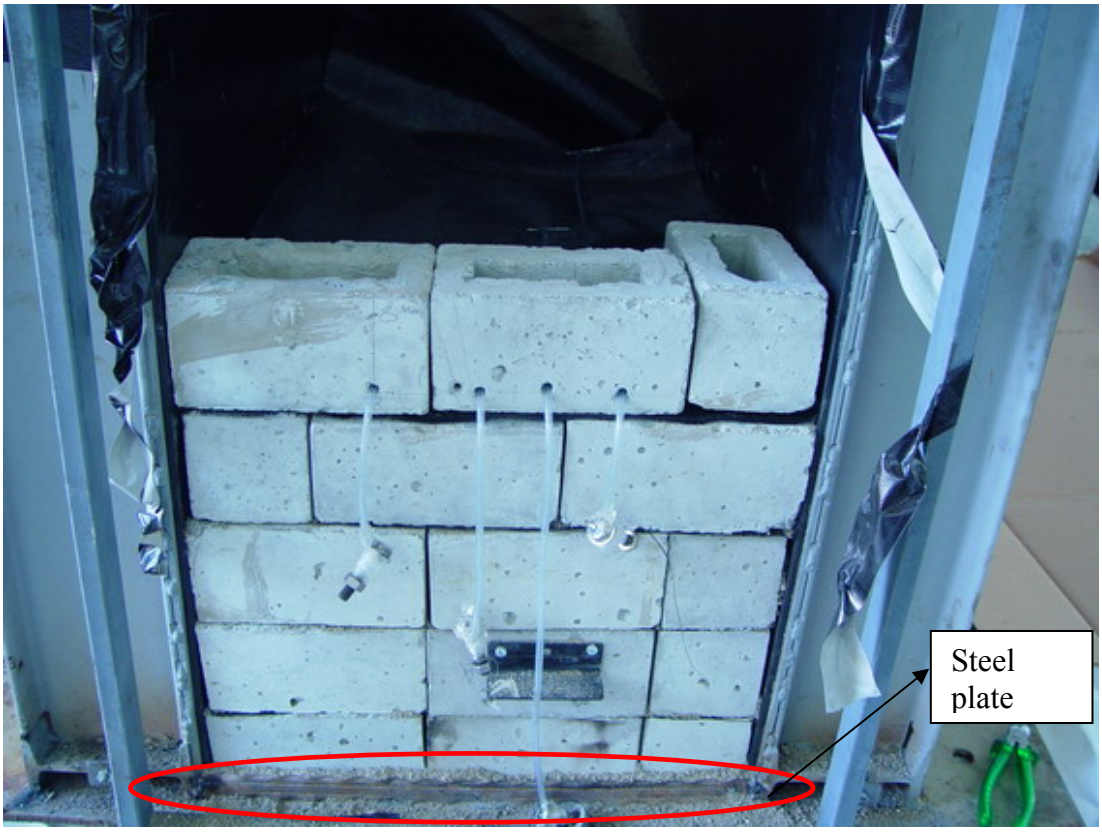

Figure 7.23. Flexible polymer pipes were passed from the drilled holes of the blocks and facing wall toe was fixed with the help of a steel plate.

Figure 7.24. The wall's movement at the bottom was restricted by welding a piece of steel plate.

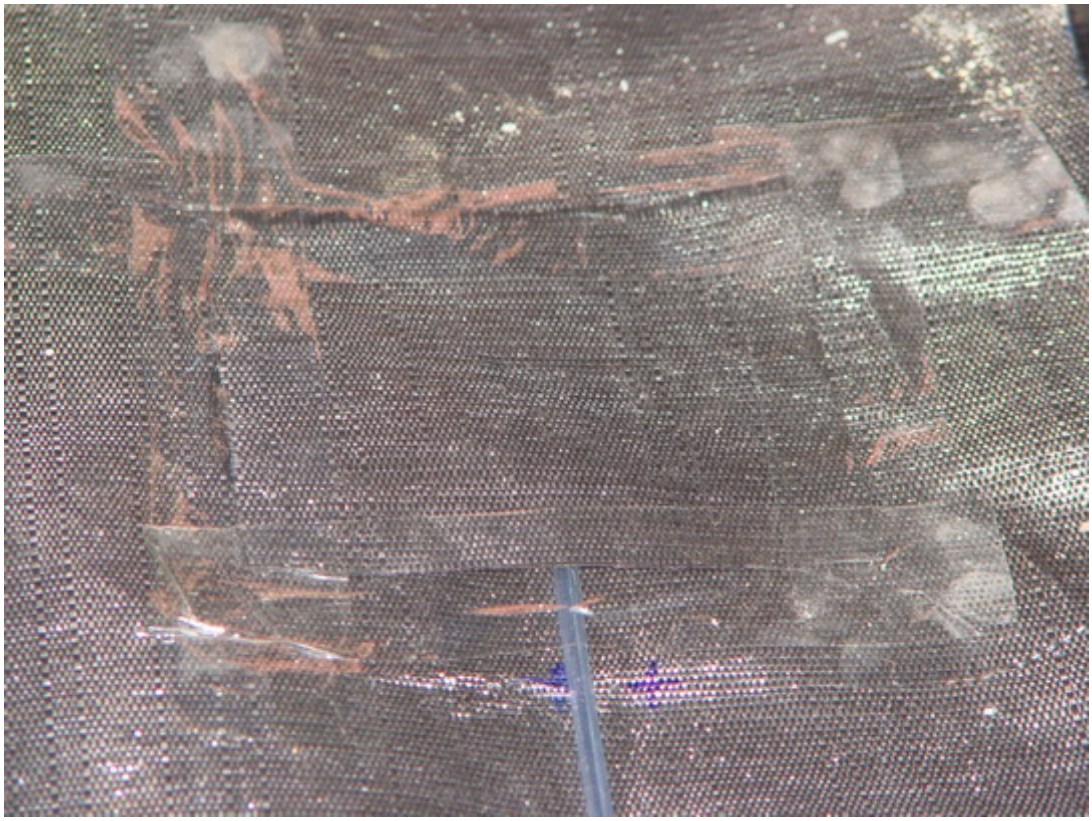

Figure 7.25. The region was isolated by covering with a patch of geotextile.

To measure the strains of the geotextiles during shaking a special test setup was designed to suit to the needs of the transducers. The two ends of the monofilament lines were passed through the holes of concrete modular blocks and met with the pulleys and the wood screws-with rings on the wooden frame. Then, the magnets were attached to the monofilament lines and cylindrical copper rods were passed from the magnet's four holes. While the pulleys, wood screws and four cylindrical copper rods ensured the magnet to move vertically in the specified region and within a horizontal distance of 4 to 8 mm from the surface of transducers, the lead weights induced a small tension to the monofilament lines providing a restraint in the vertical direction so that the monofilament lines wouldn't flee from the setup (Figure 7.26). A total of 8 transducers were installed to measure the strains in the corresponding two layers.

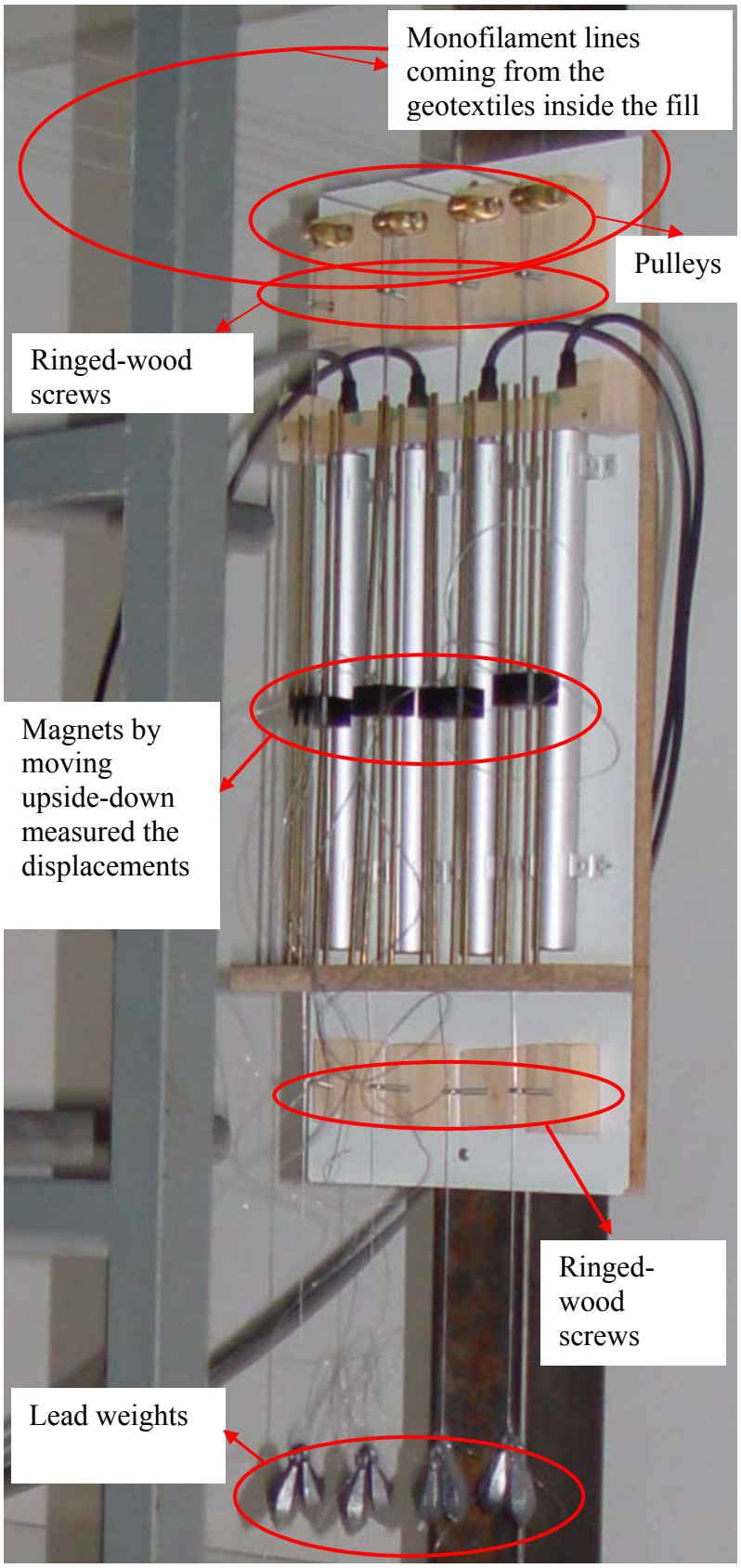

Figure 7.26. A magnified view of the strain measurement system on uppermost level

Till to the uppermost two levels of layers, the usual construction scheme of filling the inside of the modular blocks firstly with sand and then laying down of the geotextile layers and then putting the blocks on top of each other continued. But at the upper two layers instead of filling with sand the inside space of concrete blocks, three 20 cm long ∅12 type of construction steel rebars were put, penetrated from the geotextiles between the modular blocks and then the inside space of concrete blocks were filled with concrete grout resulting a more stable system at the top. Before penetration, corresponding holes were opened which were sufficiently small enough to be able to permit the penetration of the rebars through the geotextiles.

8 laser displacement sensors were installed onto the distance adjustable arms of the post by the help of certain plastic clamps. Overall view of the measurement locations of the laser displacement sensors, strain measuring transducers on the front wall and the accelerometers both on the front wall and in the top of the soil fill can be seen in detail in section 7.5 in Figures 7.34 and 7.35.

Certain precautions were taken for the possible collapse of the structure to prevent the falling down of the front wall, such as installing a metal box frame and fixing a plastic wire mesh in front of it. Also onto several places oilcloth was attached to prevent the penetration of the sand between the rails of the shaking table and to the regions where the hydraulic actuator was located (Figure 7.27).

The placement of the accelerometers onto the front wall surface and on top of the fill can be seen in Figures 7.28 to 7.31. In Figure 7.32, a general view of the placed two posts is demonstrated.

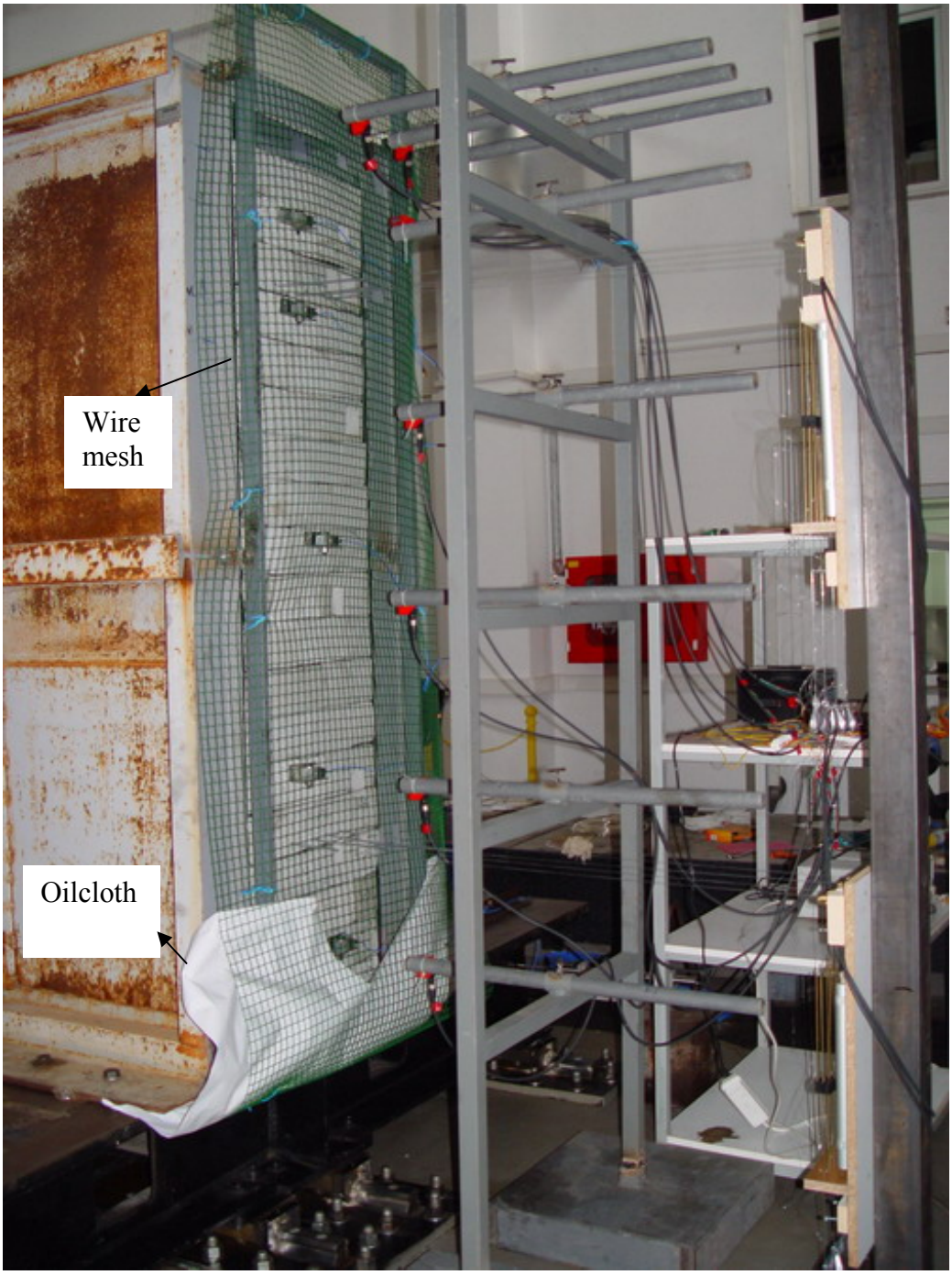

Figure 7.27**.** A rear view of the posts and front view from the frame.

Figure 7.28. The accelerometer mounted onto the surface as shown.

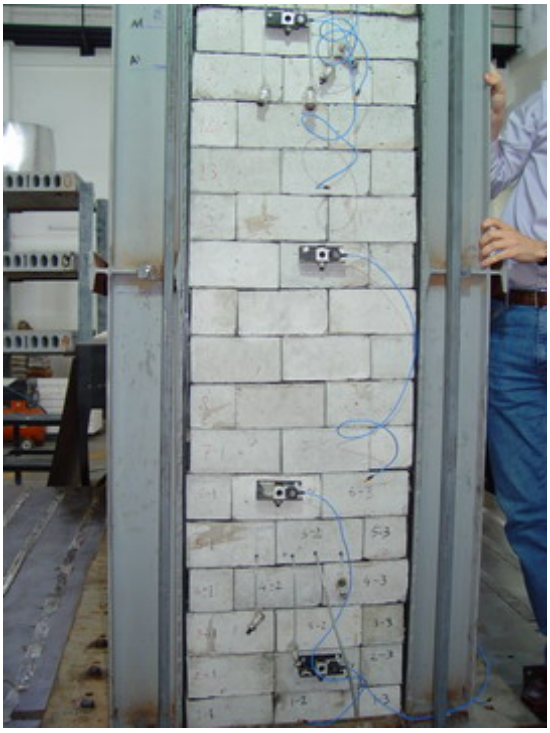

Figure 7.29. An overall front view of the wall showing the accelerometers mounted

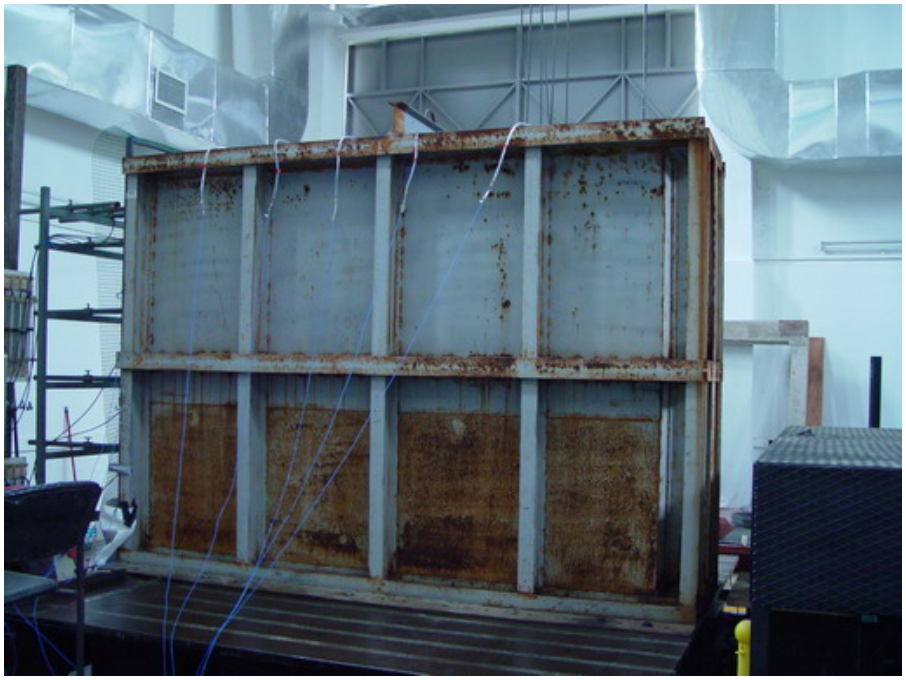

Figure 7.30. 5 accelerometers were also put on top of the sand fill.

Figure 7.31. Top view.

Figure 7.32. A general view of the posts

7.5. Instrumentation and Reinforcement Layout

Figures 7.33 through 7.35 show the instrumentation schema, reinforcement layout and the locations of the sensors, accelerometers and transducers installed.

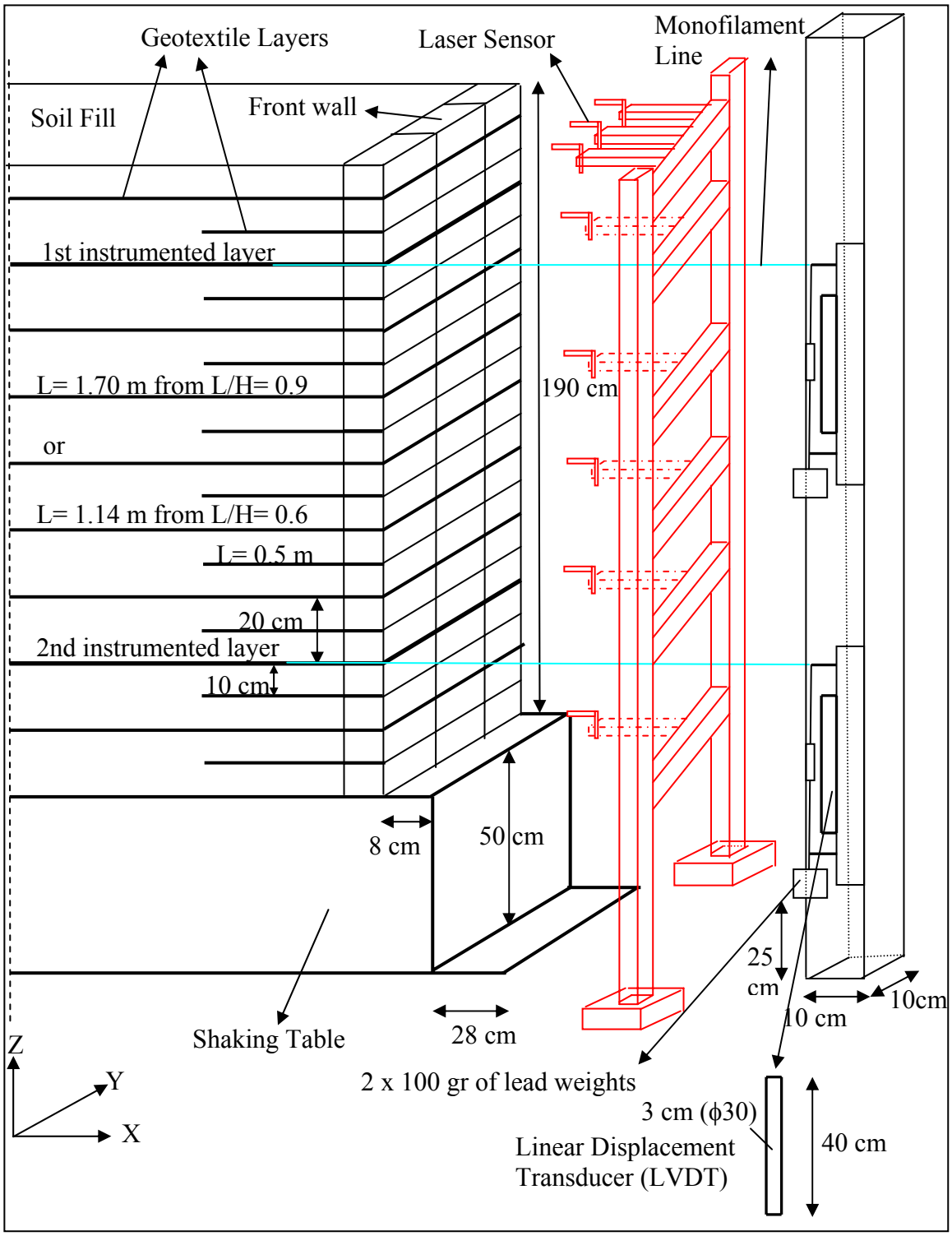

Figure 7.33. Instrumentation application plan.

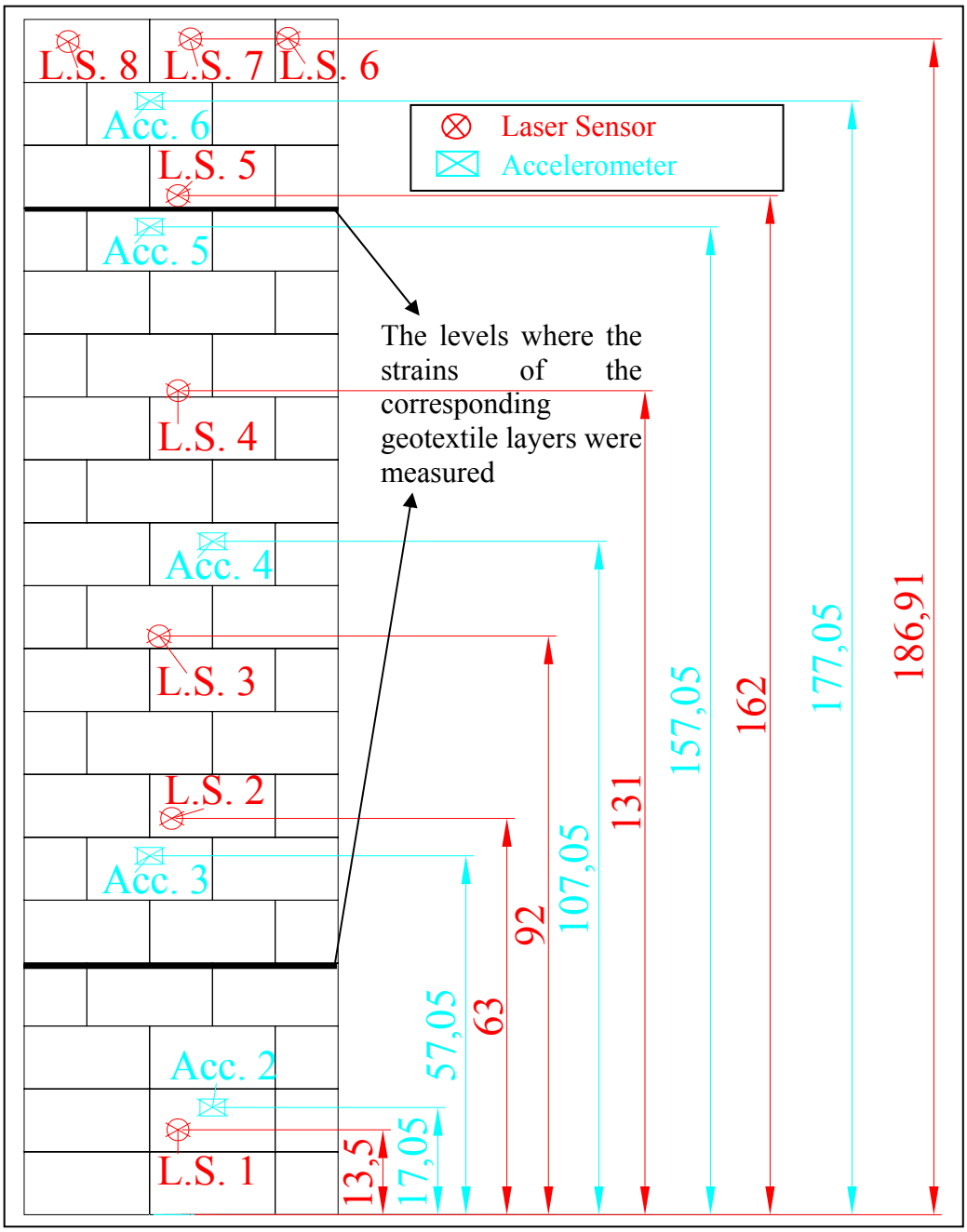

Figure 7.34. The locations of the sensors, accelerometers and transducers on the front wall.

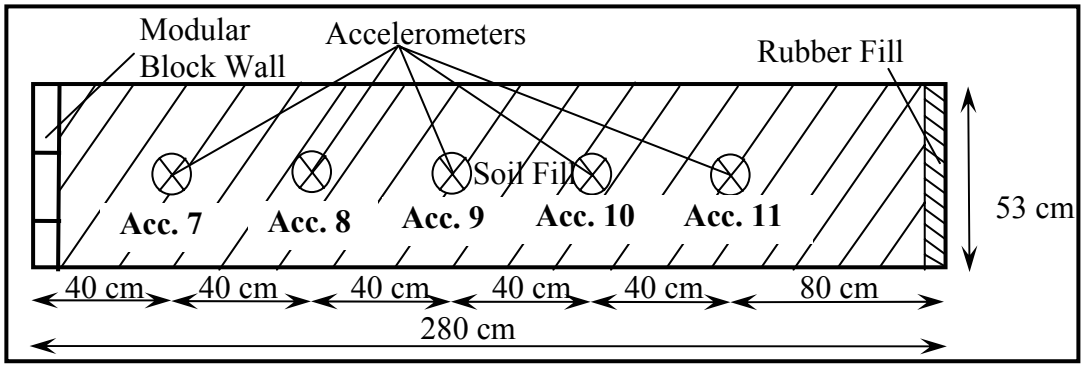

Figure 7.35. The locations of the accelerometers (Plan view).

7.6. Shaking Sequence

For the model L/H=0.9 the following motions are investigated in this study:

1. A sinusoidal wave, which was created at the moment of shaking process (Sine Motion). Since the shaking table's data acquisition and control system didn't allow a previously determined sinusoidal wave to be applied to the system, the data acquisition system and control system of the shaking table were bypassed and a sinusoidal wave was applied. As a result of this, no acceleration-time data was plotted as the accelerometers were unplugged from the data-acquisition system.
2. The 100 per cent El Centro Earthquake Motion where the frequencies bigger than 0.5 Hz were taken into account (El Centro-1).
3. After the 100 per cent El Centro excitation, the system was subjected again to the same El Centro excitation (El Centro-2).

As for the model L/H=0.6, the motions applied are:

1. A sinusoidal wave motion. (Only shaking table's acceleration-time data was plotted as the other accelerometers were unplugged from the data-acquisition system)
2. The 100 per cent El Centro Earthquake Motion where the frequencies bigger than 0.5 Hz were taken into account (El Centro-1).
3. After the 100 per cent El Centro excitation, the system was subjected again to the same El Centro excitation (El Centro-2).
4. Again another same 100 per cent El Centro excitation (El Centro-3).
5. Last 100 per cent El Centro excitation in which the frequencies lower than 0.5 Hz were included as well (El Centro-4).

7.7. Evaluation of the Test Data

In the evaluation of the data stage, it was understood that the raw data were influenced by the noise waves like the one in the base displacement-time history record of (L/H = 0.9 Sine motion) example in Figure 7.36.

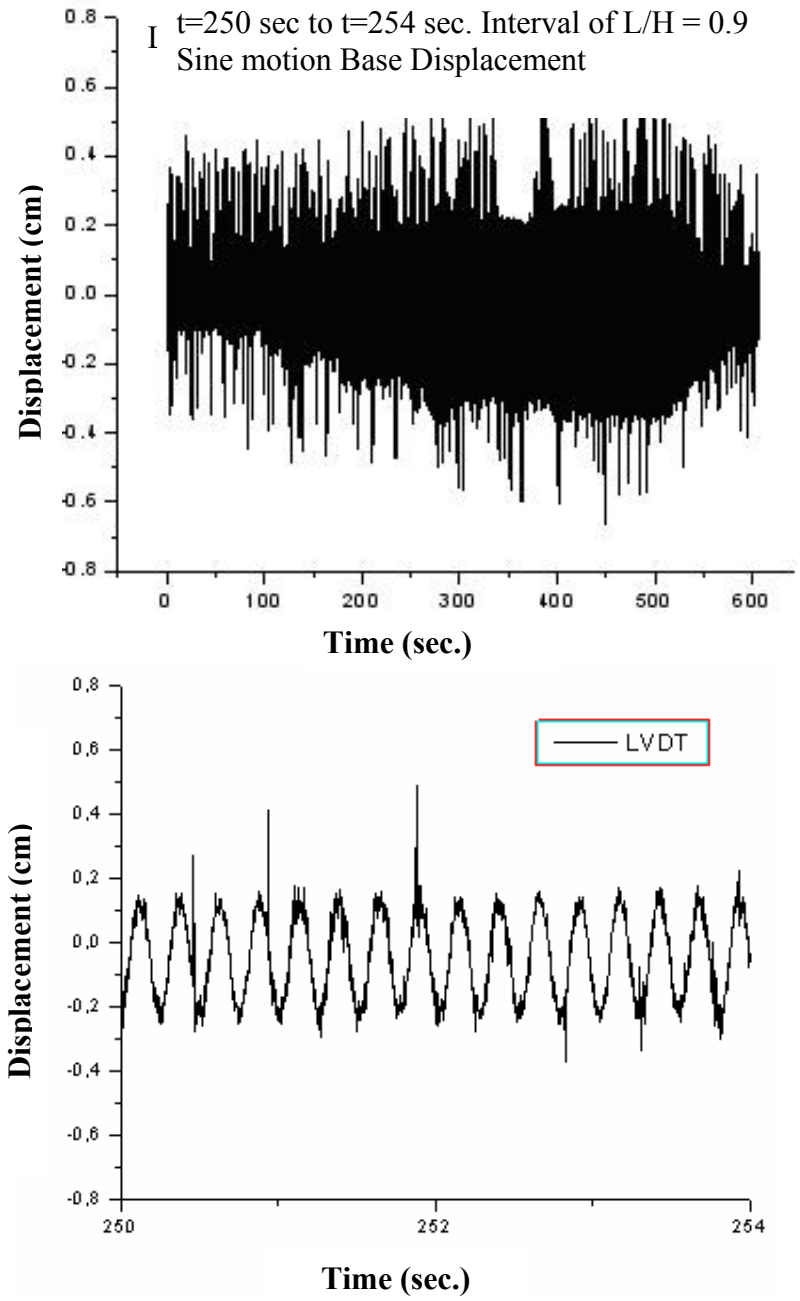

Figure 7.36. Graph plotted with noise-influenced raw data

As it can be observed, there were many sudden and big increments of displacement shifts caused by the noise occurred during the shaking. So, all of the time-history data were filtered and the frequency band between 0.0001 Hz and 20 Hz were taken into account for all of them and resultant undisturbed diagrams were obtained like the one in Figure 7.37.

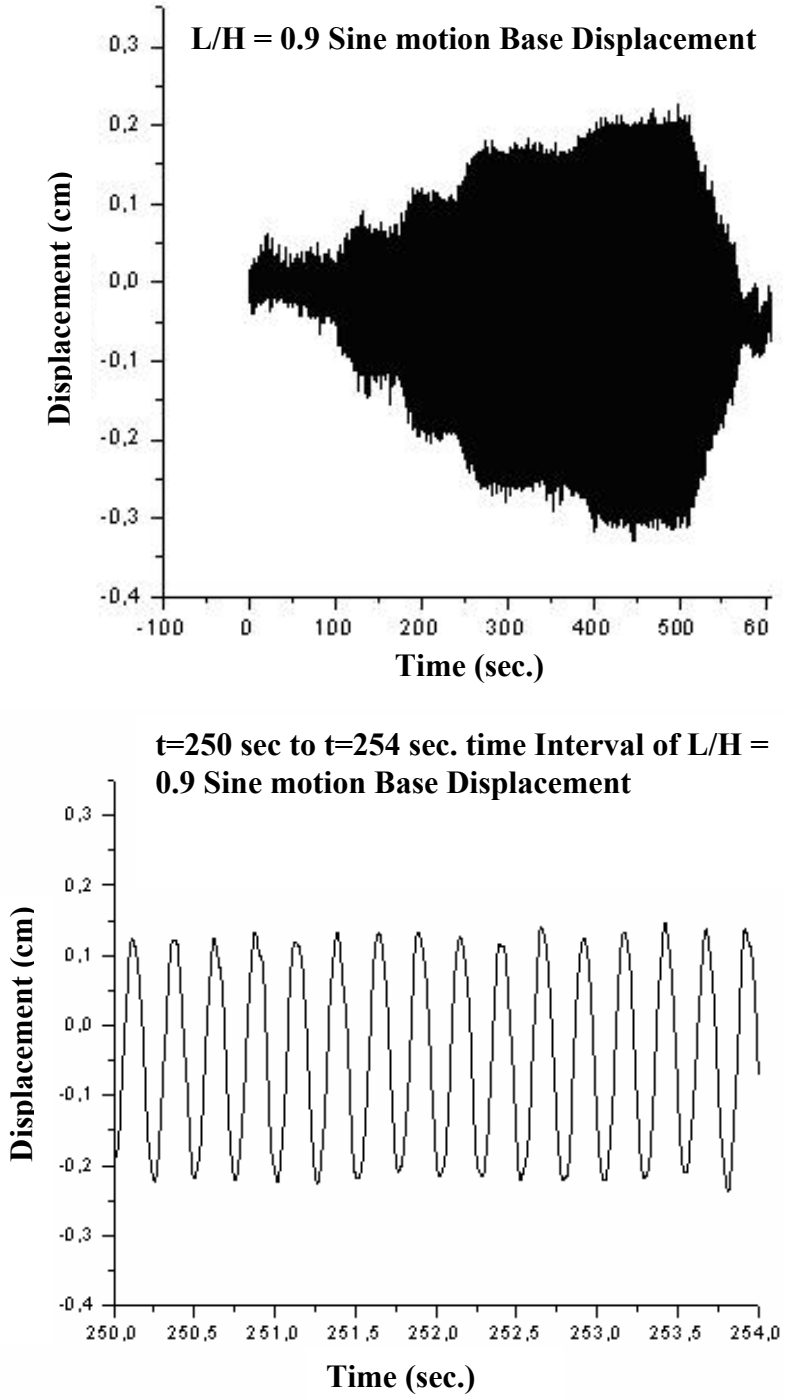

Figure 7.37. Graph plotted with filtered-data

The frequency of the sine motion excited can approximately be considered to be 4 Hz.

The shaking table's PC-based digital control system produced an analog drive signal to the actuator servo-controller, which controlled the actuator, and simulated the input

motion. Every time after the input El-Centro earthquake motion diminished after 18.732 seconds, a certain kind of minor and insignificant impulse occurred in the system, which did not have any effect on the structure.

8. Newmark's Displacement Method Analysis and Determination of the Inclination of the Failure Surface

8.1. Newmark's Displacement Method

According to Newmark theory, a potential sliding body is treated as a rigid-plastic monolithic mass under the action of seismic forces. Permanent displacement of the mass takes place whenever the seismic force induced on the body (plus the existing static force) overcomes the available resistance along the potential sliding/shear surface. Newmark's method adapted to the segmental retaining wall problem requires that the critical acceleration k_c to initiate sliding or shear failure be determined for each translation failure mechanism. The value of k_c can be determined by searching for values of k_h that give a factor of safety of unity in pseudo-static factor of safety expressions. The critical acceleration is then applied to the horizontal ground acceleration record at the site and double integration is performed to calculate cumulative displacement as illustrated in Figure 8.1 where g is the gravitational constant; a(t) is the horizontal ground acceleration function with time t; $a_m = k_m g$ is the peak value of a(t); and $a_c = k_c g$ is the critical horizontal acceleration of the sliding mass. For a given ground acceleration time history and a known critical acceleration of the sliding mass, the earthquake induced displacement is calculated by integrating those portions of the acceleration time history that are above the critical acceleration and those portions that are below until the relative velocity between the sliding mass and the sliding base reduces to zero [26].

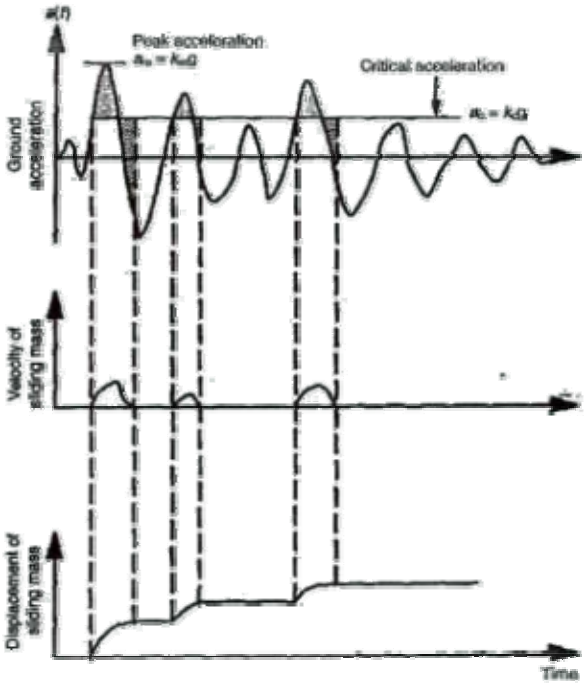

Figure 8.1. Calculation of permanent displacements (unidirectional displacement) using Newmark's Method [26]

For the test wall the criteria of the National Concrete Masonry Association's (NCMA) Segmental Retaining Walls - Seismic Design Manual is used with the procedures that were explained previously. Instead of doing hand calculations, MS Excel program is used [27].

8.1.1. Material properties

The material properties of the experimented walls are listed in Table 8.1.

Table 8.1. Material properties of the experimented walls used in the calculations

Input Data	Properties	Values
Backfill Soil	Friction angle (ϕ_b)	36°, 38° (for 1st and 2nd exp. respectively)
	Unit Weight(γ_b)	15 and 16 kN/m
	Mobilized interface friction angle (δ_b)	36°, 38° (for 1st and 2nd exp. respectively)
Reinforced Soil	Friction angle (Φ_r)	36°, 38° (for 1st and 2nd exp. respectively)
	Unit Weight(γ_r)	15 and 16 kN/m
	Mobilized interface friction angle (δ_r)	24°, 25.3° (for 1st and 2nd exp. respectively)
Geotextile (wowen polyster)	Ultimate Strength (T_{ult})	40 kN/m
	Ultimate Strain (ε_{ult})	% 11
Soil-Geotextile	Coefficient of Direct Sliding	1.00
Segmental Block	Height (H_w) Length (L_w)	0.1 m 0.1 m, 0.2 m
	Unit Weight(γ_w)	21 kN/m^3
	Block-Geotextile interface shear (Formula 3.63)	a_{cs} = 6 kN/m λ_{cs} = 30°
Wall	Height (H) Setback (ω) Backslope Angle (β) Reinforcement Spacing Reinforcement Length/Height of Wall (L/H)	1.9 m 0° 0° 0.2 m 0.90, 0.60
Seismic Data (El Centro Earthquake)	Peak Ground Acceleration a_m Peak Ground Velocity v_m	0.3 g 0.13 m/sn

8.1.2. Determination of Critical Accelerations

Permanent displacements are assumed to calculate each time the critical acceleration a_c ($a_c = k_c g$), where k_c is the critical horizontal seismic coefficient), associated with each

three displacement mechanisms; (1) external sliding along the base of total structure; (2) internal sliding along a reinforcement layer and through the facing column; and (3) block interface shear between facing column units; is exceeded by the horizontal input (ground) acceleration a(t).

The critical horizontal acceleration coefficient (k_c) for any given set of input parameters corresponds to the value of k_h that gives $FS_{dyn} = 1.0$.

8.1.3. Calculation of Permanent Displacements

The seismic displacement of a potential sliding soil mass computed using Newmark's theory has been traditionally correlated with the critical acceleration ratio (k_c/k_m) and other representative characteristic seismic parameters such as the peak ground acceleration ($k_m g$), the peak ground velocity v_m, and the predominant period (T) of the acceleration spectrum (e.g., Newmark 1965; Sarma 1975; Franklin and Chang 1977). The writers have reformulated a number of existing displacement methods based on nondimensionalized displacement terms that are common to the methods and divided them into two separate categories based on the characteristic seismic parameters referenced in each method (Cai and Bathurst 1996). The first category of methods uses the peak ground acceleration ($k_m g$) and peak ground velocity (v_m) as characteristic parameters, and the second category of methods uses the peak ground acceleration ($k_m g$) and the predominant period (T) of the ground acceleration spectrum.

For brevity, only the first category of methods is presented in Figure 8.2. These methods give correlations between the dimensionless displacement term $d/(v_m^2/k_m g)$, where d is the actual expected permanent displacement, and the critical acceleration ratio (k_c/k_m). In Figure 8.2, there are three upper bound displacement curves (a, c, e) and two mean displacement curves (b, d) that are derived based on different sources of earthquake data.

It should be pointed out, however, that since these methods have been formulated based on different earthquake data, the selection of which method to use should be based on careful evaluation of the characteristics of the earthquake record and the site conditions

under consideration. It should also be noted that the values of permanent displacement given by each method are only order-of-magnitude estimates rather than accurate predictions. Engineering judgment plays an important role in the interpretation of results using the methods given in Figure 8.2.

In this study Newmark's double integration and Bathurst and Cai's mean upper bound methods are used for calculation of permanent displacements.

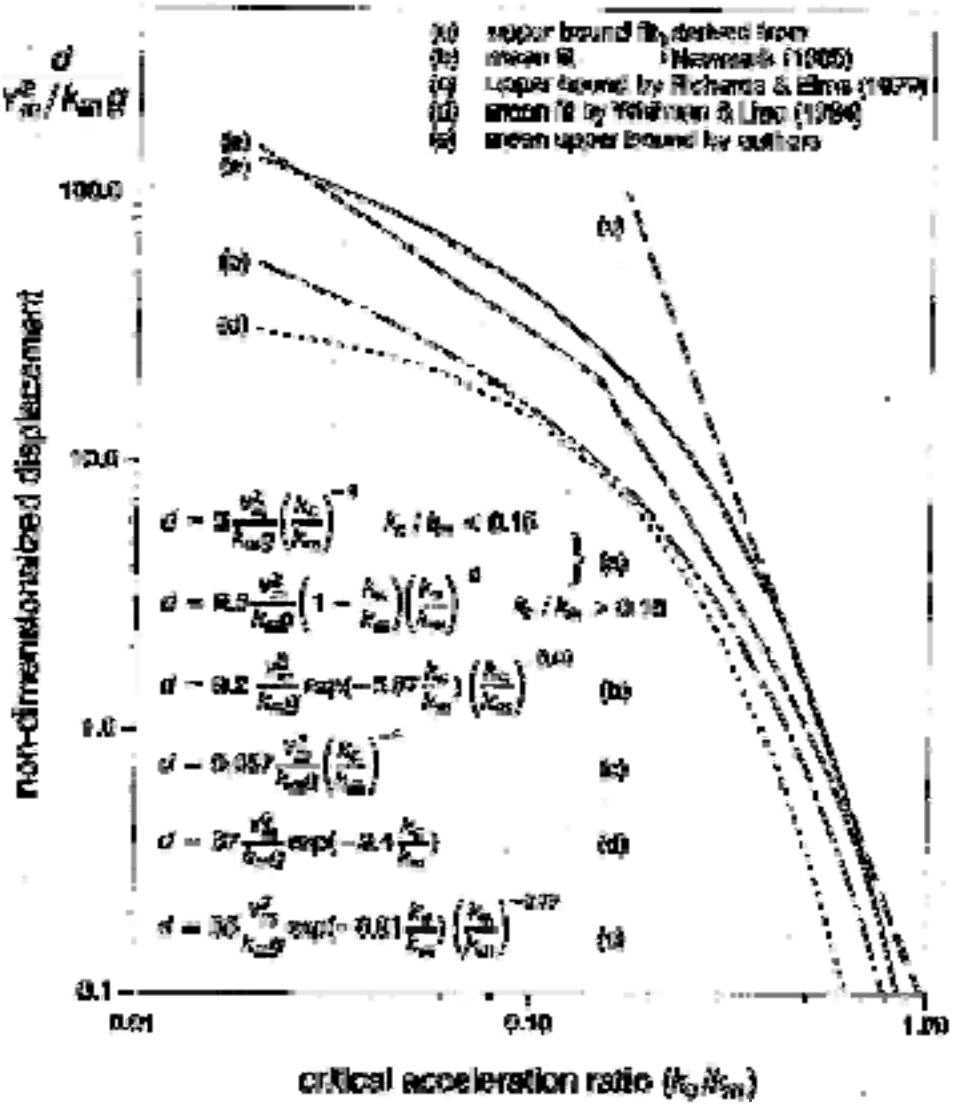

Figure 8.2. Nondimensionalized displacement in terms of $d/(v_m^2/k_m g)$ versus critical acceleration ratio k_c/k_m (after Cai and Bathurst 1996) [28].

8.1.4. Seismic Data

As seismic data, the Scaled-El Centro Earthquake, in which the maximum acceleration and velocity are 0.3g and 0.13 m/sn respectively, was opted. The related time history curves can be seen in Figure 8.3.

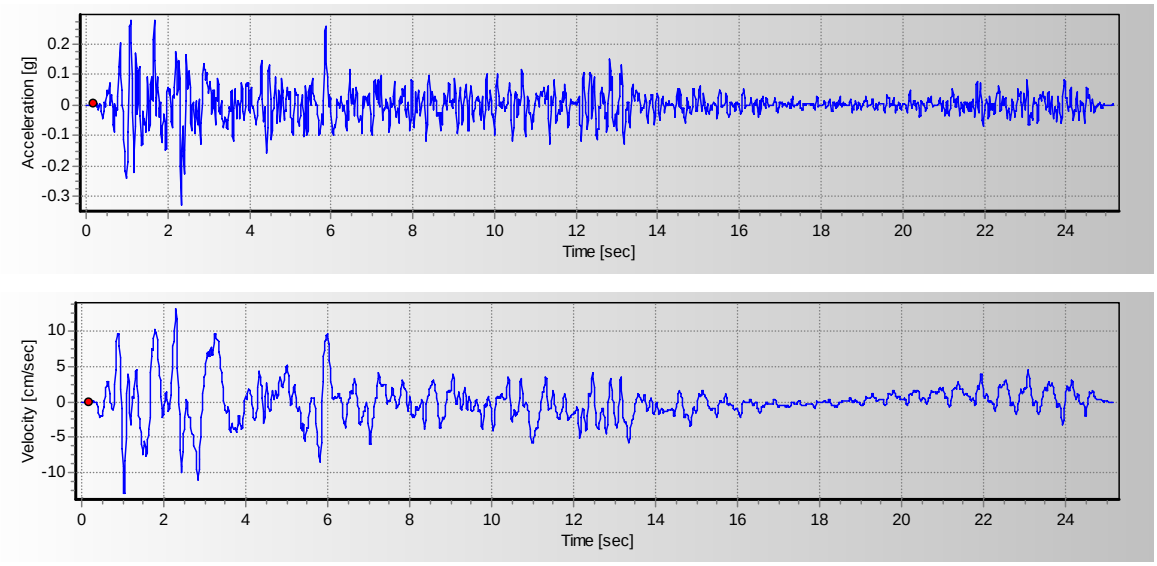

Figure 8.3. Seismic data of the scaled-El Centro earthquake.

8.1.5. The Results of the Analysis

Tables 8.2 to 8.4 and Tables 8.6 to 8.8 show the k_c values calculated according to the condition of F.S. being equal to 1. However, at some elevations seismic inertia angle (ψ) values reached to their maximum values and therefore they limited the k_c values to get higher values and as a result some F.S. values took values larger than 1 (i.e. Layer No.9 in Table 8.3). Tables 8.5 and 8.9 show that no residual displacements in the wall should be expected according to these calculations.

Table 8.2. Calculation of k_c for the external base sliding for the first test wall where L/H = 0.9

External Base Sliding			
k_c	0.607	H	1.90
ψ	31.26	L	1.71
K_A	0.21	K_{AH}	0.17
K_{AE}	1.43	K_{AEH}	1.15
ΔK_{dyn}	1.22	ΔK_{dynH}	0.99
W_w	3.99		
W_i	45.89	W_i'	24.23
W_r	49.88		
R_S	36.24		
P_{IR}	17.13		
P_{AEH}	19.11		
FS_{sl}	1.00		

Table 8.3. Calculation of k_c for the internal sliding for the first test wall where L/H = 0.9

Internal Sliding											
Layer No	Elevation	Depth	S_{vi}	Z_{vi}	L_i	H					
1	0.20	1.70	0.30	1.75	1.71	1.90					
2	0.40	1.50	0.20	1.61	1.71	1.90					
3	0.60	1.30	0.20	1.30	1.71	1.90					
4	0.80	1.10	0.20	1.10	1.71	1.90					
5	1.00	0.90	0.20	0.90	1.71	1.90					
6	1.20	0.70	0.20	0.70	1.71	1.90					
7	1.40	0.50	0.20	0.50	1.71	1.90					
8	1.60	0.30	0.20	0.30	1.71	1.90					
9	1.80	0.10	0.20	0.10	1.71	1.90					
Layer No	Elevation	Depth	ΔW_w	$\Delta W_i'$	$\Delta P_{IR}(z)$	h_{zi}	$P_{AEH}(z)$	$V_u(z)$	ΔWi	$R_S(z)$	FS_{sli}
1	0.20	1.70	3.57	21.68	17.65	1.70	19.34	8.07	41.06	36.81	1.00
2	0.40	1.50	3.15	19.13	15.59	1.50	17.62	7.83	36.23	33.18	1.00
3	0.60	1.30	2.73	16.58	13.59	1.30	16.11	7.58	31.40	29.56	1.00
4	0.80	1.10	2.31	14.03	11.60	1.10	14.68	7.34	26.57	25.94	0.99
5	1.00	0.90	1.89	11.48	9.53	0.90	12.68	7.10	21.74	22.31	1.00
6	1.20	0.70	1.47	8.93	7.51	0.70	11.45	6.85	16.91	18.69	0.99
7	1.40	0.50	1.05	6.38	5.39	0.50	9.22	6.61	12.08	15.06	1.03
8	1.60	0.30	0.63	3.83	3.23	0.30	5.69	6.37	7.25	11.44	1.28
9	1.80	0.10	0.21	1.28	1.08	0.10	1.95	6.12	2.42	7.81	2.58
Layer No	k_c	θ	K_A	K_{AE}	ΔK_{dyn}	K_{AH}	K_{AEH}	ΔK_{dynH}			
1	0.699	34.95	0.21	1.71	1.50	0.17	1.39	1.22			
2	0.700	34.99	0.21	1.72	1.51	0.17	1.40	1.23			
3	0.704	35.15	0.21	1.78	1.57	0.17	1.44	1.27			
4	0.710	35.37	0.21	1.86	1.65	0.17	1.51	1.34			
5	0.713	35.49	0.21	1.92	1.71	0.17	1.55	1.38			
6	0.723	35.85	0.21	2.15	1.94	0.17	1.74	1.57			
7	0.726	35.98	0.21	2.35	2.14	0.17	1.90	1.73			
8	0.726	35.98	0.21	2.35	2.14	0.17	1.90	1.73			
9	0.726	35.98	0.21	2.35	2.14	0.17	1.90	1.73			

Table 8.4. Calculation of k_c for the interface shear for the first test wall where L/H = 0.9

Interface Shear									
Layer No	Elevation	Depth	ΔW_w	$P_{AEH}(z)$	F_i	Sum of F_i	$S_i(z)$	$V_u(z)$	FS_{sc}
1	0.20	1.70	3.57	48.31	5.46	48.82	2.08	8.07	3.88
2	0.40	1.50	3.15	44.58	4.29	44.53	2.34	7.83	3.34
3	0.60	1.30	2.73	40.34	4.81	39.72	2.60	7.58	2.91
4	0.80	1.10	2.31	35.57	5.34	34.38	2.86	7.34	2.56
5	1.00	0.90	1.89	30.27	5.86	28.52	3.12	7.10	2.27
6	1.20	0.70	1.47	24.46	6.38	22.14	3.39	6.85	2.02
7	1.40	0.50	1.05	18.12	6.90	15.24	3.65	6.61	1.81
8	1.60	0.30	0.63	11.27	7.42	7.82	3.91	6.37	1.63
9	1.80	0.10	0.21	3.89	7.82	0.00	4.04	6.12	1.52

Layer No	k_c	θ	K_A	K_{AE}	ΔK_{dyn}	K_{AH}	K_{AEH}	ΔK_{dynH}
1	0.726	35.98	0.21	2.35	2.14	0.17	1.90	1.73
2	0.726	35.98	0.21	2.35	2.14	0.17	1.90	1.73
3	0.726	35.98	0.21	2.35	2.14	0.17	1.90	1.73
4	0.726	35.98	0.21	2.35	2.14	0.17	1.90	1.73
5	0.726	35.98	0.21	2.35	2.14	0.17	1.90	1.73
6	0.726	35.98	0.21	2.35	2.14	0.17	1.90	1.73
7	0.726	35.98	0.21	2.35	2.14	0.17	1.90	1.73
8	0.726	35.98	0.21	2.35	2.14	0.17	1.90	1.73
9	0.726	35.98	0.21	2.35	2.14	0.17	1.90	1.73

Layer No	Elevation	Depth	S_{vi}	Z_{vi}	ΔWwi	F_{stai}	F_{dyni}
1	0.20	1.70	0.30	1.75	0.63	1.34	3.66
2	0.40	1.50	0.20	1.50	0.42	0.76	3.22
3	0.60	1.30	0.20	1.30	0.42	0.66	3.85
4	0.80	1.10	0.20	1.10	0.42	0.56	4.47
5	1.00	0.90	0.20	0.90	0.42	0.46	5.09
6	1.20	0.70	0.20	0.70	0.42	0.36	5.72
7	1.40	0.50	0.20	0.50	0.42	0.25	6.34
8	1.60	0.30	0.20	0.30	0.42	0.15	6.97
9	1.80	0.10	0.20	0.15	0.42	0.08	7.43

Table 8.5. Calculation of displacements for the first test wall where L/H = 0.9

Layer	k_c	k_m	k_c/k_m	v_m (cm/sn)	d (Newmark) (cm)	d (Bathurst and Cai) (cm)
1	0.699	0.30	2.33	13.00	0.00	0.00
2	0.700	0.30	2.33	13.00	0.00	0.00
3	0.704	0.30	2.35	13.00	0.00	0.00
4	0.710	0.30	2.37	13.00	0.00	0.00
5	0.713	0.30	2.38	13.00	0.00	0.00
6	0.723	0.30	2.41	13.00	0.00	0.00
7	0.726	0.30	2.42	13.00	0.00	0.00
8	0.726	0.30	2.42	13.00	0.00	0.00
9	0.726	0.30	2.42	13.00	0.00	0.00

Table 8.6. Calculation of k_c for the external base sliding for the second test wall where L/H = 0.6

External Base Sliding			
k_c	0.550	H	1.90
ψ	28.81	L	1.14
K_A	0.21	K_{AH}	0.16
K_{AE}	1.07	K_{AEH}	0.84
ΔK_{dyn}	0.86	ΔK_{dynH}	0.68
W_w	3.99		
W_i	31.62	W_i'	25.84
W_r	35.61		
R_S	30.95		
P_{IR}	16.41		
P_{AEH}	14.50		
FS_{sl}	1.00		

Table 8.7. Calculation of k_c for the internal sliding for the second test wall where L/H = 0.6

Internal Sliding						
Layer No	**Elevation**	**Depth**	**S_{vi}**	**Z_{vi}**	**L_i**	**H**
1	0.20	1.70	0.30	1.75	1.14	1.90
2	0.40	1.50	0.20	1.04	1.14	1.90
3	0.60	1.30	0.20	1.30	1.14	1.90
4	0.80	1.10	0.20	1.10	1.14	1.90
5	1.00	0.90	0.20	0.90	1.14	1.90
6	1.20	0.70	0.20	0.70	1.14	1.90
7	1.40	0.50	0.20	0.50	1.14	1.90
8	1.60	0.30	0.20	0.30	1.14	1.90
9	1.80	0.10	0.20	0.10	1.14	1.90

Layer No	**Elevation**	**Depth**	**ΔW_w**	**$\Delta W_i'$**	**$\Delta P_{IR}(z)$**	**h_{zi}**	**$P_{AEH}(z)$**	**$V_u(z)$**	**ΔWi**	**$R_S(z)$**	**FS_{sli}**
1	0.20	1.70	3.57	23.12	15.88	1.70	12.07	8.07	28.29	27.87	1.00
2	0.40	1.50	3.15	20.40	14.25	1.50	11.01	7.83	24.96	25.30	1.00
3	0.60	1.30	2.73	17.68	12.65	1.30	10.06	7.58	21.63	22.73	1.00
4	0.80	1.10	2.31	14.96	11.05	1.10	9.19	7.34	18.30	20.15	1.00
5	1.00	0.90	1.89	12.24	9.37	0.90	8.29	7.10	14.98	17.58	1.00
6	1.20	0.70	1.47	9.52	7.62	0.70	7.44	6.85	11.65	15.01	1.00
7	1.40	0.50	1.05	6.80	5.76	0.50	6.71	6.61	8.32	12.43	1.00
8	1.60	0.30	0.63	4.08	3.66	0.30	6.20	6.37	4.99	9.86	1.00
9	1.80	0.10	0.21	1.36	1.23	0.10	2.35	6.12	1.66	7.29	2.04

Layer No	**k_c**	**θ**	**K_A**	**K_{AE}**	**ΔK_{dyn}**	**K_{AH}**	**K_{AEH}**	**ΔK_{dynH}**
1	0.595	30.75	0.21	0.97	0.76	0.17	0.77	0.60
2	0.605	31.17	0.21	1.00	0.79	0.17	0.79	0.63
3	0.620	31.80	0.21	1.05	0.84	0.17	0.83	0.67
4	0.640	32.62	0.21	1.13	0.92	0.17	0.89	0.72
5	0.663	33.54	0.21	1.23	1.02	0.17	0.97	0.80
6	0.693	34.72	0.21	1.38	1.17	0.17	1.09	0.93
7	0.734	36.28	0.21	1.69	1.48	0.17	1.33	1.16
8	0.778	37.88	0.21	2.46	2.25	0.17	1.94	1.77
9	0.781	37.99	0.21	2.69	2.48	0.17	2.12	1.96

Table 8.8. Calculation of k_c for the interface shear for the second test wall where L/H = 0.6

Interface Shear									
Layer No	Elevation	Depth	ΔW_w	$P_{AEH}(z)$	F_i	Sum of F_i	$S_i(z)$	$V_u(z)$	FS_{sc}
1	0.20	1.70	3.57	57.57	6.30	57.93	2.42	8.07	3.33
2	0.40	1.50	3.15	53.21	5.00	52.93	2.74	7.83	2.85
3	0.60	1.30	2.73	48.22	5.65	47.28	3.07	7.58	2.47
4	0.80	1.10	2.31	42.57	6.29	40.99	3.39	7.34	2.17
5	1.00	0.90	1.89	36.28	6.94	34.05	3.71	7.10	1.91
6	1.20	0.70	1.47	29.35	7.58	26.46	4.03	6.85	1.70
7	1.40	0.50	1.05	21.77	8.23	18.23	4.36	6.61	1.52
8	1.60	0.30	0.63	13.55	8.88	9.36	4.68	6.37	1.36
9	1.80	0.10	0.21	4.68	9.36	0.00	4.84	6.12	1.26

Layer No	k_c	θ	K_A	K_{AE}	ΔK_{dyn}	K_{AH}	K_{AEH}	ΔK_{dynH}
1	0.781	37.99	0.21	2.69	2.48	0.17	2.12	1.96
2	0.781	37.99	0.21	2.69	2.48	0.17	2.12	1.96
3	0.781	37.99	0.21	2.69	2.48	0.17	2.12	1.96
4	0.781	37.99	0.21	2.69	2.48	0.17	2.12	1.96
5	0.781	37.99	0.21	2.69	2.48	0.17	2.12	1.96
6	0.781	37.99	0.21	2.69	2.48	0.17	2.12	1.96
7	0.781	37.99	0.21	2.69	2.48	0.17	2.12	1.96
8	0.781	37.99	0.21	2.69	2.48	0.17	2.12	1.96
9	0.781	37.99	0.21	2.69	2.48	0.17	2.12	1.96

Layer No	Elevation	Depth	S_{vi}	Z_{vi}	ΔWwi	F_{stai}	F_{dyni}
1	0.20	1.70	0.30	1.75	0.63	1.39	4.41
2	0.40	1.50	0.20	1.50	0.42	0.79	3.88
3	0.60	1.30	0.20	1.30	0.42	0.69	4.63
4	0.80	1.10	0.20	1.10	0.42	0.58	5.38
5	1.00	0.90	0.20	0.90	0.42	0.48	6.13
6	1.20	0.70	0.20	0.70	0.42	0.37	6.89
7	1.40	0.50	0.20	0.50	0.42	0.26	7.64
8	1.60	0.30	0.20	0.30	0.42	0.16	8.39
9	1.80	0.10	0.20	0.15	0.42	0.08	8.95

Table 8.9. Calculation of displacements for the second test wall where L/H = 0.6

Layer No	k_c	k_m	k_c/k_m	v_m (cm/sn)	d (Newmark) (cm)	d (Bathurst and Cai) (cm)
1	0.595	0.30	1.98	13.00	0.00	0.00
2	0.605	0.30	2.02	13.00	0.00	0.00
3	0.620	0.30	2.07	13.00	0.00	0.00
4	0.640	0.30	2.13	13.00	0.00	0.00
5	0.663	0.30	2.21	13.00	0.00	0.00
6	0.693	0.30	2.31	13.00	0.00	0.00
7	0.734	0.30	2.45	13.00	0.00	0.00
8	0.778	0.30	2.59	13.00	0.00	0.00
9	0.781	0.30	2.60	13.00	0.00	0.00

In conclusion, these analyses demonstrate that during this type of excitation and according to these criteria k_c and its corresponding a_c stays well beyond a_{max} and no residual displacement can be predicted in the system during and after the excitation.

8.2. Determination of the Inclination of the Failure Surface

By assuming $k_h = \frac{PGA}{2g} = \frac{0.3g}{g} = 0.15$, $k_v = 0$ (Because of the absence of a_v values and since its direction also plays a role in the calculation, it is neglected), and taking the related parameters $\phi_{soil} = 37°$, $\theta = 0°$, $\delta = 2\phi/3 = 25°$ (tests by Sherif and Fang (1983) and Ichihara and Matsuzawa (1973) on dry sands show δ to range from $\phi/2$ to $2\phi/3$) and $\beta = 0°$ the value of the inclination of the initial failure surface can be found as follows:

$$\psi = \tan^{-1}\left[\frac{0.15}{1-0}\right] = 8.53° \text{ , } C_{1E} = 1.69, C_{2E} = 2.58 \qquad \text{(by Eq.s 3.21, 3.23, 3.24)}$$

$$\alpha_{AE} = 37 - 8.53 + \tan^{-1}\left[\frac{-\tan(37-8.53-0)+1.69}{2.58}\right] = 52.4° \qquad \text{(by Eq. 3.22)}$$

whereas for facing and internal stability calculations of reinforced SRW structures (NCMA) by assuming $k_h = (1.45 - 0.3) \times 0.3 = 0.345$ (AASHTO/FHWA) according to Equation 3.36 (Segrestin and Bastick) the parameters and the resultant value of the inclination of the failure surface can be obtained as:

$$\psi = \tan^{-1}\left[\frac{0.345}{1-0}\right] = 19^\circ \text{ , } C_{1E} = 2.08, C_{2E} = 4.3 \qquad \text{(by Eq.s 3.21, 3.23, 3.24)}$$

$$\alpha_{AE} = 37 - 19 + \tan^{-1}\left[\frac{-0.32 + 2.08}{4.3}\right] = 40.3^\circ \qquad \text{(by Eq. 3.22)}$$

9. EVALUATION OF THE RESULTS

9.1. Acceleration Amplification Calculation Study

The maximum amplification factor (the ratio of the maximum acceleration in the structure to the peak input base acceleration) was evaluated for all of the El Centro Earthquake motions.

Since it is the peak input base acceleration that it is needed to focus on primarily to be able to measure the amplification factors, the peak values of the base accelerations at certain time instances were taken into consideration. In the Tables 9.1 through 9.6, the yellow marked lines are the primary time instances where the acceleration amplification for the regarding experiments should be taken into consideration, whereas the orange marked lines are the secondary time instances for the calculation of the acceleration amplification factor. It can be seen that the maximum base acceleration values at these time instances are very close to the ones with primary time instances marked as yellow. The other remaining lines are only additional subsidiary data that can be looked over and compared with the other experiments with respect to the changes occurred during the shaking process.

The results show that the maximum accelerations occurred during the time instance of the maximum base acceleration or during the time instance very close to it. The peak base accelerations were observed mainly at the time instances of t=2.32 sec and t=5.8 sec. Maximum acceleration distribution on the front wall and on top of the fill can be seen in Figures 9.1 and 9.2.

For all of the output acceleration-time history curve plots one can refer to Appendix A.

Table 9.1. Accelerations observed at various locations of the GRS-RW for 1st experiment 1st El-Centro excitation

1st Experiment 1st El-Centro 100% Excitation															
Accelerations at the Facing Block															
M1		**M2**			**M3**			**M4**			**M5**			**M6**		
BASE INPUT		**H = 0.17 m**		**Amp.**	**H = 0.57 m**		**Amp.**	**H = 1.07 m**		**Amp.**	**H = 1.57 m**		**Amp.**	**H = 1.77 m**		**Amp.**
Time (sec.)	**Acc. (g)**	**Time (sec.)**	**Acc. (g)**		**Time (sec.)**	**Acc. (g)**		**Time (sec.)**	**Acc. (g)**		**Time (sec.)**	**Acc. (g)**		**Time (sec.)**	**Acc. (g)**	
0.98 sec.	-0.24 g	0.98 sec.	-0.27 g	**1.11**	0.99 sec.	-0.28 g	**1.16**	0.99 sec.	-0.29 g	**1.21**	0.99 sec.	-0.31 g	**1.30**	0.99 sec.	-0.32 g	**1.34**
1.09 sec.	0.28 g	1.09 sec.	0.28 g	**1.02**	1.09 sec.	0.29 g	**1.04**	1.09 sec.	0.29 g	**1.05**	1.08 sec.	0.31 g	**1.11**	1.08 sec.	0.32 g	**1.17**
1.67 sec.	0.28 g	1.67 sec.	0.31 g	**1.11**	1.68 sec.	0.34 g	**1.24**	1.68 sec.	0.37 g	**1.35**	1.68 sec.	0.41 g	**1.47**	1.68 sec.	0.41 g	**1.49**
2.32 sec.	-0.33 g	2.32 sec.	-0.31 g	**0.95**	2.33 sec.	-0.32 g	**0.98**	2.33 sec.	-0.37 g	**1.13**	2.33 sec.	-0.44 g	**1.35**	2.33 sec.	-0.47 g	**1.42**
5.86 sec.	0.26 g	5.86 sec.	0.23 g	**0.89**	5.86 sec.	0.24 g	**0.95**	5.86 sec.	0.27 g	**1.04**	5.86 sec.	0.30 g	**1.18**	5.86 sec.	0.33 g	**1.27**
Accelerations at the Backfill															
M1		**M7**			**M8**			**M9**			**M10**			**M11**		
BASE INPUT		**H = 1.90 m L= 0.40 m**		**Amp.**	**H = 1.90 m L= 0.80 m**		**Amp.**	**H = 1.90 m L= 1.20 m**		**Amp.**	**H = 1.90 m L= 1.60 m**		**Amp.**	**H = 1.90 m L= 2.00 m**		**Amp.**
Time (sec.)	**Acc. (g)**	**Time (sec.)**	**Acc. (g)**		**Time (sec.)**	**Acc. (g)**		**Time (sec.)**	**Acc. (g)**		**Time (sec.)**	**Acc. (g)**		**Time (sec.)**	**Acc. (g)**	
0.98 sec.	-0.24 g	0.99 sec.	-0.30 g	**1.23**	0.99 sec.	-0.28 g	**1.15**	0.99 sec.	-0.31 g	**1.27**	0.99 sec.	-0.31 g	**1.31**	0.99 sec.	-0.31 g	**1.29**
1.09 sec.	0.28 g	1.08 sec.	0.29 g	**1.04**	1.08 sec.	0.27 g	**0.98**	1.08 sec.	0.30 g	**1.09**	1.09 sec.	0.30 g	**1.10**	1.08 sec.	0.30 g	**1.09**
1.67 sec.	0.28 g	1.68 sec.	0.37 g	**1.36**	1.68 sec.	0.35 g	**1.27**	1.68 sec.	0.40 g	**1.44**	1.67 sec.	0.41 g	**1.48**	1.68 sec.	0.39 g	**1.43**
2.32 sec.	-0.33 g	2.33 sec.	-0.42 g	**1.28**	2.33 sec.	-0.39 g	**1.19**	2.32 sec.	-0.44 g	**1.33**	2.33 sec.	-0.45 g	**1.37**	2.33 sec.	-0.44 g	**1.34**
5.86 sec.	0.26 g	5.86 sec.	0.29 g	**1.13**	5.86 sec.	0.28 g	**1.08**	5.86 sec.	0.30 g	**1.16**	5.86 sec.	0.30 g	**1.18**	5.86 sec.	0.30 g	**1.16**

Table 9.2. Accelerations observed at various locations of the GRS-RW for 1st experiment 2nd El-Centro excitation

1st Experiment 2nd El-Centro 100% Excitation																
Accelerations at the Facing Block																
M1		**M2**			**M3**			**M4**			**M5**			**M6**		
BASE INPUT		**H = 0.17 m**		**Amp.**	**H = 0.57 m**		**Amp.**	**H = 1.07 m**		**Amp.**	**H = 1.57 m**		**Amp.**	**H = 1.77 m**		**Amp.**
Time (sec.)	**Acc. (g)**	**Time (sec.)**	**Acc. (g)**		**Time (sec.)**	**Acc. (g)**		**Time (sec.)**	**Acc. (g)**		**Time (sec.)**	**Acc. (g)**		**Time (sec.)**	**Acc. (g)**	
0.98 sec.	-0.26 g	0.98 sec.	-0.24 g	**0.93**	0.99 sec.	-0.25 g	**0.95**	0.99 sec.	-0.26 g	**0.97**	0.99 sec.	-0.27 g	**1.02**	0.99 sec.	-0.28 g	**1.06**
1.09 sec.	0.27 g	1.09 sec.	0.28 g	**1.03**	1.09 sec.	0.30 g	**1.09**	1.09 sec.	0.33 g	**1.21**	1.08 sec.	0.38 g	**1.40**	1.08 sec.	0.41 g	**1.48**
1.67 sec.	0.30 g	1.67 sec.	0.28 g	**0.96**	1.68 sec.	0.31 g	**1.04**	1.68 sec.	0.34 g	**1.15**	1.68 sec.	0.40 g	**1.34**	1.68 sec.	0.41 g	**1.39**
2.32 sec.	-0.30 g	2.32 sec.	-0.34 g	**1.10**	2.33 sec.	-0.36 g	**1.18**	2.33 sec.	-0.41 g	**1.33**	2.33 sec.	-0.48 g	**1.56**	2.33 sec.	-0.50 g	**1.63**
5.86 sec.	0.22 g	5.86 sec.	0.27 g	**1.20**	5.86 sec.	0.27 g	**1.24**	5.86 sec.	0.29 g	**1.31**	5.86 sec.	0.33 g	**1.49**	5.86 sec.	0.35 g	**1.56**
Accelerations at the Backfill																
M1		**M7**			**M8**			**M9**			**M10**			**M11**		
BASE INPUT		**H = 1.90 m L= 0.40 m**		**Amp.**	**H = 1.90 m L= 0.80 m**		**Amp.**	**H = 1.90 m L= 1.20 m**		**Amp.**	**H = 1.90 m L= 1.60 m**		**Amp.**	**H = 1.90 m L= 2.00 m**		**Amp.**
Time (sec.)	**Acc. (g)**	**Time (sec.)**	**Acc. (g)**		**Time (sec.)**	**Acc. (g)**		**Time (sec.)**	**Acc. (g)**		**Time (sec.)**	**Acc. (g)**		**Time (sec.)**	**Acc. (g)**	
0.98 sec.	-0.26 g	0.99 sec.	-0.26 g	**0.97**	0.99 sec.	-0.24 g	**0.91**	0.99 sec.	-0.26 g	**1.00**	0.99 sec.	-0.27 g	**1.02**	0.99 sec.	-0.26 g	**1.00**
1.09 sec.	0.27 g	1.08 sec.	0.36 g	**1.32**	1.08 sec.	0.34 g	**1.24**	1.08 sec.	0.37 g	**1.33**	1.09 sec.	0.37 g	**1.35**	1.08 sec.	0.36 g	**1.32**
1.67 sec.	0.30 g	1.68 sec.	0.36 g	**1.22**	1.68 sec.	0.34 g	**1.14**	1.68 sec.	0.38 g	**1.27**	1.67 sec.	0.39 g	**1.31**	1.68 sec.	0.38 g	**1.27**
2.32 sec.	-0.30 g	2.33 sec.	-0.45 g	**1.48**	2.33 sec.	-0.42 g	**1.38**	2.32 sec.	-0.47 g	**1.56**	2.33 sec.	-0.49 g	**1.60**	2.33 sec.	-0.47 g	**1.55**
5.86 sec.	0.22 g	5.86 sec.	0.31 g	**1.39**	5.86 sec.	0.29 g	**1.32**	5.86 sec.	0.32 g	**1.43**	5.86 sec.	0.32 g	**1.46**	5.86 sec.	0.32 g	**1.42**

Table 9.3. Accelerations observed at various locations of the GRS-RW for 2nd experiment 1st El-Centro excitation

2nd Experiment 1st El-Centro 100% Excitation																
Accelerations at the Facing Block																
M1		**M2**			**M3**			**M4**			**M5**			**M6**		
BASE INPUT		**H = 0.17 m**		**Amp.**	**H = 0.57 m**		**Amp.**	**H = 1.07 m**		**Amp.**	**H = 1.57 m**		**Amp.**	**H = 1.77 m**		**Amp.**
Time (sec.)	**Acc. (g)**	**Time (sec.)**	**Acc. (g)**		**Time (sec.)**	**Acc. (g)**		**Time (sec.)**	**Acc. (g)**		**Time (sec.)**	**Acc. (g)**		**Time (sec.)**	**Acc. (g)**	
0.95 sec.	-0.28 g	0.95 sec.	-0.29 g	**1.02**	0.95 sec.	-0.29 g	**1.05**	0.95 sec.	-0.30 g	**1.09**	0.95 sec.	-0.33 g	**1.18**	0.95 sec.	-0.37 g	**1.32**
1.68 sec.	0.31 g	1.68 sec.	0.33 g	**1.06**	1.68 sec.	0.36 g	**1.14**	1.68 sec.	0.37 g	**1.19**	1.68 sec.	0.39 g	**1.25**	1.67 sec.	0.40 g	**1.28**
2.42 sec.	-0.31 g	2.42 sec.	-0.31 g	**1.02**	2.42 sec.	-0.32 g	**1.04**	2.41 sec.	-0.33 g	**1.09**	2.41 sec.	-0.37 g	**1.22**	2.40 sec.	-0.41 g	**1.36**
5.87 sec.	0.32 g	5.87 sec.	0.33 g	**1.03**	5.87 sec.	0.34 g	**1.07**	5.87 sec.	0.35 g	**1.09**	5.87 sec.	0.39 g	**1.22**	5.86 sec.	0.39 g	**1.23**
Accelerations at the Backfill																
M1		**M7**			**M8**			**M9**			**M10**			**M11**		
BASE INPUT		**H = 1.90 m L= 0.40 m**		**Amp.**	**H = 1.90 m L= 0.80 m**		**Amp.**	**H = 1.90 m L= 1.20 m**		**Amp.**	**H = 1.90 m L= 1.60 m**		**Amp.**	**H = 1.90 m L= 2.00 m**		**Amp.**
Time (sec.)	**Acc. (g)**	**Time (sec.)**	**Acc. (g)**		**Time (sec.)**	**Acc. (g)**		**Time (sec.)**	**Acc. (g)**		**Time (sec.)**	**Acc. (g)**		**Time (sec.)**	**Acc. (g)**	
0.95 sec.	-0.28 g	0.93 sec.	-0.32 g	**1.15**	0.93 sec.	-0.29 g	**1.02**	0.93 sec.	-0.34 g	**1.20**	0.93 sec.	-0.34 g	**1.22**	0.93 sec.	-0.33 g	**1.17**
1.68 sec.	0.31 g	1.68 sec.	0.38 g	**1.21**	1.68 sec.	0.34 g	**1.09**	1.68 sec.	0.39 g	**1.25**	1.68 sec.	0.39 g	**1.25**	1.68 sec.	0.37 g	**1.18**
2.42 sec.	-0.31 g	2.41 sec.	-0.35 g	**1.16**	2.41 sec.	-0.31 g	**1.03**	2.41 sec.	-0.34 g	**1.12**	2.41 sec.	-0.33 g	**1.08**	2.42 sec.	-0.31 g	**1.03**
5.87 sec.	0.32 g	5.86 sec.	0.37 g	**1.16**	5.86 sec.	0.34 g	**1.08**	5.86 sec.	0.39 g	**1.21**	5.86 sec.	0.38 g	**1.18**	5.86 sec.	0.36 g	**1.13**

Table 9.4. Accelerations observed at various locations of the GRS-RW for 2nd experiment 2nd El-Centro excitation

2nd Experiment 2nd El-Centro 100% Excitation															
Accelerations at the Facing Block															
M1		**M2**			**M3**			**M4**			**M5**			**M6**		
BASE INPUT		**H = 0.17 m**		**Amp.**	**H = 0.57 m**		**Amp.**	**H = 1.07 m**		**Amp.**	**H = 1.57 m**		**Amp.**	**H = 1.77 m**		**Amp.**
Time (sec.)	**Acc. (g)**	**Time (sec.)**	**Acc. (g)**		**Time (sec.)**	**Acc. (g)**		**Time (sec.)**	**Acc. (g)**		**Time (sec.)**	**Acc. (g)**		**Time (sec.)**	**Acc. (g)**	
0.97 sec.	-0.21 g	0.97 sec.	-0.21 g	**1.02**	0.98 sec.	-0.21 g	**1.02**	0.98 sec.	-0.21 g	**1.03**	0.97 sec.	-0.22 g	**1.07**	0.97 sec.	-0.23 g	**1.10**
1.09 sec.	0.25 g	1.09 sec.	0.25 g	**1.02**	1.09 sec.	0.26 g	**1.03**	1.09 sec.	0.25 g	**1.01**	1.10 sec.	0.25 g	**1.02**	1.10 sec.	0.26 g	**1.04**
1.22 sec.	0.18 g	1.23 sec.	0.20 g	**1.08**	1.23 sec.	0.22 g	**1.18**	1.23 sec.	0.27 g	**1.47**	1.23 sec.	0.37 g	**1.98**	1.23 sec.	0.45 g	**2.45**
1.68 sec.	0.21 g	1.68 sec.	0.23 g	**1.05**	1.68 sec.	0.24 g	**1.13**	1.68 sec.	0.25 g	**1.18**	1.68 sec.	0.26 g	**1.21**	1.68 sec.	0.26 g	**1.23**
2.32 sec.	-0.29 g	2.32 sec.	-0.31 g	**1.05**	2.32 sec.	-0.33 g	**1.13**	2.33 sec.	-0.36 g	**1.22**	2.33 sec.	-0.41 g	**1.39**	2.35 sec.	-0.44 g	**1.51**
5.85 sec.	0.20 g	5.85 sec.	0.21 g	**1.05**	5.85 sec.	0.23 g	**1.10**	5.85 sec.	0.24 g	**1.15**	5.85 sec.	0.25 g	**1.23**	5.86 sec.	0.27 g	**1.31**
Accelerations at the Backfill															
M1		**M7**			**M8**			**M9**			**M10**			**M11**		
BASE INPUT		**H = 1.90 m L= 0.40 m**		**Amp.**	**H = 1.90 m L= 0.80 m**		**Amp.**	**H = 1.90 m L= 1.20 m**		**Amp.**	**H = 1.90 m L= 1.60 m**		**Amp.**	**H = 1.90 m L= 2.00 m**		**Amp.**
Time (sec.)	**Acc. (g)**	**Time (sec.)**	**Acc. (g)**		**Time (sec.)**	**Acc. (g)**		**Time (sec.)**	**Acc. (g)**		**Time (sec.)**	**Acc. (g)**		**Time (sec.)**	**Acc. (g)**	
1.22 sec.	0.18 g	1.23 sec.	0.35 g	**1.90**	1.23 sec.	0.30 g	**1.64**	1.23 sec.	0.33 g	**1.81**	1.23 sec.	0.34 g	**1.84**	1.23 sec.	0.33 g	**1.77**
2.32 sec.	-0.29 g	2.33 sec.	-0.39 g	**1.34**	2.33 sec.	-0.36 g	**1.22**	2.33 sec.	-0.43 g	**1.46**	2.33 sec.	-0.43 g	**1.47**	2.33 sec.	-0.40 g	**1.38**
2.41 sec.	-0.17 g	2.41 sec.	-0.32 g	**1.88**	2.41 sec.	-0.25 g	**1.50**	2.41 sec.	-0.26 g	**1.51**	2.41 sec.	-0.27 g	**1.58**	2.41 sec.	-0.26 g	**1.52**
5.85 sec.	0.20 g	5.86 sec.	0.24 g	**1.16**	5.86 sec.	0.21 g	**1.03**	5.86 sec.	0.24 g	**1.18**	5.86 sec.	0.25 g	**1.21**	5.86 sec.	0.24 g	**1.17**

Table 9.5. Accelerations observed at various locations of the GRS-RW for 2nd experiment 3rd El-Centro excitation

2nd Experiment 3rd El-Centro 100% Excitation																
Accelerations at the Facing Block																
M1		**M2**			**M3**			**M4**			**M5**			**M6**		
BASE INPUT		**H = 0.17 m**		**Amp.**	**H = 0.57 m**		**Amp.**	**H = 1.07 m**		**Amp.**	**H = 1.57 m**		**Amp.**	**H = 1.77 m**		**Amp.**
Time (sec.)	**Acc. (g)**	**Time (sec.)**	**Acc. (g)**		**Time (sec.)**	**Acc. (g)**		**Time (sec.)**	**Acc. (g)**		**Time (sec.)**	**Acc. (g)**		**Time (sec.)**	**Acc. (g)**	
0.98 sec.	-0.24 g	0.98 sec.	-0.25 g	**1.01**	0.99 sec.	-0.25 g	**1.02**	0.99 sec.	-0.25 g	**1.02**	0.99 sec.	-0.25 g	**1.03**	0.98 sec.	-0.26 g	**1.07**
1.09 sec.	0.29 g	1.09 sec.	0.29 g	**1.03**	1.09 sec.	0.30 g	**1.05**	1.08 sec.	0.31 g	**1.08**	1.08 sec.	0.39 g	**1.35**	1.08 sec.	0.40 g	**1.39**
1.67 sec.	0.29 g	1.67 sec.	0.31 g	**1.05**	1.67 sec.	0.33 g	**1.12**	1.67 sec.	0.34 g	**1.15**	1.68 sec.	0.40 g	**1.38**	1.68 sec.	0.45 g	**1.54**
2.32 sec.	-0.34 g	2.32 sec.	-0.35 g	**1.04**	2.32 sec.	-0.37 g	**1.10**	2.33 sec.	-0.38 g	**1.12**	2.33 sec.	-0.42 g	**1.23**	2.41 sec.	-0.479 g	**1.41**
5.85 sec.	0.21 g	5.85 sec.	0.22 g	**1.05**	5.85 sec.	0.23 g	**1.10**	5.85 sec.	0.25 g	**1.19**	5.85 sec.	0.30 g	**1.42**	5.85 sec.	0.33 g	**1.57**
Accelerations at the Backfill																
M1		**M7**			**M8**			**M9**			**M10**			**M11**		
BASE INPUT		**H = 1.90 m L= 0.40 m**		**Amp.**	**H = 1.90 m L= 0.80 m**		**Amp.**	**H = 1.90 m L= 1.20 m**		**Amp.**	**H = 1.90 m L= 1.60 m**		**Amp.**	**H = 1.90 m L= 2.00 m**		**Amp.**
Time (sec.)	**Acc. (g)**	**Time (sec.)**	**Acc. (g)**		**Time (sec.)**	**Acc. (g)**		**Time (sec.)**	**Acc. (g)**		**Time (sec.)**	**Acc. (g)**		**Time (sec.)**	**Acc. (g)**	
0.98 sec.	-0.24 g	0.99 sec.	-0.23 g	**0.96**	1.00 sec.	-0.21 g	**0.85**	0.99 sec.	-0.24 g	**1.00**	0.99 sec.	-0.25 g	**1.03**	0.99 sec.	-0.24 g	**1.00**
1.09 sec.	0.29 g	1.08 sec.	0.37 g	**1.29**	1.08 sec.	0.34 g	**1.17**	1.08 sec.	0.37 g	**1.28**	1.08 sec.	0.34 g	**1.19**	1.08 sec.	0.32 g	**1.10**
1.67 sec.	0.29 g	1.68 sec.	0.40 g	**1.36**	1.68 sec.	0.35 g	**1.18**	1.68 sec.	0.39 g	**1.32**	1.68 sec.	0.39 g	**1.33**	1.68 sec.	0.37 g	**1.26**
2.32 sec.	-0.34 g	2.33 sec.	-0.40 g	**1.17**	2.33 sec.	-0.36 g	**1.06**	2.33 sec.	-0.43 g	**1.27**	2.33 sec.	-0.44 g	**1.31**	2.33 sec.	-0.43 g	**1.26**
5.85 sec.	0.21 g	5.85 sec.	0.29 g	**1.38**	5.85 sec.	0.25 g	**1.19**	5.85 sec.	0.30 g	**1.40**	5.85 sec.	0.31 g	**1.47**	5.85 sec.	0.30 g	**1.44**

Table 9.6. Accelerations observed at various locations of the GRS-RW for 2nd experiment 4th El-Centro excitation

2nd Experiment 4th El-Centro 100% Excitation																
Accelerations at the Facing Block																
M1		**M2**			**M3**			**M4**			**M5**			**M6**		
BASE INPUT		**H = 0.17 m**		**Amp.**	**H = 0.57 m**		**Amp.**	**H = 1.07 m**		**Amp.**	**H = 1.57 m**		**Amp.**	**H = 1.77 m**		**Amp.**
Time (sec.)	**Acc. (g)**	**Time (sec.)**	**Acc. (g)**		**Time (sec.)**	**Acc. (g)**		**Time (sec.)**	**Acc. (g)**		**Time (sec.)**	**Acc. (g)**		**Time (sec.)**	**Acc. (g)**	
0.98 sec.	-0.267 g	0.98 sec.	-0.25 g	**0.92**	0.98 sec.	-0.29 g	**1.10**	0.98 sec.	-0.31 g	**1.18**	0.98 sec.	-0.34 g	**1.27**	1.00 sec.	-0.37 g	**1.40**
1.10 sec.	0.23 g	1.10 sec.	0.25 g	**1.06**	1.09 sec.	0.28 g	**1.19**	1.09 sec.	0.30 g	**1.28**	1.10 sec.	0.35 g	**1.53**	1.10 sec.	0.43 g	**1.84**
1.74 sec.	0.26 g	1.74 sec.	0.27 g	**1.05**	1.74 sec.	0.29 g	**1.12**	1.74 sec.	0.30 g	**1.16**	1.75 sec.	0.34 g	**1.33**	1.75 sec.	0.37 g	**1.47**
5.79 sec.	-0.24 g	5.79 sec.	-0.26 g	**1.06**	5.79 sec.	-0.27 g	**1.10**	5.79 sec.	-0.28 g	**1.14**	5.80 sec.	-0.31 g	**1.29**	5.80 sec.	-0.35 g	**1.44**
5.85 sec.	0.272 g	5.85 sec.	0.28 g	**1.04**	5.85 sec.	0.30 g	**1.12**	5.85 sec.	0.33 g	**1.23**	5.85 sec.	0.42 g	**1.55**	5.85 sec.	0.52 g	**1.90**
Accelerations at the Backfill																
M1		**M7**			**M8**			**M9**			**M10**			**M11**		
BASE INPUT		**H = 1.90 m L= 0.40 m**		**Amp.**	**H = 1.90 m L= 0.80 m**		**Amp.**	**H = 1.90 m L= 1.20 m**		**Amp.**	**H = 1.90 m L= 1.60 m**		**Amp.**	**H = 1.90 m L= 2.00 m**		**Amp.**
Time (sec.)	**Acc. (g)**	**Time (sec.)**	**Acc. (g)**		**Time (sec.)**	**Acc. (g)**		**Time (sec.)**	**Acc. (g)**		**Time (sec.)**	**Acc. (g)**		**Time (sec.)**	**Acc. (g)**	
0.98 sec.	-0.27 g	1.00 sec.	-0.32 g	**1.19**	0.98 sec.	-0.29 g	**1.08**	0.98 sec.	-0.34 g	**1.28**	0.98 sec.	-0.35 g	**1.30**	0.98 sec.	-0.33 g	**1.25**
1.09 sec.	0.23 g	1.10 sec.	0.35 g	**1.53**	1.10 sec.	0.30 g	**1.30**	1.10 sec.	0.32 g	**1.39**	1.09 sec.	0.34 g	**1.45**	1.09 sec.	0.32 g	**1.39**
1.67 sec.	0.26 g	1.76 sec.	0.33 g	**1.29**	1.76 sec.	0.29 g	**1.15**	1.76 sec.	0.33 g	**1.31**	1.76 sec.	0.34 g	**1.34**	1.76 sec.	0.33 g	**1.29**
2.32 sec.	-0.24 g	5.80 sec.	-0.29 g	**1.21**	5.80 sec.	-0.26 g	**1.07**	5.79 sec.	-0.31 g	**1.27**	5.79 sec.	-0.33 g	**1.37**	5.79 sec.	-0.34 g	**1.38**
5.85 sec.	0.272 g	5.85 sec.	0.39 g	**1.44**	5.86 sec.	0.37 g	**1.37**	5.86 sec.	0.39 g	**1.43**	5.85 sec.	0.35 g	**1.29**	5.85 sec.	0.35 g	**1.27**

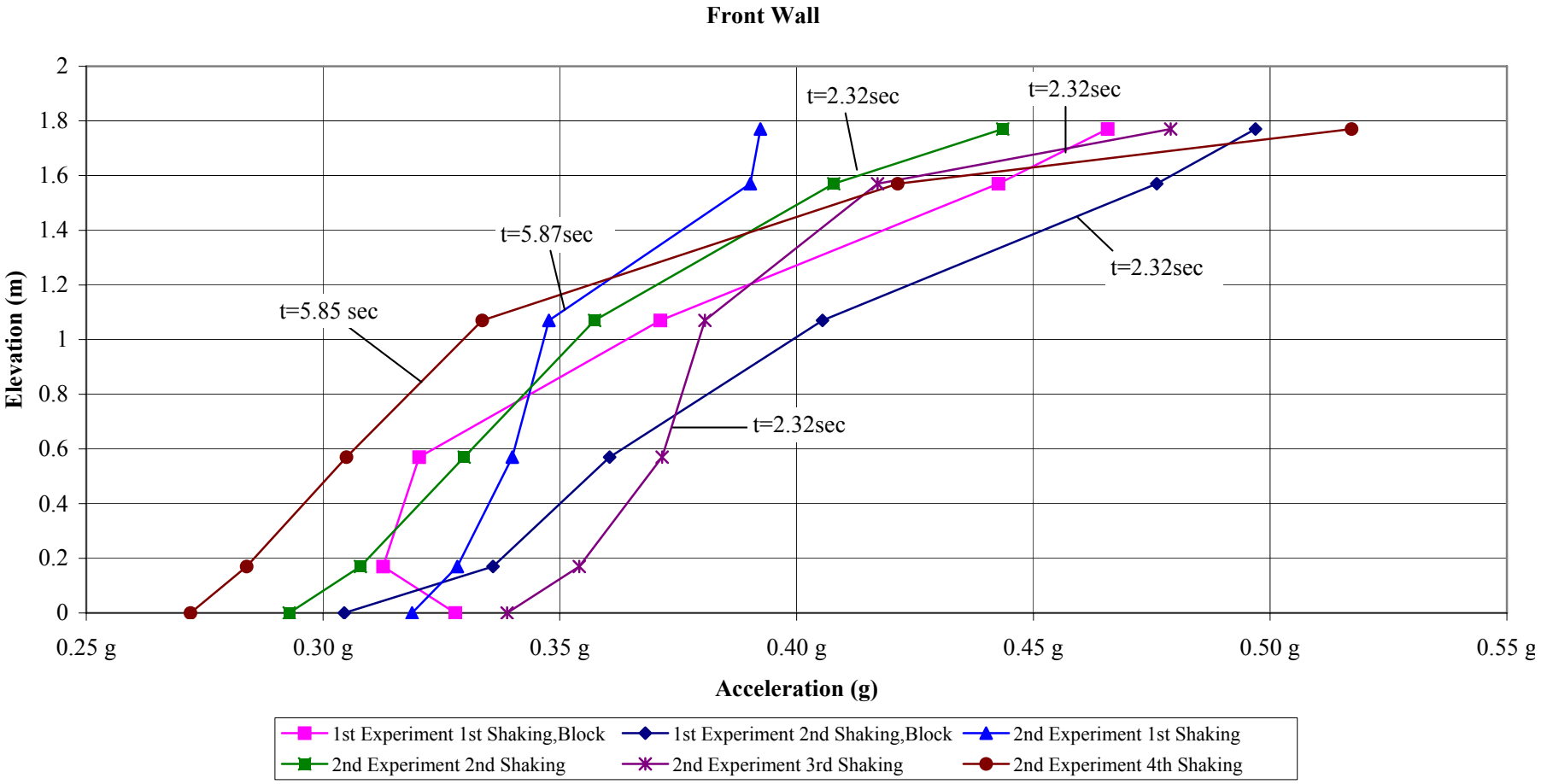

Figure 9.1. Accelerations observed on the front wall

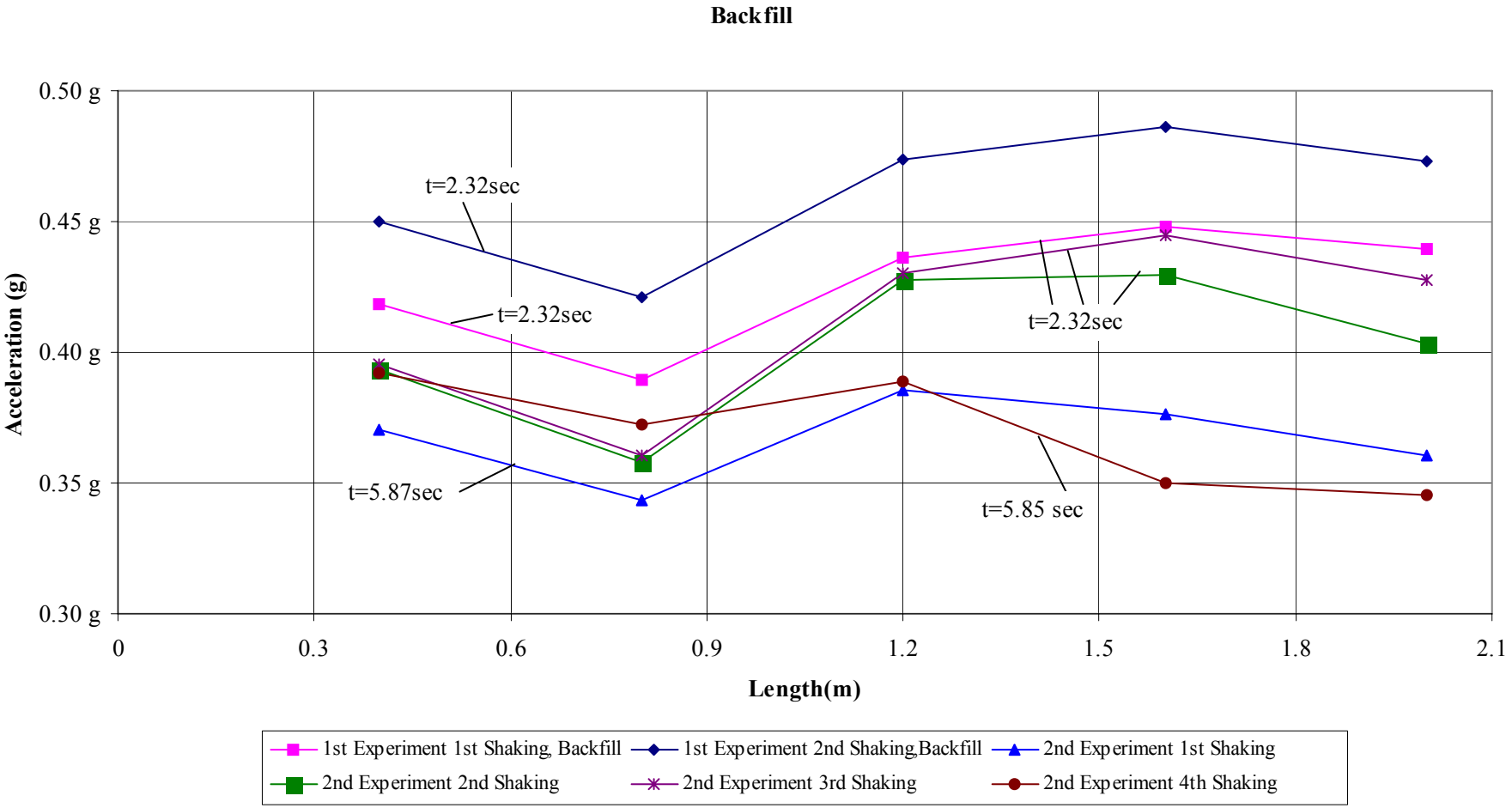

Figure 9.2. Accelerations observed on top of the backfill

As a conclusion of the acceleration amplification factor calculations it can be stated that the maximum amplification factor (the ratio of the maximum acceleration in the structure to the peak input base acceleration) increased with increased height. This was observed both on the front wall and on top of the backfill as expected. While the maximum amplification observed on the front wall for the first experiment varied between 1.42 and 1.63, for the second experiment the values between 1.21 and 1.9 were obtained. Similarly, on top of the backfill for the 1st experiment the maximum acceleration amplification factors observed were 1.37 and 1.6 for the 1st experiment and 1.21 and 1.47 in the 2nd.

Generally, after the successive shakings higher acceleration amplification factors were observed both on the front wall and on top of the backfill when considered with the previous shaking values. By taking into account the well known phenomenon of significant settlement of the dry or moist cohesionless soil deposits as a result of the compaction induced by the ground shaking [29] and also the results of new researches on drained triaxial extension tests showing that the induced maximum volumetric contraction value in extension is much more greater than the maximum value measured in compression [30], it can be stated that at the end of every shaking, sandy soil was in fact compacted to a higher relative density level and thus this densified, stiffer soil caused higher amplification factor values in the structure than the previous observed values. While stiff soils are strong and tend to amplify the accelerations, soft soils are ideal dampers and they decrease the acceleration amplification [31]. The maximums in the two experiments for every shaking were evaluated to be as in Table 9.7.

Table 9.7. Maximum acceleration amplification factors observed at El-Centro excitations

Experiments	Location	1st Shaking	2nd Shaking	3rd Shaking	4th Shaking
1st Experiment	Facing Block (at H=1.77 m)	1.42	1.63		
	Backfill (at H=1.90 m)	1.37	1.6		
2nd Experiment	Facing Block (at H=1.77 m)	1.23	1.51	1.41	1.9
	Backfill (at H=1.90 m)	1.21	1.47	1.31	1.44

9.2. Strain Measurement & Evaluation Study

It is of importance to note that the DAQ system was operated only during the dynamic excitations, so during the experiments merely the dynamic strains were measured

and evaluated in the experiments. As a result, all of the following data are related to the dynamic behavior.

9.2.1. Instrumentation and Geotextile Measurement Locations for 1st Exp. (L/H=0.9)

The instrumentation of the geotextile and the locations from where the displacement measurements recorded in the 1st Experiment are illustrated in Figure 9.3.

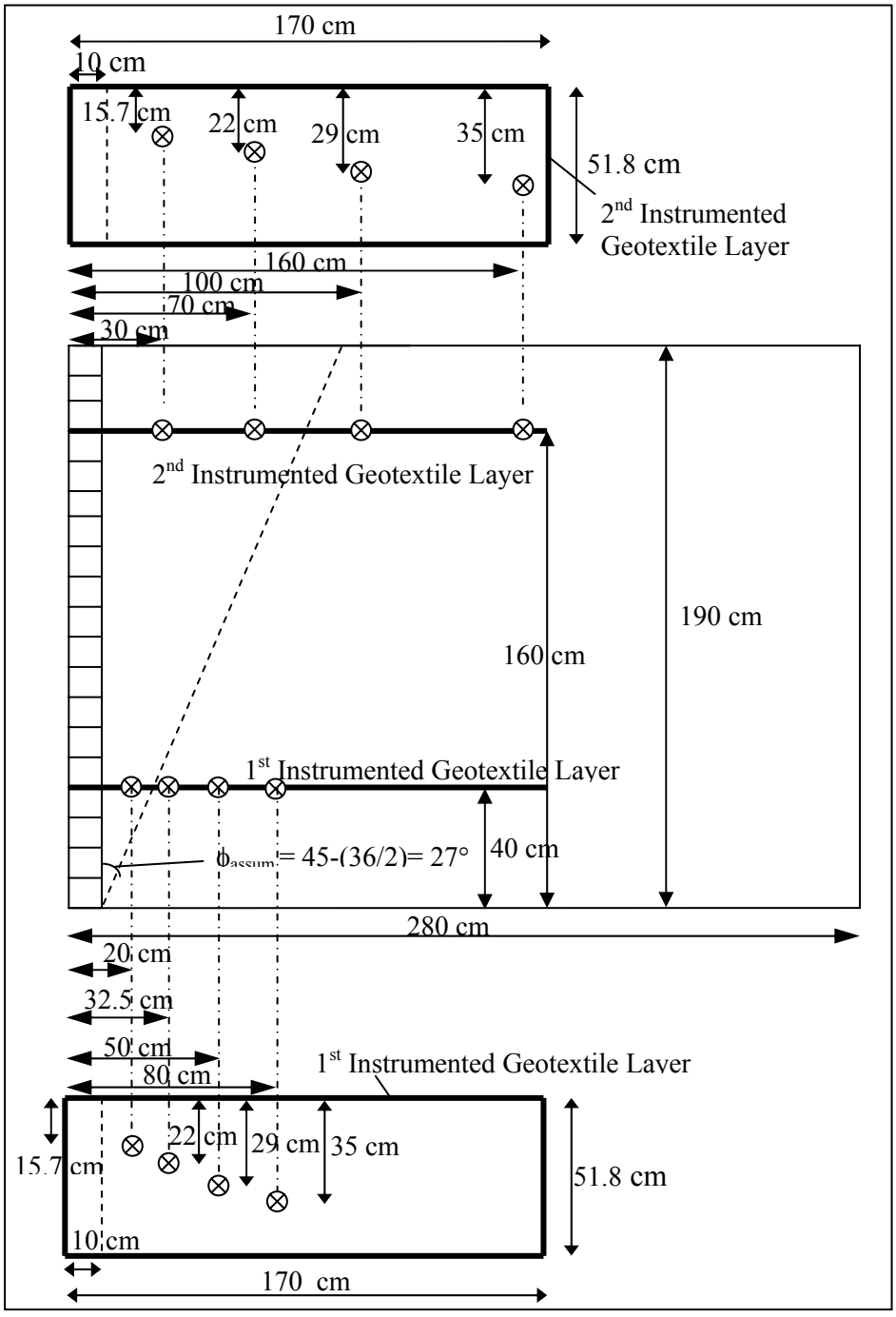

Figure 9.3. A general view of the instrumented geotextiles of the 1st experiment

9.2.1.1. Sine Wave Excitation. The displacement-time history record of the sine wave motion can be seen in Figure 9.4. Since this was the 1st motion applied to the structure for trial purposes it took approximately 500 sec. to reach to the peak amplitude and the excitation lasted for about 600 sec.

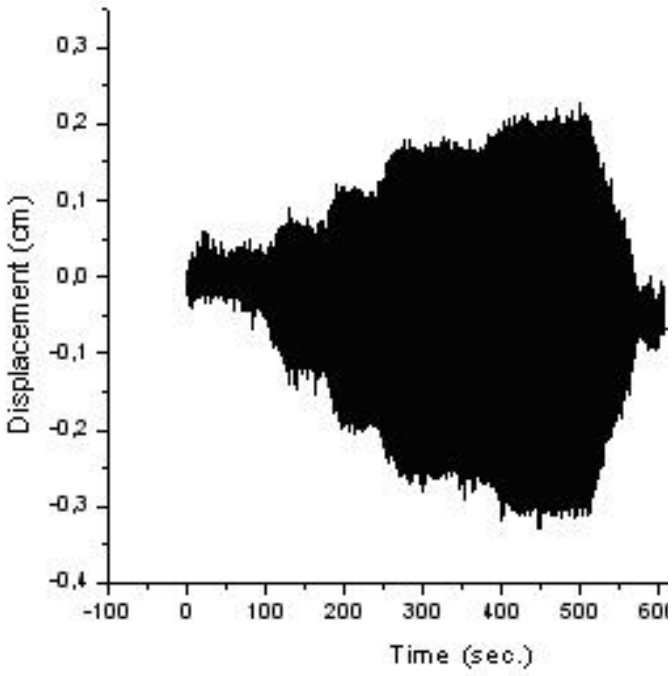

Figure 9.4. 1st Experiment sinusoidal motion excitation record

Not only the peak relative displacements (relative to base displacement) and the corresponding strains developed at these time instances are evaluated but also strain-time history curves are plotted in order to better understand the deformation behavior of the geotextiles. The peak relative displacements in both directions (positive and negative) were calculated to be as in Table 9.8 and in Figures 9.5 to 9.7 after subtracting the shaking table's displacements from the displacements observed at the locations of the geotextile members. The peak relative displacement time instances didn't coincide between the two layers of the geotextiles, so the relative displacements for the time instances where there were not any peak relative displacement observed on the other layer were also calculated in order to compare the displacement behavior of the layers (i.e. t= 289.05 sec. and t = 478.07 sec. at H=40 cm level in Table 9.8). Figures 9.5 to 9.7 indicate that during the excitation, not only tensile forces but also compression forces acted on the geotextile members.

Table 9.8. Peak relative displacements observed on the geotextile reinforcements at the sine motion of the 1st experiment (units are in cm)

Peak Relative Displacements (1st Experiment Random Sine Motion)								
H= 160 cm	**Trans. 8**		**Trans. 7**		**Trans. 6**		**Trans. 5**	
	L=30 cm		**L=70 cm**		**L=100 cm**		**L=160 cm**	
	Max. (1)	**Max. (2)**	**Max. (1)**	**Max. (2)**	**Max. (1)**	**Max. (2)**	**Max. (1)**	**Max. (2)**
t=289.04 sec	0.7319		0.7376		0.6920		0.7361	
t=418.85 sec	0.6718		0.6739		0.6123		0.6491	
t=441.15 sec		-0.8304		-0.8293		-0.7537		-0.7848
t=477.83 sec		-0.8635		-0.8692		-0.8122		-0.8241
H= 40 cm	**Trans. 4**		**Trans. 3**		**Trans. 2**		**Trans. 1**	
	L=20 cm		**L=32,5 cm**		**L=50 cm**		**L=80 cm**	
	Max. (1)	**Max. (2)**	**Max. (1)**	**Max. (2)**	**Max. (1)**	**Max. (2)**	**Max. (1)**	**Max. (2)**
t=289.05 sec	0.4595		0.3818		0.3636		0.4755	
t=411.94 sec	0.4942		0.4092		0.3714		0.5289	
t=418.87 sec	0.4952		0.3942		0.3828		0.5299	
t=467.1 sec		-0.4185		-0.3797		-0.3424		-0.4015
t=478.08 sec		-0.3388		-0.3699		-0.3372		-0.3538
t=490.23 sec		-0.3983		-0.3543		-0.3129		-0.3631

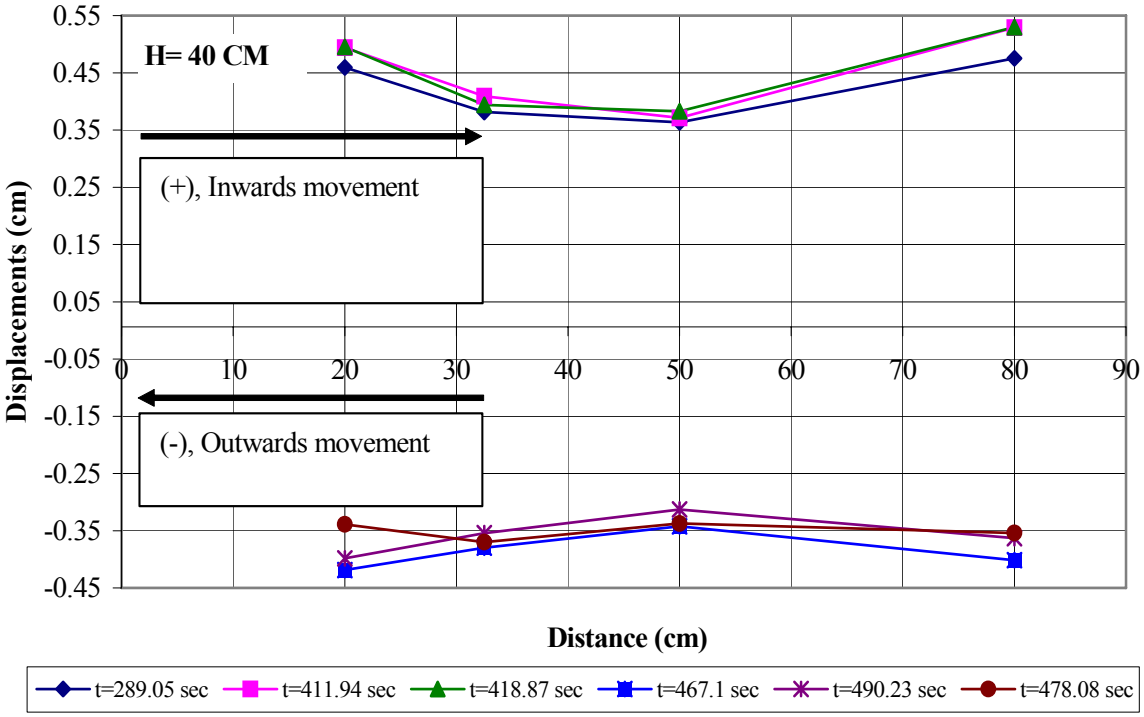

Figure 9.5. Peak relative displacements measured on the geotextile reinforcement at H=40 cm in the sine motion of the 1st experiment

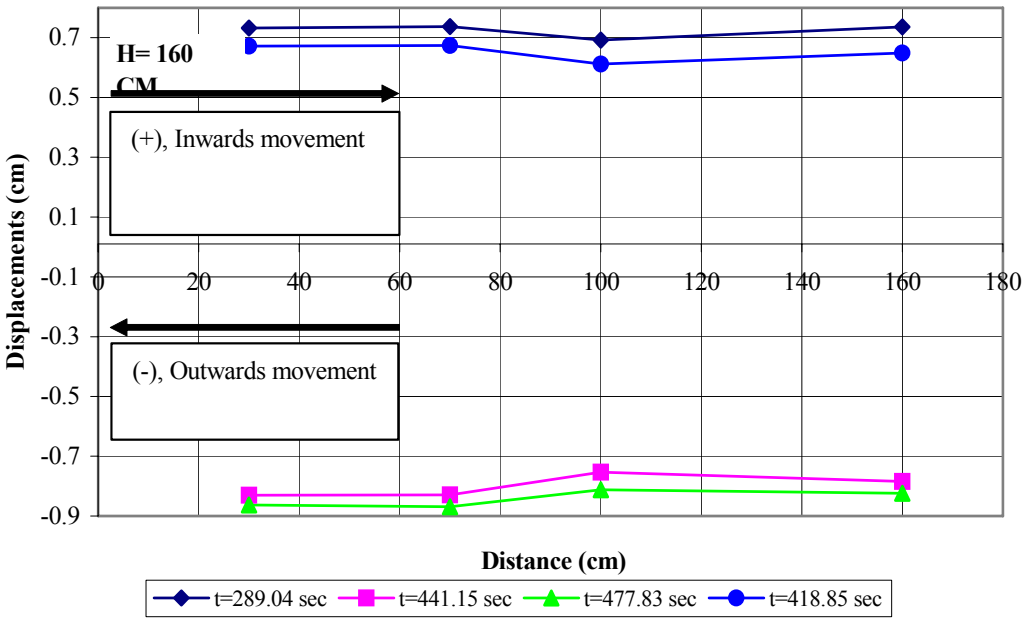

Figure 9.6. 1st experiment sine motion excitation, peak relative displacements measured on the geotextile reinforcement at H=160 cm

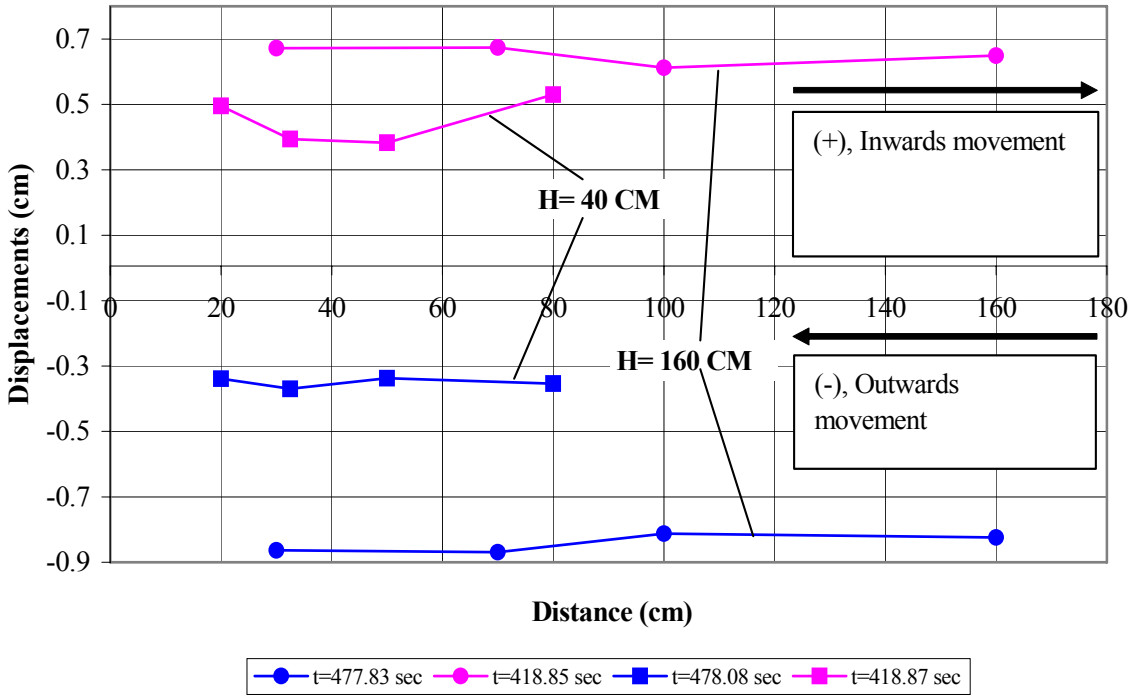

Figure 9.7. Comparisons of peak relative displacements measured on the geotextile reinforcement at H=40 cm and H=160 cm for 1st experiment sine motion excitation

In every layer, by measuring four displacements from four locations on the geotextile members an average strain in three regions can be determined. The average strains were

evaluated by dividing the differences of the relative displacements between the locations where the relative displacements were measured, to the distances between each measurement locations. In Table 9.9 and in Figures 9.8 and 9.9, calculated average strains according to the maximum relative displacements can be seen. Regions 20 – 32.5, 32.5 – 50, 50 – 80, 30 – 70, 70 – 100, 100 – 160 represent the areas between the measurement locations. While positive values represent tensile strains, negative strains denote for the pseudo-compressive strains considering the fact that geotextile members cannot transfer compressive forces. As a result, folding of the reinforcement was the phenomenon when the reinforcements were subjected to compressions during the excitation.

Table 9.9. Calculated average strain values on the geotextile reinforcements at the sine motion excitation of the 1st experiment

H= 160 cm	**Regions between the measurement locations**		
	30 - 70	**70 - 100**	**100 - 160**
t=289.04 sec	0.0001	-0.0015	0.0007
t=418.85 sec	0.0001	-0.0021	0.0006
t=441.15 sec	0.0000	0.0025	-0.0005
t=477.83 sec	-0.0001	0.0019	-0.0002
H= 40 cm	**Regions between the measurement locations**		
	20 – 32.5	**32.5 - 50**	**50 - 80**
t=289.05 sec	-0.0062	-0.0010	0.0037
t=411.94 sec	-0.0068	-0.0022	0.0052
t=418.87 sec	-0.0081	-0.0007	0.0049
t=467.1 sec	0.0031	0.0021	-0.0020
t=478.08 sec	-0.0025	0.0019	-0.0006
t=490.23 sec	0.0035	0.0024	-0.0017

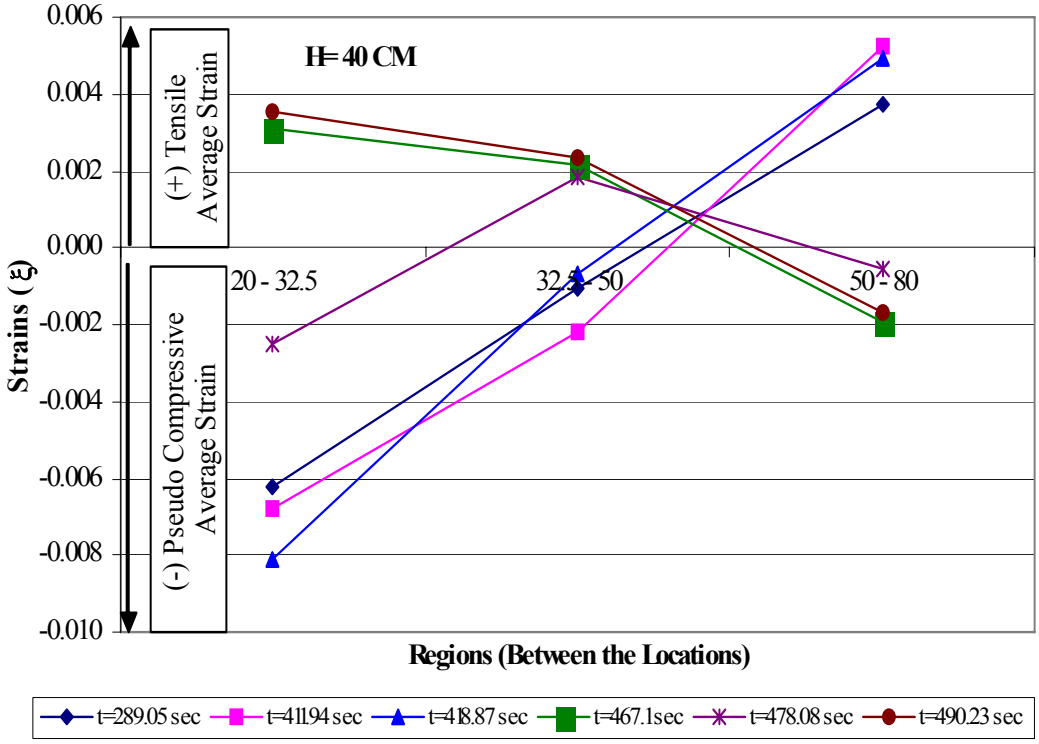

Figure 9.8. Average strains measured on the geotextile reinforcement at the regions between the measurement locations of the 1st experiment sine motion excitation at the level H = 40 cm

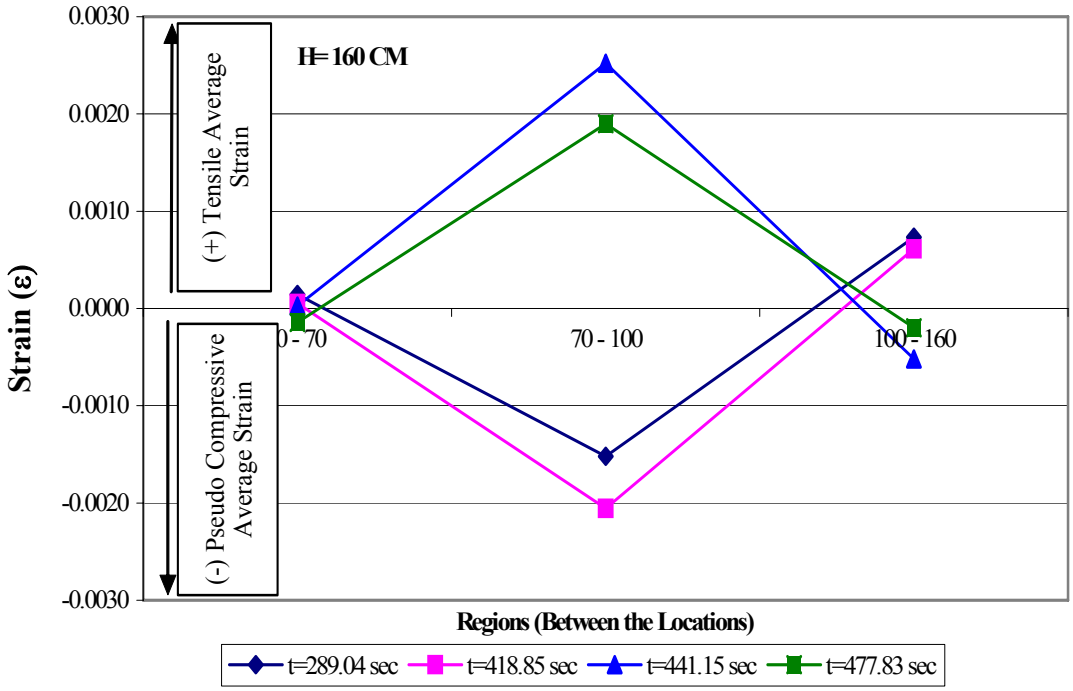

Figure 9.9. Average strains measured on the geotextile reinforcement at the regions between the measurement locations of the 1st experiment sine motion excitation at the level H = 160 cm

Presented in Figures 9.10 and 9.11 are the average-strain time history records of the geotextile members at the regions between the measurement locations mentioned previously. It can be seen from the figures that the strains developed at different regions at the same time interval have a different manner between each other. This is probably due to the pressure wave propagating within the wall, which causes compressional and dilatational zones in the fill.

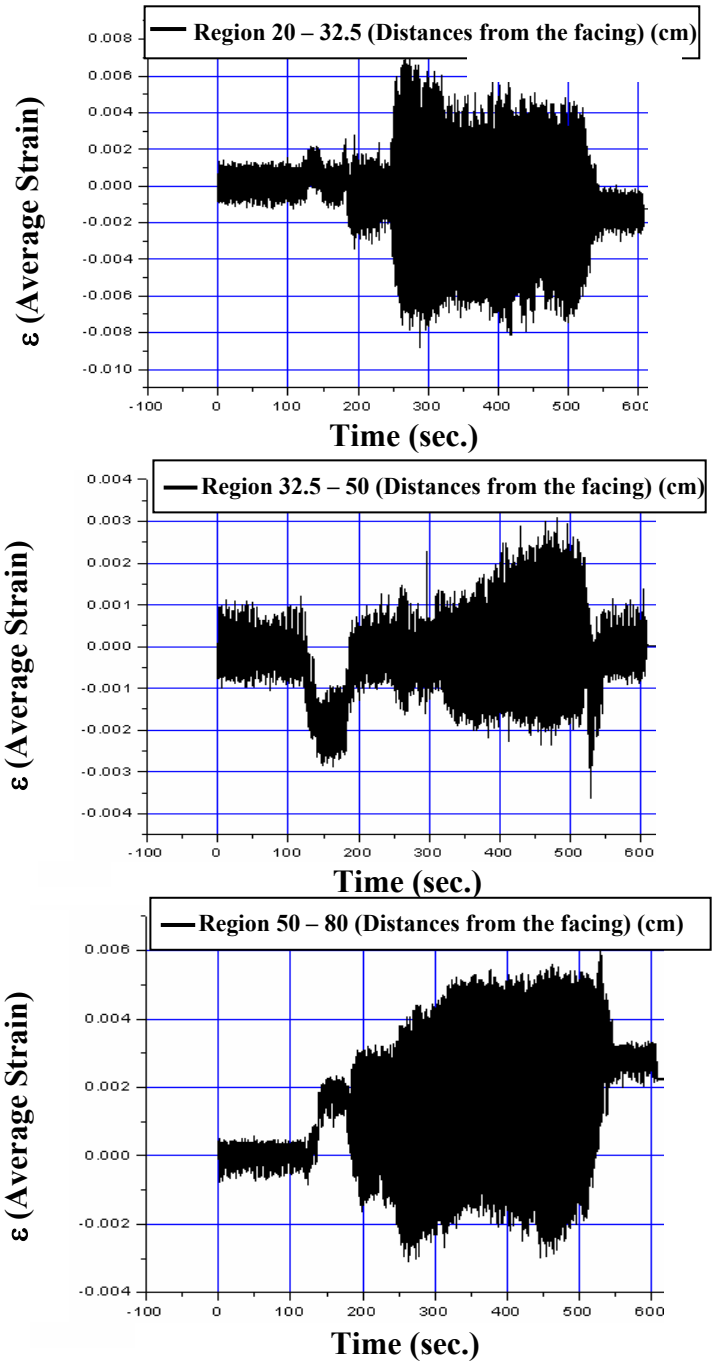

Figure 9.10. Average strains measured on the geotextile reinforcement at the regions in the 1st experiment Sine Motion excitation at level H=40 cm

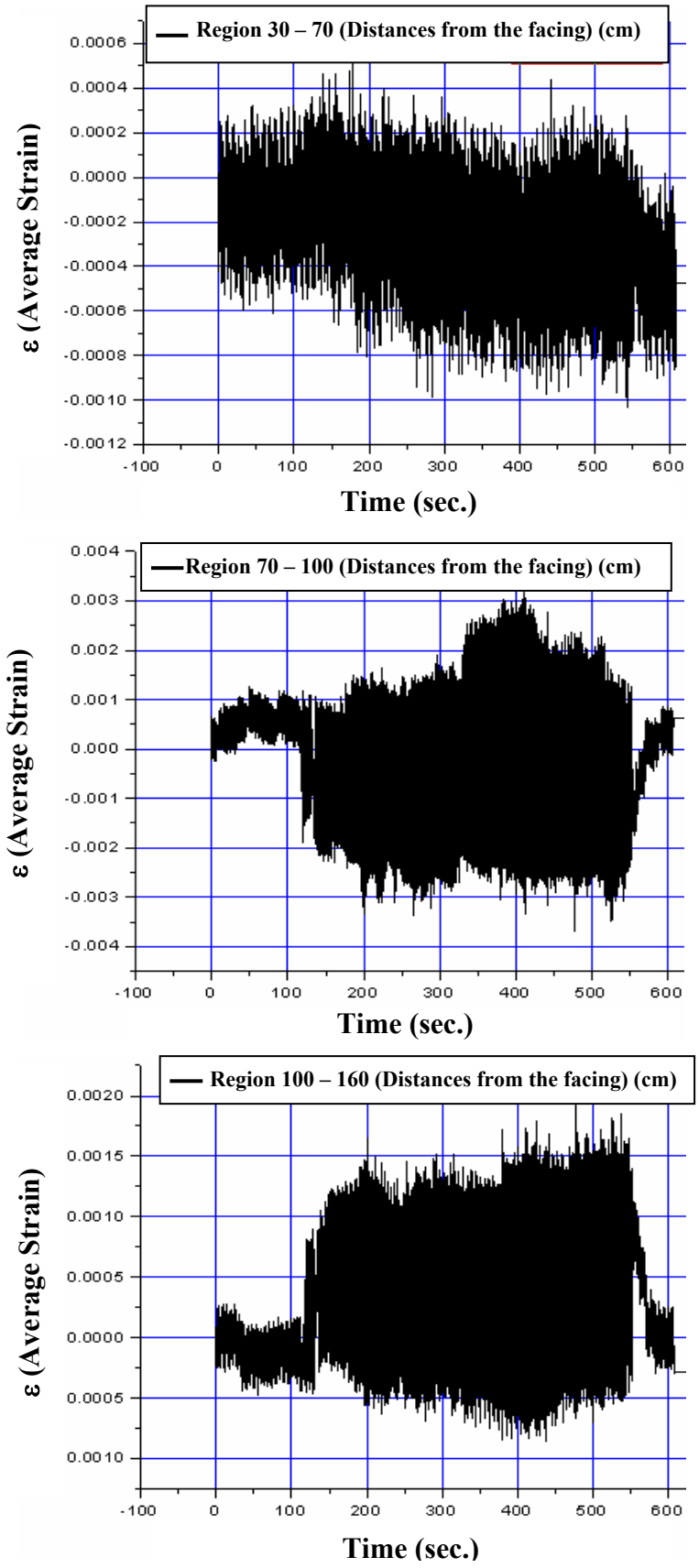

Figure 9.11. Average strains measured on the geotextile reinforcement at the regions in the 1st experiment Sine Motion excitation at level H=160 cm

Figures 9.12 and 9.13 demonstrate the deformation behavior in all of the regions between a short time interval (t=300 sec.- t=305 sec.) at levels H=40 cm and H=160 cm, respectively. At level H=40 cm direct opposite curves are observed between the regions 20-32.5 cm and 32.5-50, 50-80 cm, respectively. As stated previously, this is considered to be the demonstration of the propagating behavior of a pressure wave. (Figure 9.12).

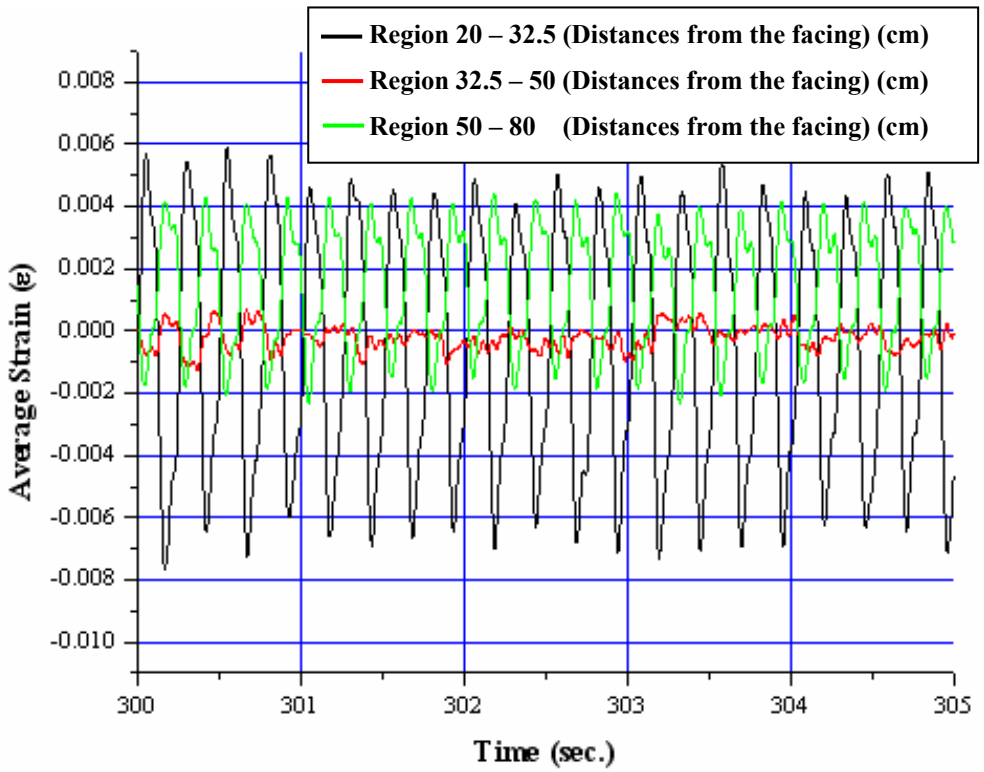

Figure 9.12. Average strains measured on the geotextile reinforcement for the time interval between t= 300 sec. and t=305 sec. at level H=40 cm

Also, at level H=160 cm direct opposite curves are observed between the regions 70-100 cm and 100-160 cm indicating that alternating compressional and dilatational forces were active, which is a typical phenomenon of the pressure waves (Figure 9.13). Because the region 30-70 cm is situated close to the facing wall and far away from the critical failure surface lower level of strains were measured as expected.

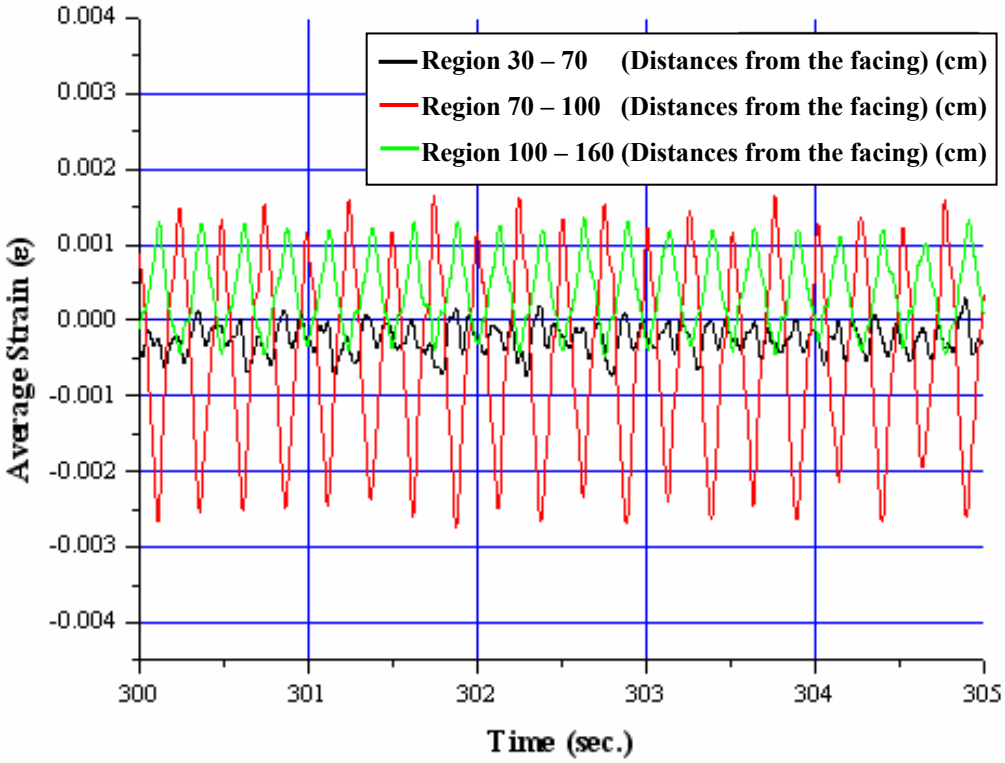

Figure 9.13. Average strains measured on the geotextile reinforcement for the time interval between t= 300 sec. and t=305 sec. at level H=160 cm

9.2.1.2. 1st El-Centro Motion Excitation. The acceleration-time history curve and displacement-time history curve of the scaled El-Centro earthquake base excitation are illustrated in Figure 9.14.

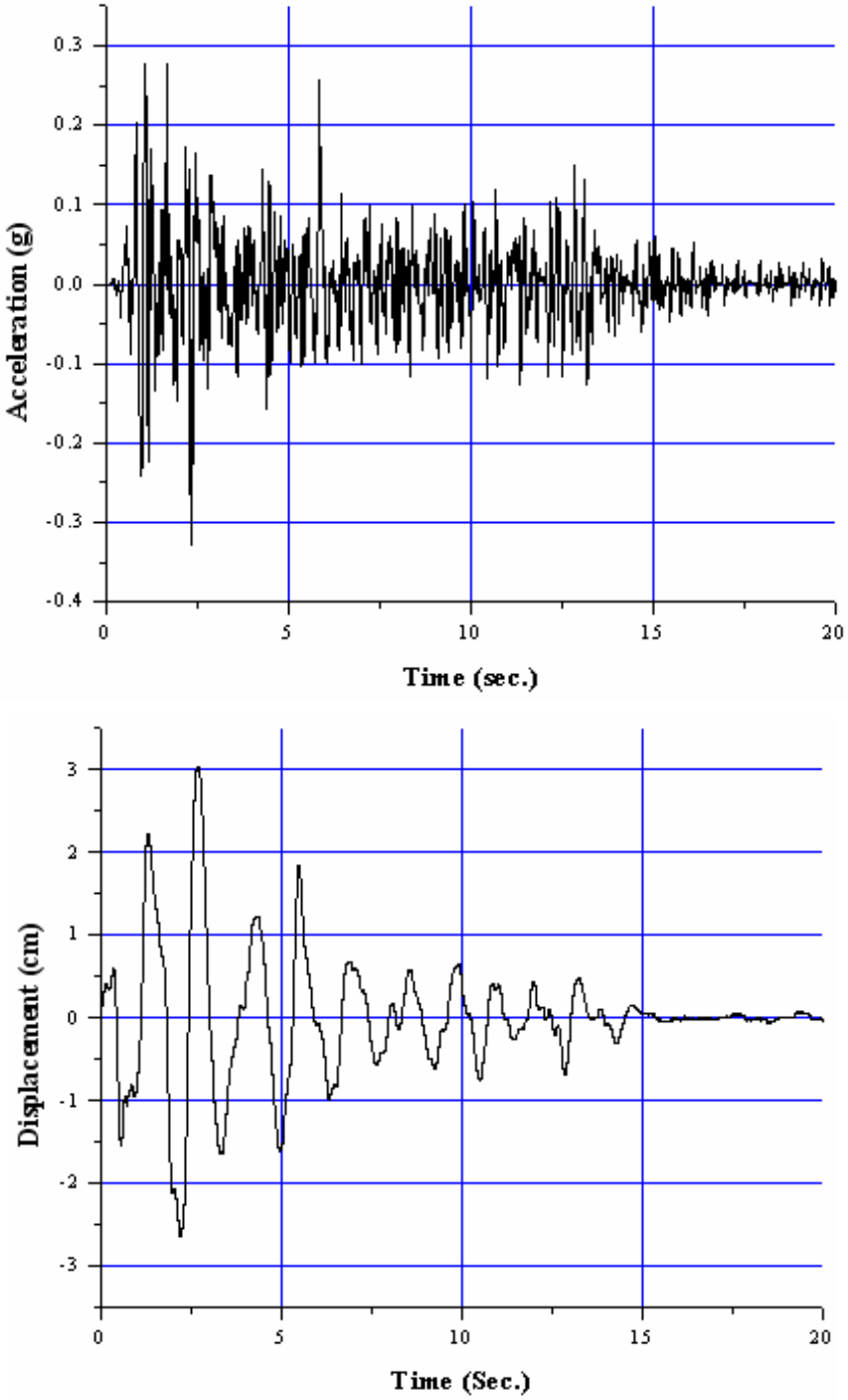

Figure 9.14. 1st El Centro motion excitation

The peak relative displacements in both directions were calculated to be as in Table 9.10 and in Figures 9.15 to 9.17. Since the peak relative displacement time instances didn't coincide between the two layers of the geotextiles, the displacements for the time instances where there were not any peak relative displacement observed on the other layer were also calculated in order to compare the displacement behavior of the layers (i.e. t = 0.5 sec. at

H=40 cm level and t = 5.3 sec. at H=160 cm level in Table 9.10). Figures 9.15 to 9.17 indicate that during the excitation, not only tensile forces but also compression forces acted on the geotextile members.

Table 9.10. Peak relative displacements observed on the geotextile reinforcement at the 1st El Centro excitation of the 1st experiment (units are in cm)

Peak Relative Displacements (1st Experiment 1st EL CENTRO %100)								
H= 160 cm	**Trans. 8**		**Trans. 7**		**Trans. 6**		**Trans. 5**	
	L=30 cm		**L=70 cm**		**L=100 cm**		**L=160 cm**	
	Max.(1)	**Max.(2)**	**Max. (1)**	**Max. (2)**	**Max. (1)**	**Max.(2)**	**Max. (1)**	**Max.(2)**
t=0,544 sec	0.3973		0.3206		0.4346		0.4092	
t=1,16 sec		-0.3745		-0.3476		-0.3543		-0.3294
t=1,8 sec	0.2398		0.1709		0.3061		0.2616	
t=2,134 sec	0.3025		0.3124		0.3776		0.3082	
t=2,4 sec		-0.3481		-0.3300		-0.3926		-0.3450
t=3,26 sec	0.3683		0.3574		0.3947		0.3704	
t=4,16 sec		-0.2968		-0.2958		-0.2844		-0.2559
t=5,3 sec		-0.2497		-0.2574		-0.2802		-0.2300
H= 40 cm	**Trans. 4**		**Trans. 3**		**Trans. 2**		**Trans. 1**	
	L=20 cm		**L=32,5 cm**		**L=50 cm**		**L=80 cm**	
	Max.(1)	**Max.(2)**	**Max. (1)**	**Max. (2)**	**Max. (1)**	**Max.(2)**	**Max. (1)**	**Max.(2)**
t=0,5sec	0.1621		0.1461		0.3958		0.2155	
t=1,8 sec	0.3403		0.2875		0.4108		0.3585	
t=2,134 sec	0.3398		0.3139		0.4191		0.4066	
t=2,4 sec		-0.4092		-0.4134		-0.5170		-0.4206
t=3,26 sec	0.3849		0.3434		0.4289		0.4175	
t=4,16 sec		-0.4496		-0.4372		-0.5149		-0.4398
t=5,3 sec		-0.4678		-0.4564		-0.5164		-0.4201

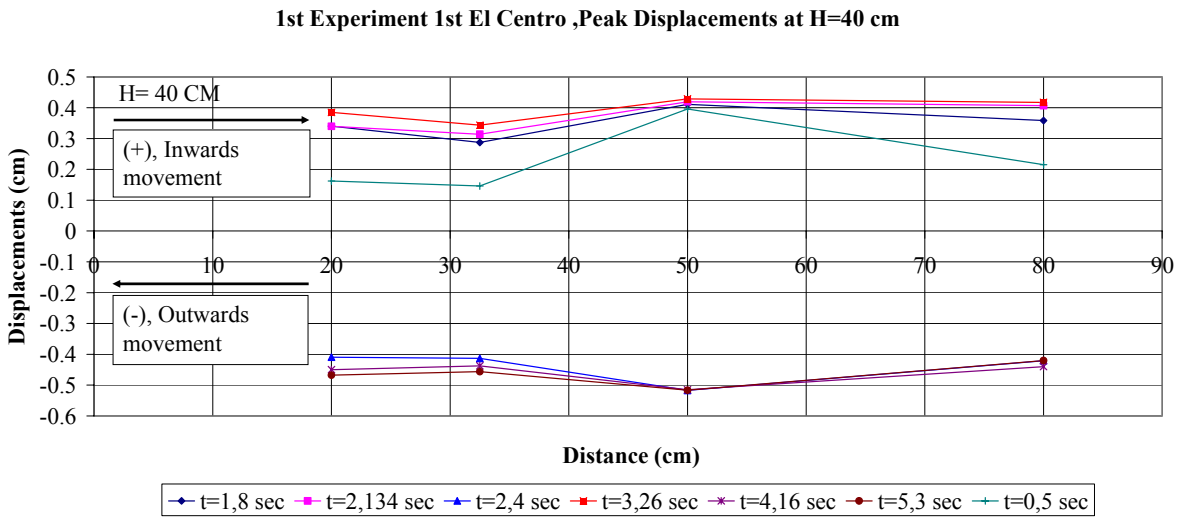

Figure 9.15. Peak relative displacements measured on the geotextile reinforcement at H = 40 cm in 1st El Centro excitation of the 1st experiment

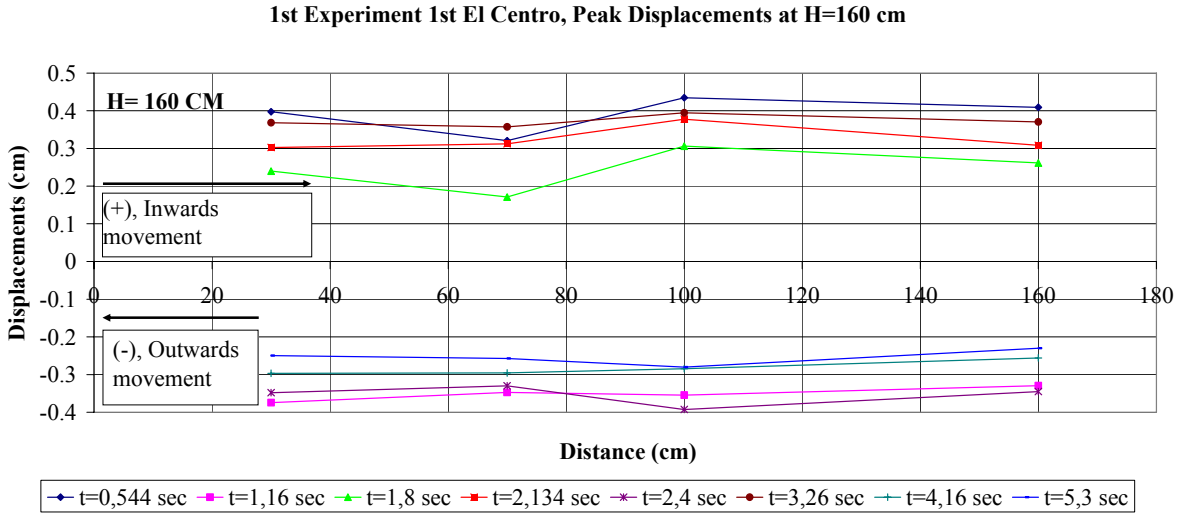

Figure 9.16. Peak relative displacements measured on the geotextile reinforcement at H = 160 cm in 1st El Centro excitation of the 1st experiment

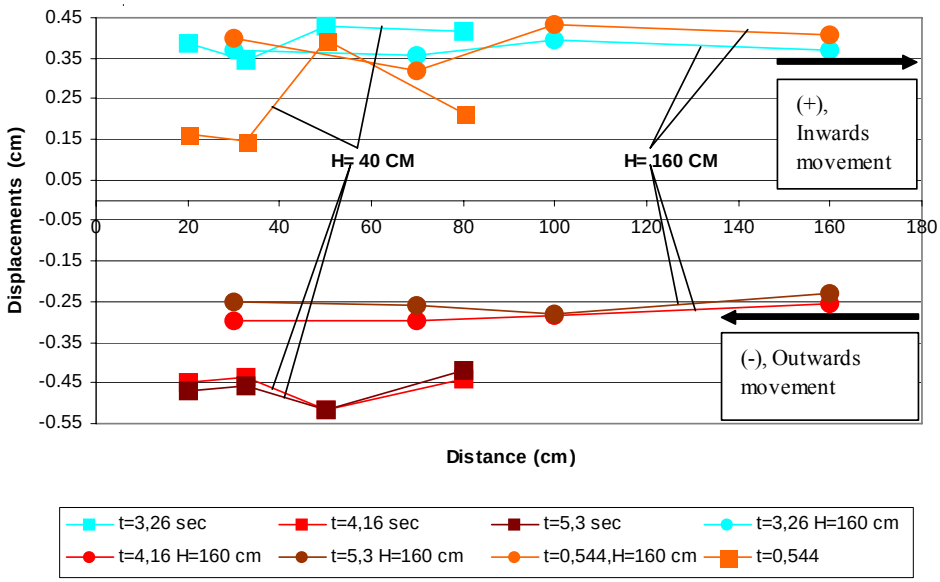

Figure 9.17. Comparisons of peak relative displacements measured on the geotextile reinforcements at H=40 cm and H=160 cm for the 1st El Centro excitation of the 1st experiment

In Table 9.11 and in Figures 9.18 and 9.19, calculated average strains according to the maximum relative displacements can be seen.

Table 9.11. Calculated average strain values on the geotextile reinforcements at the 1st El Centro excitation of the 1st experiment

H= 160 cm	**Regions between the measurement locations**		
	30 - 70	**70 - 100**	**100 - 160**
t=0.544 sec	-0.0019	0.0038	-0.0004
t=1.16 sec	0.0007	-0.0002	0.0004
t=1.8 sec	-0.0017	0.0045	-0.0007
t=2.134 sec	0.0002	0.0022	-0.0012
t=2.4 sec	0.0005	-0.0021	0.0008
t=3.26 sec	-0.0003	0.0012	-0.0004
t=4.16 sec	0.0000	0.0004	0.0005
t=5.3 sec	-0.0002	-0.0008	0.0008
H= 40 cm	**Regions between the measurement locations**		
	20 - 32.5	**32.5 - 50**	**50 - 80**
t=0.5 sec	-0.0013	0.0143	-0.0060
t=1.8 sec	-0.0042	0.0070	-0.0017
t=2.134 sec	-0.0021	0.0060	-0.0004
t=2.4 sec	-0.0003	-0.0059	0.0032
t=3.26 sec	-0.0033	0.0049	-0.0004
t=4.16 sec	0.0010	-0.0044	0.0025
t=5.3 sec	0.0009	-0.0034	0.0032

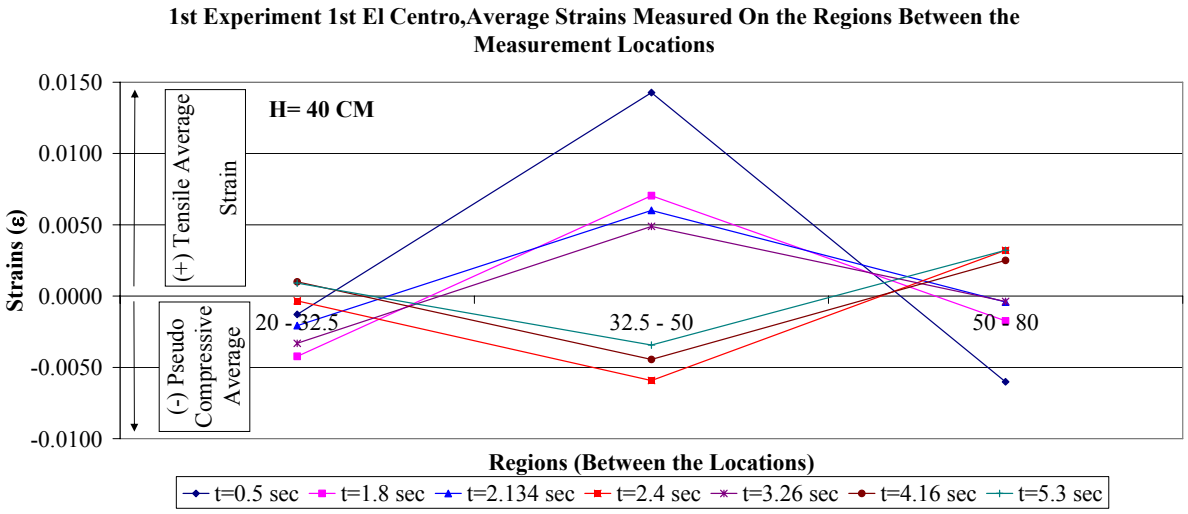

Figure 9.18. Average strains measured on the geotextile reinforcement at the regions between the measurement locations of the1st experiment 1st El Centro excitation at the level H = 40 cm

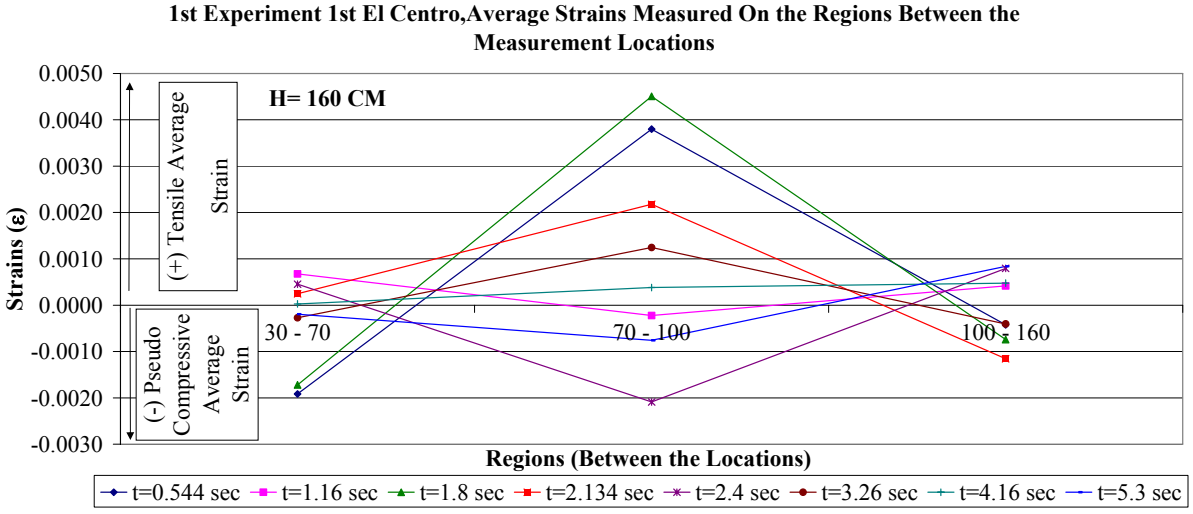

Figure 9.19. Average strains measured on the geotextile reinforcement at the regions between the measurement locations of the 1st experiment 1st El Centro excitation at the level H = 160 cm

Presented in Figures 9.20 and 9.21 are the calculated average-strain time history records of the geotextile members at the regions between the measurement locations mentioned previously.

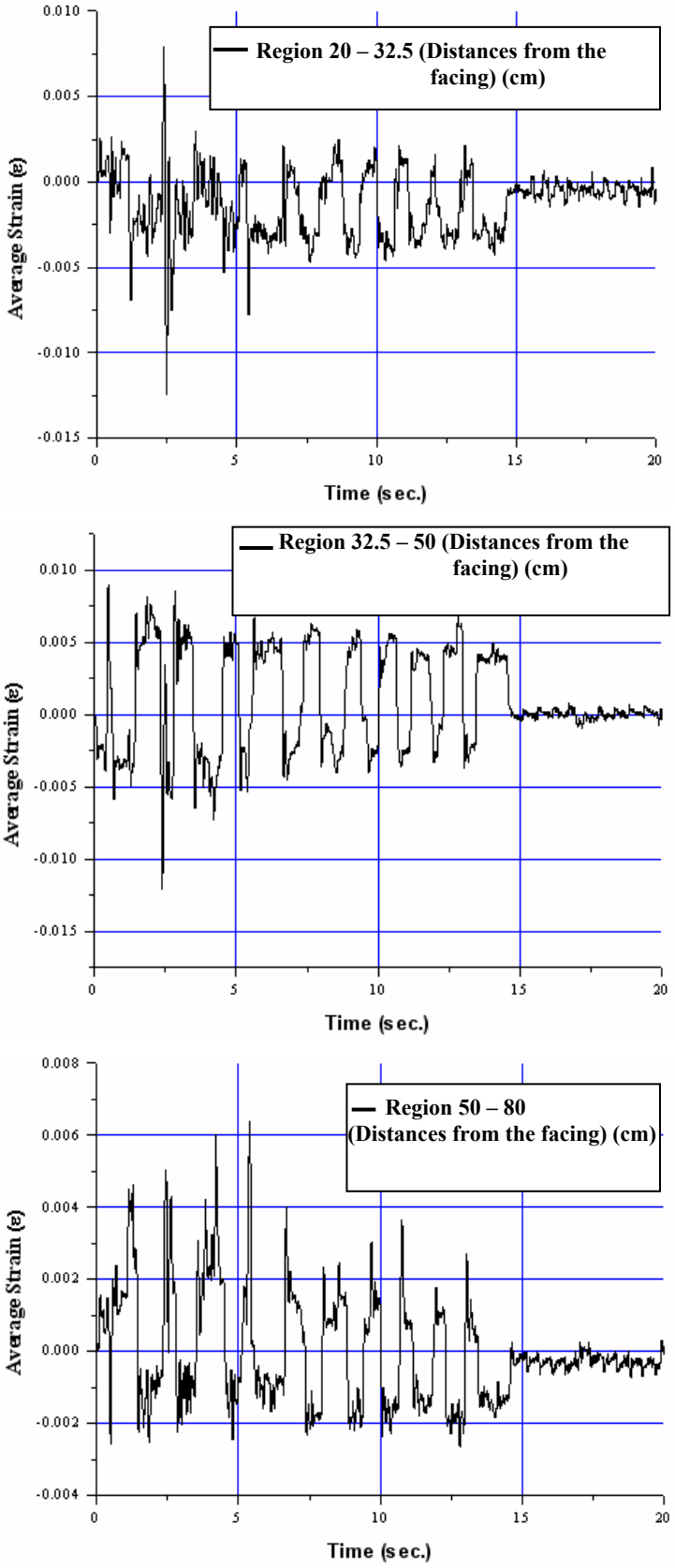

Figure 9.20. Average strains measured on the geotextile reinforcement at the regions in the 1st experiment 1st El Centro excitation at level H=40 cm

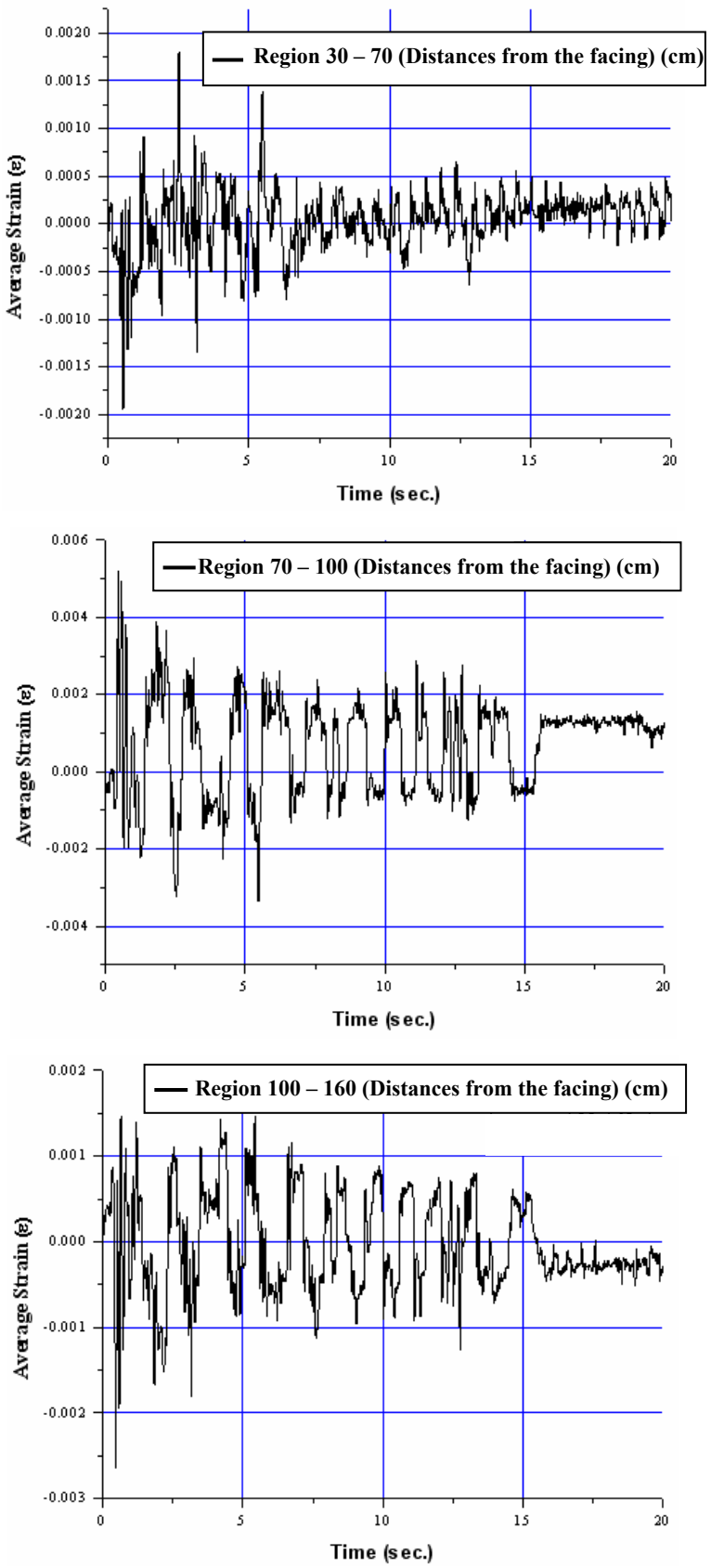

Figure 9.21. Average strains measured on the geotextile reinforcement at the regions in the 1st experiment 1st El Centro excitation at level H = 40 cm

Figures 9.22 and 9.23 demonstrate the deformation behavior in all of the regions at levels H=40 cm and H=160 cm, respectively. At level H=40 cm direct opposite curves are observed between the regions 32.5-50 and 50-80 cm, which shows the compressional and dilatational zones caused by the propagation of the pressure waves (Figure 9.22).

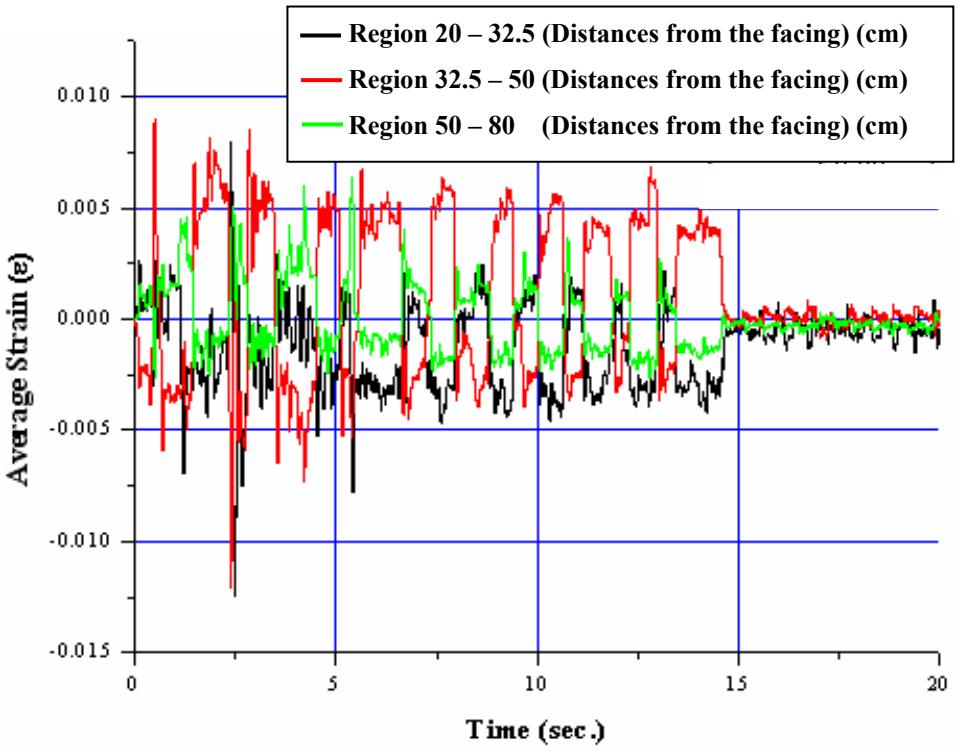

Figure 9.22. All the average strains measured on the geotextile reinforcement at the regions in the 1st experiment 1st El Centro excitation at level H = 40 cm

At level H=160 cm direct opposite curves are observed between the regions 70-100 cm and 100-160 cm (Figure 9.23). From this observation, again it can be deduced that compressive and tensile forces were active at the same time intervals in different regions of the geotextile due to the pressure waves. Because the region 30-70 cm is situated close to the facing wall and far away from the critical failure surface lower level of strains were measured as expected.

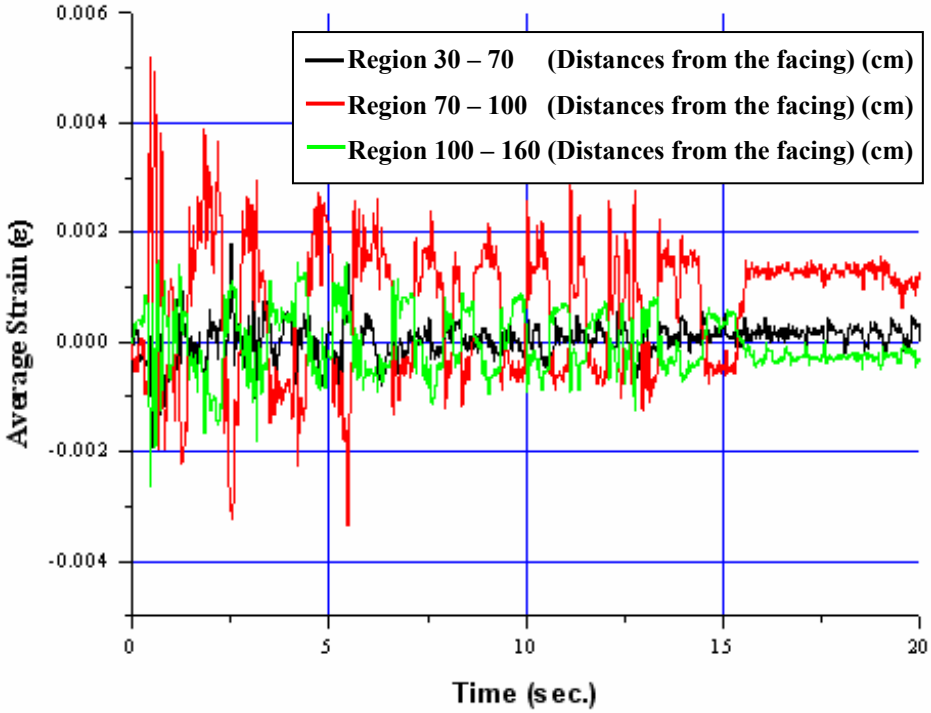

Figure 9.23. All the average strains measured on the geotextile reinforcement at the regions in the 1st experiment 1st El Centro excitation at level H = 160 cm

9.2.1.3. 2nd El-Centro Motion Excitation. Although in every excitation the input base acceleration-time history record was the same, there occurred minor changes in the acceleration amplitudes during the process of acquiring the signal by the servo-controller and controlling the actuator to match the signal. As a result, for every shaking base output motions are presented in this study. The base time-history motions for this excitation are shown in Figure 9.24.

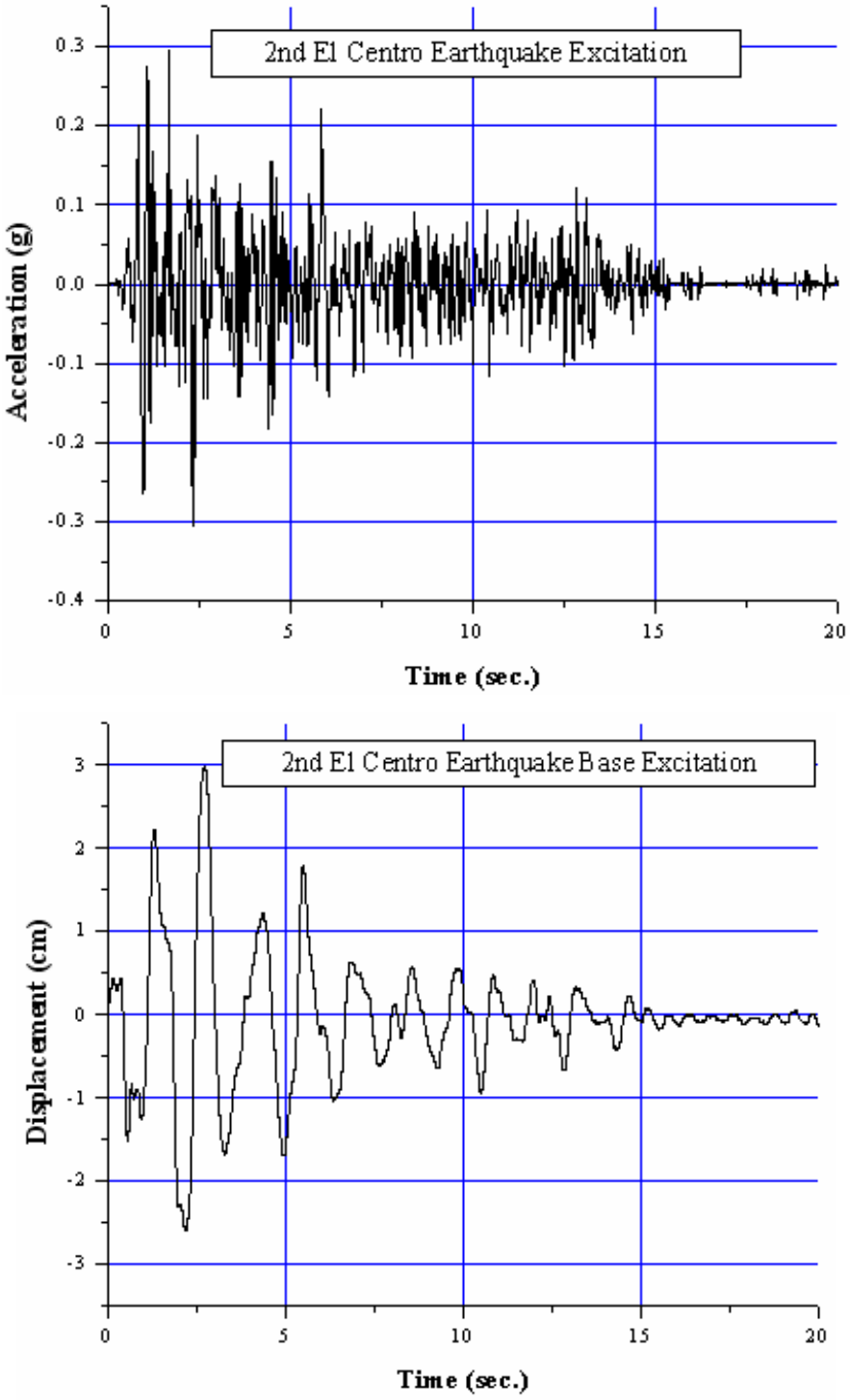

Figure 9.24. 2nd El Centro motion excitation

The peak relative displacements in both directions were calculated to be as in Table 9.12 and in Figures 9.25 to 9.27. Since the peak relative displacement time instances didn't coincide between the two layers of the geotextiles, the relative displacements for the time

instances where there were not any peak relative displacement observed on the other layer were also calculated in order to compare the displacement behavior of the layers.

Table 9.12. Peak relative displacements observed on the geotextile reinforcements at the 2nd El Centro excitation of the 1st experiment (units are in cm)

Peak Relative Displacements (1st Experiment 2nd EL CENTRO %100)								
H= 160 cm	**Trans. 8**		**Trans. 7**		**Trans. 6**		**Trans. 5**	
	L=30 cm		**L=70 cm**		**L=100 cm**		**L=160 cm**	
	Max.(1)	**Max.(2)**	**Max.(1)**	**Max.(2)**	**Max.(1)**	**Max.(2)**	**Max.(1)**	**Max.(2)**
t=0.5 sec	0.435		0.359		0.461		0.445	
t=1.16 sec		-0.366		-0.346		-0.384		-0.324
t=1.82 sec	0.413		0.395		0.478		0.428	
t=1.98 sec	0.382		0.433		0.482		0.401	
t=2.43 sec		-0.215		-0.218		-0.285		-0.203
t=2.9 sec	0.427		0.426		0.482		0.470	
H= 40 cm	**Trans. 4**		**Trans. 3**		**Trans. 2**		**Trans. 1**	
	L=20 cm		**L=32,5 cm**		**L=50 cm**		**L=80 cm**	
	Max.(1)	**Max.(2)**	**Max.(1)**	**Max.(2)**	**Max.(1)**	**Max.(2)**	**Max.(1)**	**Max.(2)**
t=1.2 sec		-0.425		-0.398		-0.423		-0.330
t=1.82 sec	0.467		0.417		0.516		0.496	
t=2.13 sec	0.392		0.384		0.490		0.488	
t=2.9sec	0.267		0.261		0.383		0.299	
t=2.41 sec		-0.358		-0.361		-0.418		-0.326
t=5.39 sec		-0.320		-0.377		-0.439		-0.276

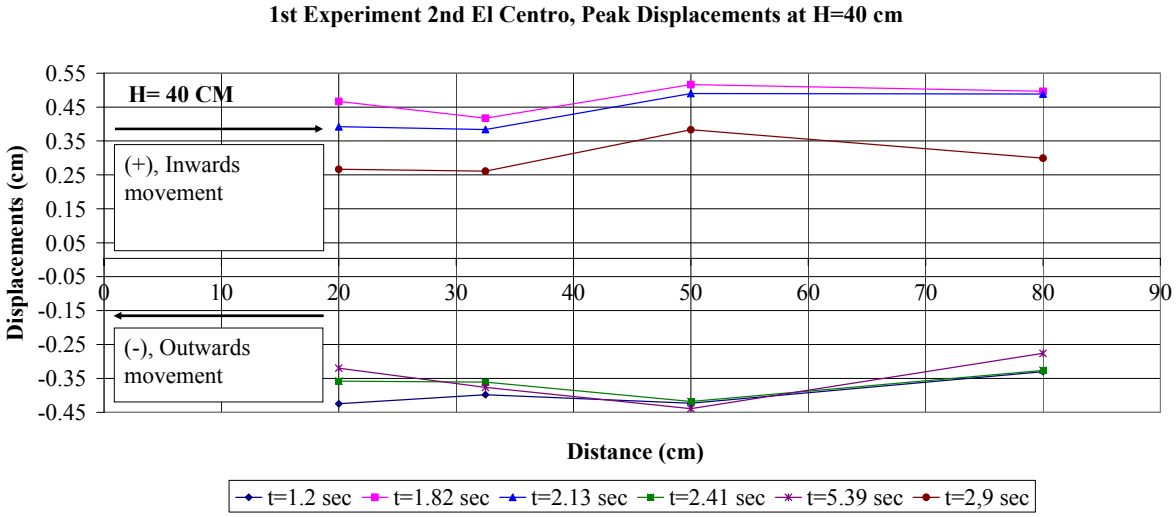

Figure 9.25. Peak relative displacements observed on the geotextile reinforcement at H = 40 cm in 2nd El Centro excitation of the 1st experiment

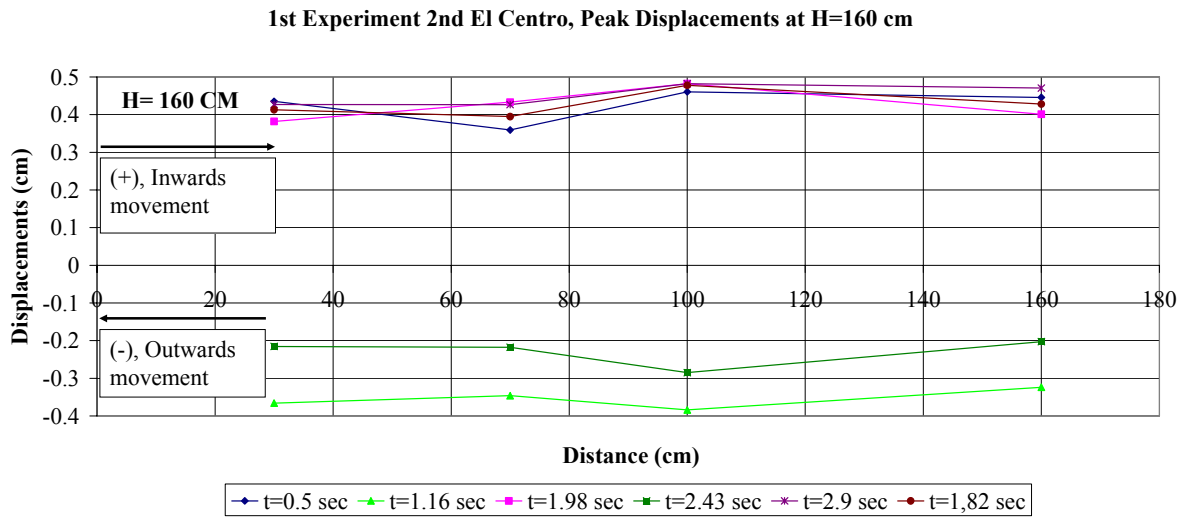

Figure 9.26. Peak relative displacements observed on the geotextile reinforcement at H = 160 cm in 2nd El Centro excitation of the 1st experiment

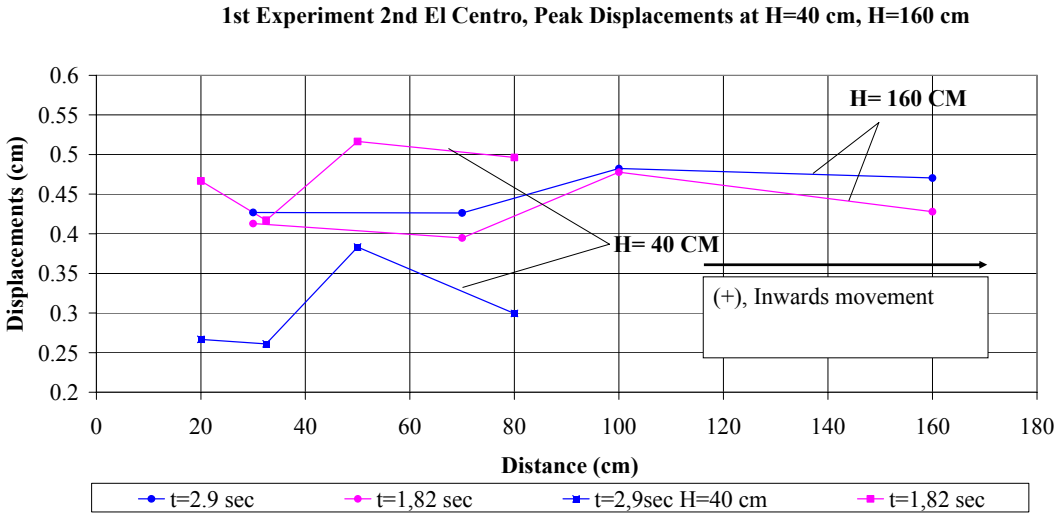

Figure 9.27. Comparisons of peak relative displacements measured on the geotextile reinforcements at H=40 cm and H=160 cm for the 2nd El Centro excitation of the 1st experiment

In Table 9.13 and in Figures 9.28 and 9.29, calculated average strains according to the maximum relative displacements can be seen.

Table 9.13. Calculated average strain values on the geotextile reinforcements at the 2nd El Centro excitation of the 1st experiment

H= 160 cm	Regions between the measurement locations		
	30 - 70	70 - 100	100 - 160
t=0.5 sec	-0.0019	0.0034	-0.0003
t=1.16 sec	0.0005	-0.0013	0.0010
t=1.82 sec	-0.0005	0.0028	-0.0008
t=1.98 sec	0.0013	0.0016	-0.0014
t=2.43 sec	-0.0001	-0.0022	0.0014
t=2.9 sec	0.0000	0.0019	-0.0002
H= 40 cm	**Regions between the measurement locations**		
	20 - 32.5	**32.5 - 50**	**50 - 80**
t=1.2 sec	0.0022	-0.0015	0.0031
t=1.82 sec	-0.0040	0.0057	-0.0007
t=2.13 sec	-0.0007	0.0061	-0.0001
t=2.9sec	-0.0005	0.0070	-0.0028
t=2.41 sec	-0.0002	-0.0033	0.0031
t=5.39 sec	-0.0046	-0.0036	0.0054

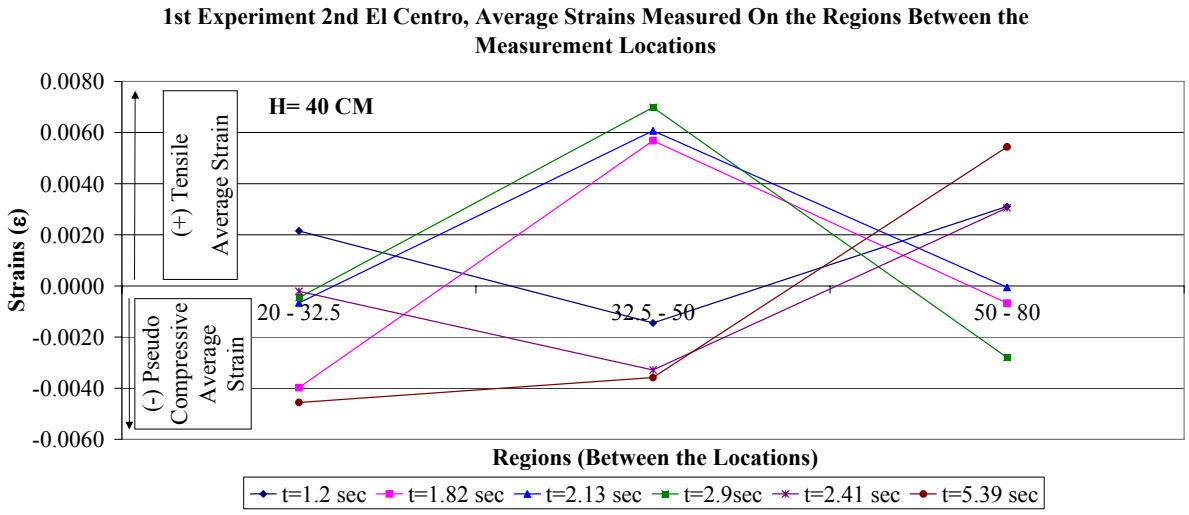

Figure 9.28. Average strains measured on the geotextile reinforcement at the regions between the measurement locations of the1st experiment 2nd El Centro excitation at the level H = 40 cm

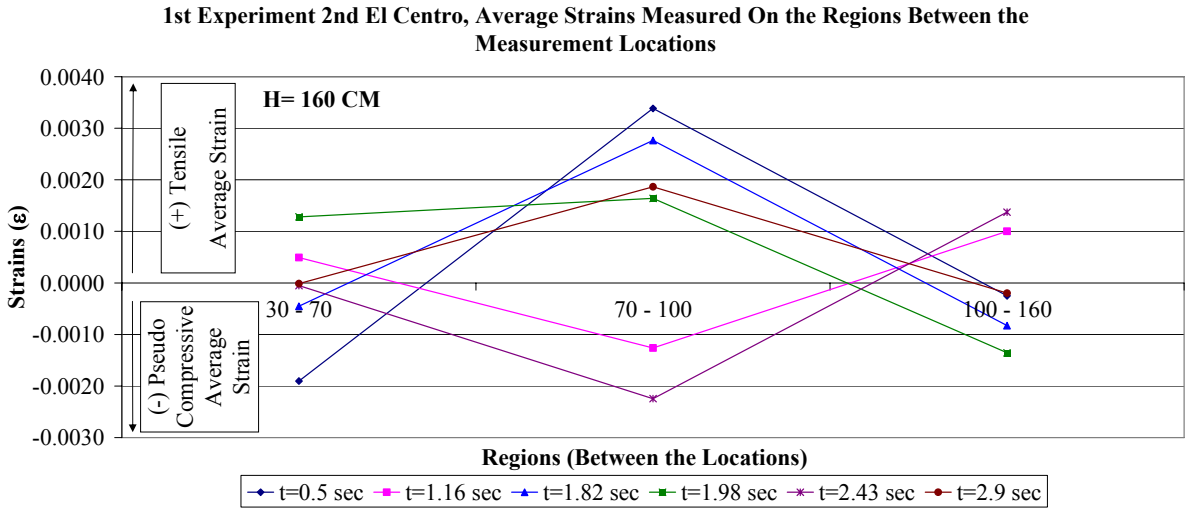

Figure 9.29. Average strains measured on the geotextile reinforcement at the regions between the measurement locations of the1st experiment 2nd El Centro excitation at the level H = 160 cm

Presented in Figures 9.30 and 9.31 are the calculated average-strain time history records of the geotextile members at the regions between the measurement locations.

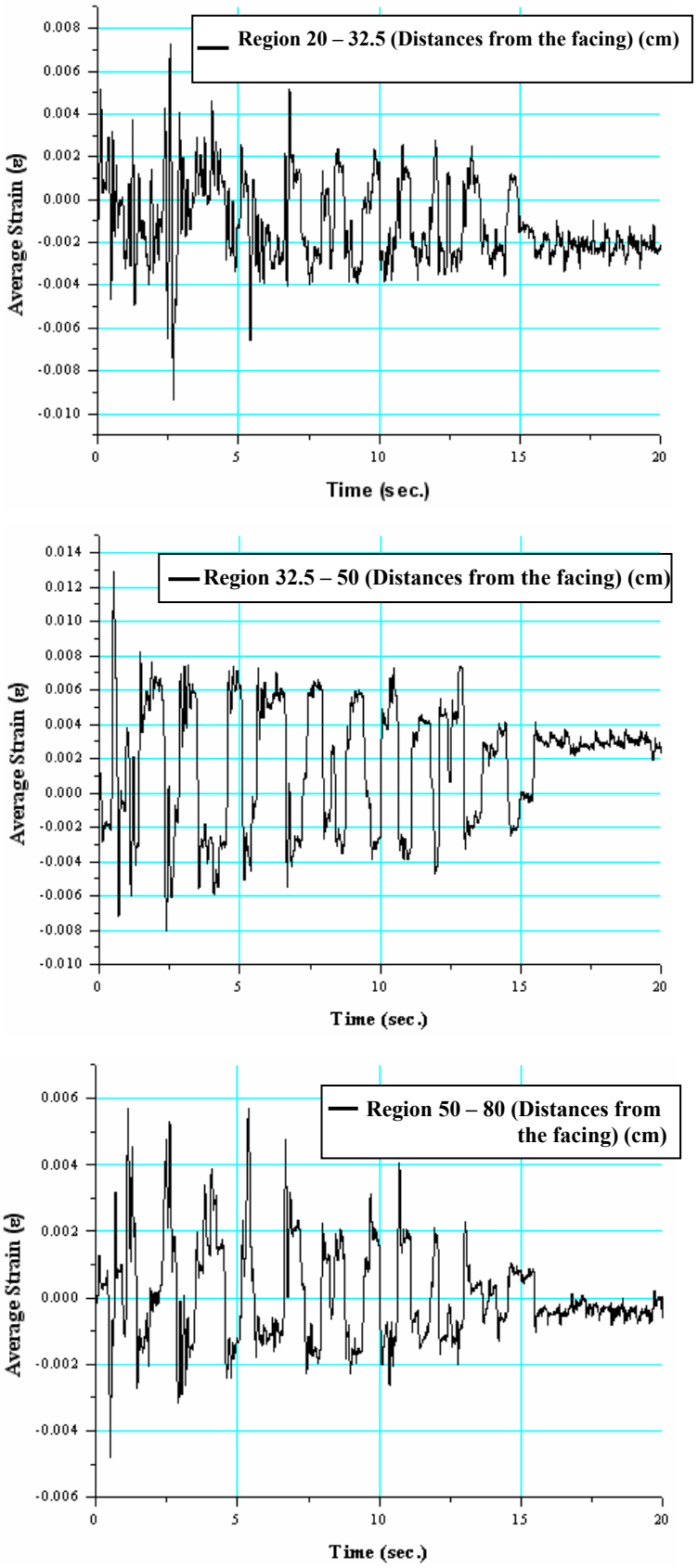

Figure 9.30. Average strains measured on the geotextile reinforcement at the regions in the 1st experiment 2nd El Centro excitation at level H=40 cm

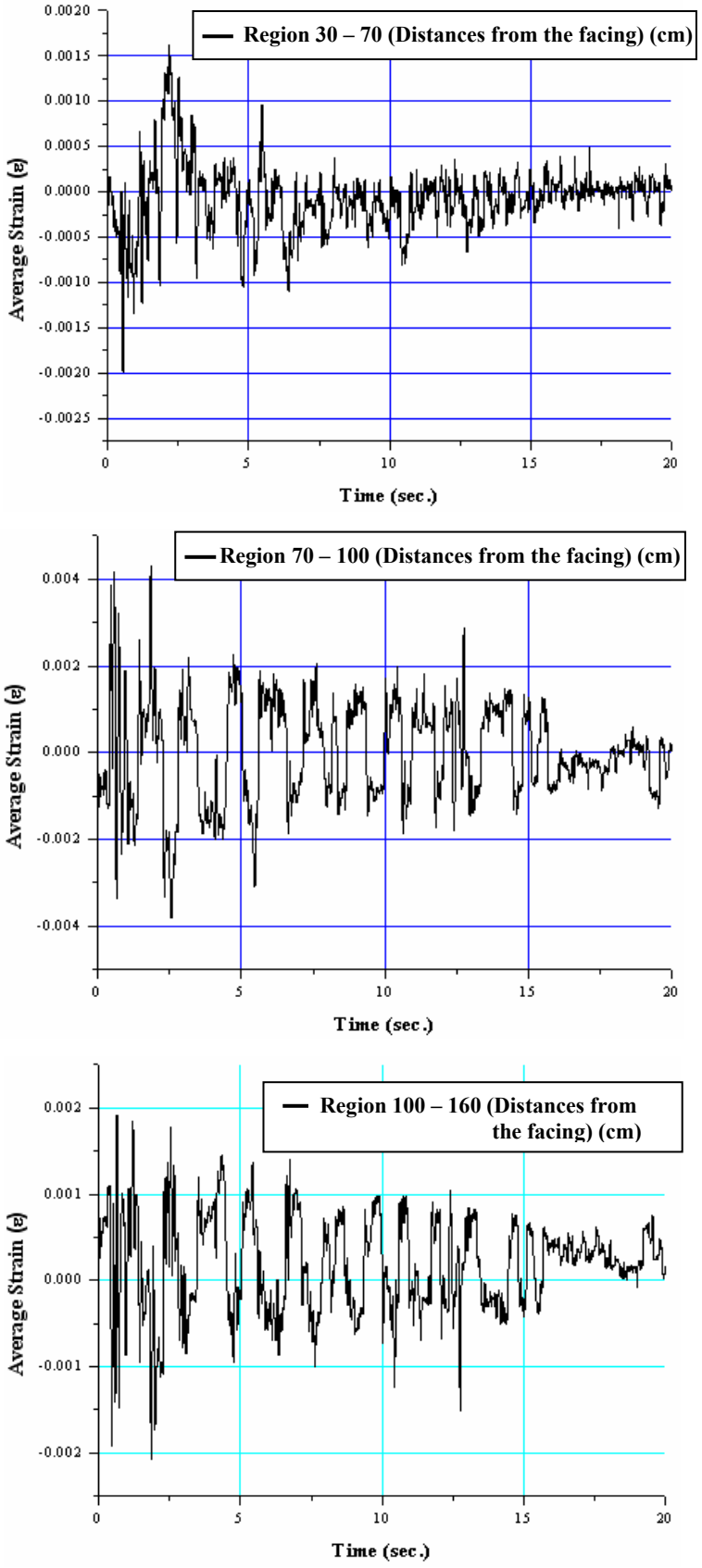

Figure 9.31. Average strains measured on the geotextile reinforcement at the regions in the 1st experiment 2nd El Centro excitation at level H = 160 cm

Figures 9.32 and 9.33 demonstrate the deformation behavior in all of the regions at levels H=40 cm and H=160 cm, respectively. At level H=40 cm direct opposite curves are observed between the regions 32.5-50 and 50-80 cm, which is an indication that compressive and tensile forces acted to the geotextile reinforcement due to the propagation of the pressure waves (Figure 9.32).

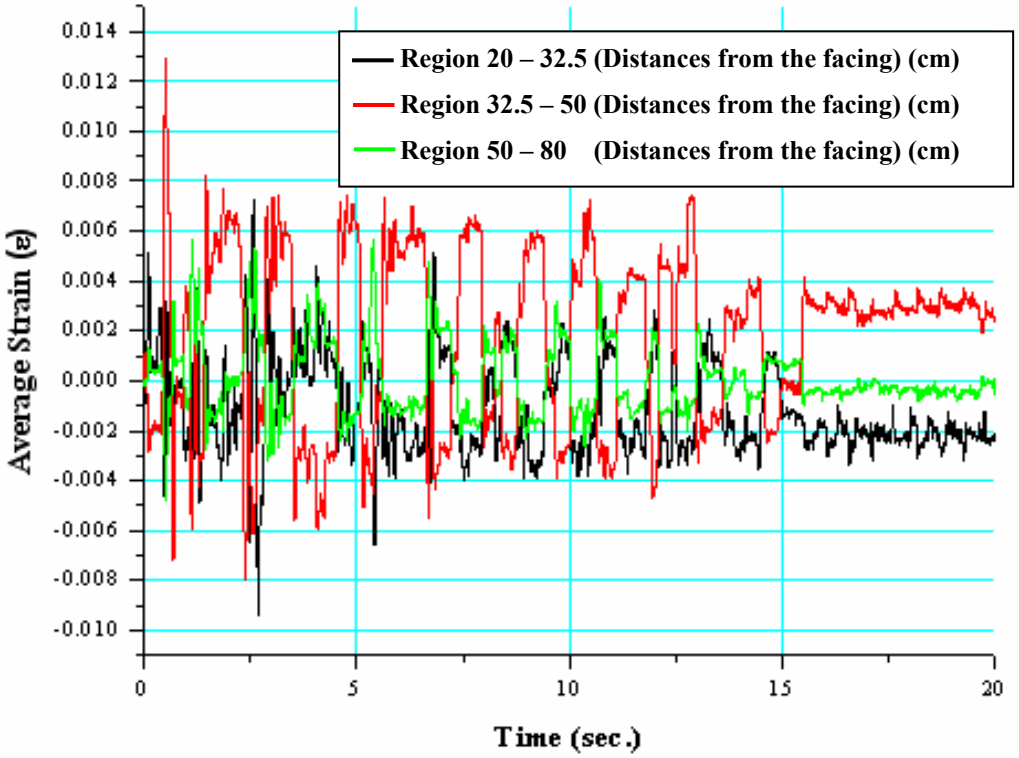

Figure 9.32. All the average strains measured on the geotextile reinforcement at the regions in the 1st experiment 2nd El Centro excitation at level H=40 cm

At level H=160 cm direct opposite curves are observed between the regions 70-100 cm and 100-160 cm at the same time intervals, which shows the compressive and tensile effects of the pressure waves when they are propagating in the soil (Figure 9.33). Because the region 30-70 cm is situated close to the facing wall and far away from the critical failure surface lower level of strains were measured as expected.

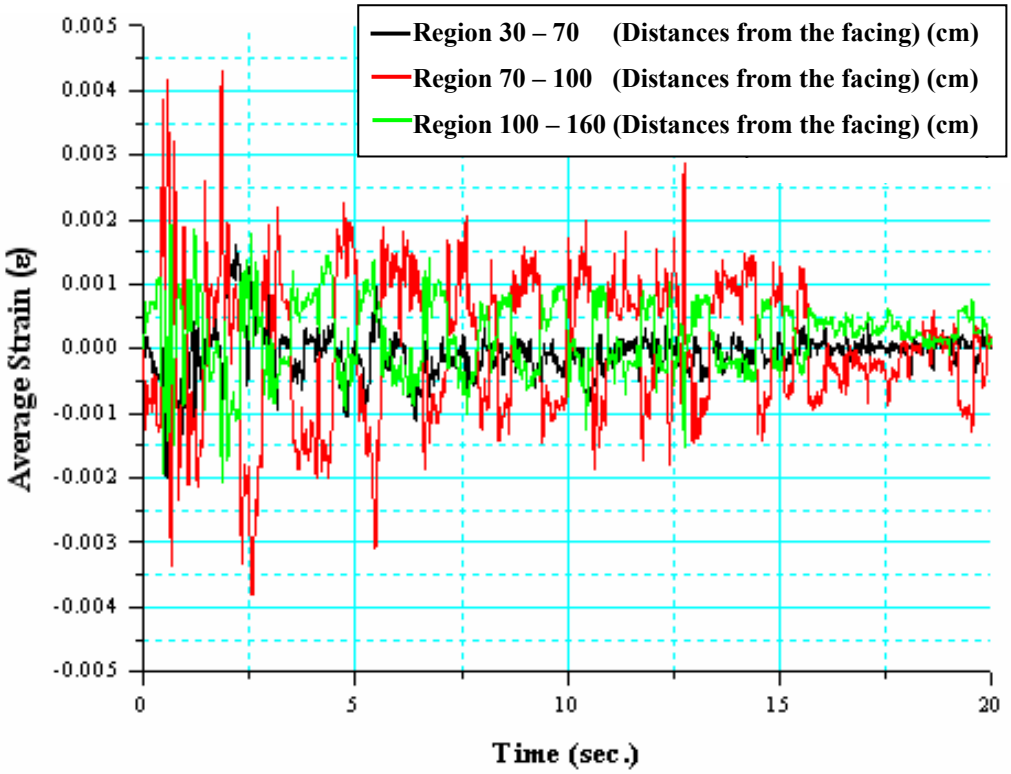

Figure 9.33. All the average strains measured on the geotextile reinforcement at the regions in the 1st experiment 2nd El Centro excitation at level H = 160 cm

9.2.1.4. Conclusions.

- The Peak relative displacements observed on the geotextiles during the Sine Motion excitation indicates that maximum relative displacements occurred at different locations on the geotextile layers, not on the assumed internal failure surface.

- By observing direct opposite average strain-time history curves between the regions 20-32.5 cm and 32.5-50 cm, 50-80 cm and between the regions 70-100 cm and 100-160 cm at the same time intervals, it can be concluded that compressional and dilatational zones developed during the sine motion excitation caused by the propagation of the pressure waves (Figure 9.12 and 9.13).

- An actual internal failure surface can be predicted by intersecting the intermediate points of the regions, where peak average tensile strains were measured, with the

toe of the wall (Figure 9.34). Inclination of the internal surface is very close to the assumed failure surface.

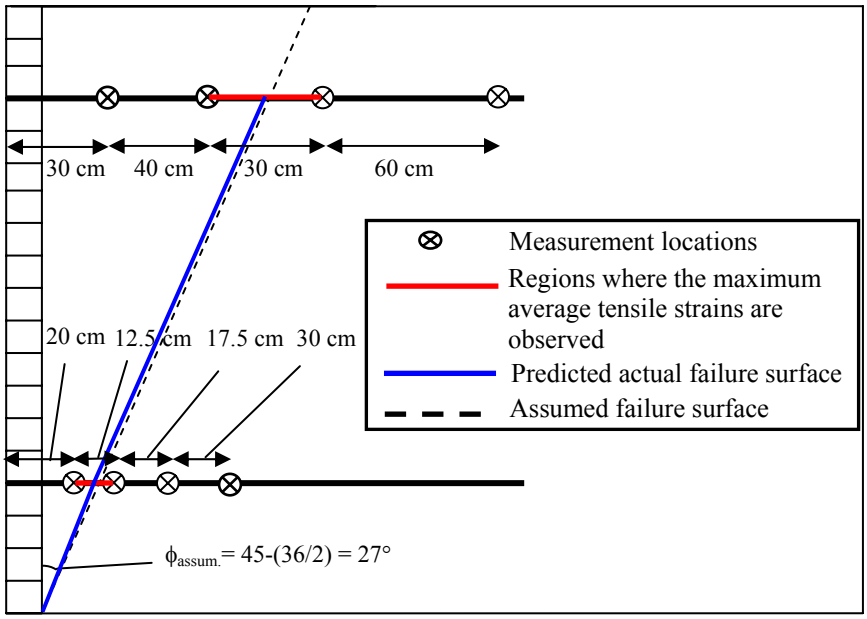

Figure 9.34. Internal failure surface determination and the regions where peak average tensile strains are observed during the sine motion excitation

- The relative displacements observed on the geotextile elements during the two El Centro motions indicate that all the maximum relative displacements occurred at the points close to or on the assumed internal failure surface.

- With the observation of direct opposite average strain-time history curves between 32.5–50 cm region and 50-80 cm region and between 70-100 cm region and 100-160 cm region at the same time intervals it can be deduced that compressional and dilatational zones developed during the El Centro excitations caused by the propagation of the pressure waves.

- For El Centro earthquake excitations, a bilinear internal failure surface can be predicted by intersecting the intermediate points of the regions, where peak average tensile strains were measured, with the toe of the wall (Figure 9.35). Inclination of the predicted actual internal failure surface is very close to the assumed failure surface like the one for the sine motion.

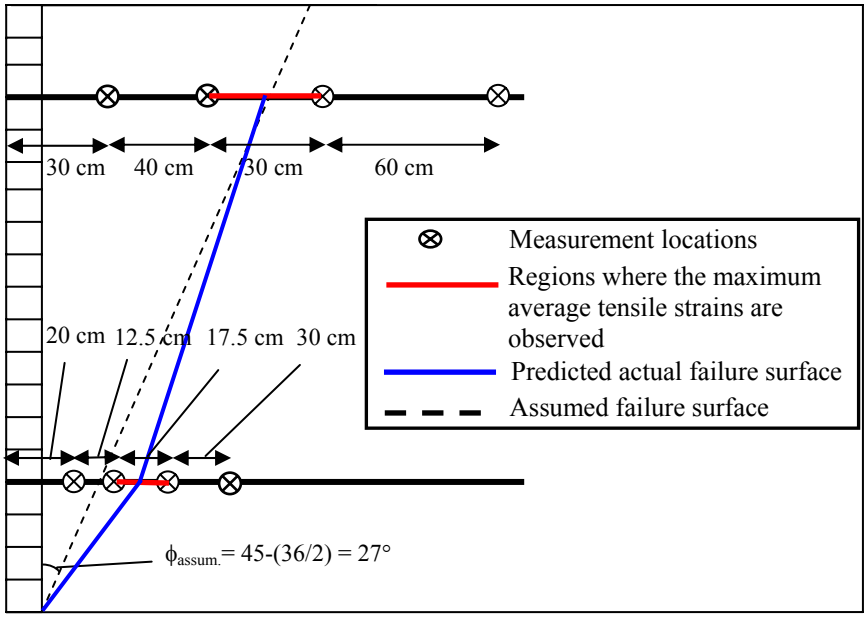

Figure 9.35. Internal failure surface determination and the regions where peak average tensile strains are observed during the El Centro excitations

- The results indicate that the maximum average strains observed does not coincide with the time instances where maximum relative displacements are observed.

- The maximum resultant dynamic tensile stress occurred in the sine motion is 2.51 kN/m whereas for El-Centro motion in the 2nd Shaking it is 4.732 kN/m (for Jgeotextile=364 kN/m).

- The reinforcement tensile average strains observed at the level H=40 cm are significantly higher than the ones at the level H=160 cm confirming the pseudo-static approach of the dynamic load increment pressure distribution for internal stability analysis opted by FHWA when calculating the reinforcement loads.

- Listed in Tables 9.14 to 9.16, are the maximum relative displacements, maximum average tensile strains and maximum average pseudo-compressive strains observed during the excitations, respectively.

Table 9.14. Summary of the measured maximum relative displacements on the geotextile reinforcements during the excitations

Maximum Relative Displacements (cm)				
1st Experiment	**Locations**	**Sine Motion**	**El Centro-1**	**El Centro-2**
H = 40 cm	**L = 20 cm**	0.495	-0.468	0.467
	L = 32.5 cm	0.409	-0.456	0.417
	L = 50 cm	0.383	-0.517	0.516
	L = 80 cm	0.530	-0.440	0.496
H = 160 cm	**L = 30 cm**	-0.864	0.397	0.435
	L = 70 cm	-0.869	0.357	0.433
	L = 100 cm	-0.812	0.435	0.482
	L = 160 cm	-0.824	0.409	0.470

Table 9.15. Summary of the calculated maximum average tensile strains on the geotextile reinforcements during the excitations

Maximum Average Tensile Strain (ε)				
1st Experiment	**Regions**	**Sine Motion**	**El Centro-1**	**El Centro-2**
H = 40 cm	**20-32.5**	0.0069	0.0079	0.0073
	32.5-50	0.0031	0.0090	0.0130
	50-80	0.0060	0.0064	0.0057
H = 160 cm	**30-70**	0.0005	0.0018	0.0016
	70-100	0.0032	0.0052	0.0043
	100-160	0.0019	0.0015	0.0019

Table 9.16. Summary of the calculated maximum average pseudo compressive strains on the geotextile reinforcements during the excitations

Maximum Average Pseudo Compressive Strain (ε)				
1st Experiment	**Regions**	**Sine Motion**	**El Centro-1**	**El Centro-2**
H = 40 cm	**20-32.5**	-0.0088	-0.0124	-0.0094
	32.5-50	-0.0036	-0.0121	-0.0080
	50-80	-0.0031	-0.0027	-0.0048
H = 160 cm	**30-70**	-0.0010	-0.0019	-0.0020
	70-100	-0.0037	-0.0033	-0.0038
	100-160	-0.0008	-0.0026	-0.0021

9.2.2. The Instrumentation and measurement locations of the Geotextiles for the 2nd Experiment (L/H=0.6) (Figure 9.36)

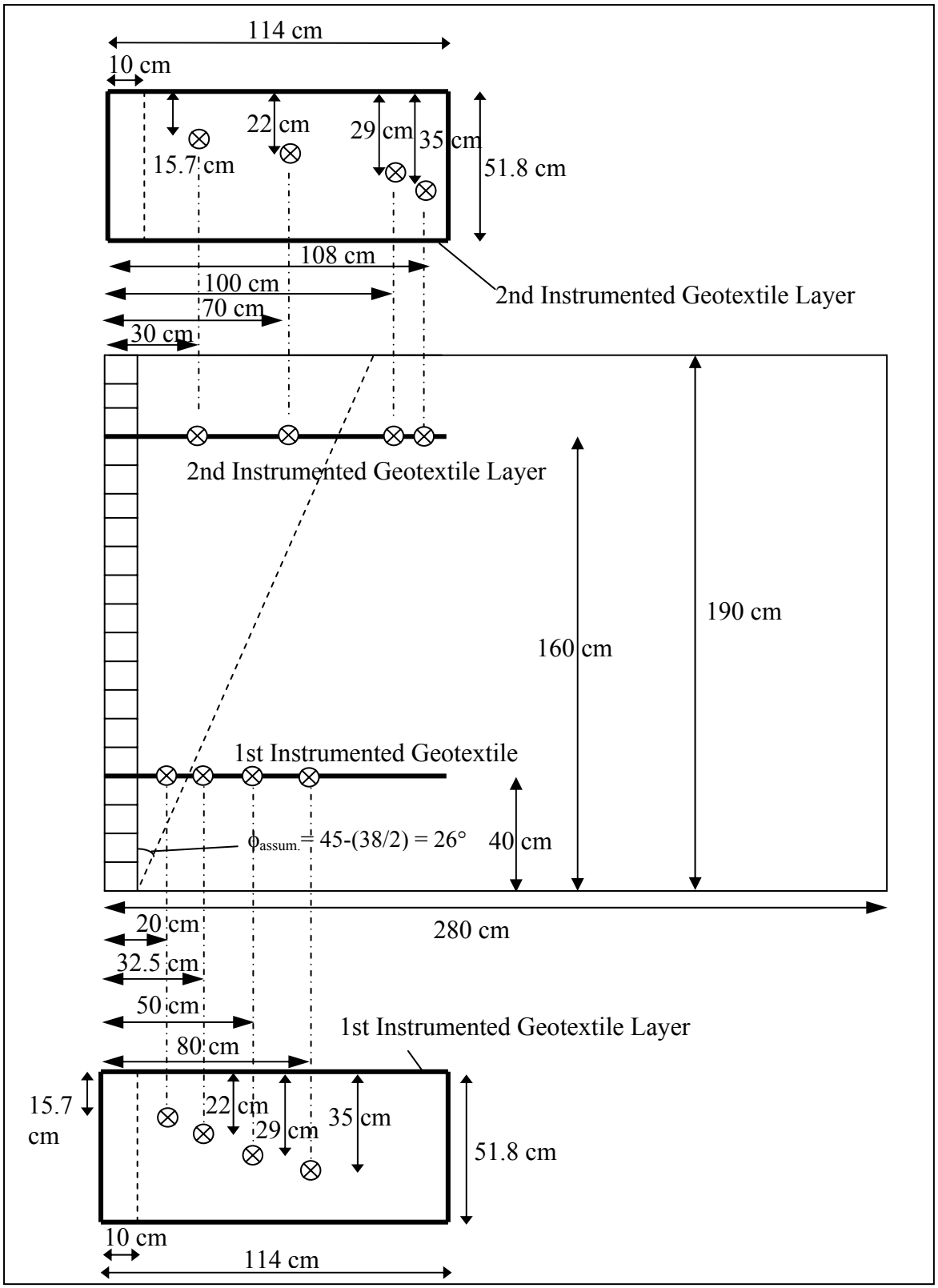

Figure 9.36. General view of the instrumented geotextiles of the 2nd Experiment

9.2.2.1. Sine Wave Excitation. The displacement-time history record of the sine wave motion can be seen in Figure 9.37.

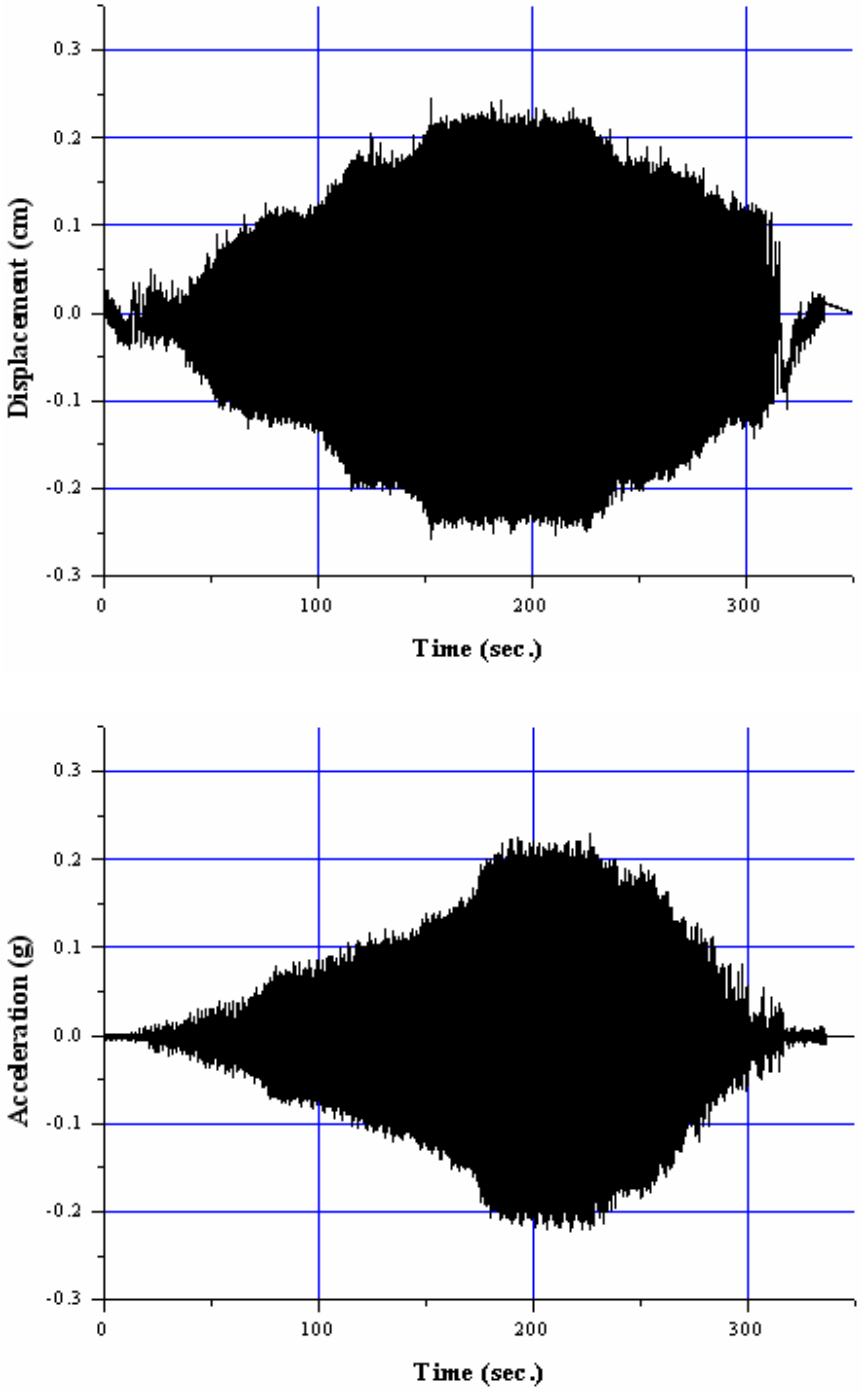

Figure 9.37. 2nd experiment sinusoidal motion excitation record

The peak relative displacements on the geotextile reinforcements in both directions (positive and negative) were measured to be as in Table 9.17 and in Figures 9.38 to 9.40.

Table 9.17. Peak relative displacements observed on the geotextile reinforcements at the sine motion excitation of the 2nd experiment (units are in cm)

Peak Relative Displacements (2nd Experiment Random Sine Motion)								
H= 160 cm	**Trans. 8**		**Trans. 7**		**Trans. 6**		**Trans. 5**	
	L=30 cm		**L=70 cm**		**L=100 cm**		**L=108 cm**	
	Max.(1)	**Max. 2)**	**Max.(1)**	**Max.(2)**	**Max.(1)**	**Max.(2)**	**Max.(1)**	**Max.(2)**
t=152.9 sec		-0.4507		-0.4154		-0.4170		-0.4061
t=171.954 sec	0.3802		0.4429		0.3642		0.3781	
t=172.844 sec		-0.4543		-0.4274		-0.4123		-0.4128
t=225.562 sec	0.3429		0.4341		0.3284		0.3243	
H= 40 cm	**Trans. 4**		**Trans. 3**		**Trans. 2**		**Trans. 1**	
	L=20 cm		**L=32,5 cm**		**L=50 cm**		**L=80 cm**	
	Max.(1)	**Max.(2)**	**Max.(1)**	**Max.(2)**	**Max.(1)**	**Max.(2)**	**Max.(1)**	**Max.(2)**
t=152.902 sec		-0.1911		-0.2326		-0.1642		-0.2512
t=171.954 sec	0.3548		0.2776		0.4413		0.3781	
t=172.844 sec		-0.1481		-0.1911		-0.1140		-0.2222
t=225.564 sec	0.3652		0.2958		0.4527		0.3942	

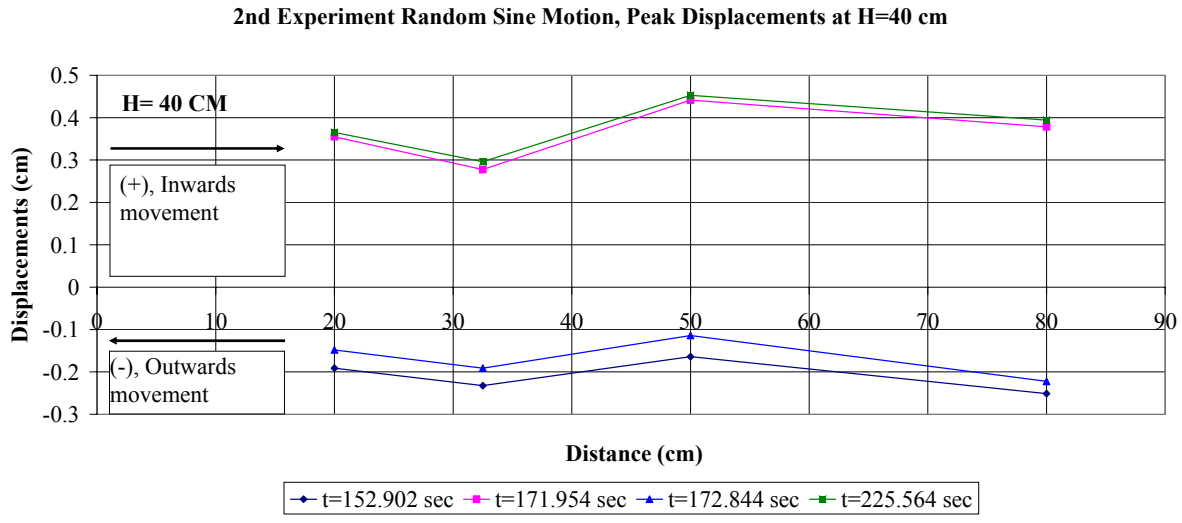

Figure 9.38. Peak relative displacements measured on the geotextile reinforcement at H = 40 cm in sine motion excitation of the 2nd experiment

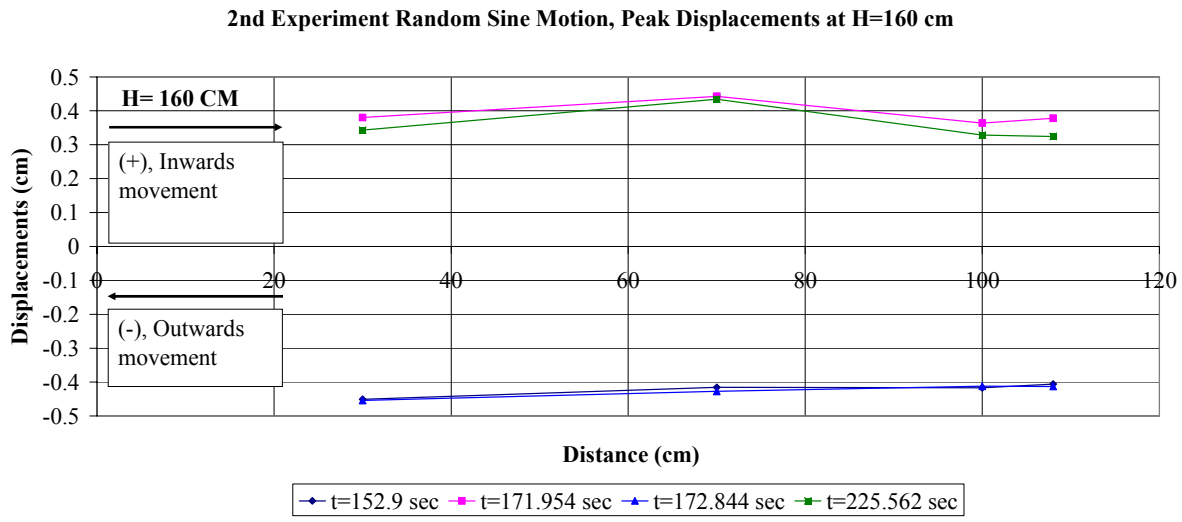

Figure 9.39. Peak relative displacements measured at H = 160 cm in sine motion excitation of the 2nd experiment

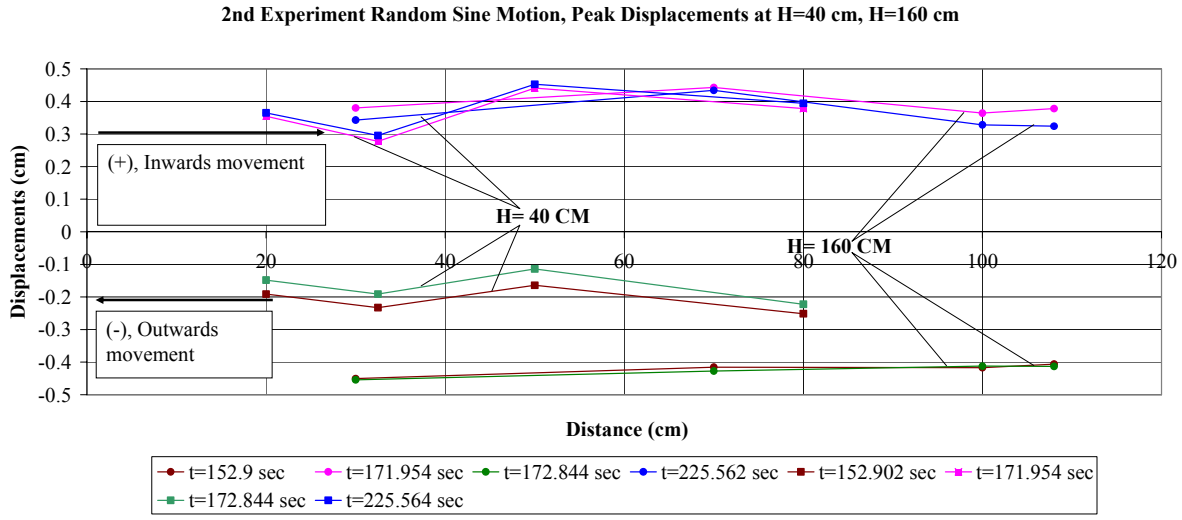

Figure 9.40. Comparisons of peak relative displacements measured on the geotextile reinforcements at H=40 cm and H=160 cm for the sine motion excitation of the 2nd experiment

In Table 9.18 and in Figures 9.41 and 9.42, calculated average strains according to the maximum relative displacements can be seen. Regions 20 – 32.5, 32.5 – 50, 50 – 80, 30 – 70, 70 – 100, 100 – 108 represent the areas between the measurement locations.

Table 9.18. Calculated average strain values on the geotextile reinforcements at the sine motion excitation of the 2nd experiment

H= 160 cm	**Regions between the measurement locations**		
	30 - 70	**70 - 100**	**100 - 108**
t=152.9 sec	0.0009	-0.0001	0.0014
t=171.954 sec	0.0016	-0.0026	0.0017
t=172.844 sec	0.0007	0.0005	-0.0001
t=225.562 sec	0.0023	-0.0035	-0.0005
H= 40 cm	**Regions between the measurement locations**		
	20 - 32.5	**32.5 - 50**	**50 - 80**
t=152.902 sec	-0.0033	0.0039	-0.0029
t=171.954 sec	-0.0062	0.0094	-0.0021
t=172.844 sec	-0.0034	0.0044	-0.0036
t=225.564 sec	-0.0056	0.0090	-0.0020

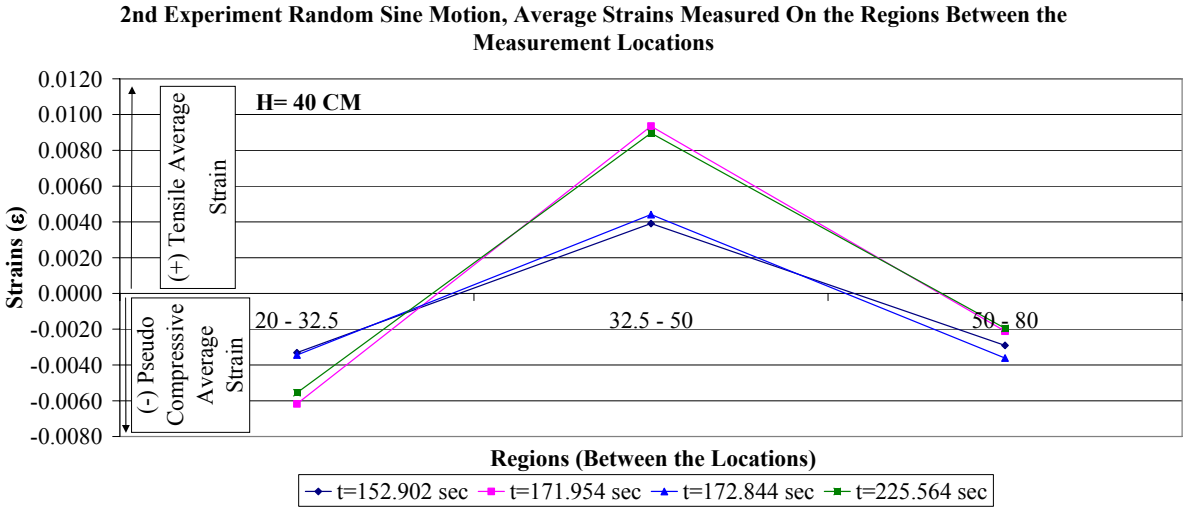

Figure 9.41. Average strains measured on the geotextile reinforcement at the regions between the measurement locations of the 2nd experiment sine motion excitation at the level H = 40 cm

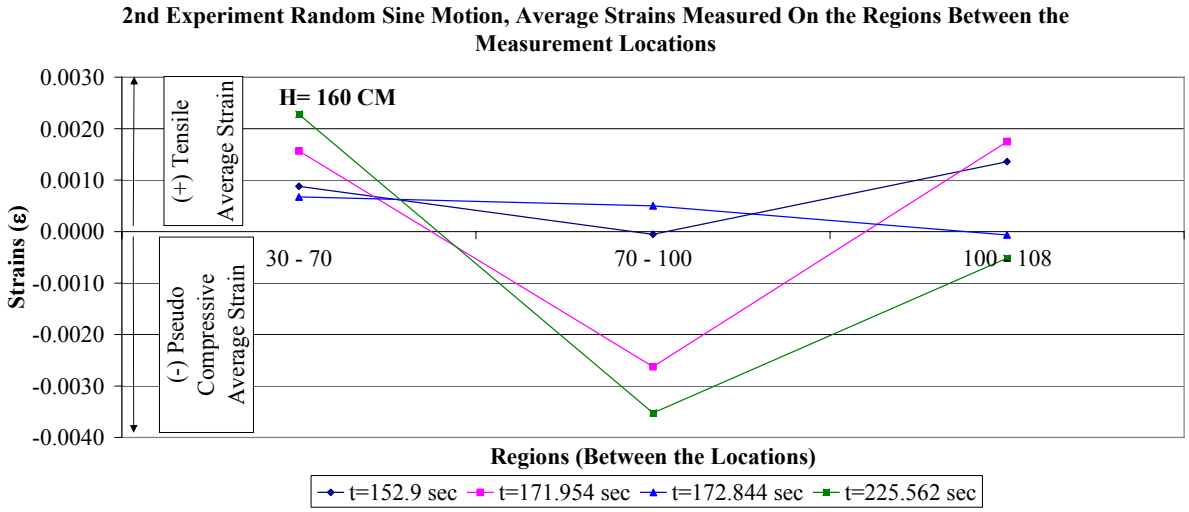

Figure 9.42. Average strains measured on the geotextile reinforcement at the regions between the measurement locations of the 2nd experiment sine motion excitation at the level H = 160 cm

Presented in Figures 9.43 and 9.44 are the average-strain time history records of the geotextile members at the regions between the measurement locations.

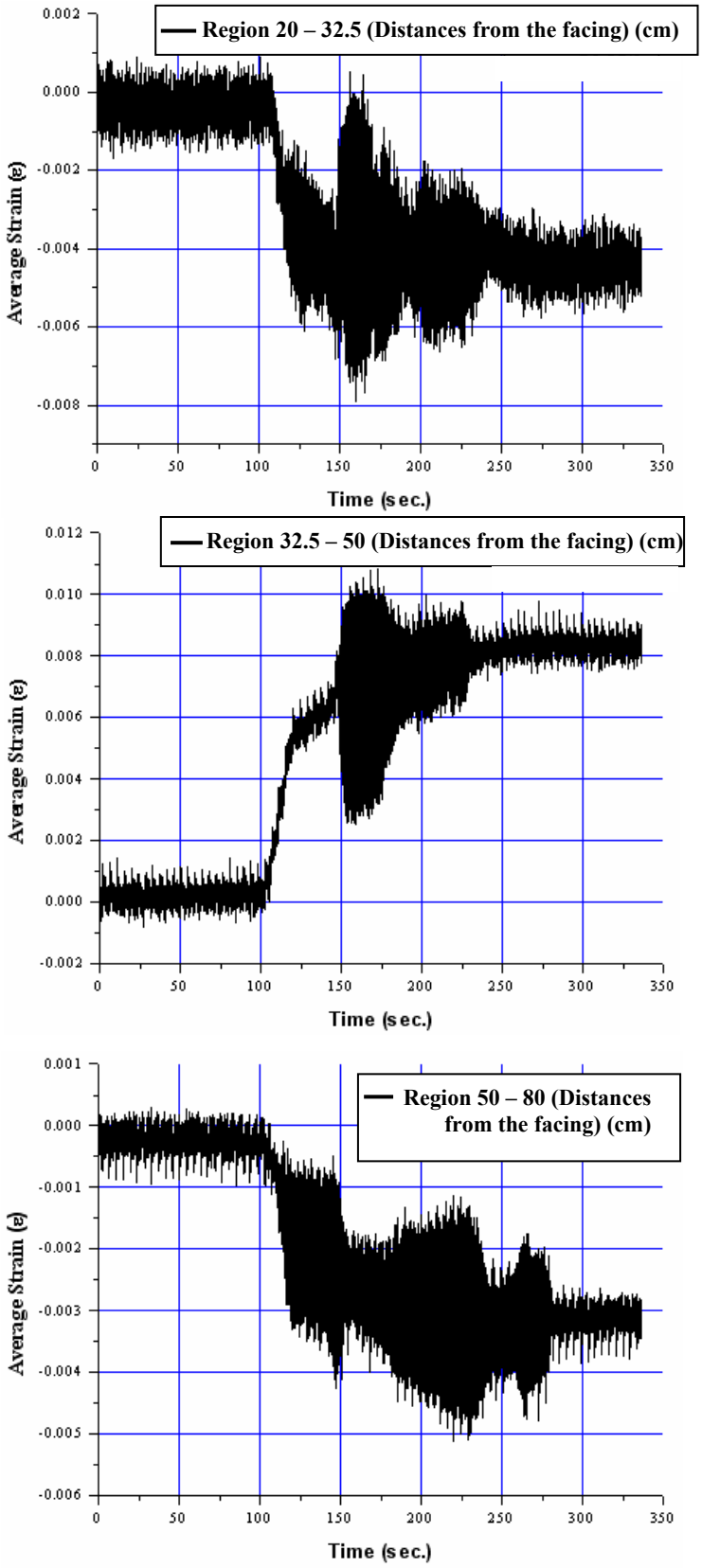

Figure 9.43. Average strains measured on the geotextile reinforcement at the regions in the 2nd experiment sine motion excitation at level H = 40 cm

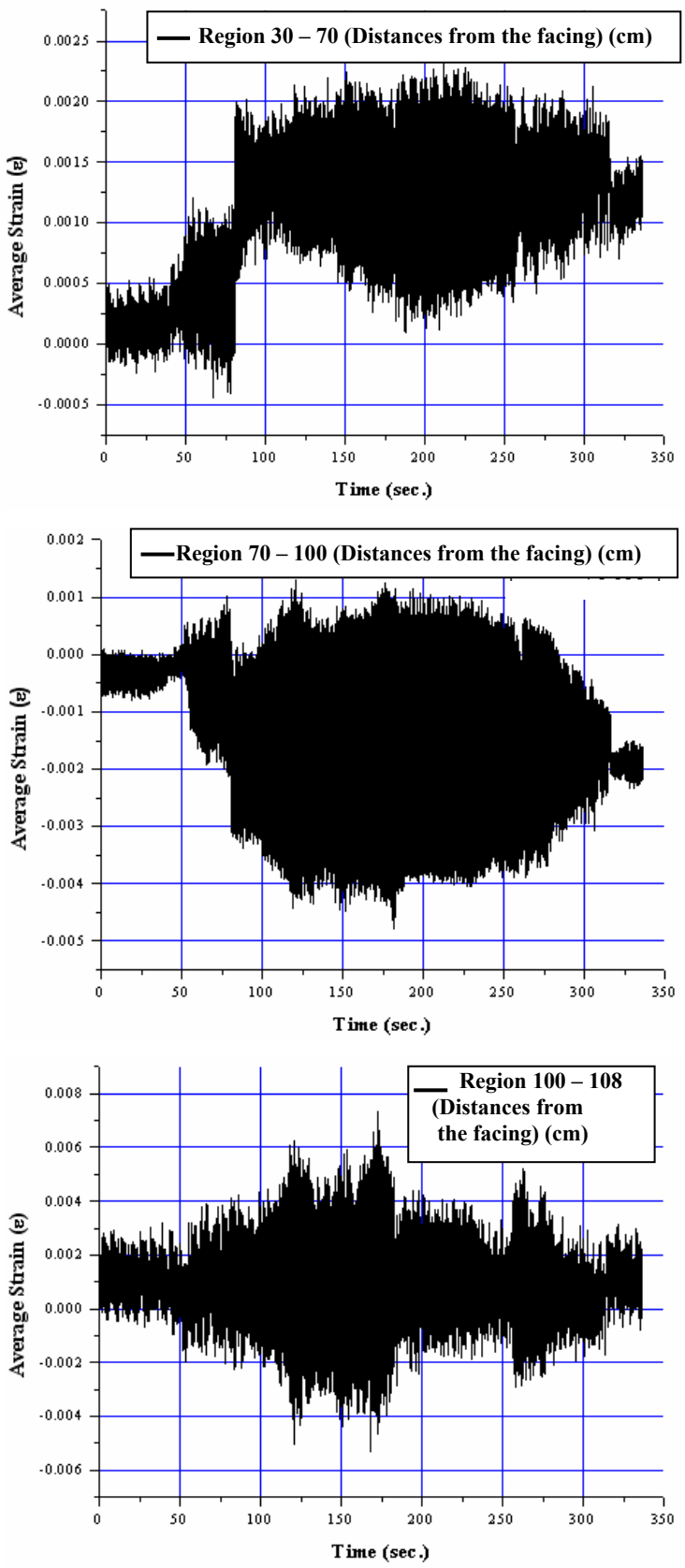

Figure 9.44. Average strains measured on the geotextile reinforcement at the regions in the 2nd experiment sine motion excitation at level H = 160 cm

Figures 9.45 to 9.48 demonstrate the deformation behavior in all of the regions at levels H=40 cm and H=160 cm, respectively. From Figure 9.45, it can be deduced that after 100 seconds the while region 32.5-50 cm undergoes to tensile forces, the other regions endure compressional forces.

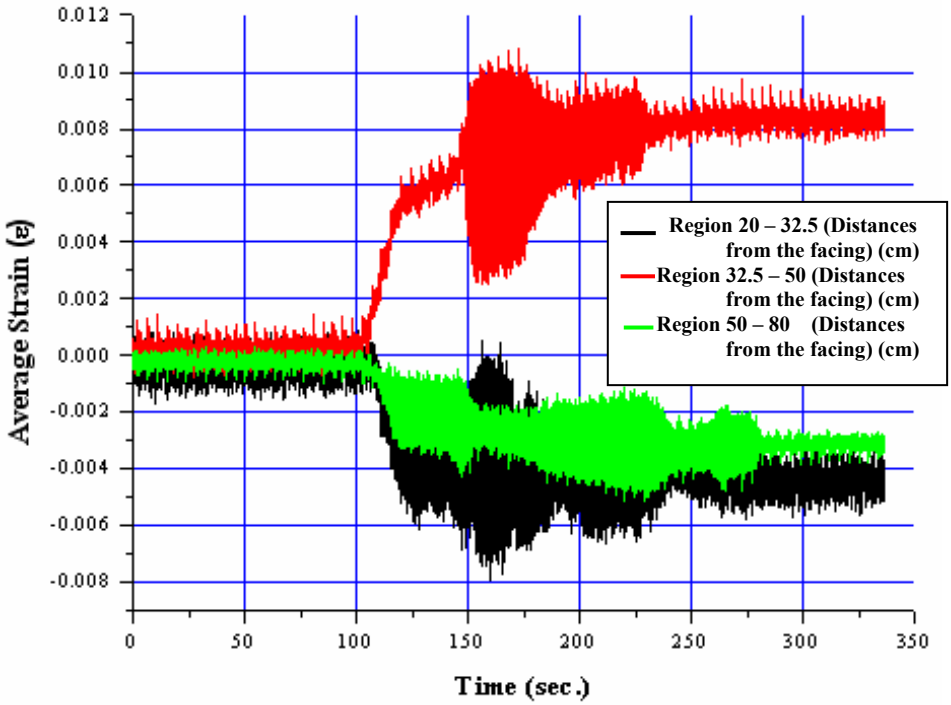

Figure 9.45. All the average strains measured on the geotextile reinforcement at the regions in the 2nd experiment sine motion excitation at level H = 40 cm

At level H=40 cm direct opposite curves are observed between the regions 20-32.5 cm and 32.5-50 and between regions 20-32.5 cm and 50-80 at the same time intervals (Figure 9.46). This indicates that the propagation of the pressure waves in the soil generates compressional and tensional zones to develop in different regions.

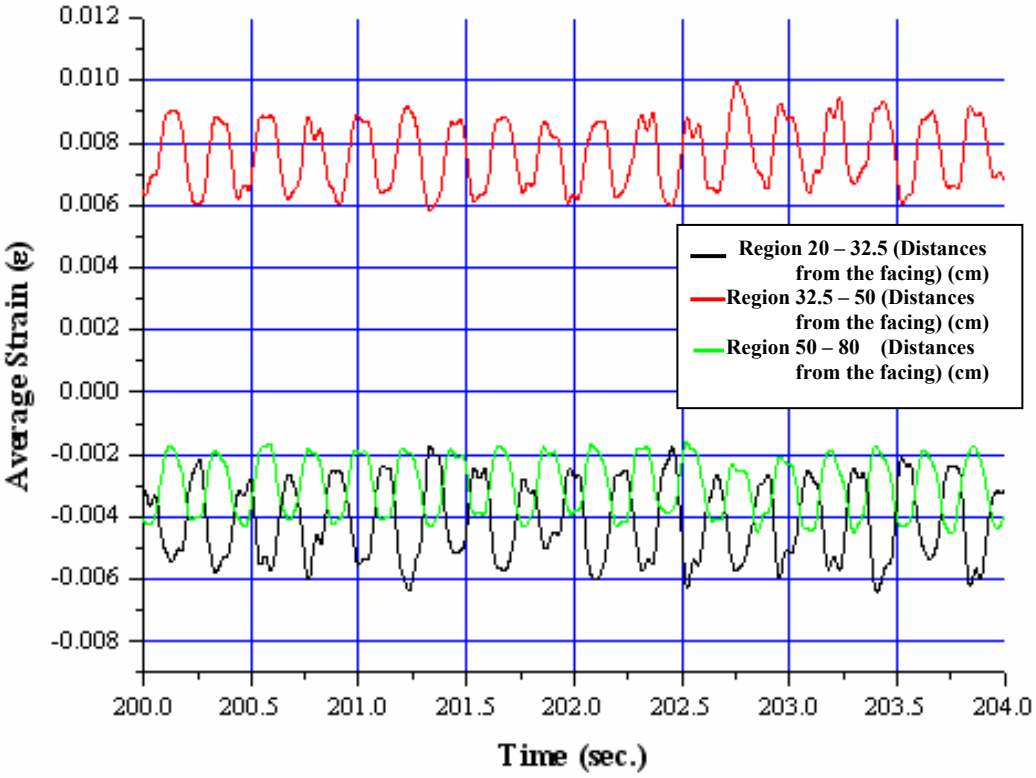

Figure 9.46. Average strains measured on the geotextile reinforcement for the time interval between t= 200 sec. and t=204 sec. at level H=40 cm

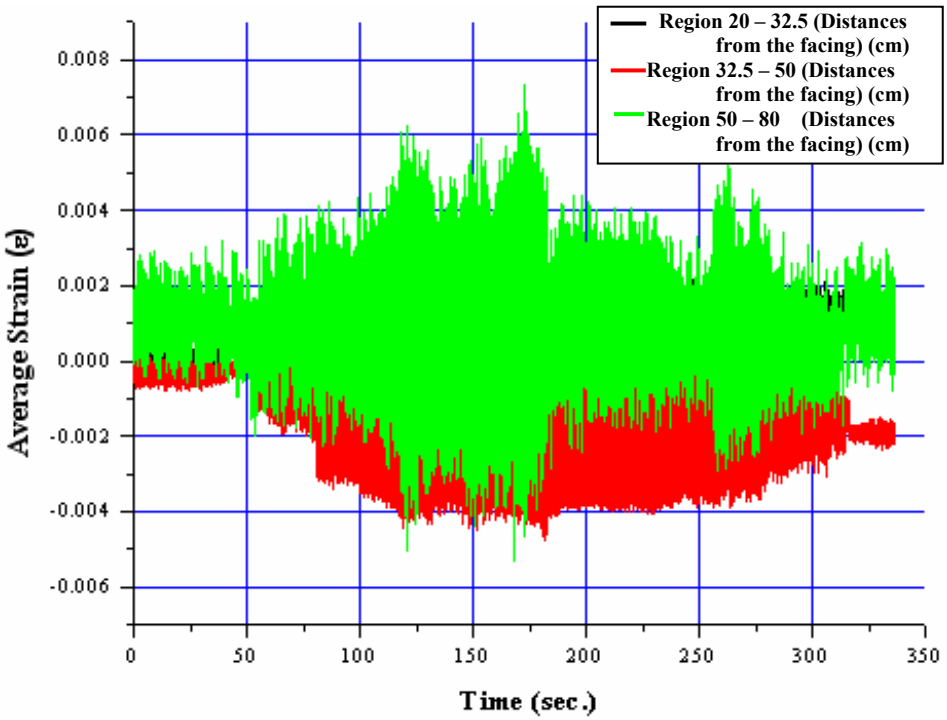

Figure 9.47. All the average strains measured on the geotextile reinforcement at the regions in the 2nd experiment sine motion excitation at level H = 160 cm

At level H=160 cm direct opposite curves are observed between the regions 70-100 cm and 100-108 cm and between the regions 30-70 cm and 70-100 cm at the same time intervals signifying the development of compresional and dilatational forces acting on the geotextile reinforcement due to the propagating effect of pressure waves (Figure 9.48).

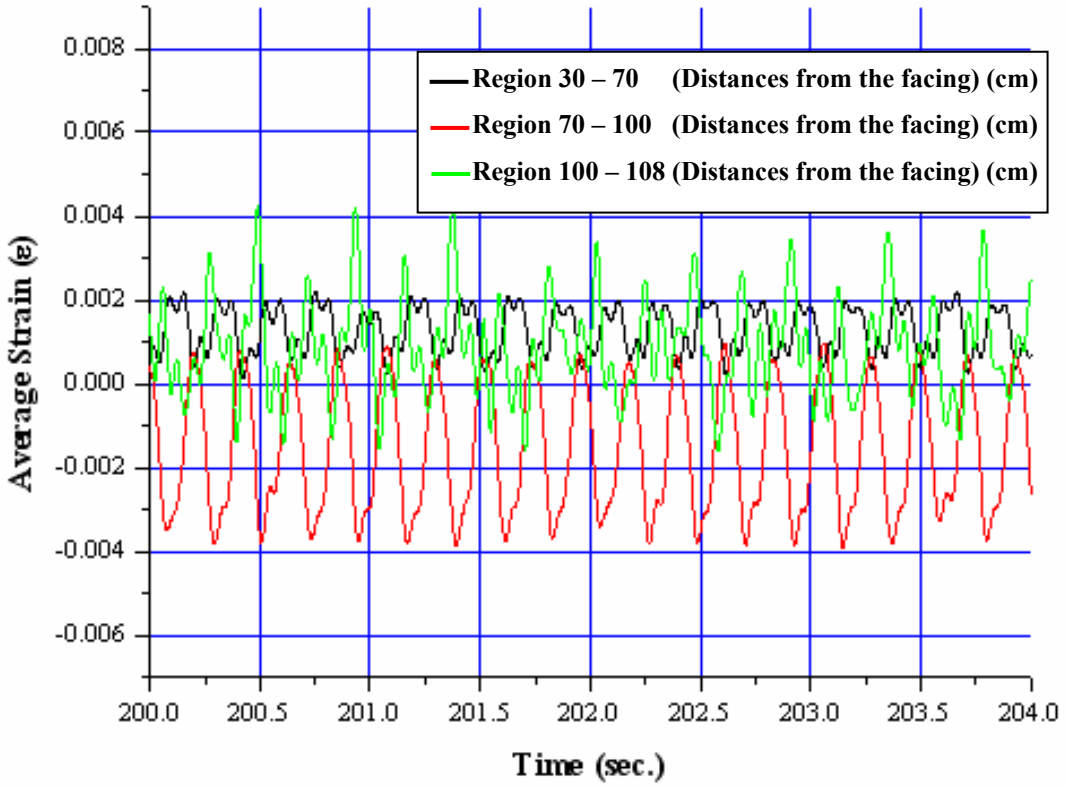

Figure 9.48. Average strains measured on the geotextile reinforcement for the time interval between t= 200 sec. and t=204 sec. at level H=160 cm

9.2.2.2. 1st El Centro Excitation. The base time-history motions for this excitation are shown in Figure 9.49.

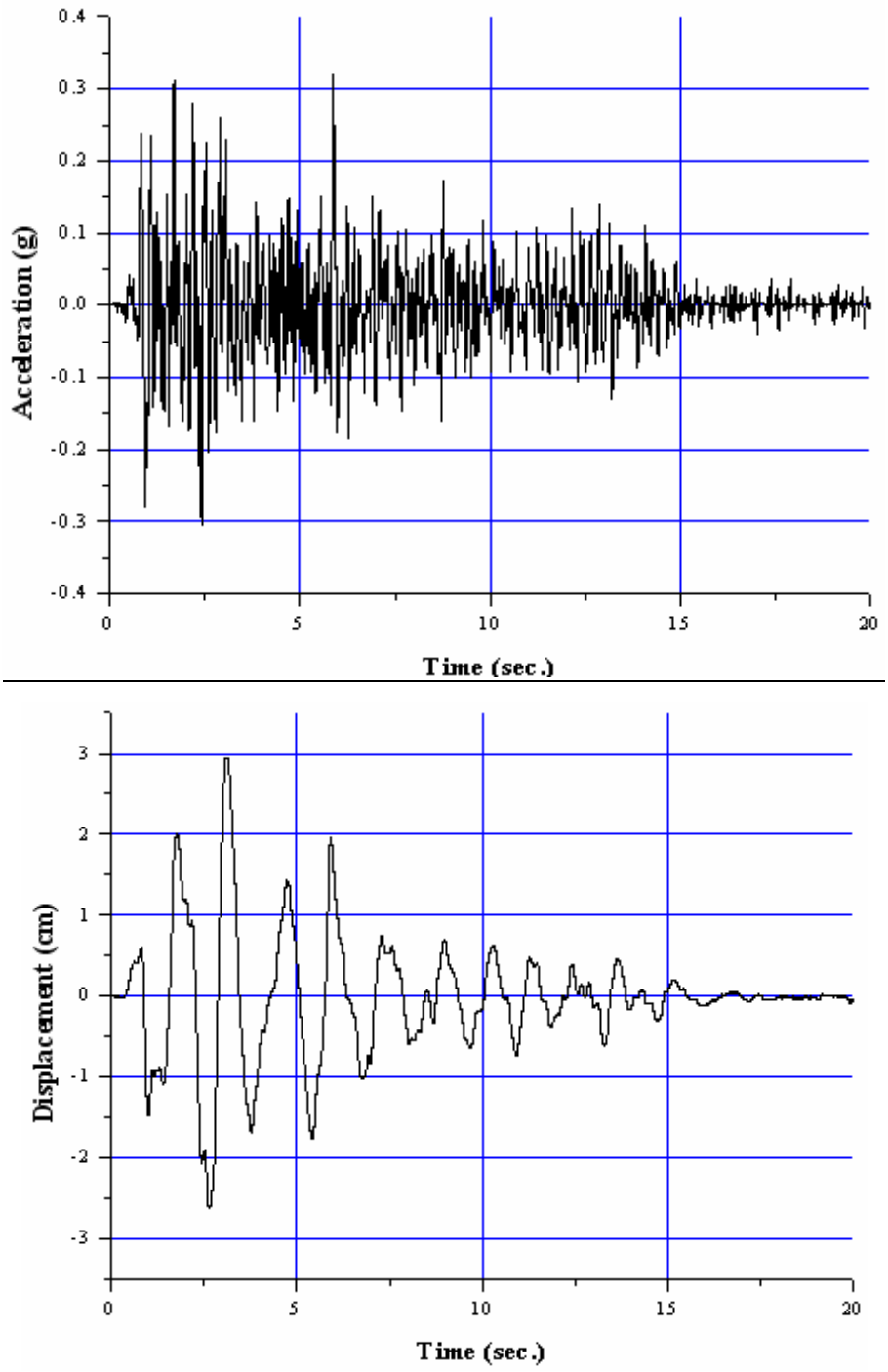

Figure 9.49. 2nd experiment 1st El Centro excitation record

The peak relative displacements in both directions were calculated to be as in Table 9.19 and in Figures 9.50 to 9.52. Since the peak relative displacement time instances didn't coincide between the two layers of the geotextiles, the relative displacements for the time instances where there were not any peak relative displacement observed on the other layer were also calculated in order to compare the displacement behavior of the layers.

Table 9.19. Peak relative displacements observed on the geotextile reinforcements at the 1st El Centro excitation of the 2nd experiment (units are in cm)

Peak Relative Displacements (2nd Experiment 1st EL CENTRO %100)								
H= 160 cm	**Trans. 8**		**Trans. 7**		**Trans. 6**		**Trans. 5**	
	L=30 cm		**L=70 cm**		**L=100 cm**		**L=108 cm**	
	Max.(1)	**Max.(2)**	**Max.(1)**	**Max.(2)**	**Max.(1)**	**Max.(2)**	**Max.(1)**	**Max. (2)**
t=1.60 sec	-0.2150		-0.2761		-0.3129		-0.2808	
t=2.35 sec		0.3714		0.3901		0.4040		0.4372
t=2.59 sec		0.2989		0.3776		0.4843		0.3797
t=2.97 sec	-0.1352		-0.1580		-0.2953		-0.2046	
t=5.82 sec	-0.2124		-0.2574		-0.3279		-0.2839	
H= 40 cm	**Trans. 4**		**Trans. 3**		**Trans. 2**		**Trans. 1**	
	L=20 cm		**L=32,5 cm**		**L=50 cm**		**L=80 cm**	
	Max.(1)	**Max.(2)**	**Max.(1)**	**Max.(2)**	**Max.(1)**	**Max.(2)**	**Max.(1)**	**Max. (2)**
t=2.25 sec		0.4393		0.4610		0.3823		0.3787
t=2.6 sec		0.4460		0.4812		0.4237		0.4077
t=2.98 sec	-0.5802		-0.7169		-0.5874		-0.5672	
t=5.85 sec	-0.4797		-0.6200		-0.5071		-0.5196	

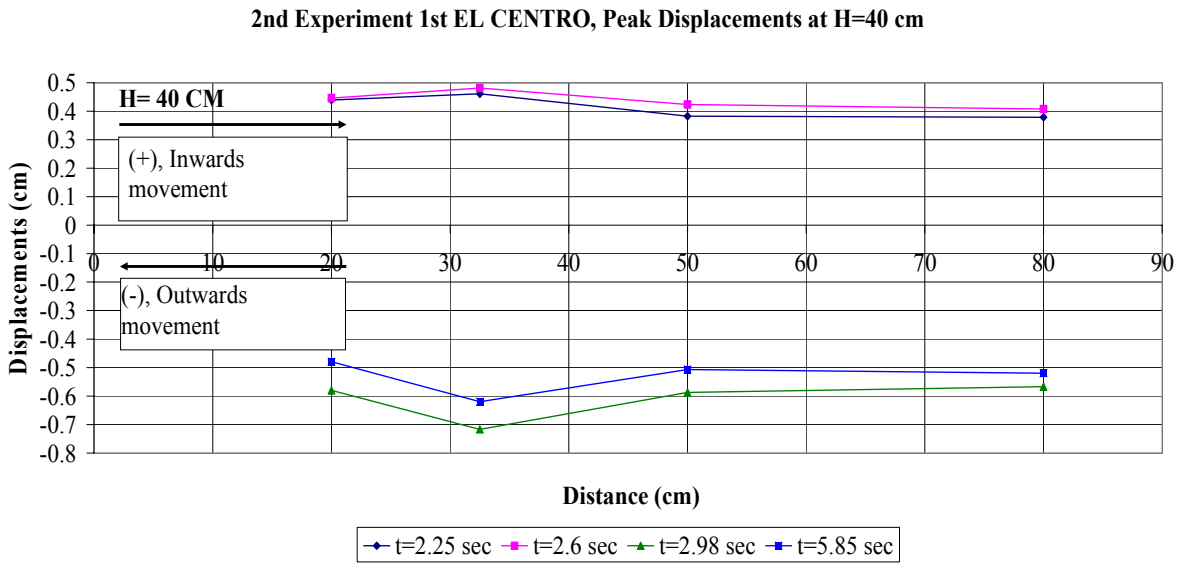

Figure 9.50. Peak relative displacements observed on the geotextile reinforcement at H = 40 cm in 1st El Centro excitation of the 2nd experiment

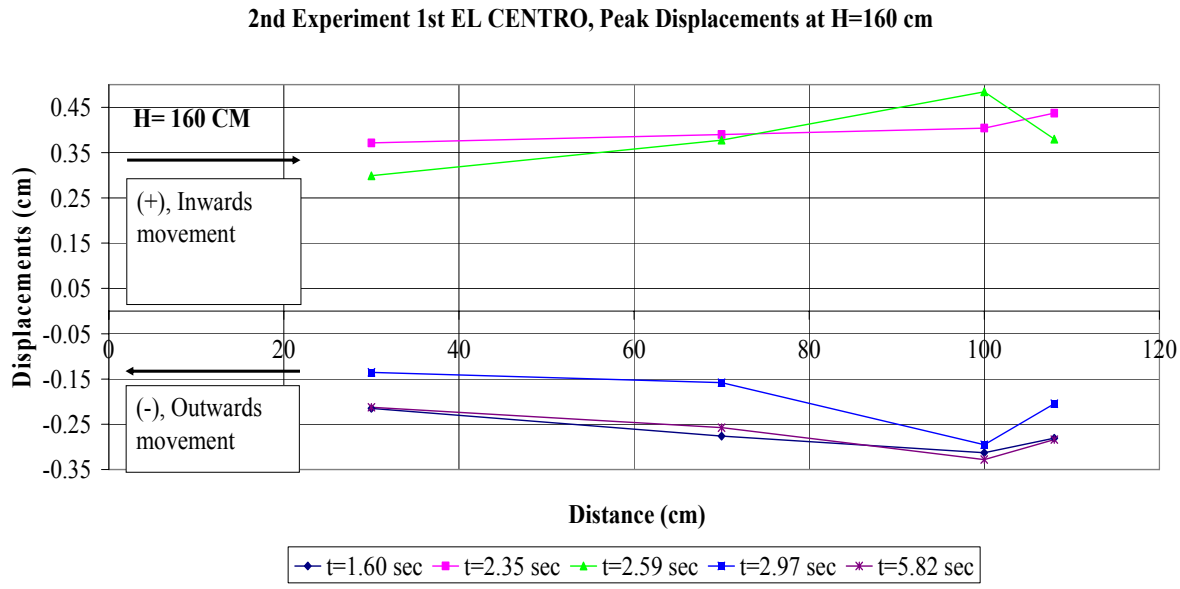

Figure 9.51. Peak relative displacements observed on the geotextile reinforcement at H = 160 cm in 1st El Centro excitation of the 2nd experiment

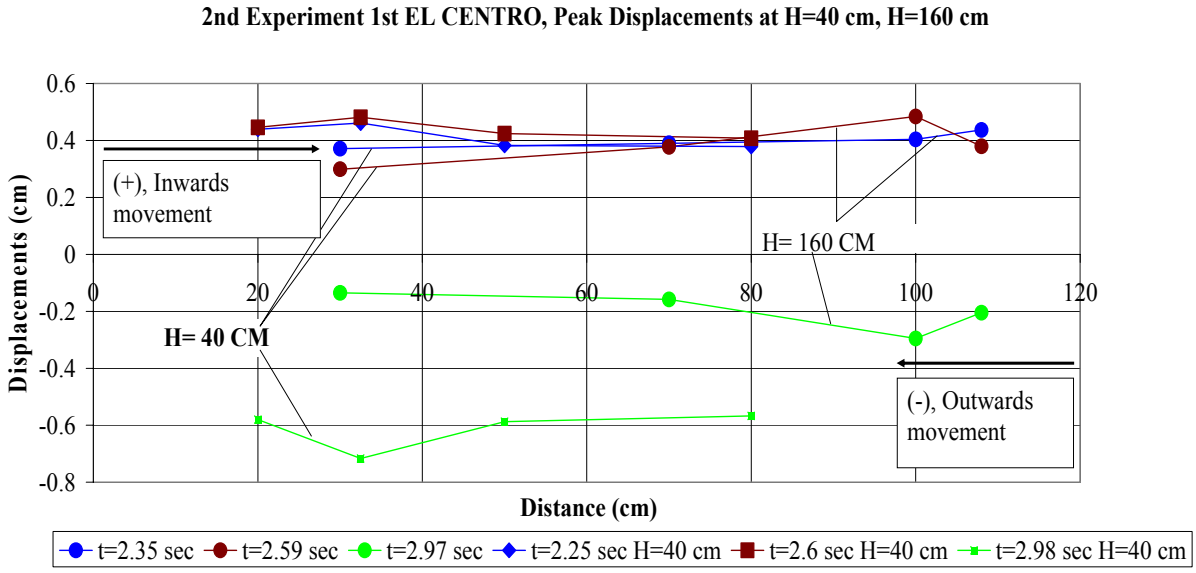

Figure 9.52. Comparisons of peak relative displacements measured on the geotextile reinforcements at H=40 cm and H=160 cm for the 1st El Centro excitation of the 2nd experiment

In Table 9.20 and in Figures 9.53 and 9.54, calculated average strains according to the maximum relative displacements can be seen.

Table 9.20. Calculated average strain values on the geotextile reinforcements at the 1st El Centro excitation of the 2nd experiment

H= 160 cm	Regions between the measurement locations		
	30 - 70	**70 - 100**	**100 - 108**
t=1.60 sec	-0.0015	-0.0012	0.0040
t=2.35 sec	0.0005	0.0005	0.0041
t=2.59 sec	0.0020	0.0036	-0.0131
t=2.97 sec	-0.0006	-0.0046	0.0113
t=5.82 sec	-0.0011	-0.0023	0.0055
H= 40 cm	**Regions between the measurement locations**		
	20 - 32.5	**32.5 - 50**	**50 - 80**
t=2.25 sec	0.0017	-0.0045	-0.0001
t=2.6 sec	0.0028	-0.0033	-0.0005
t=2.98 sec	-0.0109	0.0074	0.0007
t=5.85 sec	-0.0112	0.0065	-0.0004

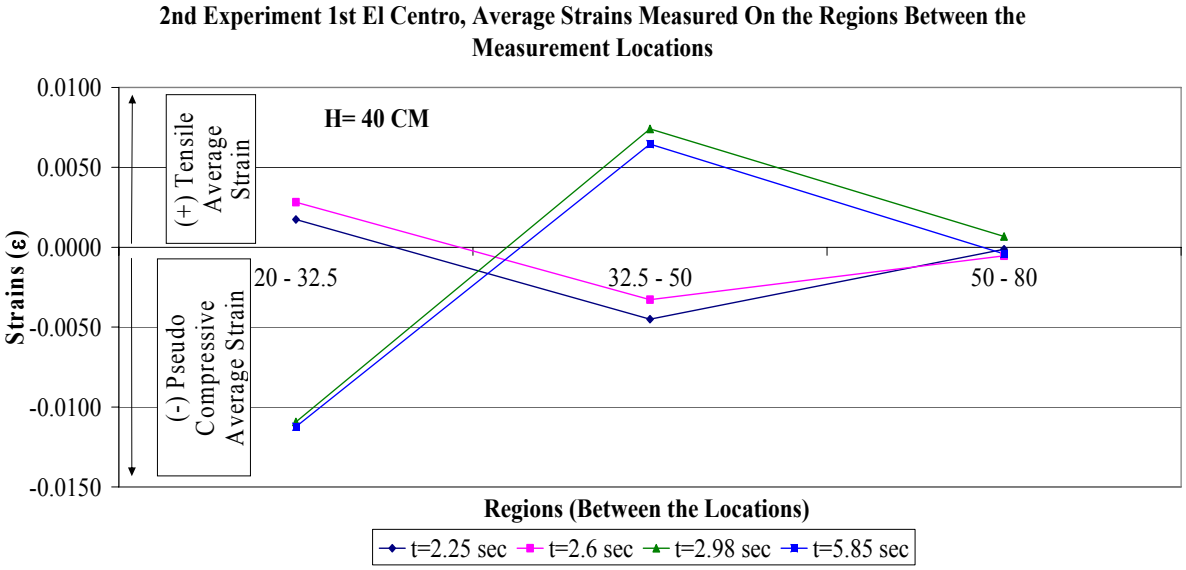

Figure 9.53. Average strains measured on the geotextile reinforcement at the regions between the measurement locations of the 2nd experiment 1st El Centro excitation at thelevel H = 40 cm

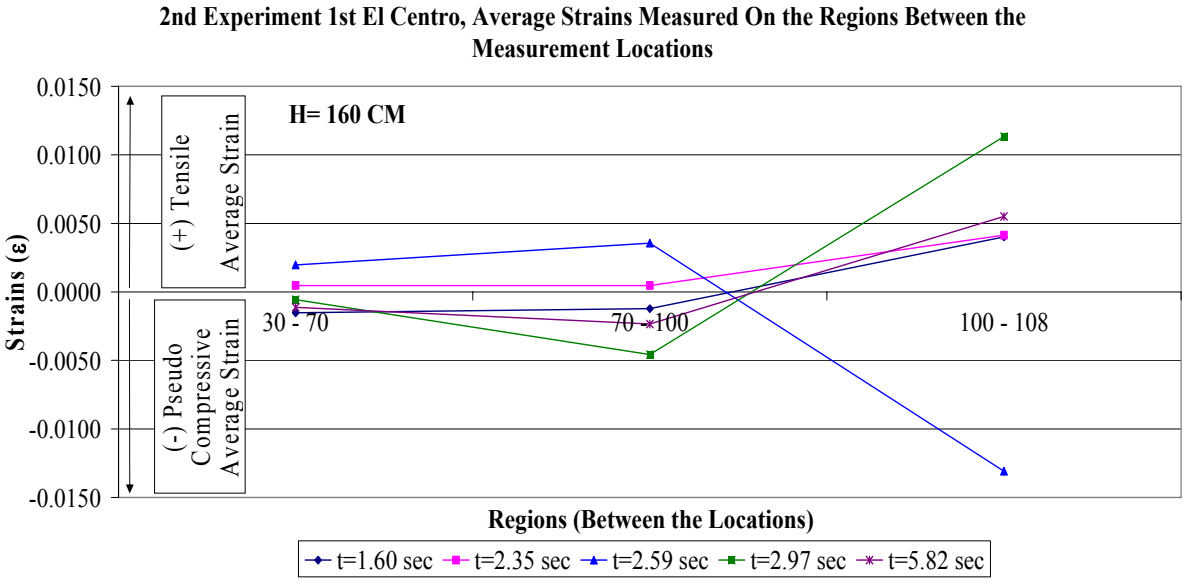

Figure 9.54. Average strains measured on the geotextile reinforcement at the regions between the measurement locations of the 2nd experiment 1st El Centro excitation at the level H = 160 cm

Presented in Figures 9.55 and 9.56 are the calculated average-strain time history records of the geotextile members at the regions between the measurement locations.

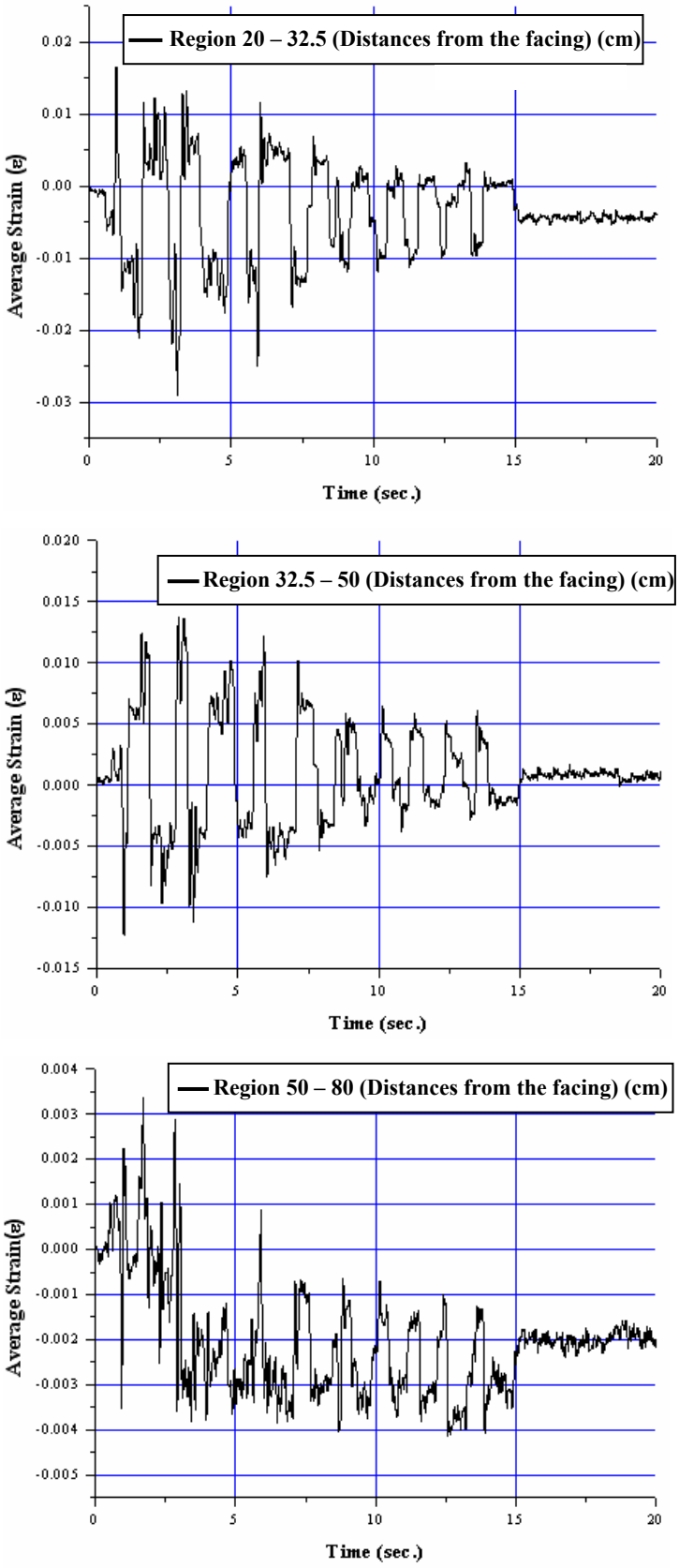

Figure 9.55. Average strains measured on the geotextile reinforcement at the regions in the 2nd experiment 1st El Centro excitation at level H = 40 cm

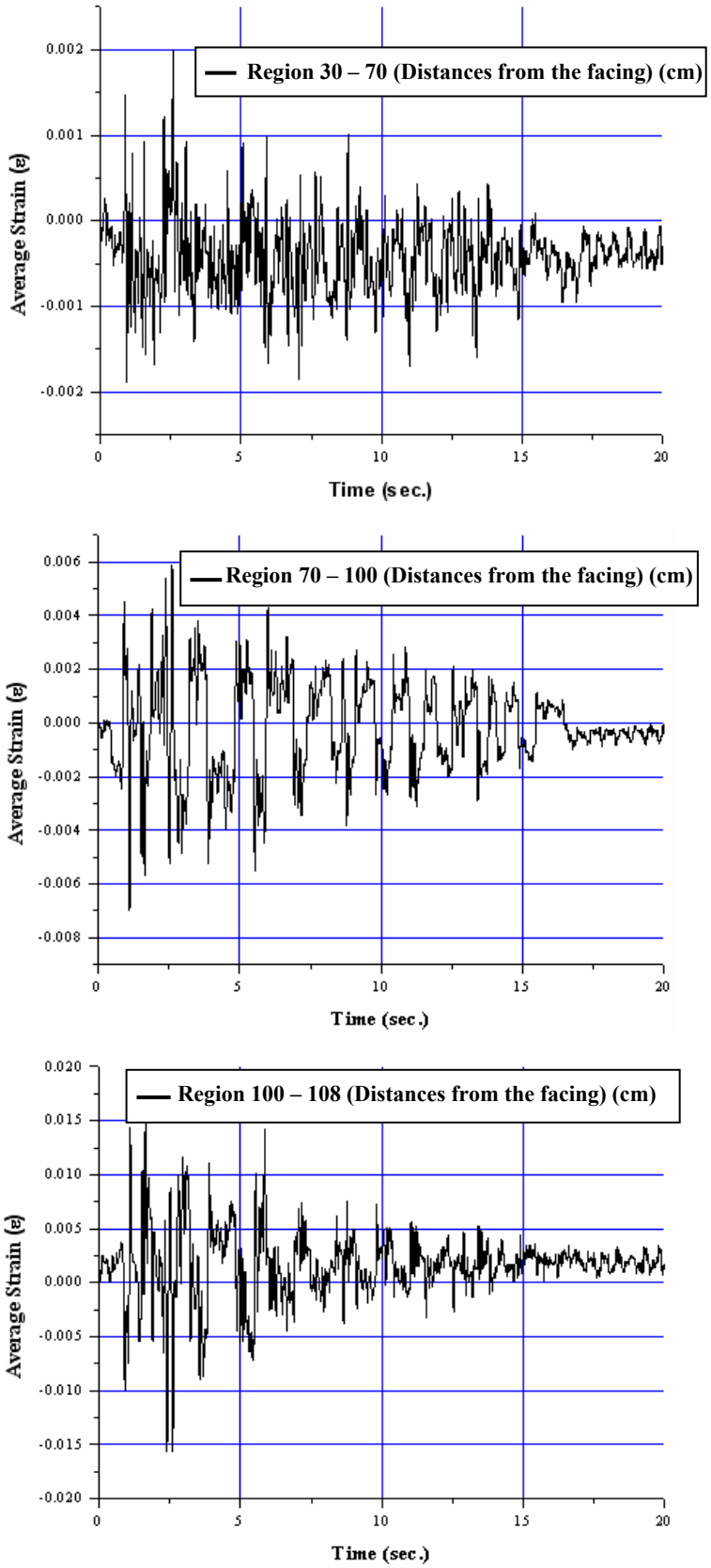

Figure 9.56. Average strains measured on the geotextile reinforcement at the regions in the 2nd experiment 1st El Centro excitation at level H = 160 cm

Figures 9.57 and 9.58 demonstrate the deformation behavior in all of the regions at levels H=40 cm and H=160 cm, respectively. At level H=40 cm direct opposite curves are observed between the regions 20-32.5 and 32.5-50 cm at the same time intervals, which indicates the advancement of pressure waves and resultant compressive and tensile zones (Figure 9.57). The behavior of the 50-80 cm region is similar to 32.5-50 cm region, but much lower values of strains are observed. This shows that as the distance to the failure surface increases, the strains diminish.

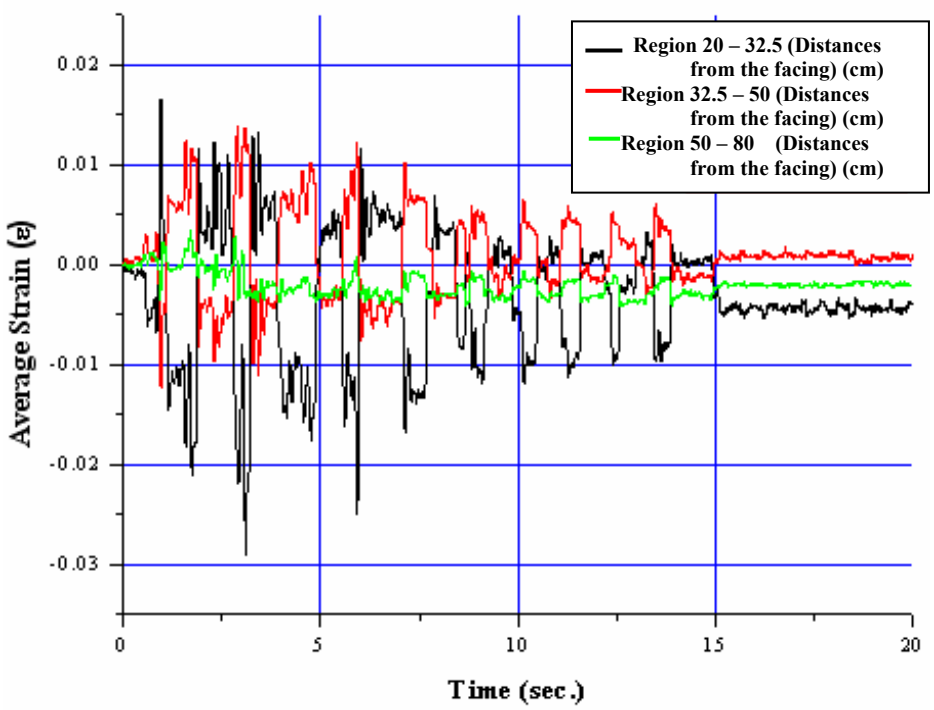

Figure 9.57. All the average strains measured on the geotextile reinforcement at the regions in the 2nd experiment 1st El Centro excitation at level H = 40 cm

At level H=160 cm by observing direct opposite curves between the regions 70-100 cm and 100-108 cm at the same time intervals, again it can be deduced that propagation of the pressure waves took place causing tensile and compressive zones to develop in the soil (Figure 9.58). Because the region 30-70 cm is situated close to the facing wall and far away from the critical failure surface lower level of strains were measured as expected.

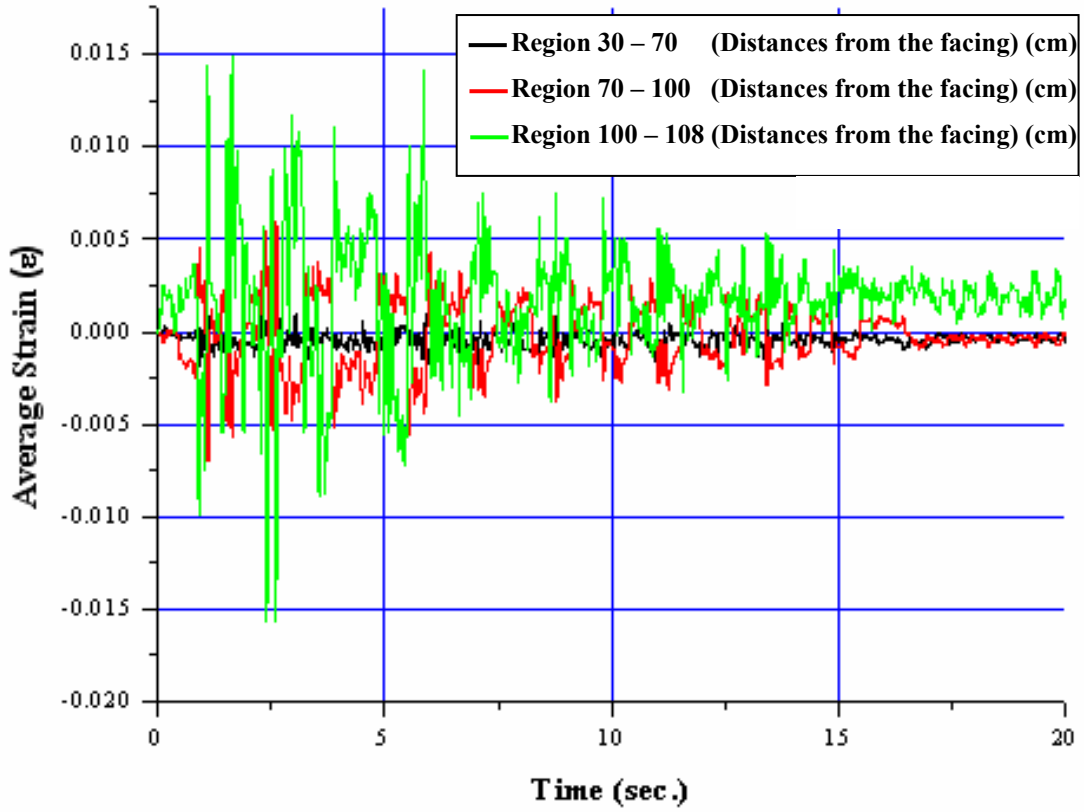

Figure 9.58. All the average strains measured on the geotextile reinforcement at the regions in the 2nd experiment 1st El Centro excitation at level H = 160 cm

9.2.2.3. 2nd El Centro Excitation. The base time-history motions for this excitation are shown in Figure 9.59.

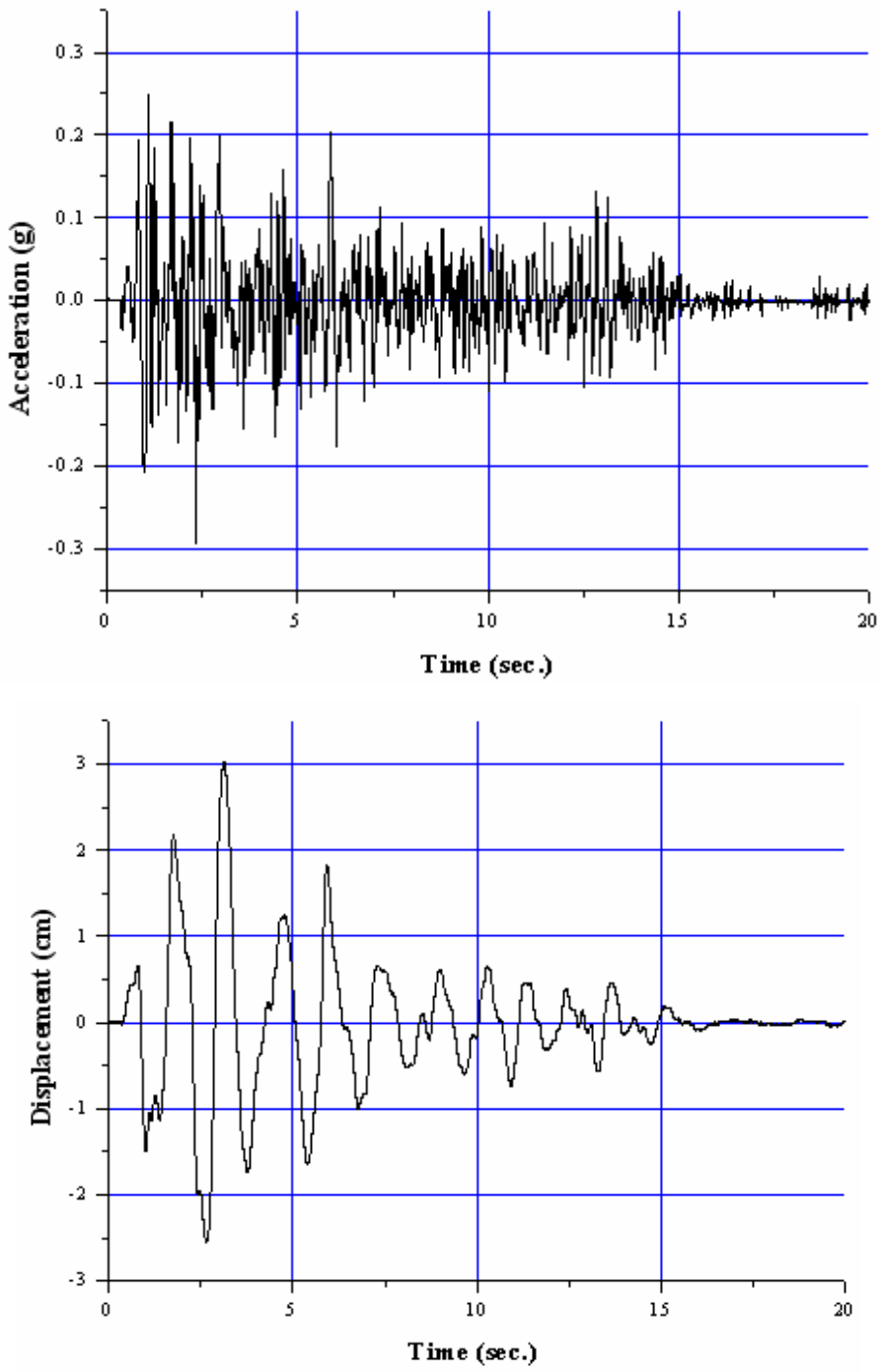

Figure 9.59. 2nd experiment 2nd El Centro excitation record

The peak relative displacements measured on the geotextile reinforcements in both directions were calculated to be as in Table 9.21 and in Figures 9.60 to 9.62.

Table 9.21. Peak relative displacements observed on the geotextile reinforcement at the 2nd El Centro excitation of the 2nd experiment (units are in cm)

H= 160 cm	Trans. 8		Trans. 7		Trans. 6		Trans. 5	
	L=30 cm		L=70 cm		L=100 cm		L=108 cm	
	Max. (1)	Max. (2)	Max. (1)	Max. (2)	Max. (1)	Max. (2)	Max.(1)	Max.(2)
t=0.97 sec	0.2694		0.2347		0.2678		0.2647	
t=2.57 sec	0.3341		0.3994		0.3973		0.3372	
t=2.8 sec		-0.0321		-0.0337		-0.1953		-0.1248
t=3.05 sec		-0.2253		-0.2486		-0.3367		-0.2813
t=5.82 sec		-0.1880		-0.1958		-0.2813		-0.2486
H= 40 cm	Trans. 4		Trans. 3		Trans. 2		Trans. 1	
	L=20 cm		L=32,5 cm		L=50 cm		L=80 cm	
	Max. (1)	Max. (2)	Max. (1)	Max. (2)	Max. (1)	Max. (2)	Max.(1)	Max.(2)
t=0.9 sec	0.3828		0.4869		0.3864		0.3657	
t=2.6 sec	0.3875		0.3704		0.3807		0.2559	
t=2.8 sec		-0.4662		-0.6589		-0.4999		-0.4672
t=5.81 sec		-0.4937		-0.5988		-0.4465		-0.4092

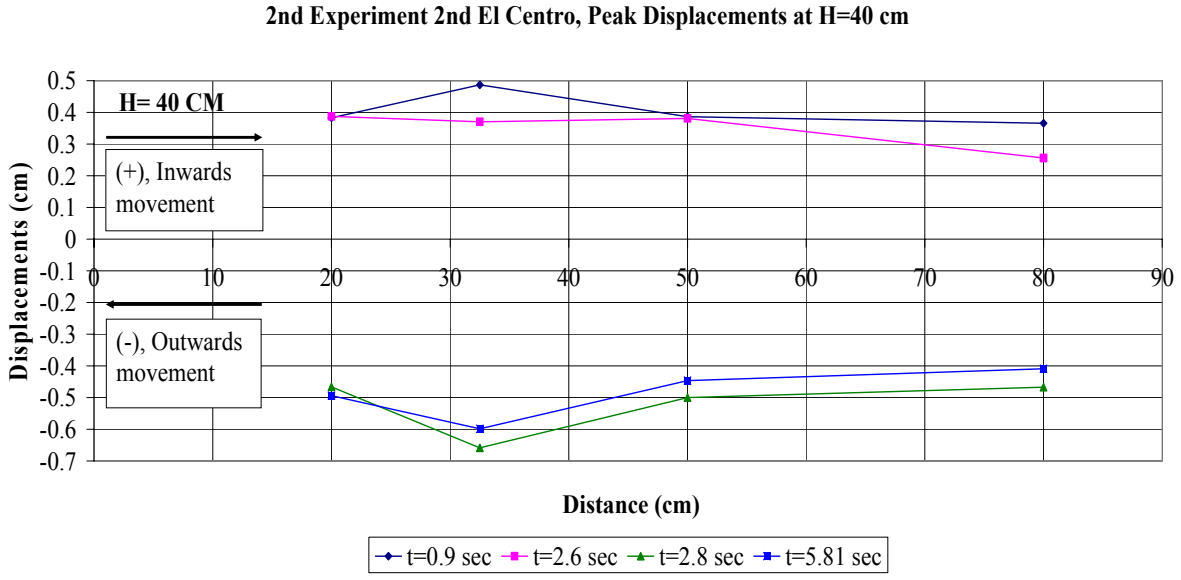

Figure 9.60. Peak relative displacements observed on the geotextile reinforcement at H = 40 cm in 2nd El Centro excitation of the 2nd experiment

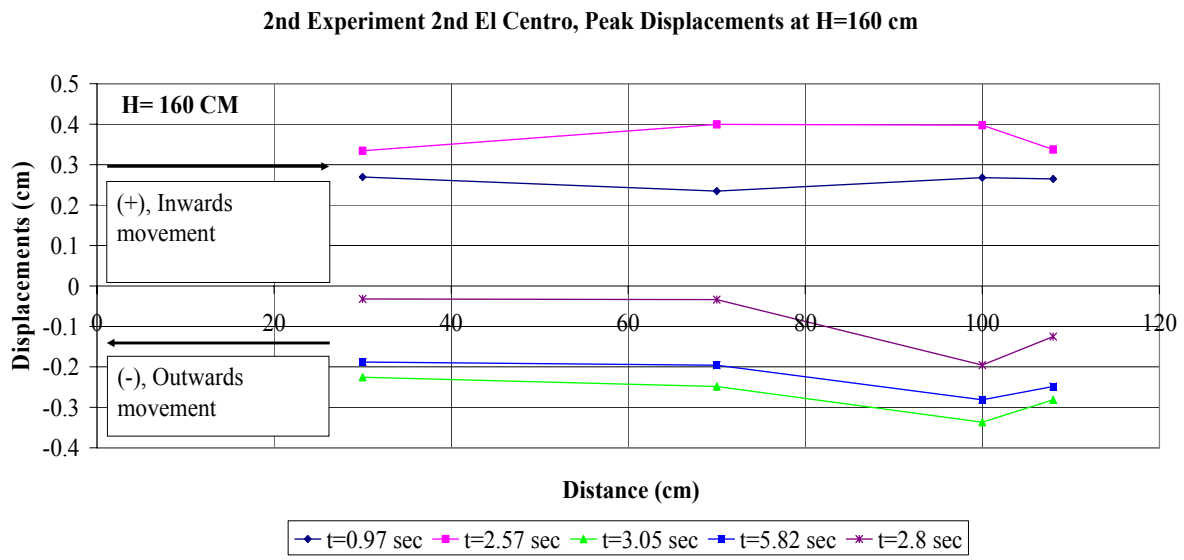

Figure 9.61. Peak relative displacements observed on the geotextile reinforcement at H = 160 cm in 2nd El Centro excitation of the 2nd experiment

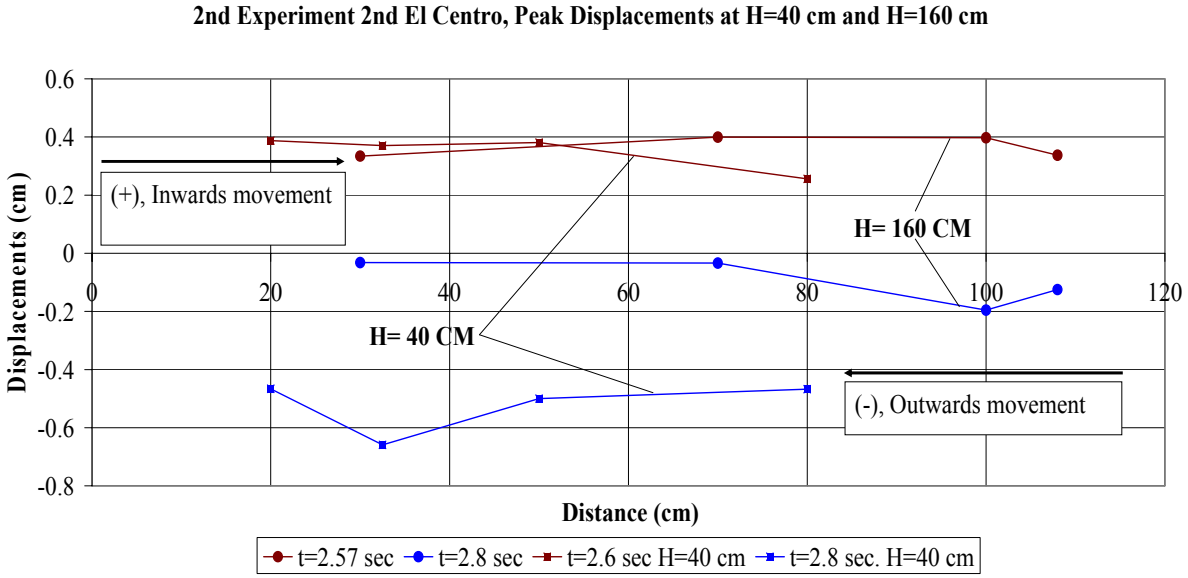

Figure 9.62. Comparisons of peak relative displacements measured on the geotextile reinforcements at H=40 cm and H=160 cm for the 2nd El Centro excitation of the 2nd experiment

In Table 9.22 and in Figures 9.63 and 9.64, calculated average strains according to the maximum relative displacements can be seen.

Table 9.22. Calculated average strain values on the geotextile reinforcements at the 2nd El Centro excitation of the 2nd experiment

H= 160 cm	Regions between the measurement locations		
	30 - 70	**70 - 100**	**100 - 108**
t=0.97 sec	-0.0009	0.0011	-0.0004
t=2.57 sec	0.0016	-0.0001	-0.0075
t=2.8 sec	0.0000	-0.0054	0.0088
t=3.05 sec	-0.0006	-0.0029	0.0069
t=5.82 sec	-0.0002	-0.0028	0.0041
H= 40 cm	**Regions between the measurement locations**		
	20 - 32.5	**32.5 - 50**	**50 - 80**
t=0.9 sec	0.0083	-0.0057	-0.0007
t=2.6 sec	-0.0014	0.0006	-0.0042
t=2.8 sec	-0.0154	0.0091	0.0011
t=5.81 sec	-0.0084	0.0087	0.0012

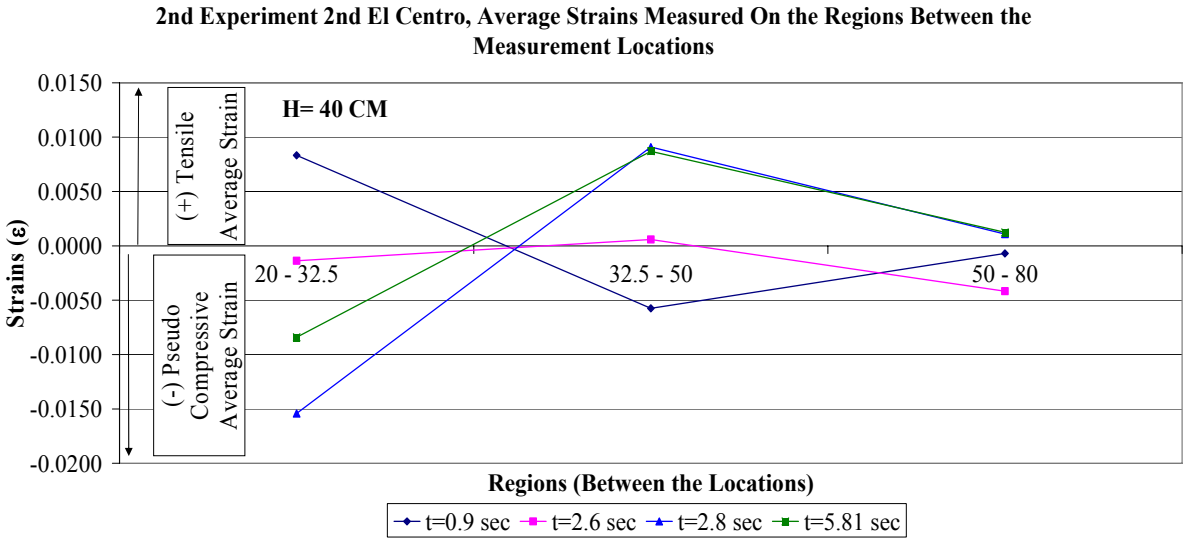

Figure 9.63. Average strains measured on the geotextile reinforcement at the regions between the measurement locations of the 2nd experiment 2nd El Centro excitation at the level H = 40 cm

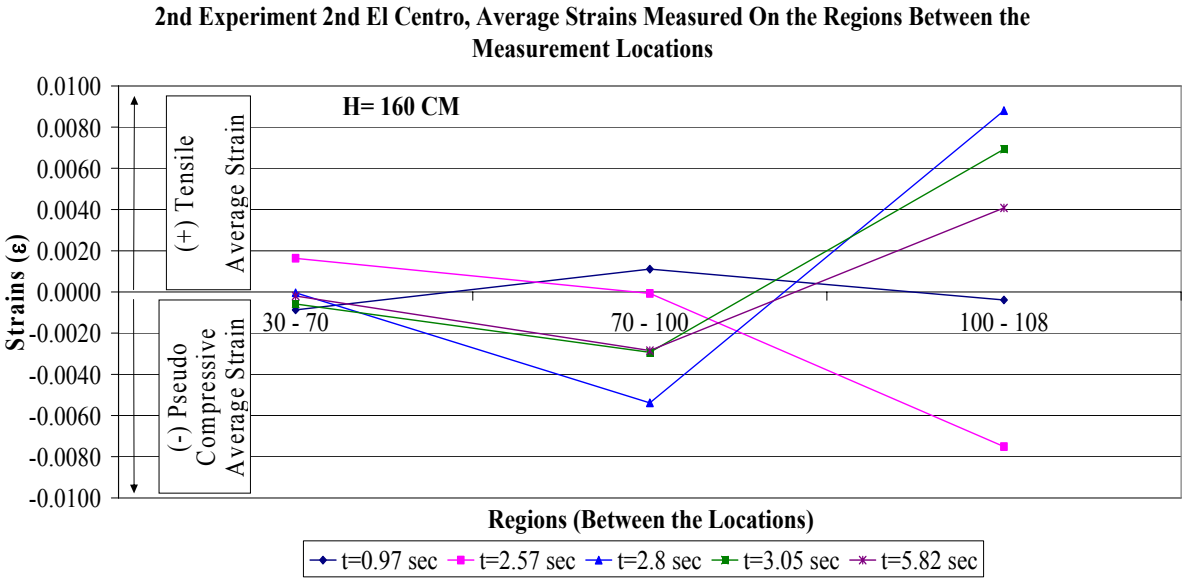

Figure 9.64. Average strains measured on the geotextile reinforcement at the regions between the measurement locations of the 2nd experiment 2nd El Centro excitation at thelevel H = 160 cm

Presented in Figures 9.65 and 9.66 are the calculated average-strain time history records of the geotextile members at the regions between the measurement locations.

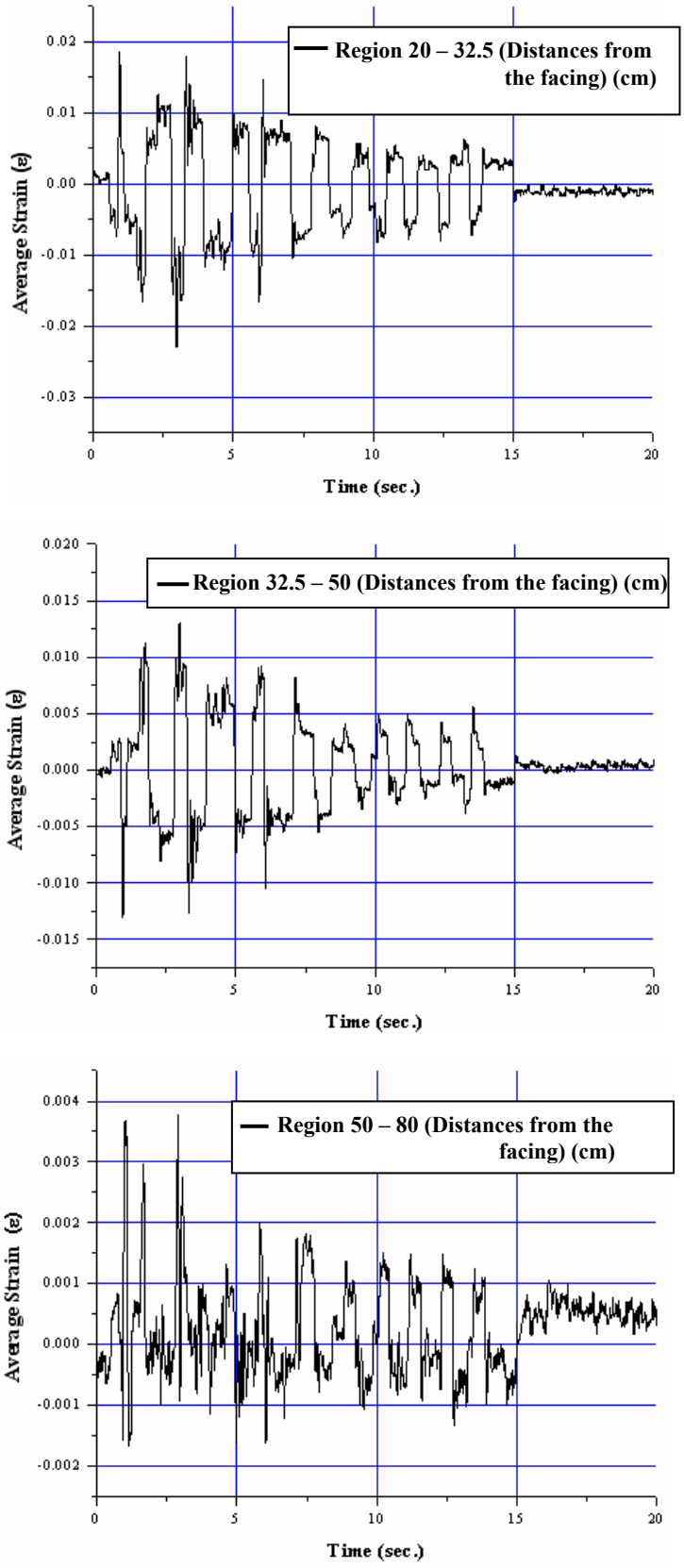

Figure 9.65. Average strains measured on the geotextile reinforcement at the regions in the 2nd experiment 2nd El Centro excitation at level H = 40 cm

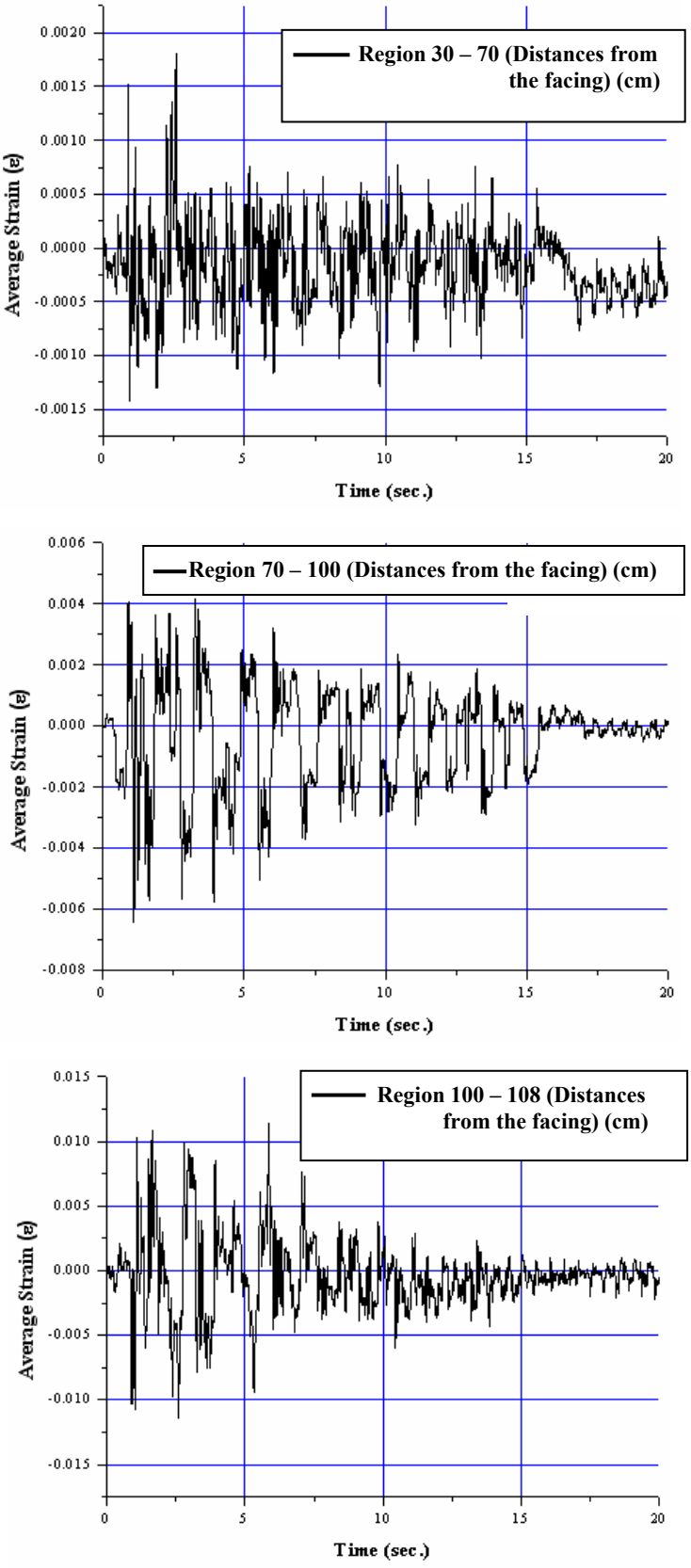

Figure 9.66. Average strains measured on the geotextile reinforcement at the regions in the 2nd experiment 2nd El Centro excitation at level H = 160 cm

Figures 9.67 and 9.68 demonstrate the deformation behavior in all of the regions at levels H=40 cm and H=160 cm, respectively. At level H=40 cm direct opposite curves are observed between the regions 20-32.5 and 32.5-50 cm, which is a possible indication that there is a transition point from active to resistant passive zones situated most probably in the region where maximum average strains were measured (Figure 9.67). The behavior of the 50-80 cm region is similar to 32.5-50 cm region, but much lower values of strains are observed. This indicates that as the distance to the failure surface increases, the strains diminish.

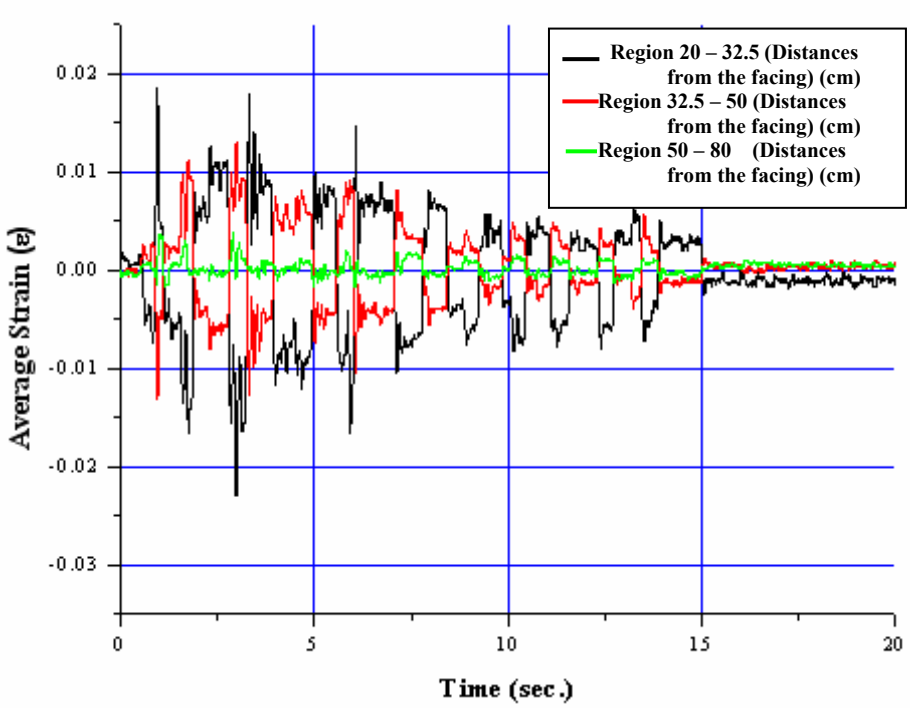

Figure 9.67. All the average strains measured on the geotextile reinforcement at the regions in the 2nd experiment 2nd El Centro excitation at level H = 40 cm

At level H=160 cm direct opposite curves are observed between the regions 70-100 cm and 100-108 cm (Figure 9.68) indicating that there is a transition point from active to resistant passive zones situated most probably in the region where maximum average strains were measured. Because the region 30-70 cm is situated close to the facing wall and far away from the critical failure surface lower level of strains were measured as expected.

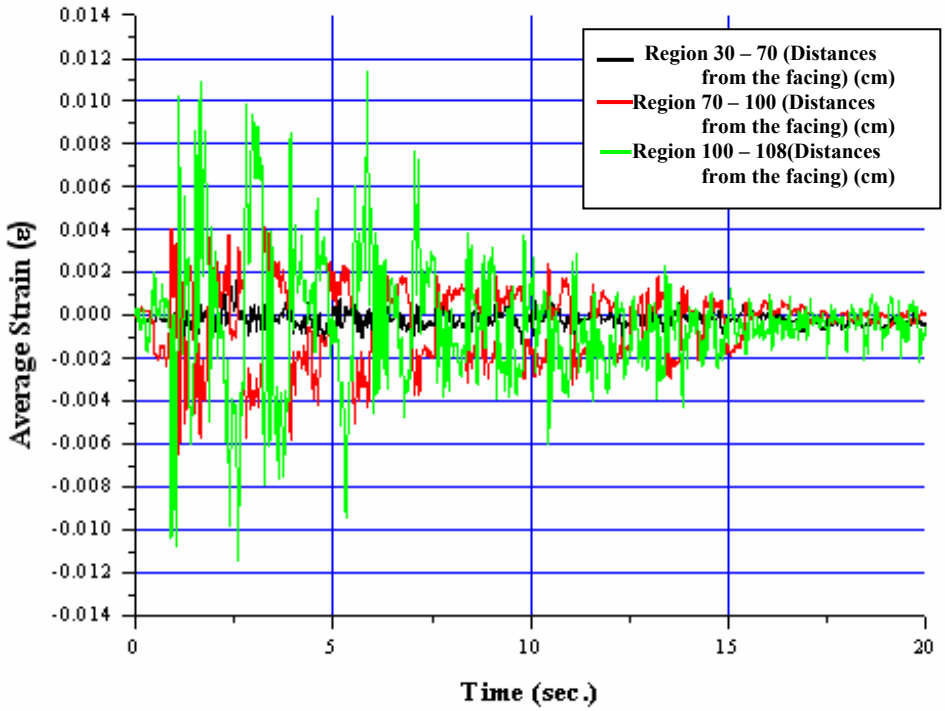

Figure 9.68. All the average strains measured on the geotextile reinforcement at the regions in the 2nd experiment 2nd El Centro excitation at level H = 160 cm

9.2.2.4. 3rd El Centro Excitation. The base time-history motions for this excitation are shown in Figure 9.69.

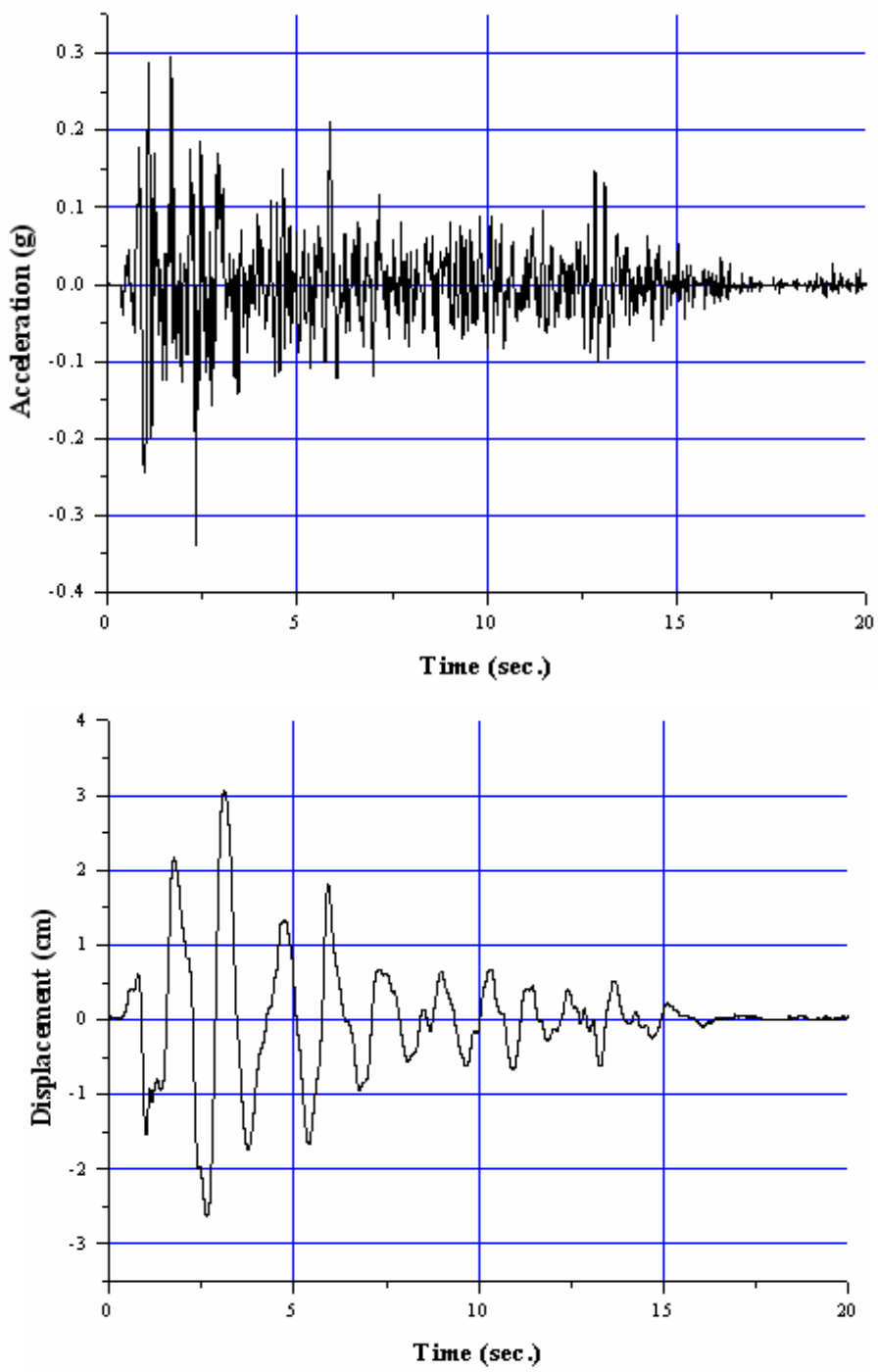

Figure 9.69. 2nd experiment 3rd El Centro excitation record

The relative peak displacements observed on the geotextile reinforcements in both directions were calculated to be as in Table 9.23 and in Figures 9.70 to 9.72.

Table 9.23. Relative peak displacements observed on the geotextile reinforcements at the 3rd El Centro excitation of the 2nd experiment (units are in cm)

Relative Peak Displacements (2nd Experiment 3rd EL CENTRO %100)								
H= 160 cm	**Trans. 8**		**Trans. 7**		**Trans. 6**		**Trans. 5**	
	L=30 cm		**L=70 cm**		**L=100 cm**		**L=108 cm**	
	Max.(1)	**Max.(2)**	**Max.(1)**	**Max.(2)**	**Max.(1)**	**Max.(2)**	**Max.(1)**	**Max.(2)**
t=0.89 sec	0.2117		0.1871		0.2763		0.2325	
t=2.32 sec	0.2988		0.3010		0.3267		0.3242	
t=2.55 sec	0.2630		0.3267		0.3403		0.2832	
t=2.86 sec		-0.1439		-0.1730		-0.2705		-0.2458
t=4.55 sec		-0.2082		-0.2169		-0.2974		-0.2564
t=5.82 sec		-0.1768		-0.1808		-0.2854		-0.2467
H= 40 cm	**Trans. 4**		**Trans. 3**		**Trans. 2**		**Trans. 1**	
	L=20 cm		**L=32.5 cm**		**L=50 cm**		**L=80 cm**	
	Max.(1)	**Max.(2)**	**Max.(1)**	**Max.(2)**	**Max.(1)**	**Max.(2)**	**Max.(1)**	**Max.(2)**
t=0.91 sec	0.3808		0.5006		0.3763		0.3711	
t=2.31 sec	0.2526		0.3748		0.2503		0.2443	
t=2.55 sec	0.2996		0.4075		0.3228		0.3023	
t=2.8 sec		-0.4749		-0.6589		-0.4959		-0.4836
t=4.58 sec		-0.4794		-0.5463		-0.4685		-0.4523
t=5.77 sec		-0.5002		-0.5800		-0.4753		-0.4356

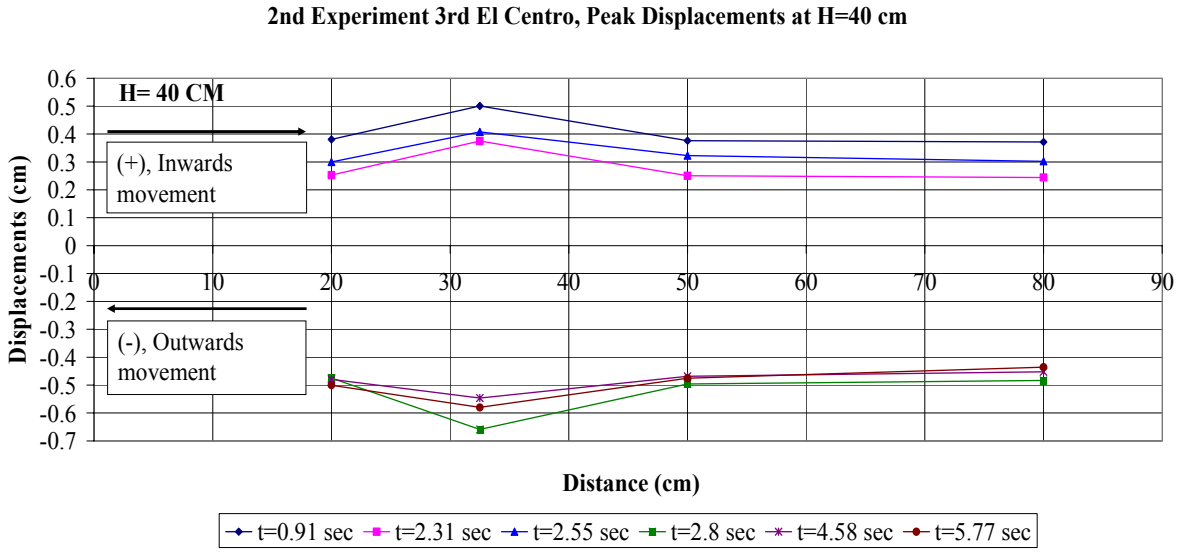

Figure 9.70. Relative peak displacements measured on the geotextile reinforcement at H = 40 cm in 3rd El Centro excitation of the 2nd experiment

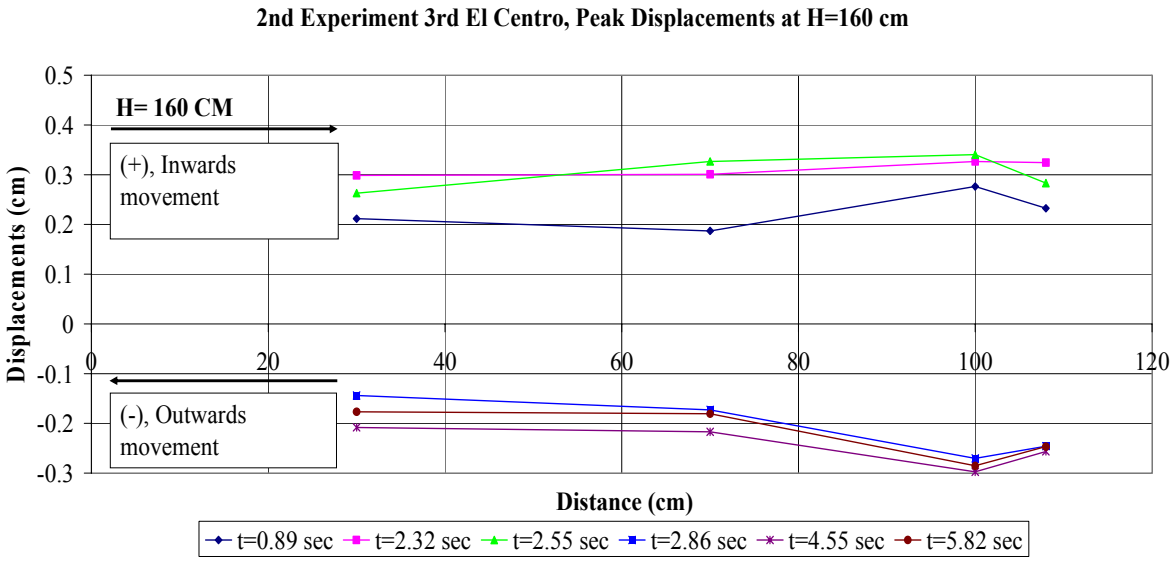

Figure 9.71. Relative peak displacements measured on the geotextile reinforcement at H = 160 cm in 3rd El Centro excitation of the 2nd experiment

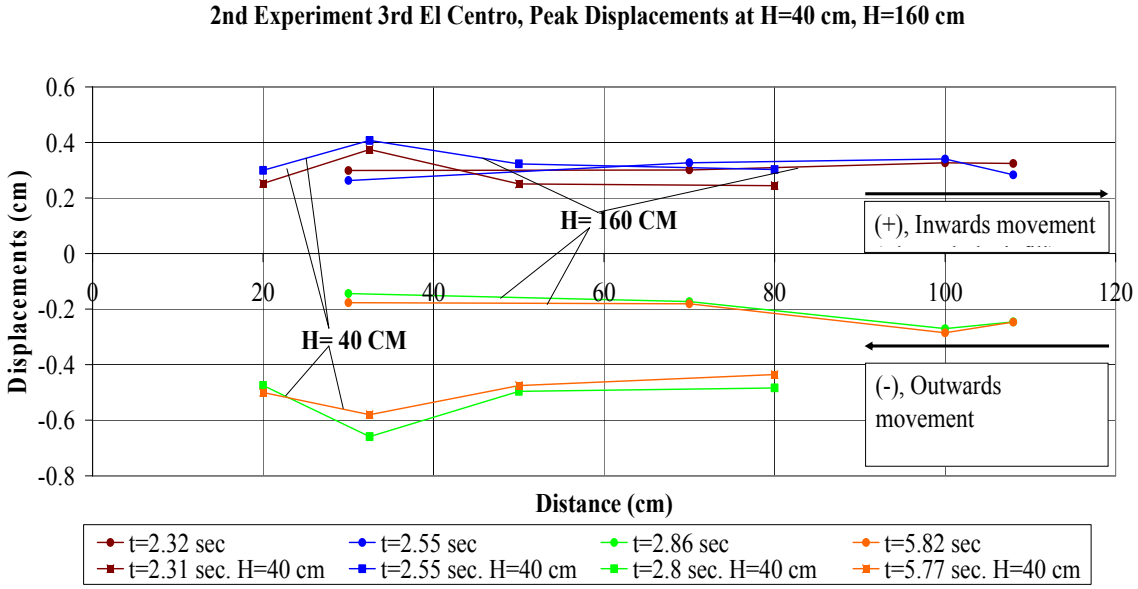

Figure 9.72. Comparisons of relative peak displacements measured on the geotextile reinforcements at H=40 cm and H=160 cm for the 3rd El Centro excitation of the 2nd experiment

In Table 9.24 and in Figures 9.73 and 9.74, calculated average strains on the geotextile reinforcements according to the maximum relative displacements can be seen.

Table 9.24. Calculated average strain values on the geotextile reinforcements at the 3rd El Centro excitation of the 2nd experiment

H= 160 cm	Regions between the measurement locations		
	30 - 70	70 - 100	100 - 108
t=0.89 sec	-0.0006	0.0030	-0.0055
t=2.32 sec	0.0001	0.0009	-0.0003
t=2.55 sec	0.0016	0.0005	-0.0071
t=2.86 sec	-0.0007	-0.0032	0.0031
t=4.55 sec	-0.0002	-0.0027	0.0051
t=5.82 sec	-0.0001	-0.0035	0.0048
H= 40 cm	**Regions between the measurement locations**		
	20 - 32.5	**32.5 - 50**	**50 - 80**
t=0.91 sec	0.0096	-0.0071	-0.0002
t=2.31 sec	0.0098	-0.0071	-0.0002
t=2.55 sec	0.0086	-0.0048	-0.0007
t=2.8 sec	-0.0147	0.0093	0.0004
t=4.58 sec	-0.0054	0.0044	0.0005
t=5.77 sec	-0.0064	0.0060	0.0013

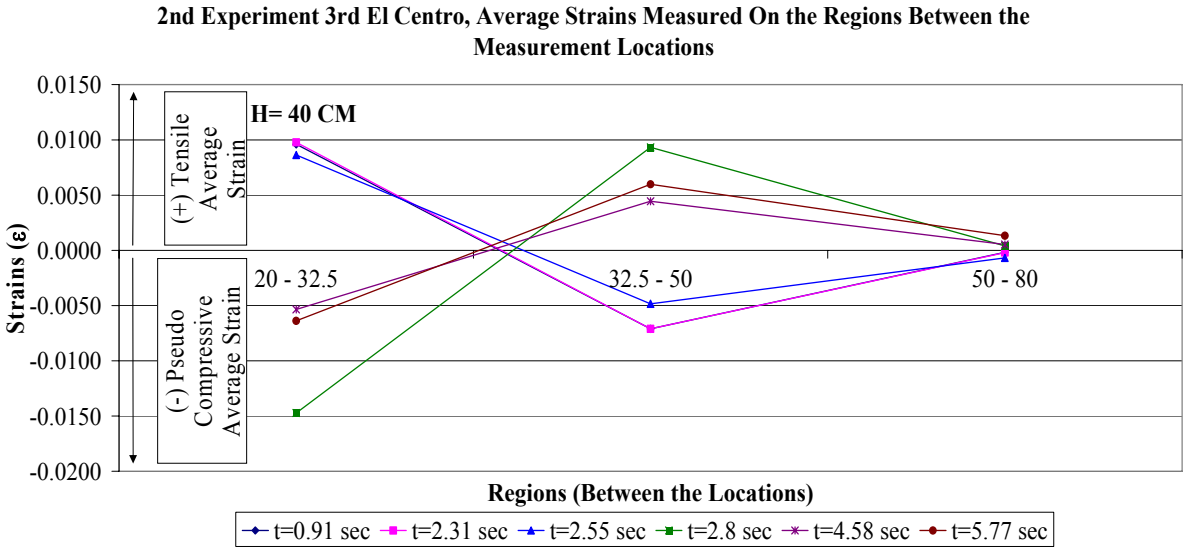

Figure 9.73. Average strains measured on the geotextile reinforcement at the regions between the measurement locations of the 2nd experiment 3rd El Centro excitation at the level H = 40 cm

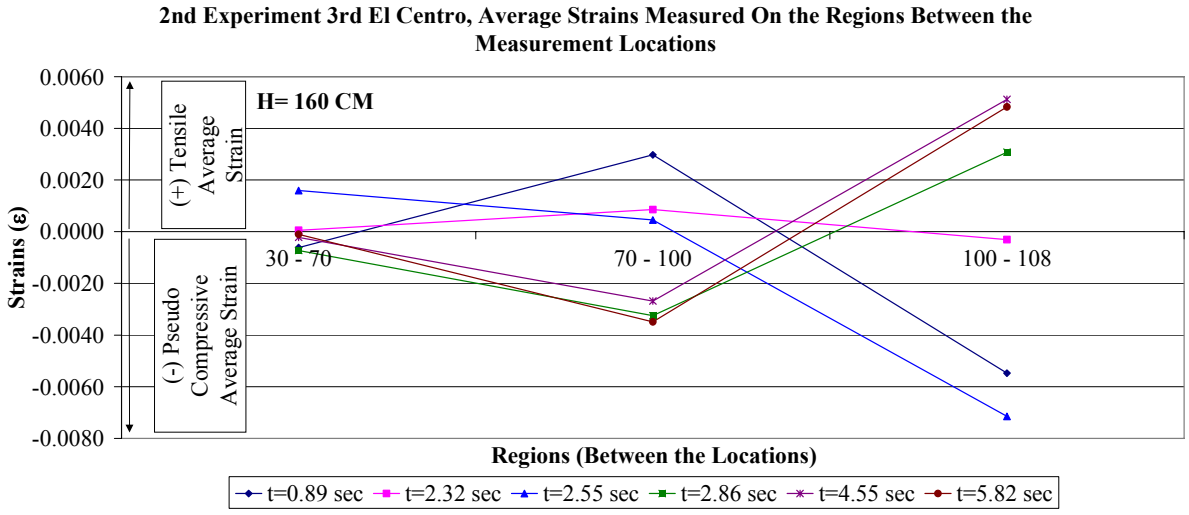

Figure 9.74. Average strains measured on the geotextile reinforcement at the regions between the measurement locations of the 2nd experiment 3rd El Centro excitation at the level H = 160 cm

Presented in Figures 9.75 and 9.76 are the calculated average-strain time history records of the geotextile members at the regions between the measurement locations.

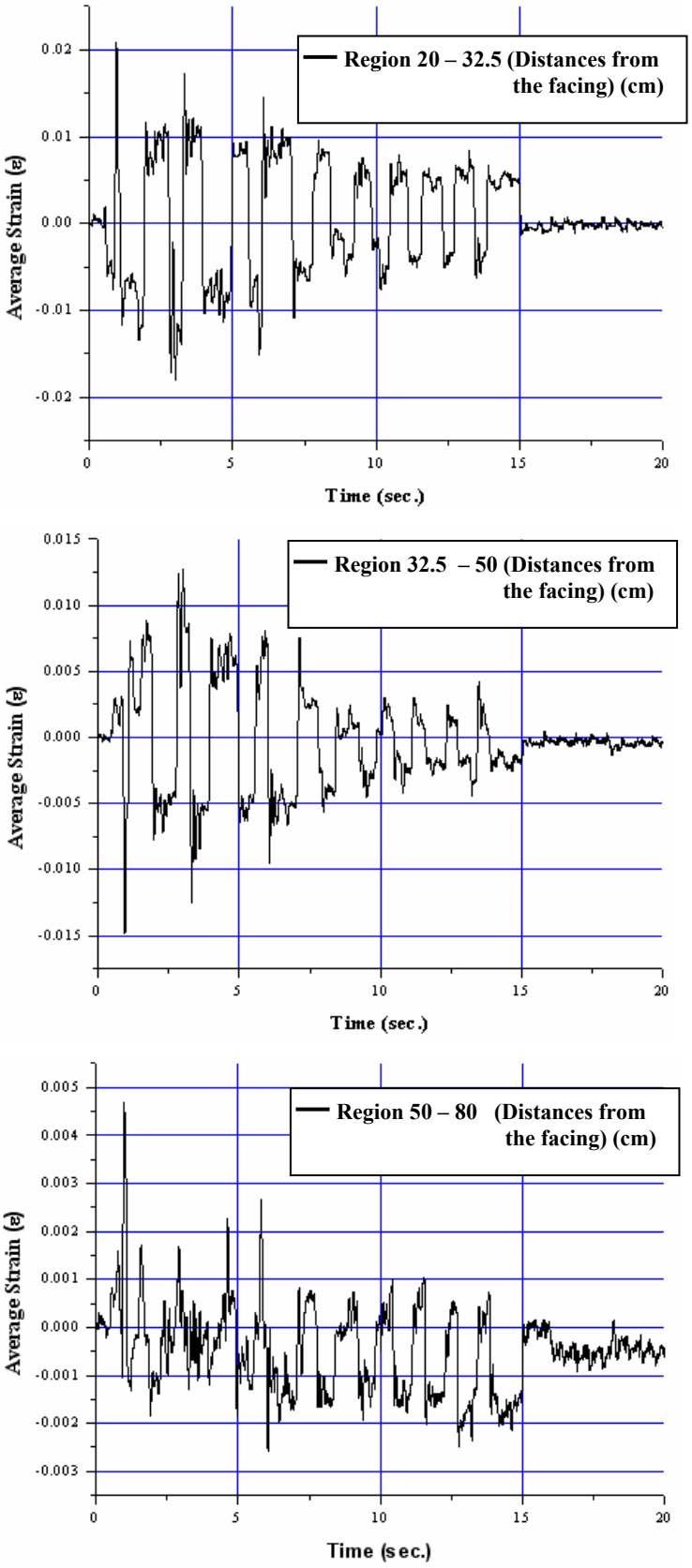

Figure 9.75. Average strains measured on the geotextile reinforcement at the regions in the 2nd experiment 3rd El Centro excitation at level H = 40 cm

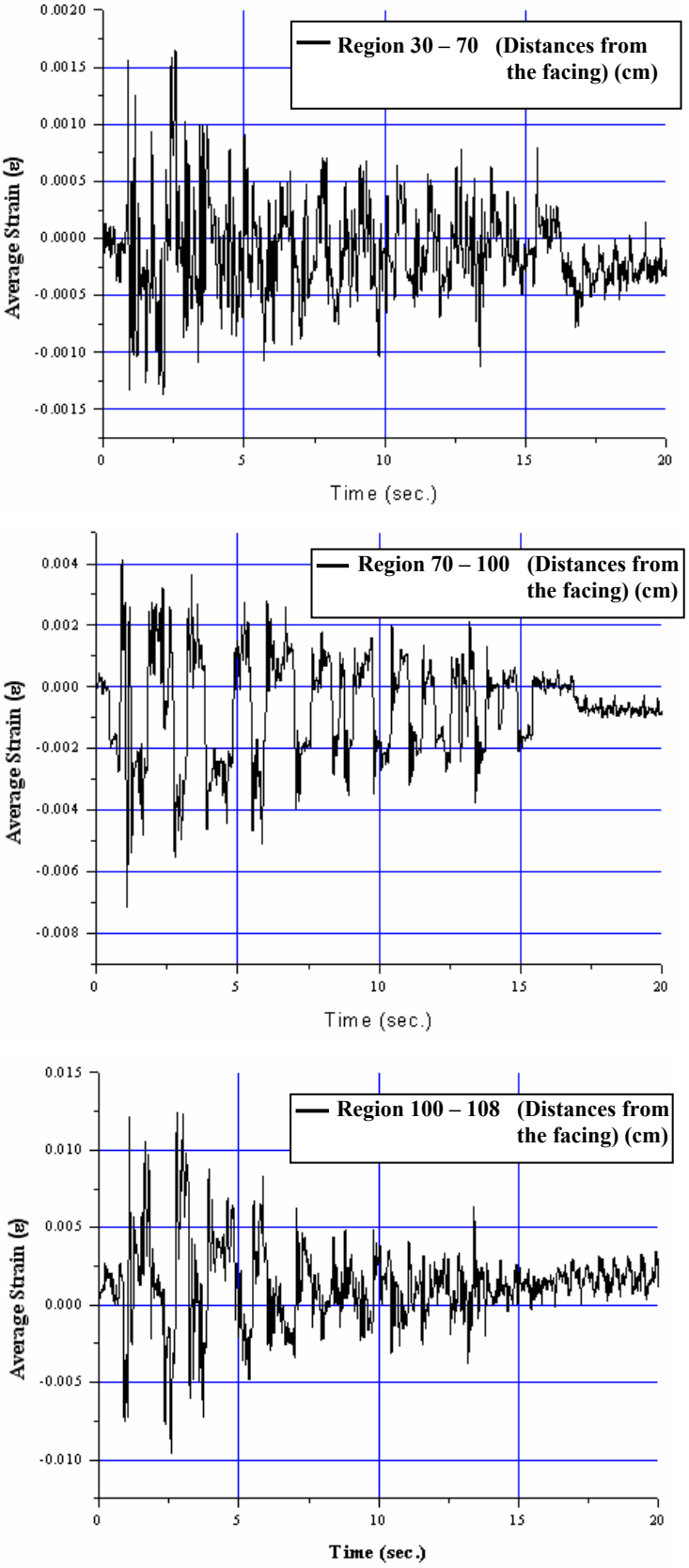

Figure 9.76. Average strains measured on the geotextile reinforcement at the regions in the 2nd experiment 3rd El Centro excitation at level H = 160 cm

Figures 9.77 and 9.78 demonstrate the deformation behavior in all of the regions at levels H=40 cm and H=160 cm, respectively. At level H=40 cm direct opposite curves are observed between the regions 20-32.5 and 32.5-50 cm at the same time intervals, which is the manifestation of tensile and compressive forces that are active in the presence of pressure waves (Figure 9.77). The behavior of the 50-80 cm region is similar to 32.5-50 cm region, but much lower values of strains are observed. This indicates that as the distance to the failure surface increases, the strains diminish.

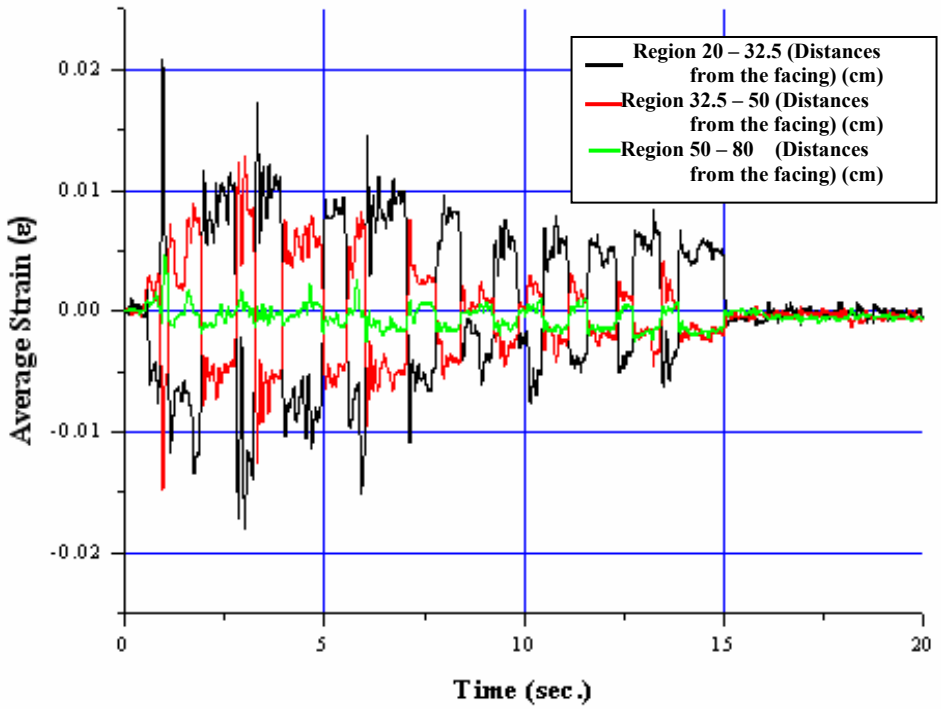

Figure 9.77. All the average strains measured on the geotextile reinforcement at the regions in the 2nd experiment 3rd El Centro excitation at level H = 40 cm

At level H=160 cm direct opposite curves are observed between the regions 70-100 cm and 100-108 cm at the same time intervals, which is an indication of the pressure waves propagating in the soil (Figure 9.78). Because the region 30-70 cm is situated close to the facing wall and far away from the critical failure surface lower level of strains were measured as expected.

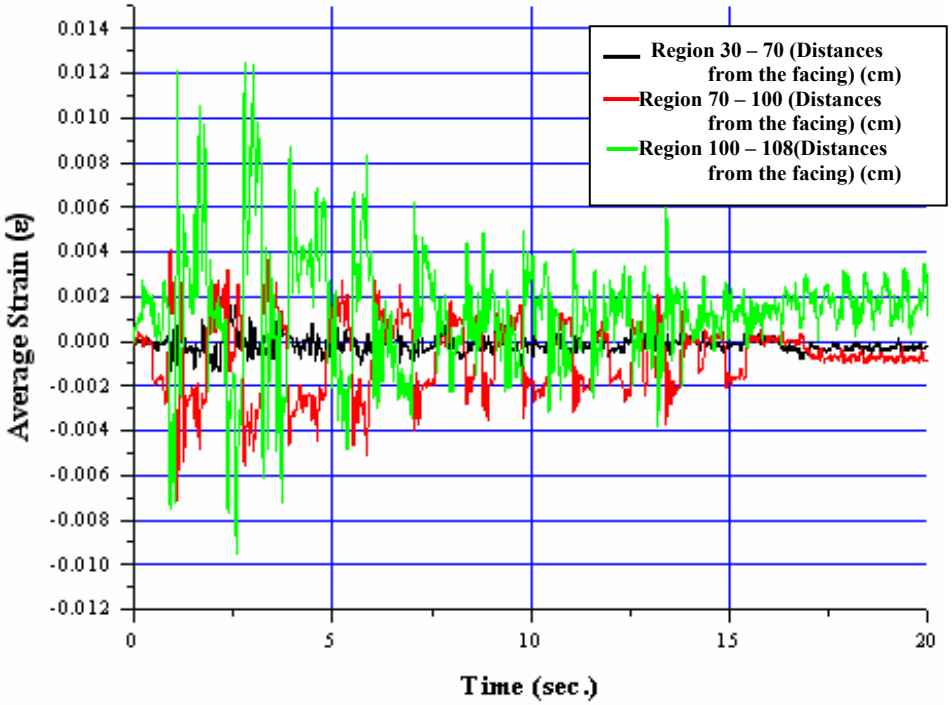

Figure 9.78. All the average strains measured on the geotextile reinforcement at the regions in the 2nd experiment 3rd El Centro excitation at level H = 160 cm

9.2.2.5. 4th El Centro Excitation. The base time-history motions for this excitation are shown in Figure 9.79.

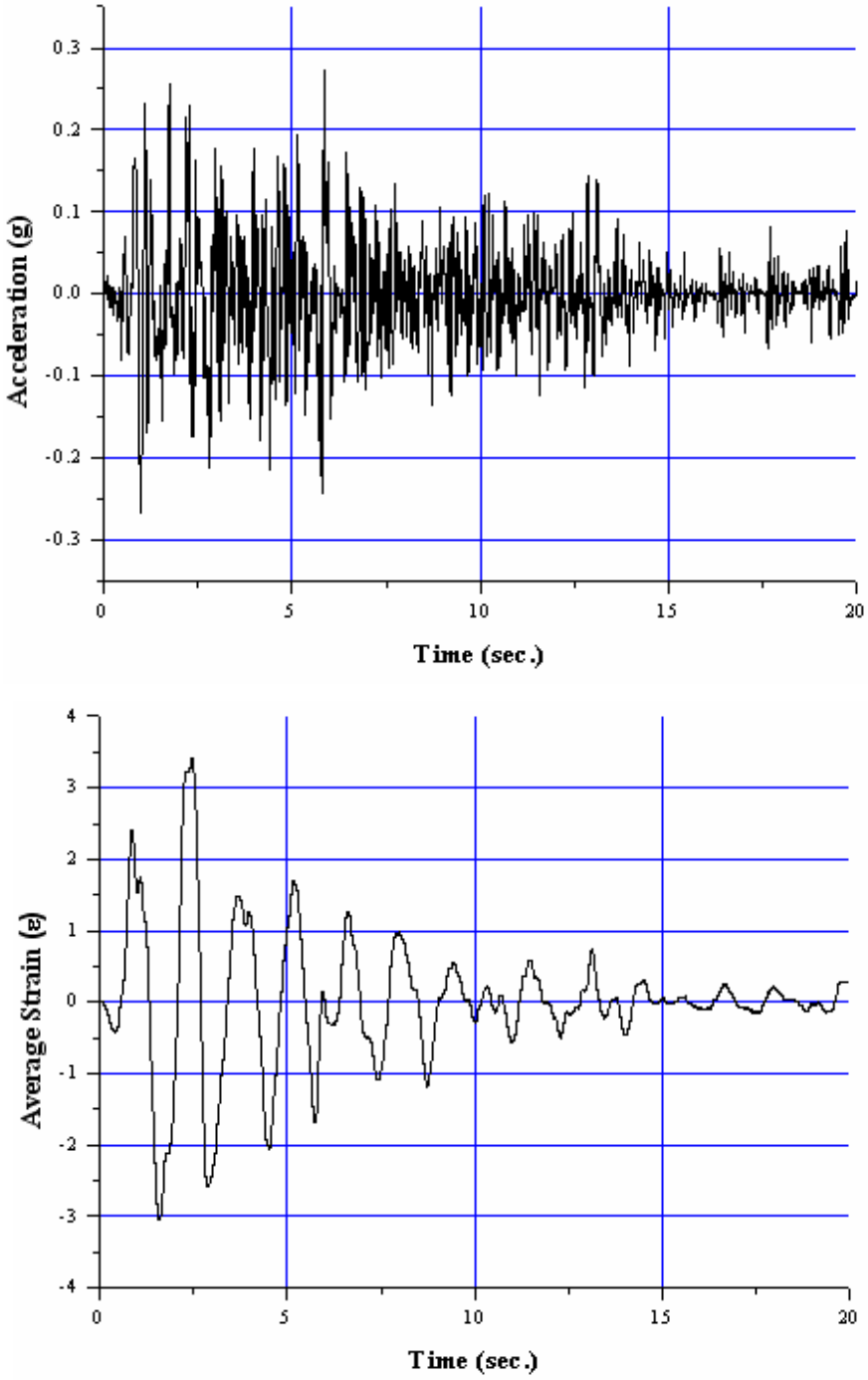

Figure 9.79. 2nd experiment 4th El Centro excitation record

The peak relative displacements in both directions were calculated to be as in Table 9.25 and in Figures 9.80 to 9.82.

Table 9.25. Peak relative displacements observed on the geotextile reinforcements at the 4th El Centro excitation of the 2nd experiment (units are in cm)

Peak Relative Displacements (2nd Experiment 4th EL CENTRO %100)								
H= 160 cm	**Trans. 8**		**Trans. 7**		**Trans. 6**		**Trans. 5**	
	L=30 cm		**L=70 cm**		**L=100 cm**		**L=108 cm**	
	Max. (1)	**Max. (2)**	**Max. (1)**	**Max. (2)**	**Max. (1)**	**Max. (2)**	**Max. (1)**	**Max.(2)**
t=1.4 sec	0.3989		0.3906		0.5097		0.4258	
t=1.54 sec	0.2745		0.2823		0.3424		0.2808	
t=2.14 sec		-0.2352		-0.2455		-0.3823		-0.3289
t=2.63 sec	0.2590		0.2476		0.2543		0.2828	
t=4.34 sec	0.3206		0.3719		0.3838		0.3776	
t=5.82 sec		-0.2305		-0.2652		-0.4160		-0.3693
H= 40 cm	**Trans. 4**		**Trans. 3**		**Trans. 2**		**Trans. 1**	
	L=20 cm		**L=32,5 cm**		**L=50 cm**		**L=80 cm**	
	Max. (1)	**Max. (2)**	**Max. (1)**	**Max. (2)**	**Max. (1)**	**Max. (2)**	**Max. (1)**	**Max.(2)**
t=1.42 sec	0.2885		0.4071		0.3238		0.2699	
t=1.54 sec	0.2419		0.3771		0.3191		0.2916	
t=2.16 sec		-0.7123		-0.6620		-0.6154		-0.5569
t=2.62 sec	0.1874		0.4356		0.2471		0.1046	
t=4.35 sec	0.2678		0.4217		0.3056		0.2616	
t=5.84 sec		-0.5988		-0.6087		-0.5346		-0.5610

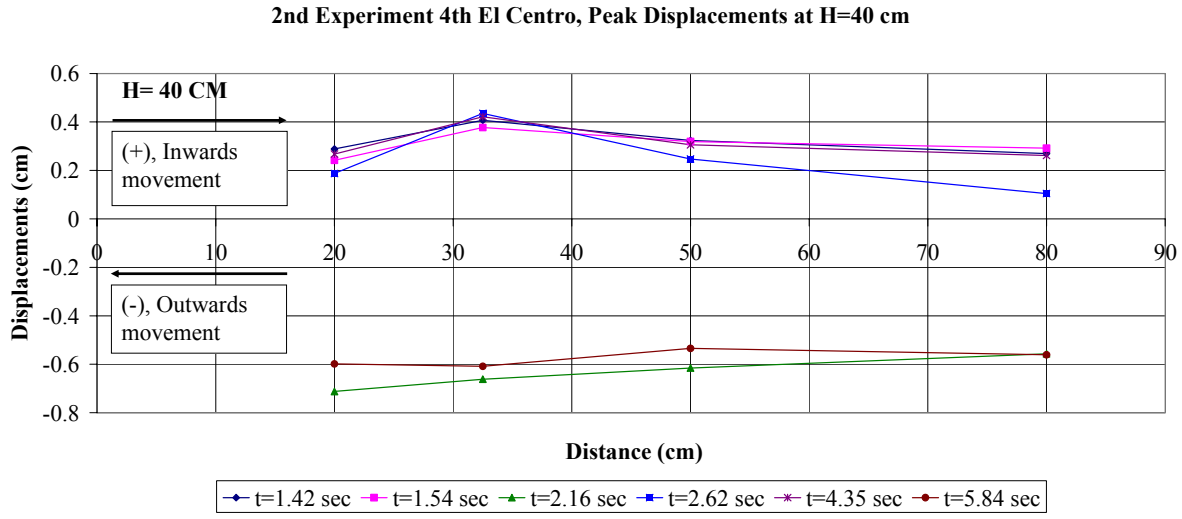

Figure 9.80. Peak relative displacements on the geotextile reinforcement at H = 40 cm in 4th El Centro excitation of the 2nd Experiment

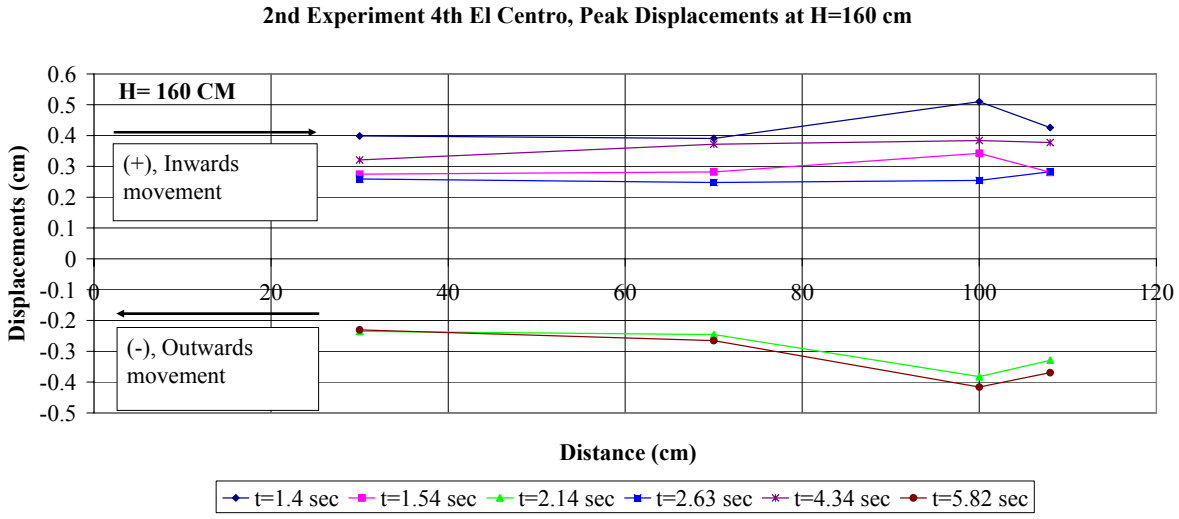

Figure 9.81. Peak relative displacements on the geotextile reinforcement at H = 160 cm in 4th El Centro excitation of the 2nd Experiment

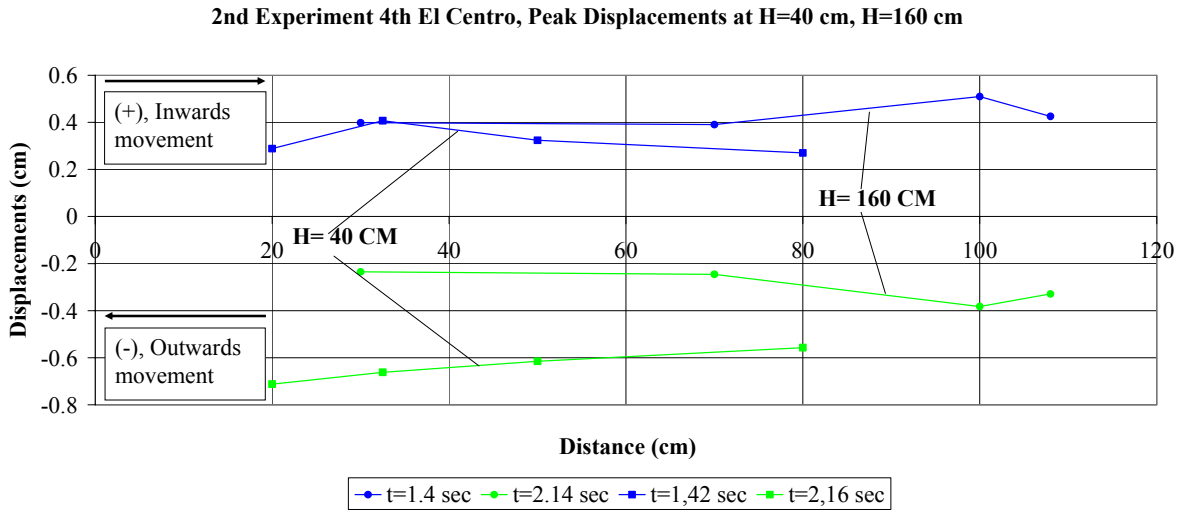

Figure 9.82. Comparisons of peak relative displacements measured on the geotextile reinforcements at H=40 cm and H=160 cm for the 4th El Centro excitation of the 2nd experiment

In Table 9.26 and in Figures 9.83 and 9.84, calculated average strains on the geotextile reinforcement according to the maximum relative displacements can be seen.

Table 9.26. Calculated average strain values on the geotextile reinforcements at the 4th El Centro excitation of the 2nd experiment

H= 160 cm	Regions between the measurement locations		
	30 - 70	70 - 100	100 - 108
t=1.4 sec	-0.0002	0.0040	-0.0105
t=1.54 sec	0.0002	0.0020	-0.0077
t=2.14 sec	-0.0003	-0.0046	0.0067
t=2.63 sec	-0.0003	0.0002	0.0036
t=4.34 sec	0.0013	0.0004	-0.0008
t=5.82 sec	-0.0009	-0.0050	0.0058
H= 40 cm	**Regions between the measurement locations**		
	20 - 32.5	**32.5 - 50**	**50 - 80**
t=1.42 sec	0.0095	-0.0048	-0.0018
t=1.54 sec	0.0108	-0.0033	-0.0009
t=2.16 sec	0.0040	0.0027	0.0020
t=2.62 sec	0.0199	-0.0108	-0.0047
t=4.35 sec	0.0123	-0.0066	-0.0015
t=5.84 sec	-0.0008	0.0042	-0.0009

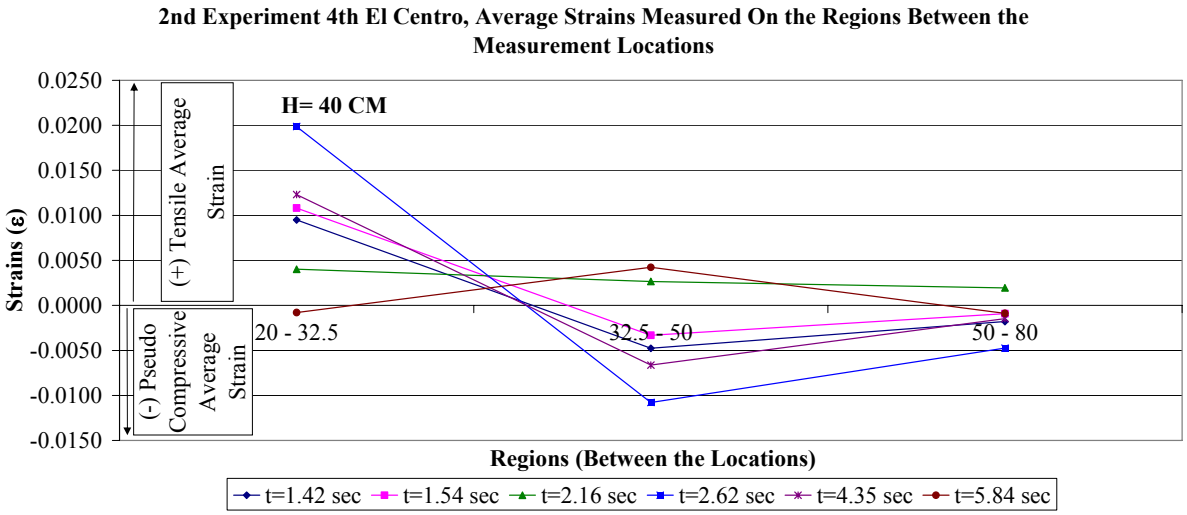

Figure 9.83. Average strains measured on the geotextile reinforcement at the regions between the measurement locations of the 2nd experiment 4th El Centro excitation at the level H = 40 cm

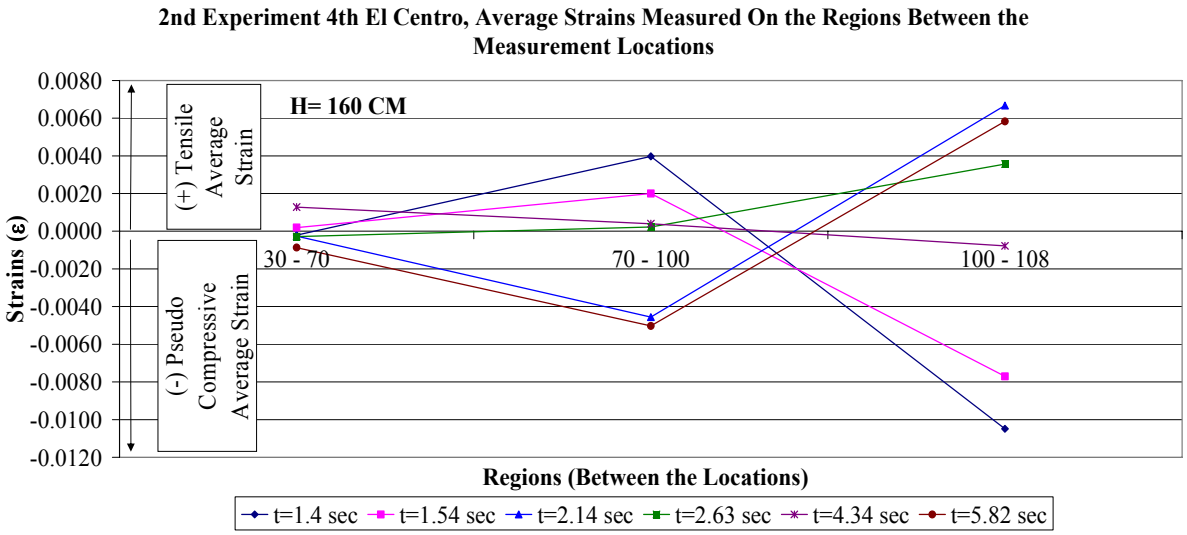

Figure 9.84. Average strains measured on the geotextile reinforcement at the regions between the measurement locations of the 2nd experiment 4th El Centro excitation at the level H = 160 cm

Presented in Figures 9.85 and 9.86 are the calculated average-strain time history records of the geotextile members at the regions between the measurement locations.

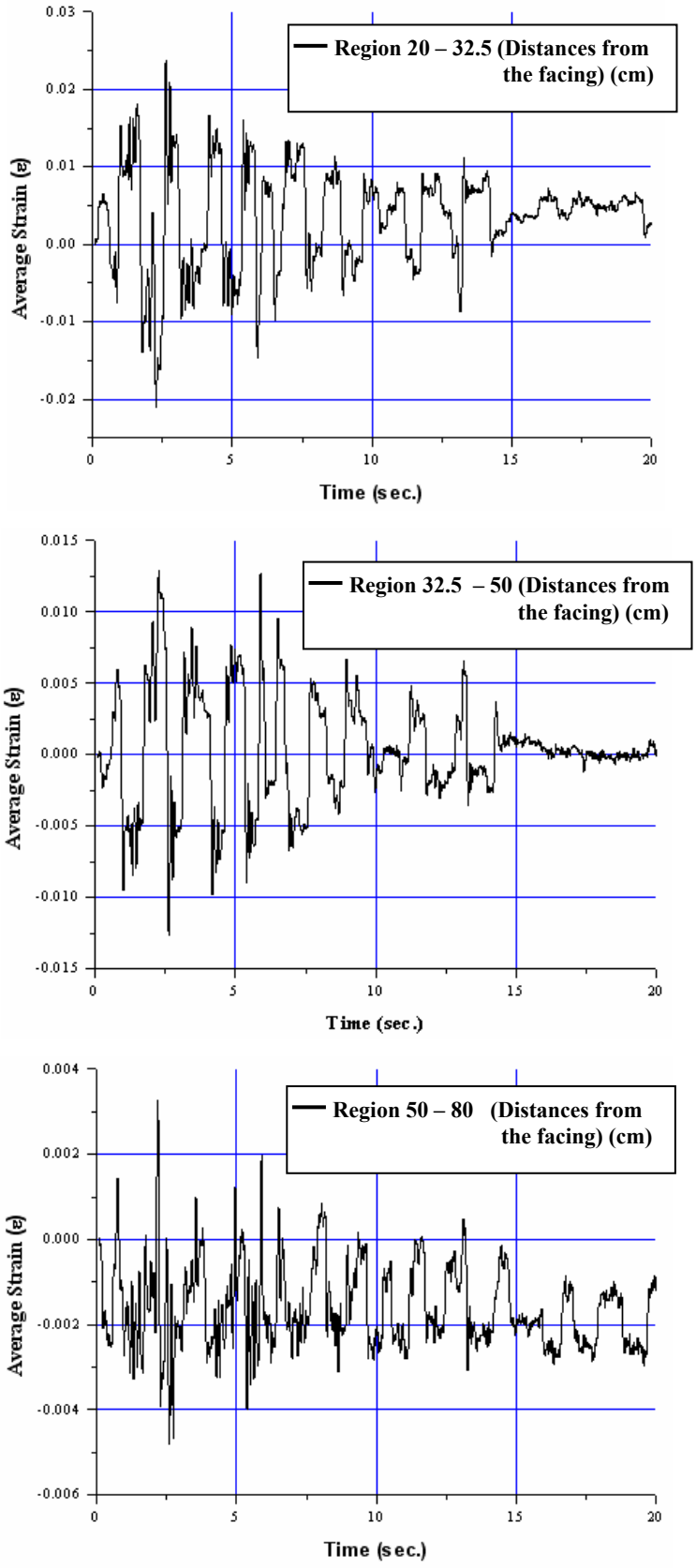

Figure 9.85. Average strains measured on the geotextile reinforcement at the regions in the 2nd experiment 4th El Centro excitation at level H = 40 cm

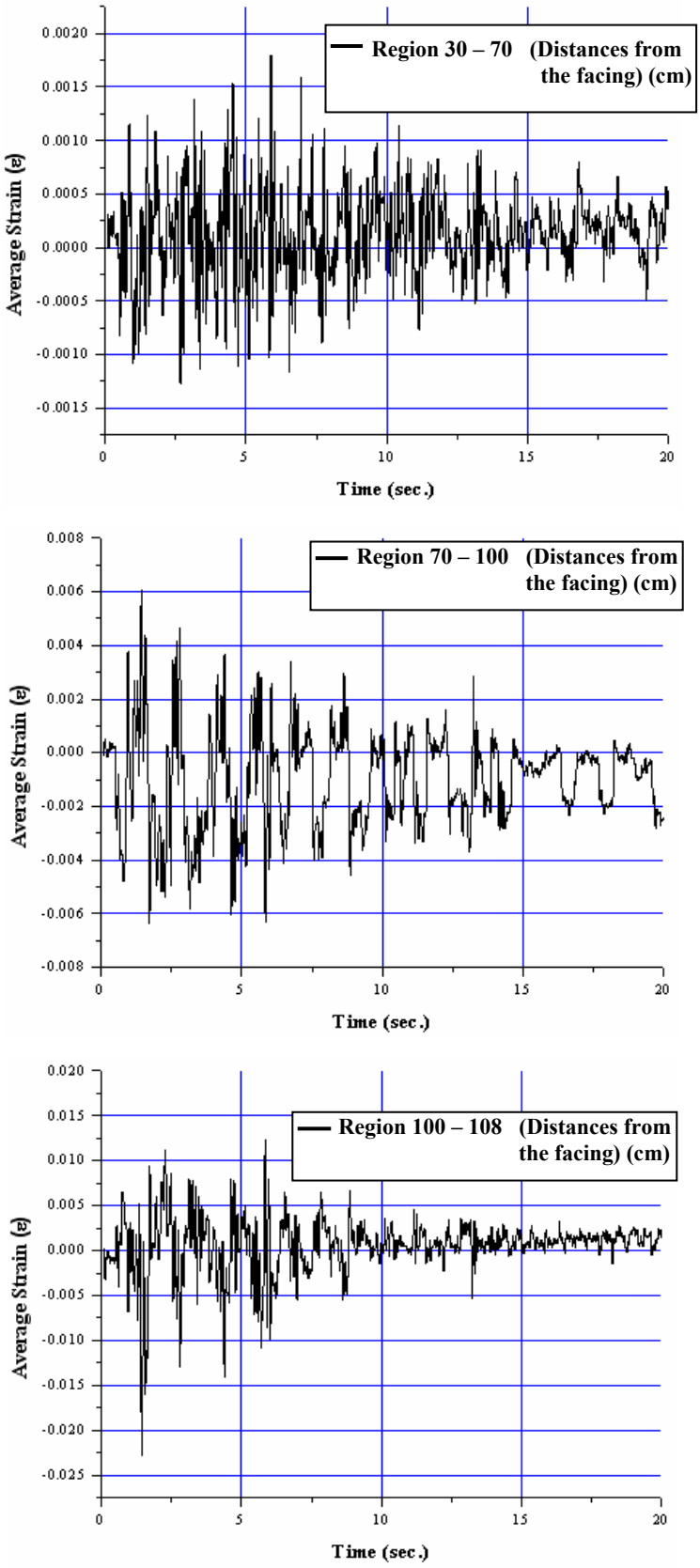

Figure 9.86. Average strains measured on the geotextile reinforcement at the regions in the 2nd experiment 4th El Centro excitation at level H = 160 cm

Figures 9.87 and 9.88 demonstrate the deformation behavior in all of the regions at levels H=40 cm and H=160 cm, respectively. At level H=40 cm direct opposite curves are observed between the regions 20-32.5 and 32.5-50 cm at the same time intervals. This is a manifestation of the pressure waves propagating in the soil (Figure 9.87). The behavior of the 50-80 cm region is similar to 32.5-50 cm region, but much lower values of strains are observed. This indicates that as the distance to the failure surface increases, the strains diminish.

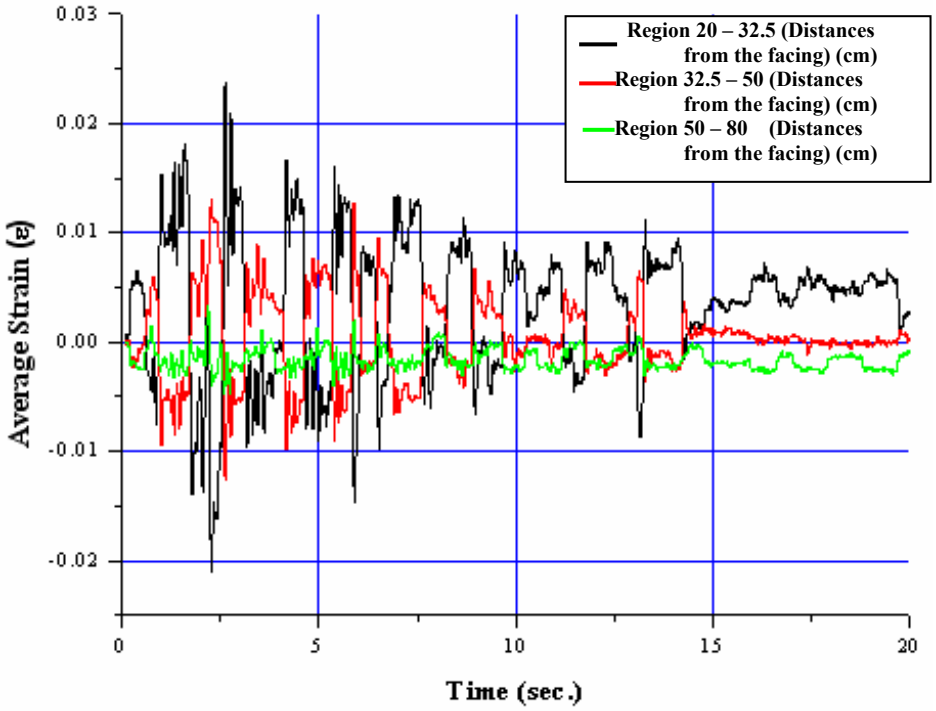

Figure 9.87. All the average strains measured on the geotextile reinforcement at the regions in the 2nd experiment 4th El Centro excitation at level H = 40 cm

At level H=160 cm direct opposite curves are observed between the regions 70-100 cm and 100-108 cm at the same time intervals. This again shows the presence of the pressure waves in the soil (Figure 9.88). Because the region 30-70 cm is situated close to the facing wall and far away from the critical failure surface lower level of strains were measured as expected.

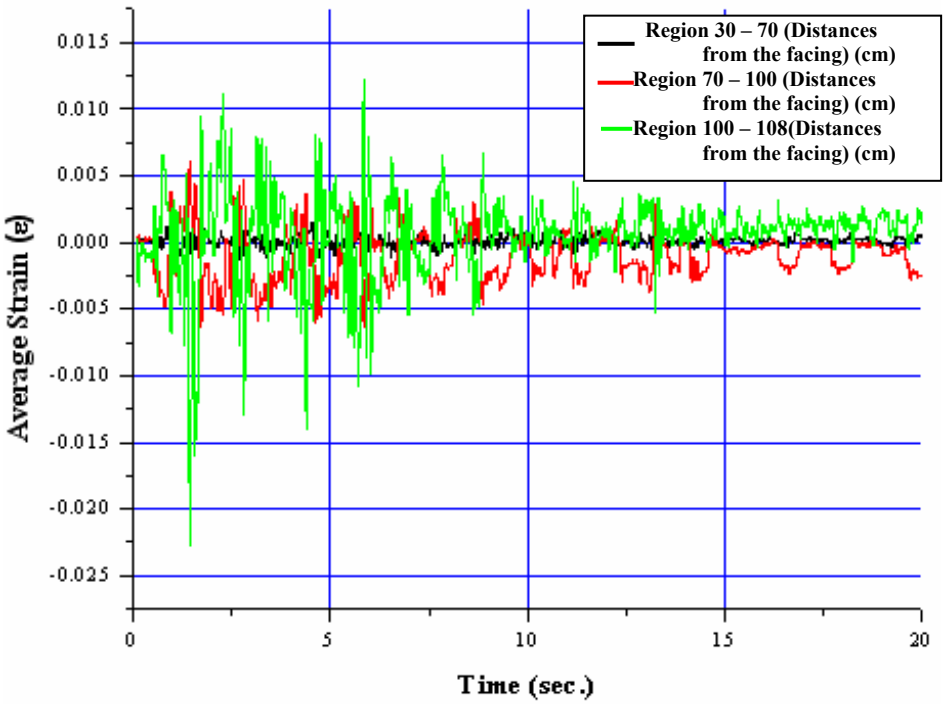

Figure 9.88. All the average strains measured on the geotextile reinforcement at the regions in the 2nd experiment 4th El Centro excitation at level H = 160 cm

9.2.2.6. Conclusions.

- The peak relative displacements observed on the geotextiles during the Sine Motion excitation indicates that maximum relative displacements developed at different locations at the geotextile layers, not on the assumed internal failure surface.

- By observing direct opposite average strain-time history curves between the regions 20-32.5 cm and 32.5-50 cm and between the regions 70-100 cm and 100-108 cm, it can be concluded that compressional and tensional zones developed during the sine motion excitation caused by the propagation of the pressure waves.

- An actual internal failure surface can be predicted by intersecting the intermediate points of the regions, where peak average tensile strains were measured, with the toe of the wall (Figure 9.89). Inclination of the internal surface is close to the assumed failure surface.

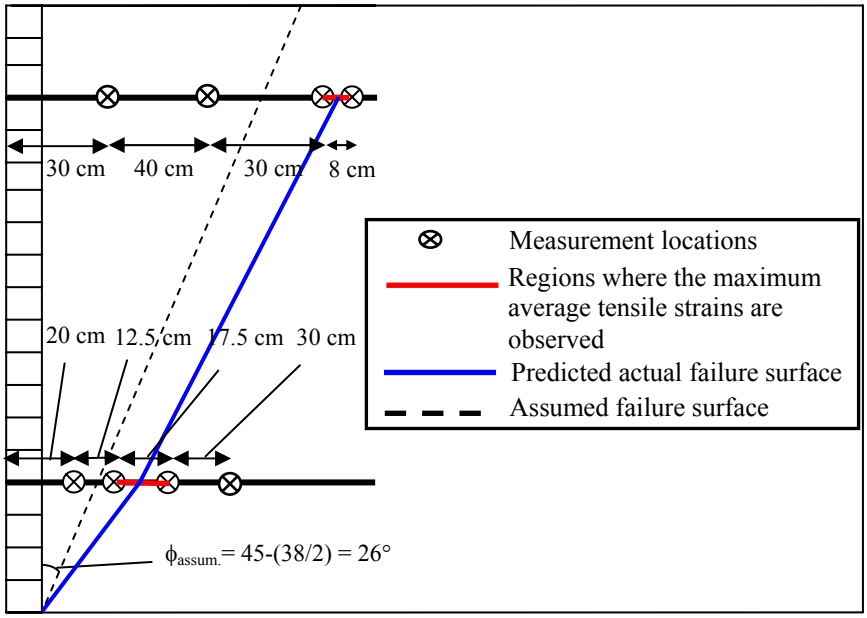

Figure 9.89. Internal failure surface determination and the regions where peak average tensile strains are observed during the sine motion excitation

- The relative displacements observed of the geotextile elements during the four El Centro motions indicate that almost all the peak relative displacements developed on the assumed internal failure surface. Only, at the last El-Centro motion excitation, the maximum displacement at H=40 cm elevation is observed at L = 20 cm location (Figure 9.90).

- With the observation of direct opposite average strain-time history curves between 20–32.5 cm region and 32.5-50 cm region at the level H = 40 cm and between 70-100 cm region and 100-108 cm region at the level H = 160 cm at the same time intervals it can be deduced that compressional and dilatational zones developed during the El Centro excitations caused by the propagation of the pressure waves.

- For El Centro earthquake excitations, a bilinear internal failure surface can be predicted by intersecting the intermediate points of the regions, where peak average tensile strains were measured, with the toe of the wall (Figure 9.90).

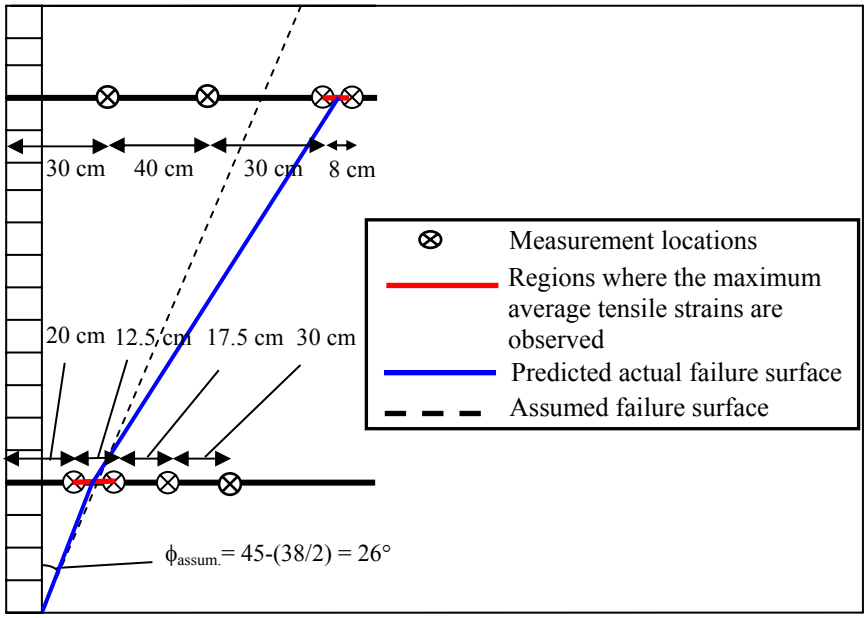

Figure 9.90. Internal failure surface determination and the regions where peak average tensile strains are observed during the El Centro excitations

- For the sine Motion excitation, the region where the maximum average dynamic tensile strain is measured at H = 40 cm level in the region of 32.5-50 cm with the value ε=0.0108 corresponding to 3.93 kN/m of dynamic tensile stress (for $J_{geotextile}$=364 kN/m). Whereas in the El Centro earthquake maximum average dynamic tensile strain is observed at H = 40 cm level and in the region of 20-32.5 cm with the value of ε = 0.02374 corresponding to a dynamic tensile average stress of 8.64 kN/m in the 4th El Centro excitation.

- Maximum average tensile strains did not occur at the time instances when the maximum relative displacements are observed.

- The reinforcement tensile average strains observed at the level H=40 cm are significantly higher than the ones at the level H=160 cm confirming the pseudo-static approach of dynamic load increment pressure distribution for internal stability analysis opted by FHWA when calculating the reinforcement loads.

- Listed in Tables 9.27 to 9.29, are the maximum relative displacements, average tensile strains and average pseudo-compressive strains on the geotextile reinforcements during the excitations.

Table 9.27. Summary of the measured maximum relative displacements on the geotextile reinforcements during the excitations

Maximum Relative Displacements (cm)						
2nd Experiment	Measurement Locations	Sine Motion	El Centro-1	El Centro-2	El Centro-3	El Centro-4
H = 40 cm	L = 20 cm	0.3652	-0.5802	-0.4937	-0.4794	-0.7123
	L = 32.5 cm	0.2958	-0.7169	-0.6589	-0.6589	-0.6620
	L = 50 cm	0.4527	-0.5874	-0.4999	-0.4959	-0.6154
	L = 80 cm	0.3942	-0.5672	-0.4672	-0.4836	-0.5610
H = 160 cm	L = 30 cm	-0.4543	0.3714	0.3341	0.2988	0.3989
	L = 70 cm	0.4429	0.3901	0.3994	0.3267	0.3906
	L = 100 cm	-0.4170	0.4843	0.3973	0.3403	0.5097
	L = 108cm	-0.4128	0.4372	0.3372	0.3242	0.4258

Table 9.28. Summary of the calculated maximum average tensile strains on the geotextile reinforcements during the excitations

Maximum Average Tensile Strain (ε)						
2nd Experiment	Regions	Sine Motion	El Centro-1	El Centro-2	El Centro-3	El Centro-4
H = 40 cm	20-32.5	0.0009	0.0166	0.0186	0.02084	0.02374
	32.5-50	0.0108	0.0138	0.0130	0.01276	0.01294
	50-80	0.0003	0.0034	0.0038	0.00468	0.00327
H = 160 cm	30-70	0.0023	0.0020	0.0018	0.00165	0.00179
	70-100	0.0013	0.0059	0.0042	0.0041	0.00606
	100-108	0.0074	0.0149	0.0114	0.01246	0.01227

Table 9.29. Summary of the calculated maximum average pseudo compressive strains on the geotextile reinforcements during the excitations

Maximum Average Pseudo Compressive Strains (ε)						
2nd Experiment	Regions	Sine Motion	El Centro-1	El Centro-2	El Centro-3	El Centro-4
H = 40 cm	20-32.5	-0.0079	-0.0290	-0.0229	-0.01798	-0.02111
	32.5-50	-0.0008	-0.0123	-0.0130	-0.01479	-0.0126
	50-80	-0.0051	-0.0041	-0.0017	-0.00257	-0.00479
H = 160 cm	30-70	-0.0004	-0.0019	-0.0014	-0.00136	-0.00128
	70-100	-0.0048	-0.0070	-0.0064	-0.00715	-0.00631
	100-108	-0.0053	-0.0156	-0.0114	-0.00954	-0.02271

9.3. Evaluation of the Fundamental Frequency of the Wall

The fundamental frequency of vibration for a two dimensional, linear elastic medium of width "B" and height "H", which contained by two rigid vertical boundaries, a rigid base and subjected to horizontal base excitation was given by (Wu, 1994) as:

$$f_{11} = \frac{1}{4H}\sqrt{\frac{G}{Q}}\sqrt{1+\left(\frac{2}{1-\nu}\right)\left(\frac{H}{B}\right)^2} \tag{9.1}$$

where f_{11} is frequency in Hz corresponding to the first mode shape of the medium in both the horizontal and vertical directions, G is the shear modulus; Q is density and ν is the Poisson ratio of the soil medium. In the limit of an infinitely wide medium ($B\rightarrow\infty$), Equation 6.12 becomes the well known expression for the fundamental frequency of a one-dimensional elastic medium with height H [32].

Since H = 1.9 m, B = 2.8 m and if we consider $\gamma_{approx.}$ = 17 kN/m^3. Q becomes 17/9.81= 1.73 gr/cm^3. G = 11220 kN/m^2 for E=29180 kN/m^2. In conclusion, the fundamental frequency of the wall approximately equals to:

$$f = \frac{1}{4\times 1.9}\times\sqrt{\frac{11220}{1.73}}\times\sqrt{1+\left(\frac{2}{1-0.3}\right)\left(\frac{1.9}{2.80}\right)^2} = 16.11 Hz. \qquad \text{(by eq. 9.1)}$$

Other than the proposed empirical formula above, the acceleration-time history data recorded in the experiments were used in order to understand the exact natural frequency of the structure. For this purpose, the SeismoSignal program (from Seismosoft) was used as a tool to plot the acceleration response spectra of the motions. Several applied motions were plotted like the 1st experiment 20 per cent El Centro excitation, 1st experiment 40 per cent El Centro excitation, 2nd experiment 50 per cent El Centro excitation and 2nd experiment 3rd shaking 100 per cent El Centro excitation (the per cent excitations represent the trial experimental excitations in which the El Centro acceleration amplitudes were reduced with the related per cent). Around them the predominant frequency of T_p =0.08

sec., where the spectral acceleration value becomes maximum as shown in Figure 9.91, corresponding to a frequency of 12.5 Hz was seen to be frequent (Table 9.30).

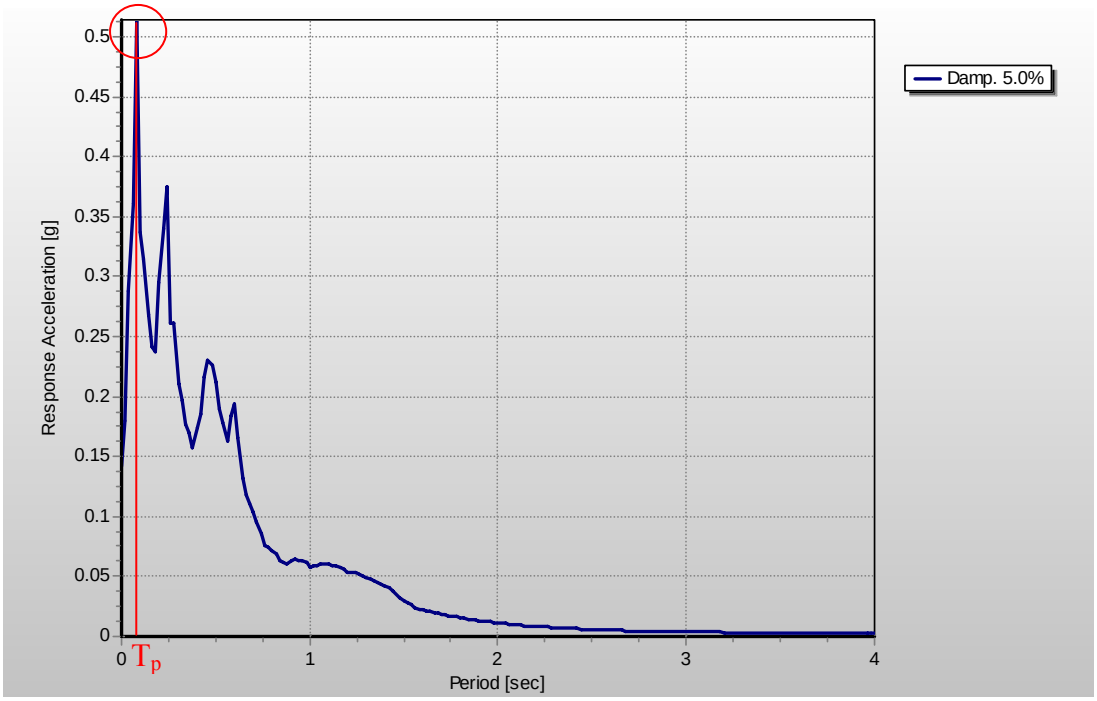

Figure 9.91. Response Spectra Acceleration according to the Acc.2 record of the 1st experiment %40 El Centro excitation motion

Table 9.30. Predominant periods evaluated according to the plotted acceleration response spectrums

Accelerometers	**Predominant Period (T_p) (sec.)**			
	1st Experiment		**2nd Experiment**	
	% 20 El Centro	**% 40 El Centro**	**% 50 El Centro**	**% 100 El Centro**
Acc. 1	0.28	0.08	0.28	0.26
Acc. 2	0.28	0.08	0.08	0.26
Acc. 3	0.28	0.08	0.08	0.26
Acc. 4	0.08	0.08	0.08	0.08
Acc. 5	0.08	0.08	0.08	0.08
Acc. 6	0.08	0.08	0.06	0.08
Acc. 7	0.08	0.08	0.08	0.08
Acc. 8	0.1	0.08	0.08	0.08
Acc. 9	0.08	0.08	0.08	0.08
Acc. 10	0.08	0.08	0.08	0.08
Acc. 11	0.08	0.08	0.08	0.08

Lastly, Plaxis v 7.2 program was used to evaluate the natural frequency of our system. A reference point on top of the front wall as in Figure 9.92 was selected and its displacement-time history curves were plotted by applying several harmonic motions with

different frequencies that have the same amplitude and by applying the same number of cycles to each model.

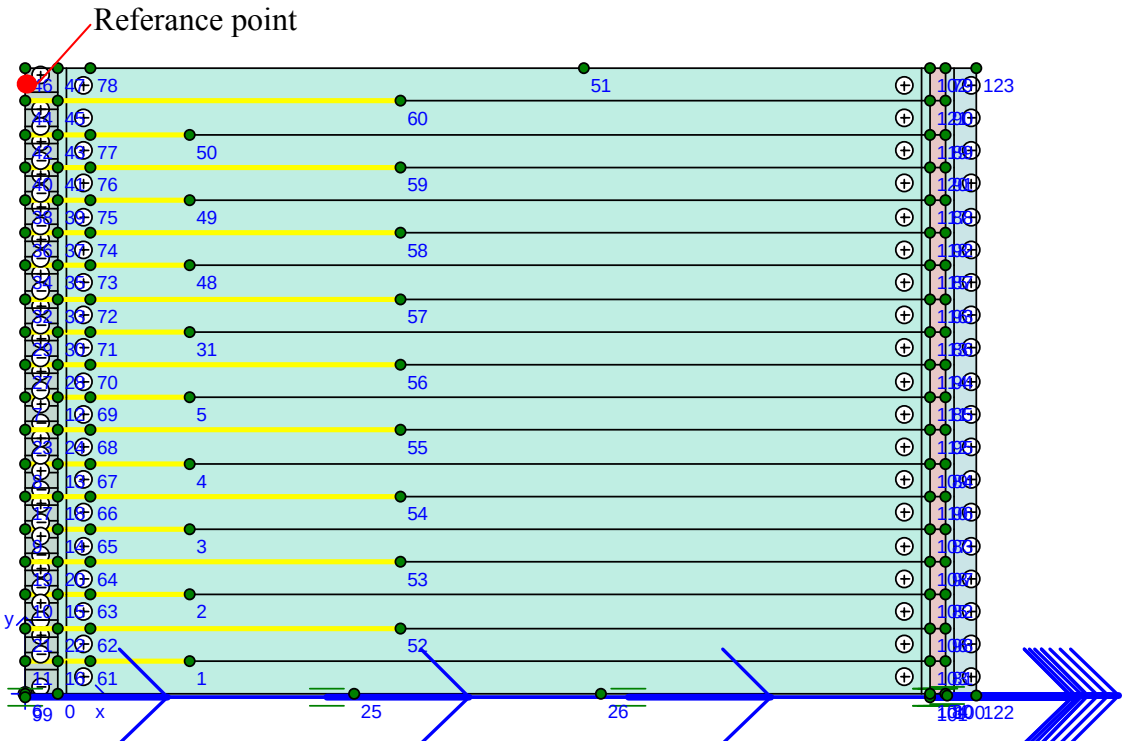

Figure 9.92. The reference point selected on the GR-SRW

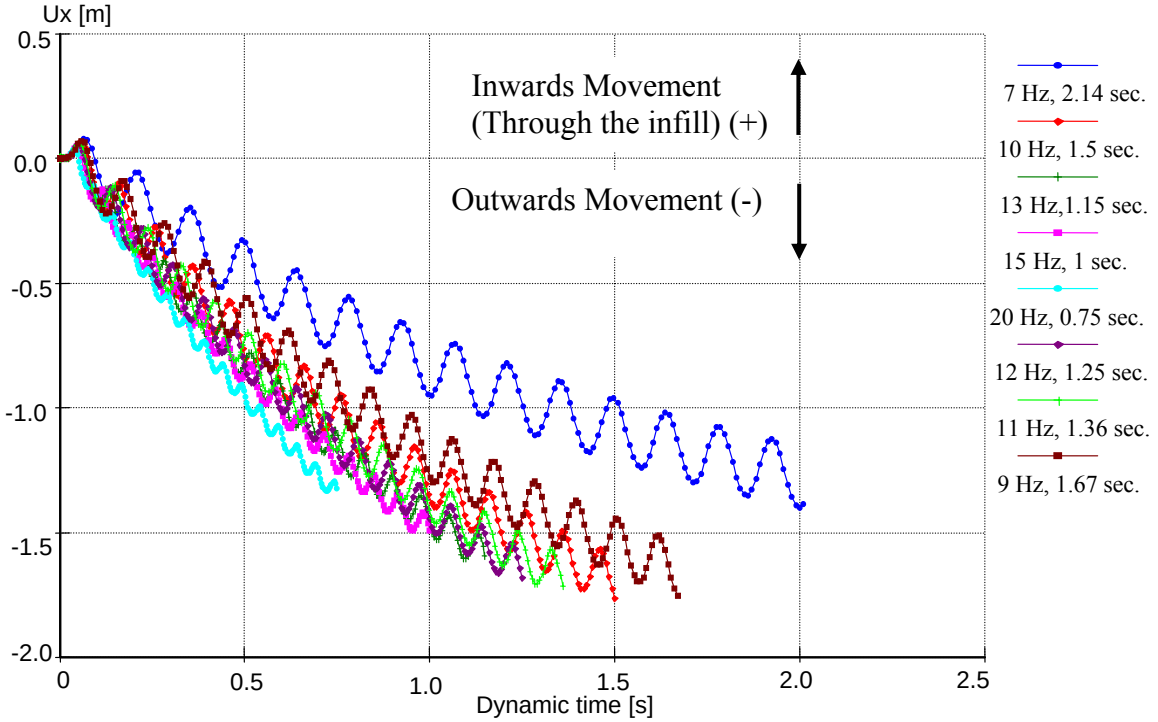

Figure 9.93. Displacement-Time history curves of the reference point

From the curves illustrated in Figure 9.93, a frequency of 10 Hz is seen to be deflected more than the others. As a result, it can be concluded that a frequency between 10 to 12.5 Hz best represents our structure's natural frequency and because it was impossible to attain to these kinds of frequent predominant frequencies both with the harmonic motion and with scaled El-Centro earthquake records, a resonant behavior of the wall was not observed.

9.4. Front Wall Displacement Measurement Study

The front wall displacements are analyzed for many time instances to give a brief opinion about the acquired data. Out of these data, mainly the time instances where the primary and secondary peak displacements in the (+) direction and in (–) direction were taken into consideration. While the (+) direction represents the direction inwards movement, (-) direction represents the outwards movement of the facing wall. Additionally, the displacement results of certain time instances, where many of the laser displacement sensors (for example 4 out of 8) gave peak displacements at that time while the others didn't, also were investigated and considered whether this observed phenomena could represent a possible mode shape of the structure or not.

9.4.1. 1st Experiment Sine Wave Excitation

In Table 9.31 the primary and secondary peak displacements and in Table 9.32 only the primary peak displacements in both directions during the sine motion excitation can be seen. Figure 9.94 shows that the facing wall displaced almost similarly and in the same manner in both directions.

Table 9.31. 1st experiment, displacements observed at the front wall in sine motion

1st Experiment, Displacements Observed at the Front Wall							
Random Sine Motion		**Elevation (m)**					
Laser Sensors	**Time (sec.)**	**0.135**	**0.63**	**0.92**	**1.31**	**1.62**	**1.87**
LS1	226.78	0.109 cm					
	491.85	-0.074 cm					
LS2	251.42		0.107 cm				
	494.81		-0.093 cm				
LS3				-			
LS4	432.28				-0.091 cm		
	441.53				0.074 cm		
	602.27				0.080 cm		
LS5	349.08					-0.072 cm	
	409.75					0.162 cm	
	591.81					-0.115 cm	
LS6	384.06						0.161 cm
	497.37						-0.155 cm
	591.91						-0.157 cm
LS7	311.75						-0.202 cm
	413.41						0.114 cm
	591.68						-0.101 cm
LS8	537.61						0.086 cm
	590.55						0.194 cm
	432.29						-0.100 cm
	591.83						-0.162 cm

Table 9.32. 1st experiment, peak displacements observed at the front wall in sine motion

1stExperiment, Displacements Observed at the Front Wall					
Random Sine Motion	**Elevation (m)**	**Time (sec.)**	**Peak Displacements (+ Direction) (cm)**	**Time (sec.)**	**Peak Displacements (- Direction) (cm)**
Laser Sensors	**0**		0	0	0
LS1	**0.135**	226.78	0.109	491.85	-0.074
LS2	**0.63**	251.42	0.107	494.81	-0.093
LS3	**-**	-	-	-	-
LS4	**1.31**	602.27	0.080	432.28	-0.091
LS5	**1.62**	409.75	0.162	591.81	-0.115
LS6	**1.87**	384.06	0.161	591.91	-0.157
LS7	**1.87**	413.41	0.114	311.75	-0.202
LS8	**1.87**	590.55	0.194	591.83	-0.162

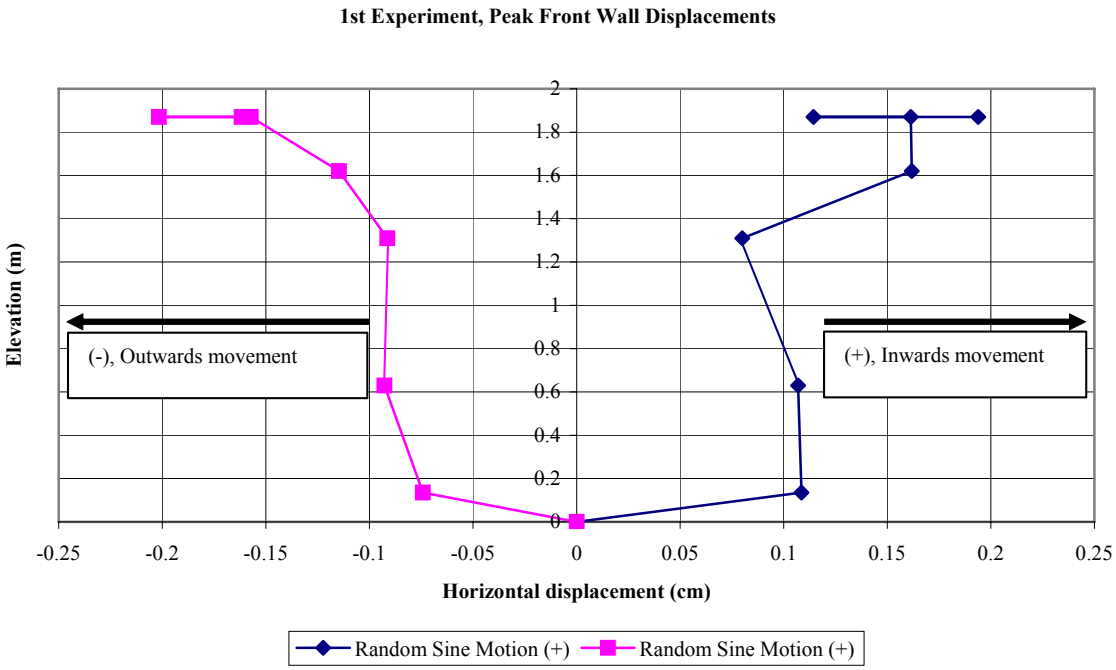

Figure 9.94. 1st experiment, peak displacements observed at the front wall in sine motion

9.4.2. 1st Experiment El Centro Earthquake Excitations

The displacement values at certain time instances are presented in Tables 9.33 and 9.35. In these tables not only the maximum displacements but also secondary maximum displacements and also displacement values at specific time instances where possible mode shape of the structure is developed are listed as well. The tables following these general tables show the peak displacement values in (+) and (–) directions and the displacement values of a specified time instance at which a possible mode shape of the structure is developed (Tables 9.34 and 9.36).

Table 9.33. 1st Experiment, displacements observed at the front wall in 1st El Centro excitation

1st Experiment, Displacements Observed at the Front Wall							
EL CENTRO-1		**Elevation (m)**					
Laser Sensors	**Time (sec.)**	**0.135**	**0.63**	**0.92**	**1.31**	**1.62**	**1.87**
LS1	**2.18**	0.146 cm					
	2.29	0.141 cm					
	2.59	-0.401 cm					
	2.81	-0.438 cm					
LS2	**1.38**		-0.281 cm				
	1.87		0.062 cm				
	2.59		-0.266 cm				
	2.80		-0.264 cm				
	4.88		0.068 cm				
	5.54		-0.246 cm				
LS3				-			
LS4	**2.10**				0.225 cm		
	2.74				-0.313 cm		
	2.80				-0.307 cm		
	5.49				-0.198 cm		
LS5	**2.41**					-0.103 cm	
	2.66					0.210 cm	
	2.78					0.222 cm	
	3.08					-0.097 cm	
LS6	**2.43**						-0.281 cm
	2.53						-0.182 cm
	2.67						0.238 cm
	2.78						0.248 cm
	5.39						-0.231 cm
LS7	**1.25**						0.070 cm
	1.57						0.069 cm
	2.80						-0.011 cm
	3.66						-0.205 cm
	3.76						-0.220 cm
LS8	**1.22**						-0.480 cm
	1.38						0.275 cm
	1.44						-0.500 cm
	2.55						-0.564 cm
	2.76						0.581 cm
	5.54						-0.471 cm

Table 9.34. 1st experiment, peak displacements observed at the front wall in 1st El Centro excitation

1stExperiment, Displacements Observed at the Front Wall							
EL CENTRO-1	**Elevation (m)**	**Time (sec.)**	**Displacement (cm)**	**Time (sec.)**	**Peak Displacements (- Direction) (cm)**	**Time (sec.)**	**Peak Displacements (+ Direction) (cm)**
Laser Sensors	**0**	0	0	0	0	0	0
LS1	**0.135**	2.81	-0.438	2.81	-0.438	2.18	0.146
LS2	**0.63**	2.80	-0.264	1.38	-0.281	4.88	0.068
LS3	**-**	-	-	-	-	-	-
LS4	**1.31**	2.80	-0.307	2.74	-0.313	2.10	0.225
LS5	**1.62**	2.78	0.222	2.41	-0.103	2.78	0.222
LS6	**1.87**	2.78	0.248	2.43	-0.281	2.78	0.248
LS7	**1.87**	2.80	-0.011	3.76	-0.220	1.25	0.070
LS8	**1.87**	2.76	0.581	2.55	-0.564	2.76	0.581

Table 9.35. 1st Experiment, displacements observed at the front wall in 2nd El Centro excitation

EL CENTRO-2		Elevation (m)					
Laser Sensors	**Time (sec.)**	**0.135**	**0.63**	**0.92**	**1.31**	**1.62**	**1.87**
LS1	**2.16**	0.262 cm					
	2.22	0.270 cm					
	2.61	-0.354 cm					
	2.65	-0.153 cm					
	2.84	-0.322 cm					
	5.45	-0.094 cm					
LS2	**1.28**		-0.231 cm				
	2.17		0.118 cm				
	2.59		-0.251 cm				
	2.64		-0.266 cm				
	2.79		-0.207 cm				
	4.90		0.120 cm				
	5.50		-0.214 cm				
LS3				-			
LS4	**2.11**				0.223 cm		
	2.19				0.215 cm		
	2.67				-0.290 cm		
	2.75				-0.303 cm		
	2.82				-0.253 cm		
	5.50				-0.180 cm		
LS5	**2.42**					-0.046 cm	
	2.65					0.278 cm	
	2.81					0.262 cm	
	3.05					-0.041 cm	
LS6	**1.17**						-0.093 cm
	2.43						-0.160 cm
	2.49						-0.120 cm
	2.66						0.227 cm
	2.81						0.325 cm
	5.38						-0.119 cm
LS7	**1.26**						0.020 cm
	2.44						-0.240 cm
	2.67						-0.117 cm
	2.82						-0.037 cm
	5.33						-0.265 cm
	5.96						-0.235 cm
	8.95						-0.231 cm
LS8	**1.30**						-0.274 cm
	2.59						-0.329 cm
	2.63						0.464 cm
	2.73						0.562 cm
	2.80						0.477 cm
	5.50						-0.384 cm

Table 9.36. 1st experiment, peak displacements observed at the front wall in 2nd El Centro excitation

1stExperiment, Displacements Observed at the Front Wall							
EL CENTRO-2	**Elevation (m)**	**Time (sec.)**	**Displacement (cm)**	**Time (sec.)**	**Peak Displacements (- Direction) (cm)**	**Time (sec.)**	**Peak Displacements (+ Direction) (cm)**
Laser Sensor	**0**		0	0	0	0	0
LS1	**0,135**	2,61	-0,354	2,61	-0,354	2,22	0,270
LS2	**0,63**	2,64	-0,266	2,64	-0,266	4,90	0,120
LS3	**-**	-	-	-	-	-	-
LS4	**1,31**	2,67	-0,290	2,75	-0,303	2,11	0,223
LS5	**1,62**	2,65	0,278	2,42	-0,046	2,65	0,278
LS6	**1,87**	2,66	0,227	2,43	-0,160	2,81	0,325
LS7	**1,87**	2,67	-0,117	5,33	-0,265	1,26	0,020
LS8	**1,87**	2,63	0,464	5,50	-0,384	2,73	0,562

A possible dominant mode shape developed is illustrated in Figure 9.95.

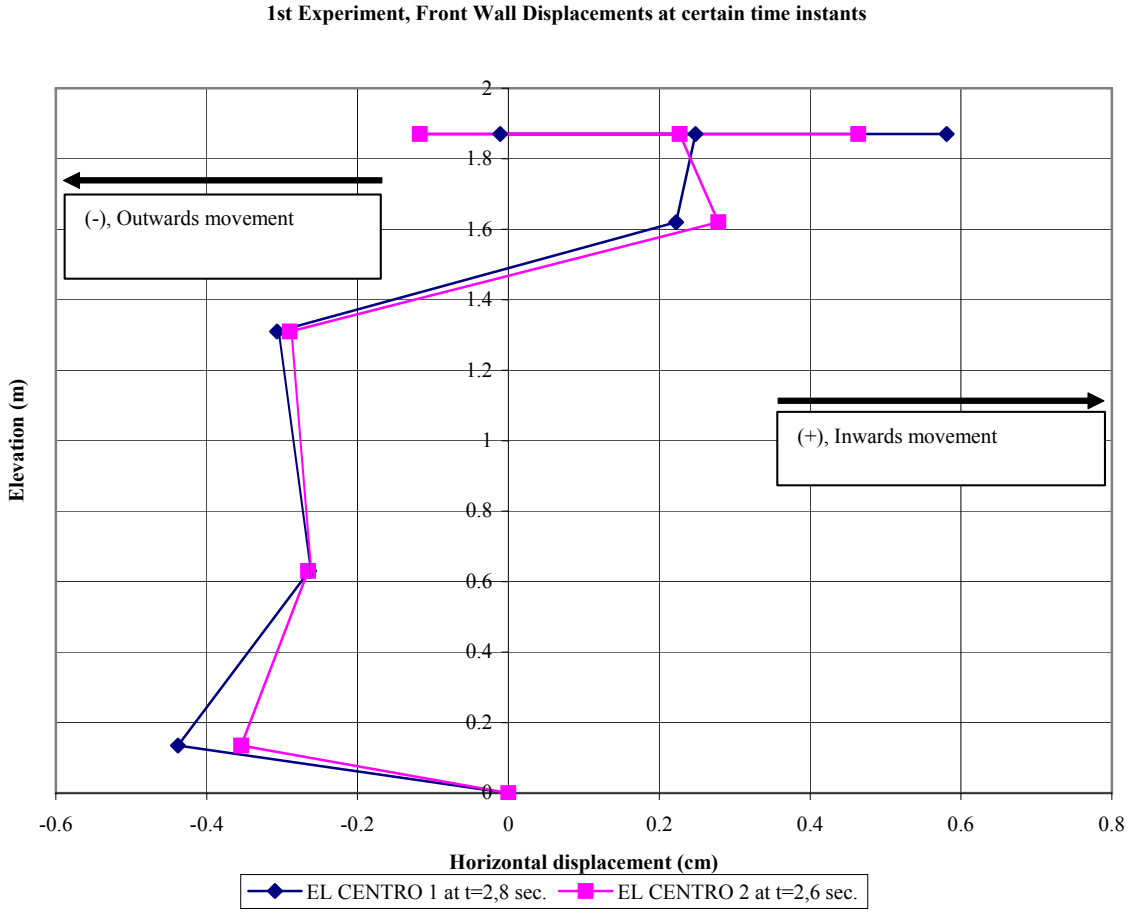

Figure 9.95. 1st Experiment, displacements observed at the front wall for certain time instances in the ElCentro excitations

The maximum displacements observed on the front wall are at the levels H = 0.135 m and H = 1.87 m with the values of 0.438 cm and 0.562 cm, respectively in the outwards direction. However, it must be noted that during the 1st experiment LS8 showed a stressed behavior in comparison with the other laser sensors, which is a possible indication that the laser ray hit to a non-smooth location of the modular block. In Figure 9.96, maximum displacements at every elevation in both directions are illustrated.

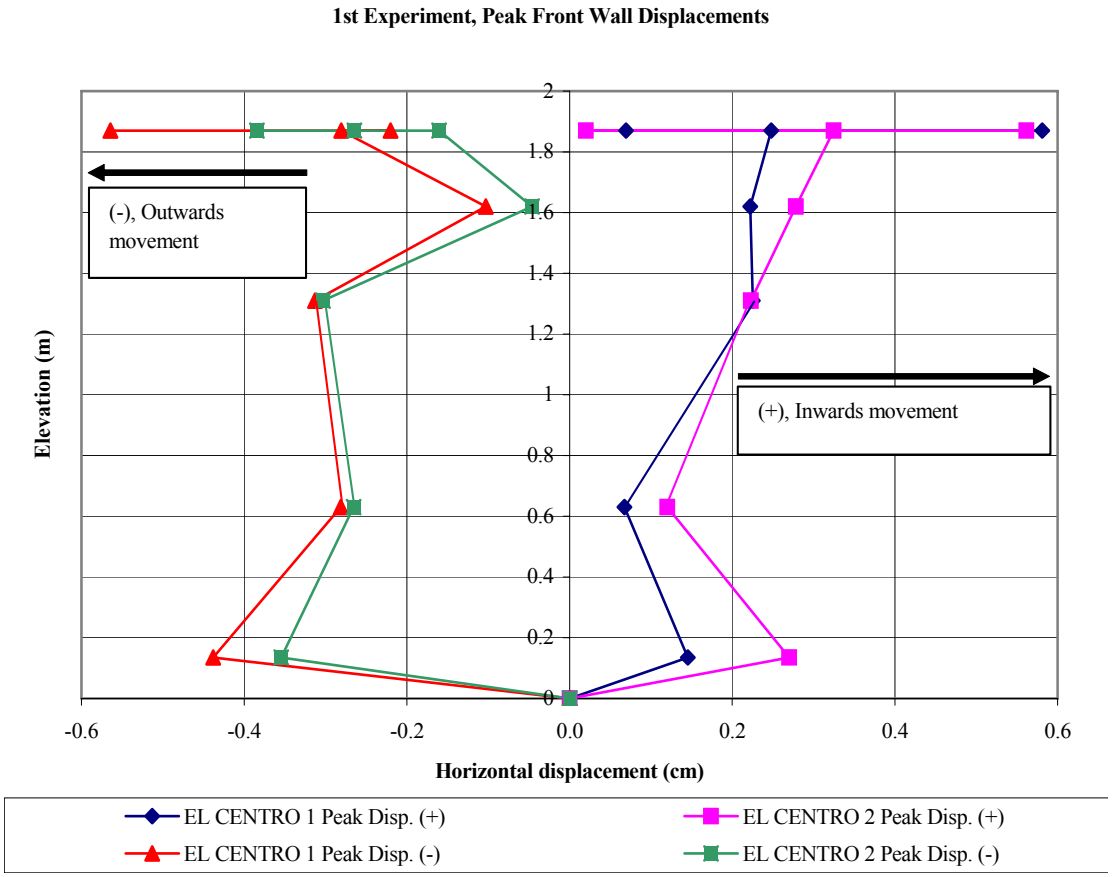

Figure 9.96. 1st experiment, peak displacements observed at the front wall in the El Centro excitations

9.4.3. 2nd Experiment Sine Motion Excitation

In Table 9.37 the primary and secondary peak displacements and in Table 9.38 only the primary peak displacements in both directions during the sine motion excitation can be seen. Figure 9.94 shows that maximum displacement was developed at H=0.135 cm level.

Table 9.37. 2nd experiment, displacements observed at the front wall in sine motion excitation

2nd Experiment, Displacements Observed at the Front Wall							
Random Sine Motion		**Elevation (m)**					
Laser Sensors	**Time(sec.)**	**0.135**	**0.63**	**0.92**	**1.31**	**1.62**	**1.87**
LS1	283.32	-0.464 cm					
	135.34	0.070 cm					
LS2	183.58		-0.292 cm				
	222.59		0.182 cm				
LS3	132.77			0.250 cm			
	300.34			-0.112 cm			
LS4	152.20				0.131 cm		
	244.55				-0.088 cm		
LS5	277.65					-0.112 cm	
	117.40					0.070 cm	
LS6	69.03						0.123 cm
	300.40						-0.103 cm
LS7	129.94						0.150 cm
	269.83						-0.135 cm
LS8	116.27						0.099 cm
	279.48						-0.091 cm

Table 9.38. 2nd Experiment, peak displacements observed at the front wall in sine motion excitation

Random Sine Motion	**Elevation (m)**	**Time (sec.)**	**Peak Displacements (+ Direction) (cm)**	**Time (sec.)**	**Peak Displacements (- Direction) (cm)**
Laser Sensors	**0**	0	0	0	0
LS1	**0.135**	135.34	0.070	283.32	-0.464
LS2	**0.63**	222.59	0.182	183.58	-0.292
LS3	**0.92**	132.77	0.250	300.34	-0.112
LS4	**1.31**	152.20	0.131	244.55	-0.088
LS5	**1.62**	117.40	0.070	277.65	-0.112
LS6	**1.87**	69.03	0.123	300.40	-0.103
LS7	**1.87**	129.94	0.150	269.83	-0.135
LS8	**1.87**	116.27	0.099	279.48	-0.091

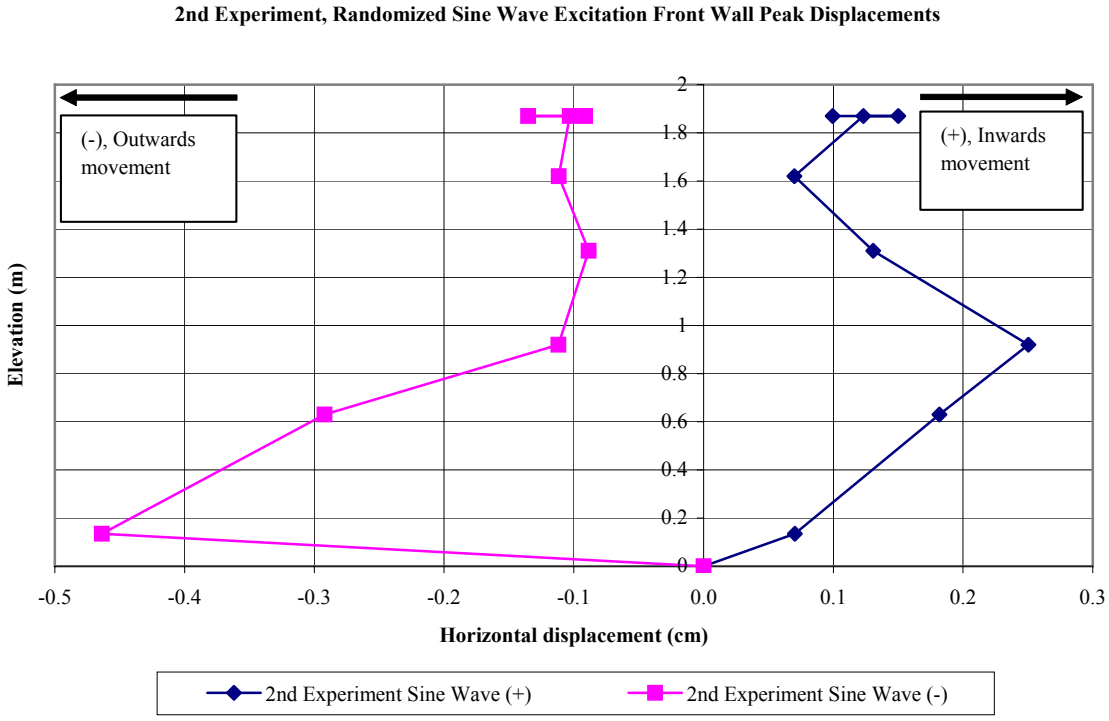

Figure 9.97. 2nd experiment, peak displacements observed at the front wall in sine motion excitation

9.4.4. 2nd Experiment El-Centro Earthquake Excitations

The displacement values at certain time instances are presented in Tables 9.39, 9.41, 9.43 and 9.45. In these tables not only the maximum displacements but also secondary maximum displacements and also displacement values at specific time instances where possible mode shape of the structure is developed are listed as well. The tables following these general tables show the peak displacement values in (+) and (–) directions and the displacement values of a specified time instance at which a possible mode shape of the structure is developed (Tables 9.40, 9.42, 9.44 and 9.46).

Table 9.39. 2nd experiment, displacements observed at the front wall in 1st El Centro excitation

2nd Experiment, Displacements Observed at the Front Wall							
EL CENTRO-1		**Elevation (m)**					
Laser Sensors	**Time (sec.)**	**0.135**	**0.63**	**0.92**	**1.31**	**1.62**	**1.87**
LS1	**3.12**	-0.161 cm					
	5.26	0.314 cm					
	5.79	-0.349 cm					
LS2	**0.92**		0.233 cm				
	3.13		-0.213 cm				
	3.18		-0.219 cm				
	5.24		0.226 cm				
LS3	**3.12**			-0.392 cm			
	9.03			0.114 cm			
	5.29			-0.049 cm			
LS4	**2.68**				0.151 cm		
	3.12				-0.331 cm		
	5.25				0.097 cm		
LS5	**3.12**					-0.322 cm	
	5.26					0.116 cm	
	8.16					0.193 cm	
	13.35					0.194 cm	
LS6	**2.57**						0.265 cm
	3.05						-0.310 cm
	3.11						-0.216 cm
	5.26						0.226 cm
	5.32						0.229 cm
LS7	**2.63**						-0.224 cm
	3.12						-0.160 cm
	5.28						-0.136 cm
	9.03						0.201 cm
LS8	**1.69**						-0.238 cm
	2.97						-0.226 cm
	3.10						0.362 cm
	5.25						0.204 cm

Table 9.40. 2nd Experiment, peak displacements observed at the front wall in 1st El Centro excitation

2nd Experiment, Displacements Observed at the Front Wall							
EL CENTRO-1	**Elevation (m)**	**Time (sec.)**	**Displacement (cm)**	**Time (sec.)**	**Peak Displacements (- Direction) (cm)**	**Time (sec.)**	**Peak Displacements (+ Direction) (cm)**
Laser Sensor	**0**	0	0	0	0	0	0
LS1	**0.135**	3.12	-0.161	5.79	-0.349	5.26	0.314
LS2	**0.63**	3.13	-0.213	3.18	-0.219	0.92	0.233
LS3	**0.92**	3.12	-0.392	3.12	-0.392	9.03	0.114
LS4	**1.31**	3.12	-0.331	3.12	-0.331	2.68	0.151
LS5	**1.62**	3.12	-0.322	3.12	-0.322	13.35	0.194
LS6	**1.87**	3.11	-0.216	3.05	-0.310	2.57	0.265
LS7	**1.87**	3.12	-0.160	2.63	-0.224	9.03	0.201
LS8	**1.87**	3.10	0.362	1.69	-0.238	3.10	0.362

Table 9.41. 2nd experiment, displacements observed at the front wall in 2nd El Centro excitation

EL CENTRO-2		**Elevation (m)**					
Laser Sensors	**Time (sec.)**	**0.135**	**0.63**	**0.92**	**1.31**	**1.62**	**1.87**
LS1	**0.91**	0.305 cm					
	3.11	-0.151 cm					
	4.48	-0.324 cm					
	5.25	0.297 cm					
LS2	**0.92**		0.279 cm				
	3.14		-0.241 cm				
LS3	**2.30**			0.128 cm			
	3.14			-0.418 cm			
LS4	**2.63**				0.128 cm		
	3.04				-0.372 cm		
	3.14				-0.321 cm		
LS5	**2.70**					0.201 cm	
	3.14					-0.273 cm	
	8.14					0.224 cm	
LS6	**2.56**						0.310 cm
	3.12						-0.320 cm
	5.47						0.276 cm
LS7	**2.22**						0.123 cm
	2.35						-0.267 cm
	3.15						-0.174 cm
	7.56						0.120 cm
LS8	**1.69**						-0.260 cm
	1.87						-0.248 cm
	3.12						0.305 cm
	5.96						-0.247 cm

Table 9.42. 2nd experiment, peak displacements observed at the front wall in 2nd El Centro excitation

2nd Experiment, Displacements Observed at the Front Wall							
EL CENTRO-2	**Elevation (m)**	**Time (sec.)**	**Displacement (cm)**	**Time (sec.)**	**Peak Displacements (- Direction) (cm)**	**Time (sec.)**	**Peak Displacements (+ Direction) (cm)**
Laser Sensor	**0**	0	0	0	0	0	0
LS1	**0.135**	3.11	-0.151	4.48	-0.324	0.91	0.305
LS2	**0.63**	3.14	-0.241	3.14	-0.241	0.92	0.279
LS3	**0.92**	3.14	-0.418	3.14	-0.418	2.30	0.128
LS4	**1.31**	3.14	-0.321	3.04	-0.372	2.63	0.128
LS5	**1.62**	3.14	-0.273	3.14	-0.273	8.14	0.224
LS6	**1.87**	3.12	-0.320	3.12	-0.320	2.56	0.310
LS7	**1.87**	3.15	-0.174	2.35	-0.267	2.22	0.123
LS8	**1.87**	3.12	0.305	1.69	-0.260	3.12	0.305

Table 9.43. 2nd experiment, displacements observed at the front wall in 3rd El Centro excitation

EL CENTRO-3		**Elevation (m)**					
Laser Sensors	**Time (sec.)**	**0.135**	**0.63**	**0.92**	**1.31**	**1.62**	**1.87**
LS1	**0.90**	0.218 cm					
	2.36	0.213 cm					
	3.13	-0.210 cm					
	5.24	0.227 cm					
	5.30	0.221 cm					
	7.19	-0.431 cm					
LS2	**0.92**		0.221 cm				
	3.17		-0.226cm				
LS3	**2.29**			0.080 cm			
	3.17			-0.437 cm			
LS4	**2.56**				0.086 cm		
	3.16				-0.317 cm		
LS5	**3.10**					-0.296 cm	
	3.19					-0.264 cm	
	9.76					0.160 cm	
LS6	**2.55**						0.245 cm
	3.11						-0.347cm
	5.48						0.205 cm
LS7	**0.80**						0.174 cm
	2.35						-0.316cm
	3.14						-0.123cm
LS8	**1.68**						-0.269cm
	3.09						0.337 cm
	5.94						-0.249cm

Table 9.44. 2nd experiment, peak displacements observed at the front wall in 3rd El Centro excitation

2nd Experiment, Displacements Observed at the Front Wall							
EL CENTRO-3	**Elevation (m)**	**Time (sec.)**	**Displacement (cm)**	**Time (sec.)**	**Peak Displacements (- Direction) (cm)**	**Time (sec.)**	**Peak Displacements (+ Direction) (cm)**
Laser Sensor	**0**	0	0	0	0	0	0
LS1	**0.135**	3.13	-0.210	7.19	-0.431	5.24	0.227
LS2	**0.63**	3.17	-0.226	3.17	-0.226	0.92	0.221
LS3	**0.92**	3.17	-0.437	3.17	-0.437	2.29	0.080
LS4	**1.31**	3.16	-0.317	3.16	-0.317	2.56	0.086
LS5	**1.62**	3.19	-0.264	3.10	-0.296	9.76	0.160
LS6	**1.87**	3.11	-0.347	3.11	-0.347	2.55	0.245
LS7	**1.87**	3.14	-0.123	2.35	-0.316	0.80	0.174
LS8	**1.87**	3.09	0.337	1.68	-0.269	3.09	0.337

Table 9.45. 2nd experiment, displacements observed at the front wall in 4th El Centro excitation

EL CENTRO-4		**Elevation (m)**					
Laser Sensors	**Time (sec.)**	**0.135**	**0.63**	**0.92**	**1.31**	**1.62**	**1.87**
LS1	**2.40**	-0.180 cm					
	8.61	0.335 cm					
	9.48	-0.466 cm					
LS2	**2.44**		-0.271 cm				
	8.59		0.236 cm				
LS3	**2.32**			-0.436 cm			
	13.15			0.082 cm			
LS4	**2.40**				-0.397 cm		
	2.98				0.200 cm		
LS5	**2.40**					-0.371 cm	
	2.98					0.213 cm	
LS6	**1.48**						0.296 cm
	2.43						-0.299 cm
LS7	**2.43**						-0.208 cm
	5.80						-0.331 cm
	9.46						0.126 cm
LS8	**1.00**						-0.280 cm
	2.47						0.370 cm
	5.20						-0.240 cm

Table 9.46. 2nd experiment, peak displacements observed at the front wall in 4th El Centro excitation

2nd Experiment, Displacements Observed at the Front Wall							
EL CENTRO-4	**Elevation (m)**	**Time (sec.)**	**Displacement (cm)**	**Time (sec.)**	**Peak Displacements (- Direction) (cm)**	**Time (sec.)**	**Peak Displacements (+ Direction) (cm)**
Laser Sensor	**0**	0	0	0	0	0	0
LS1	**0.135**	2.40	-0.180	9.48	-0.466	8.61	0.335
LS2	**0.63**	2.44	-0.271	2.44	-0.271	8.59	0.236
LS3	**0.92**	2.32	-0.436	2.32	-0.436	13.15	0.082
LS4	**1.31**	2.40	-0.397	2.40	-0.397	2.98	0.200
LS5	**1.62**	2.40	-0.371	2.40	-0.371	2.98	0.213
LS6	**1.87**	2.43	-0.299	2.43	-0.299	1.48	0.296
LS7	**1.87**	2.43	-0.208	5.80	-0.331	9.46	0.126
LS8	**1.87**	2.47	0.370	1.00	-0.280	2.47	0.370

A possible dominant mode shape developed is illustrated in Figure 9.98.

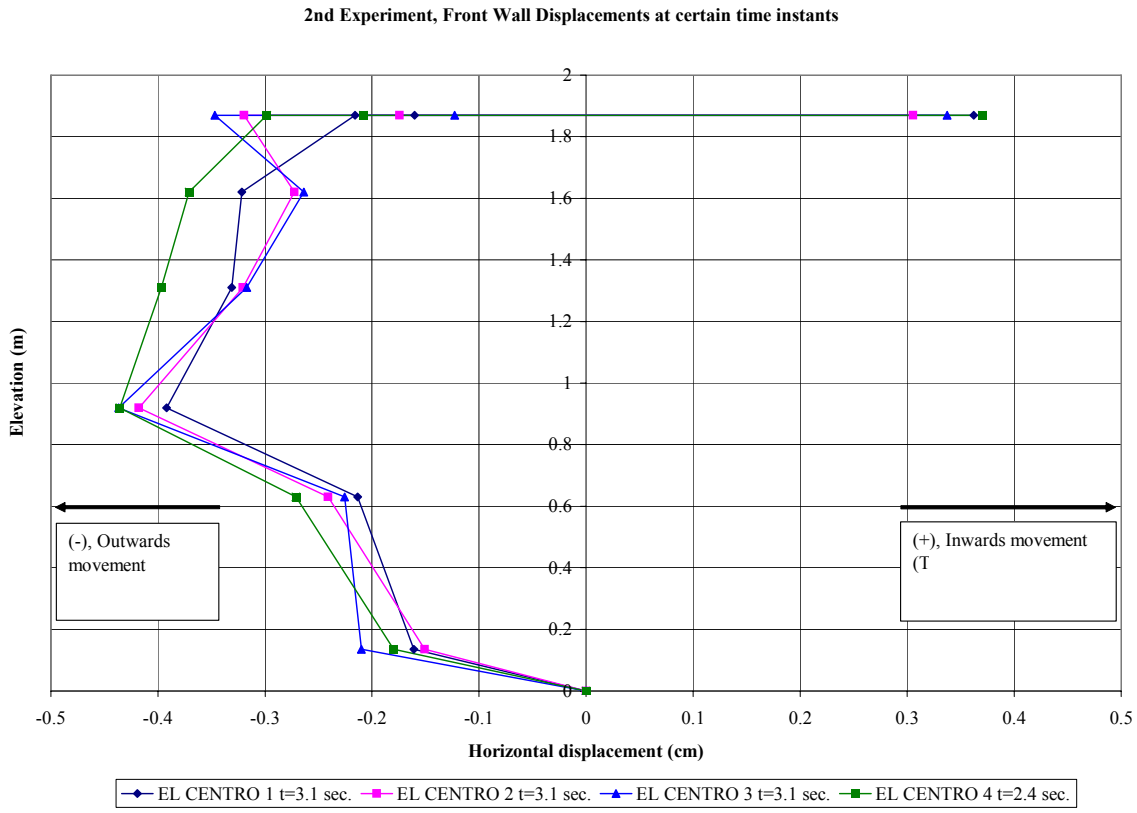

Figure 9.98. 2nd experiment, displacements observed at the front wall for certain time instances in the ElCentro excitations

The maximum displacements observed on the front wall are at the levels H = 0.135 m and H = 0.92 m with the values of 0.466 cm and 0.436 cm, respectively in the outwards direction as it can be seen in Figure 9.99.

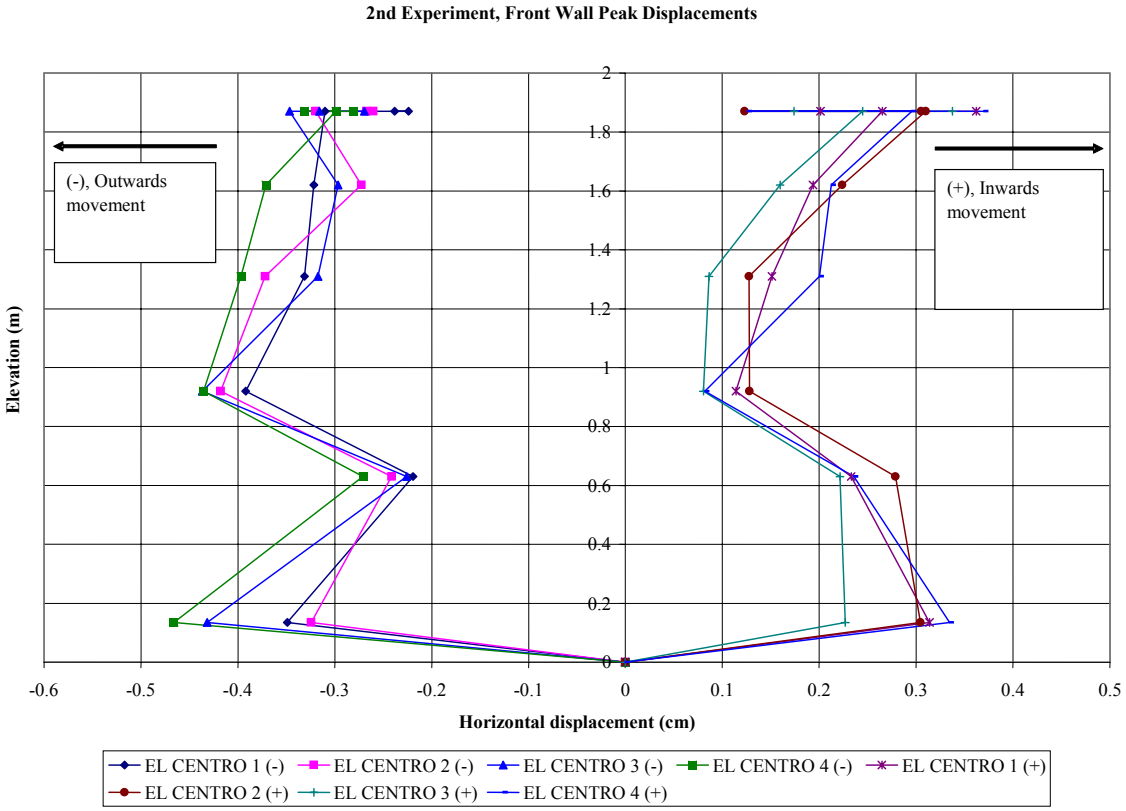

Figure 9.99. 2nd experiment, peak displacements observed at the front wall in the El Centro excitations

9.4.5. Conclusions

The results of the experimental analyses show that the test walls behaved rigidly without the presence of almost any residual displacements.

The relative displacement plots at certain time instances (i.e. t=2.8 sec. and t=2.6 sec. in the 1st experiment and t=3.1 sec. and t=2.4 sec. in the 2nd experiment) where 4 or 5 out of 8 laser displacement sensors measured the maximum displacements in the time-history excitation, indicate that possible predominant mode shapes of the structure developed during these time periods. Considering the structure as a lumped mass system having a

three-degree of freedom (Carotti and Rimoldi, 1998) as shown in Figure 9.100 one obtains three shear model shapes, which are illustrated in Figure 9.101.

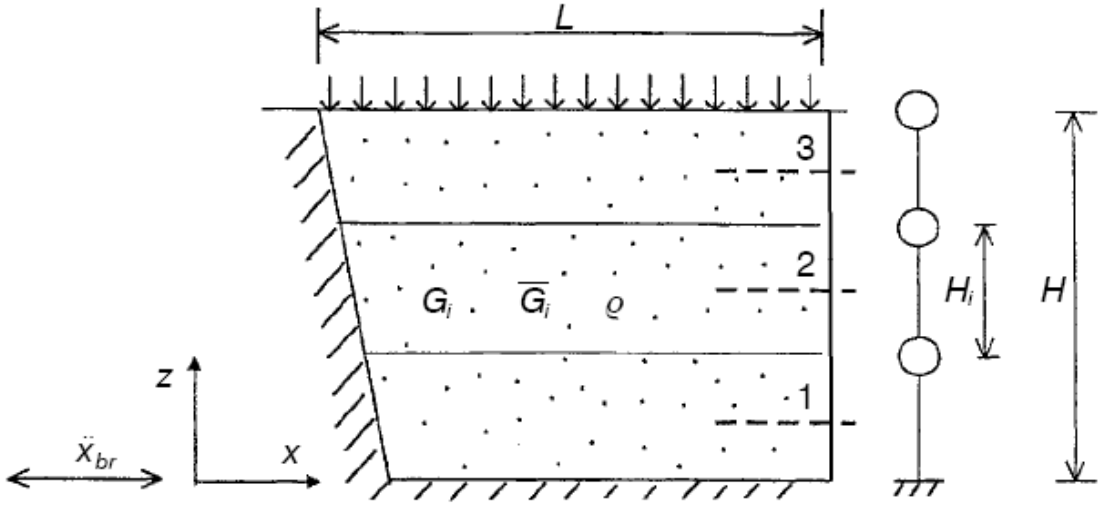

Figure 9.100. Schematic of a soil wall as a stack of soil layers and the lumped mass model [33]

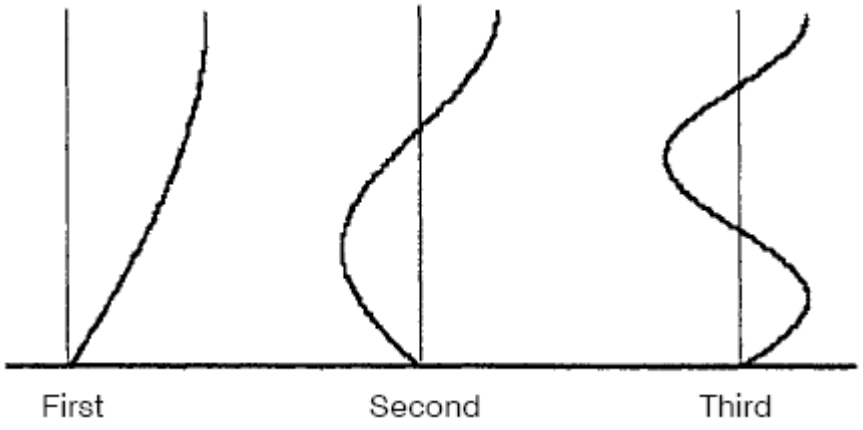

Figure 9.101. Three shear modal shapes used in the modal analysis of the dynamic wall response [33]

Considering the structure as a lumped mass system, according to the above shear modal shapes it can be figured out that in the 1st and 2nd experiments, 2nd and 1st shear mode shapes were developed, respectively (Figure 9.95 and Figure 9.98) due to the wide-range of frequency content of the earthquake record as seen from the Fourier amplitude-frequency plot in Figure 9.102.

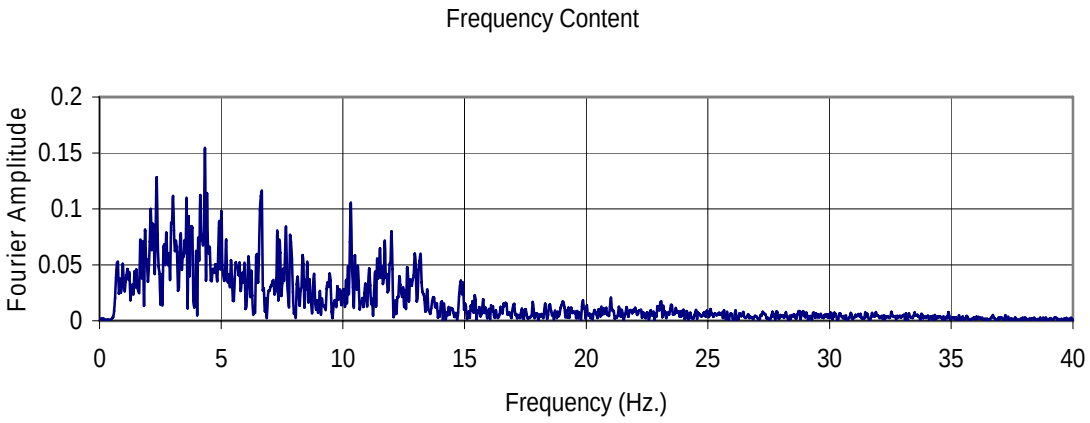

Figure 9.102. Frequency content of the El-Centro earthquake record applied

10. COMPARISON OF THE EXPERIMENT RESULTS WITH THE NUMERICAL ANALYSIS RESULTS

In Figure 10.1 the base displacement-time history record of the 1st El Centro Earthquake motion in 1st experiment is shown.

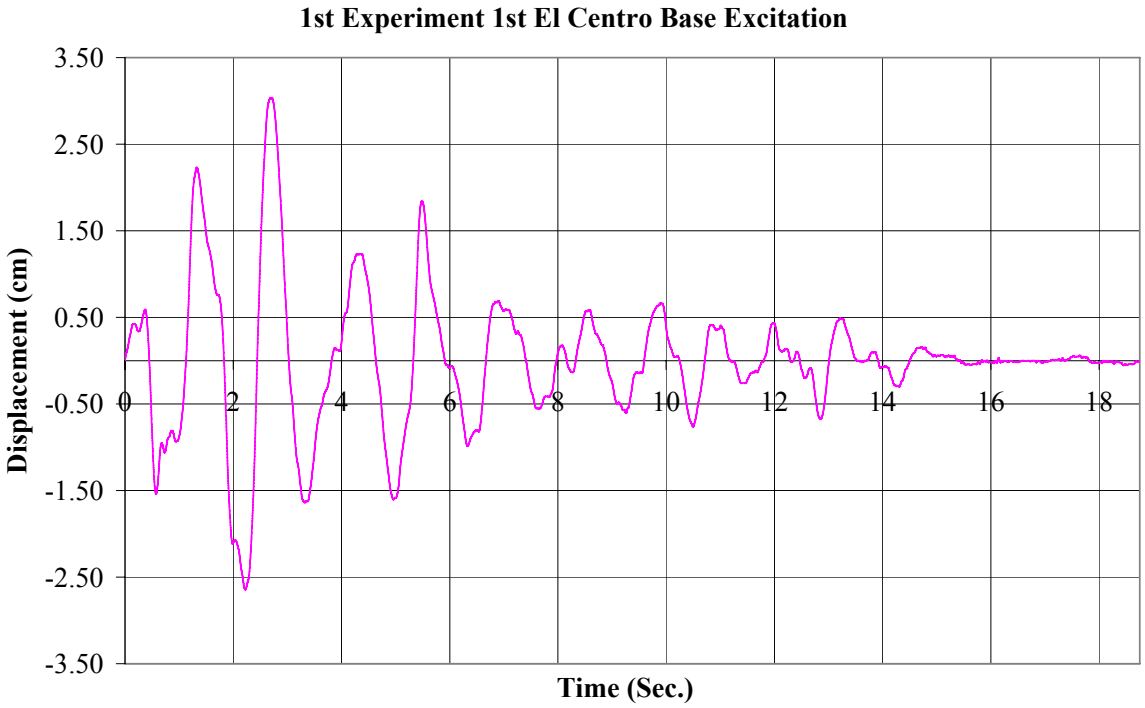

Figure 10.1. 1st experiment 1st El-Centro shaking base excitation

In Figures 10.2 to 10.7, the comparisons of the 1st experiments' results with the numerical analysis results can be seen. In these comparisons, the top relative displacements obtained from laser sensors LS6, LS7 and LS8, which correspond to right, middle and left points as shown in Figure 7.34 and the top relative displacements of the Plaxis program's rubber-filled back model were taken into consideration.

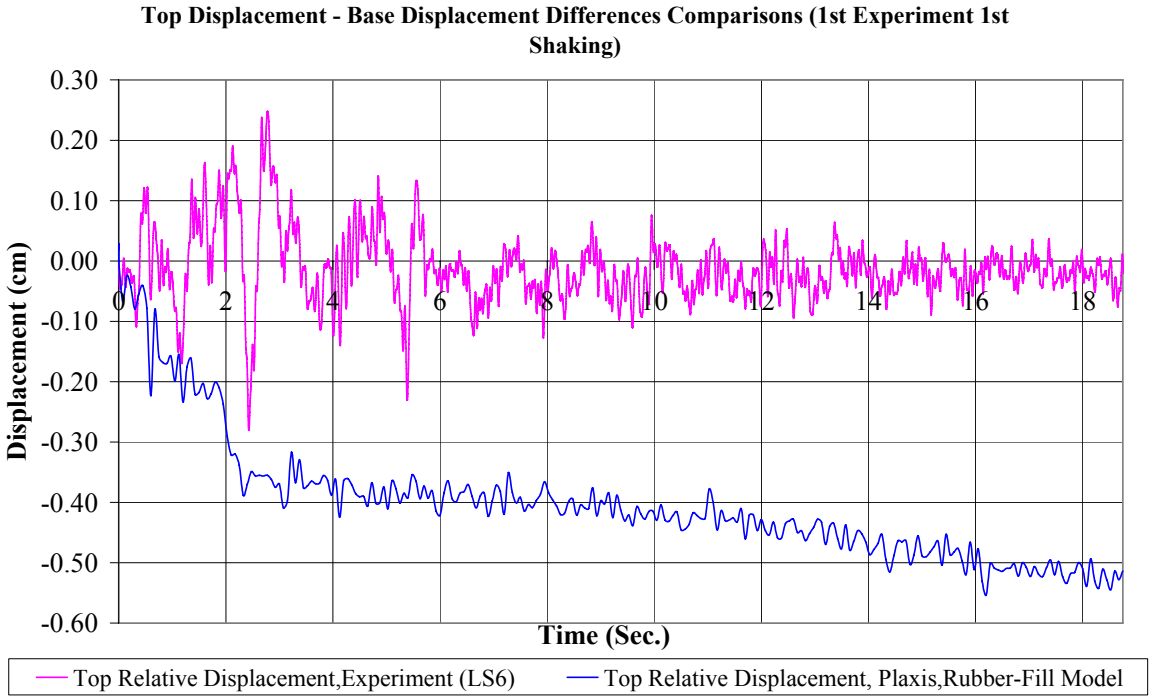

Figure 10.2. The top displacements (relative to base) measured by LS6 and Plaxis program in the 1st experiment 1st El-Centro earthquake motion

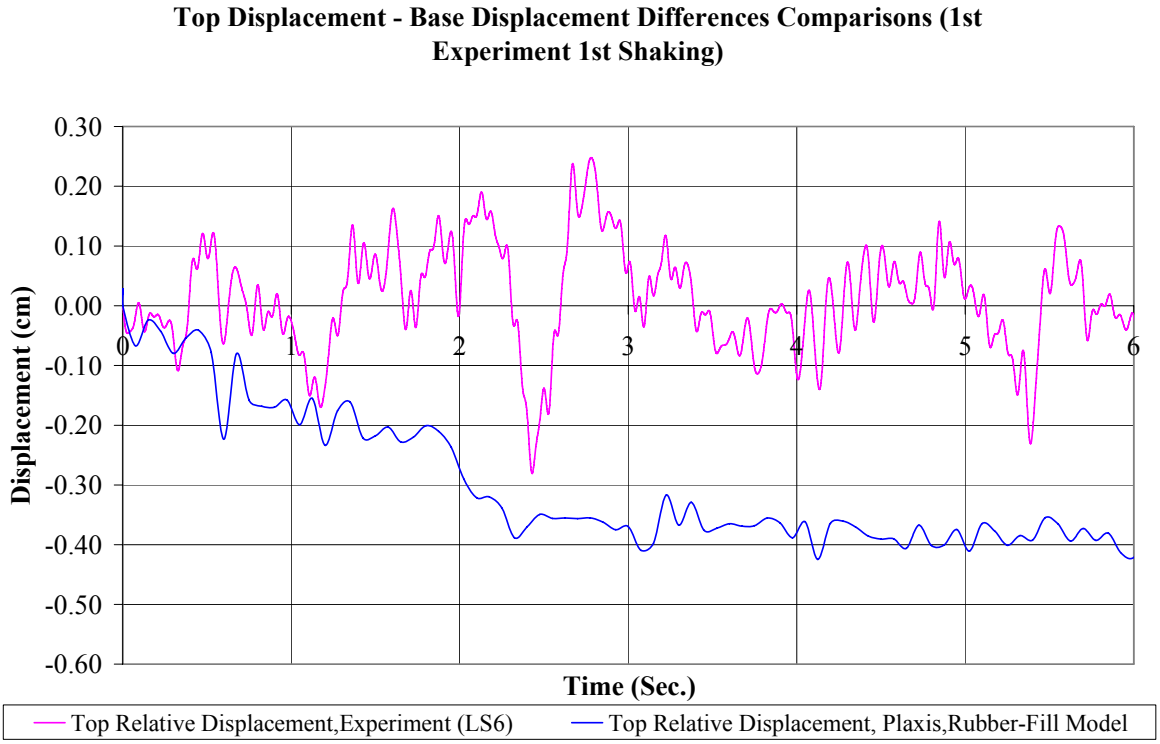

Figure 10.3. The top displacements (relative to base) measured by LS6 and Plaxis program in the 1st experiment 1st El-Centro earthquake motion (1st 6 sec.)

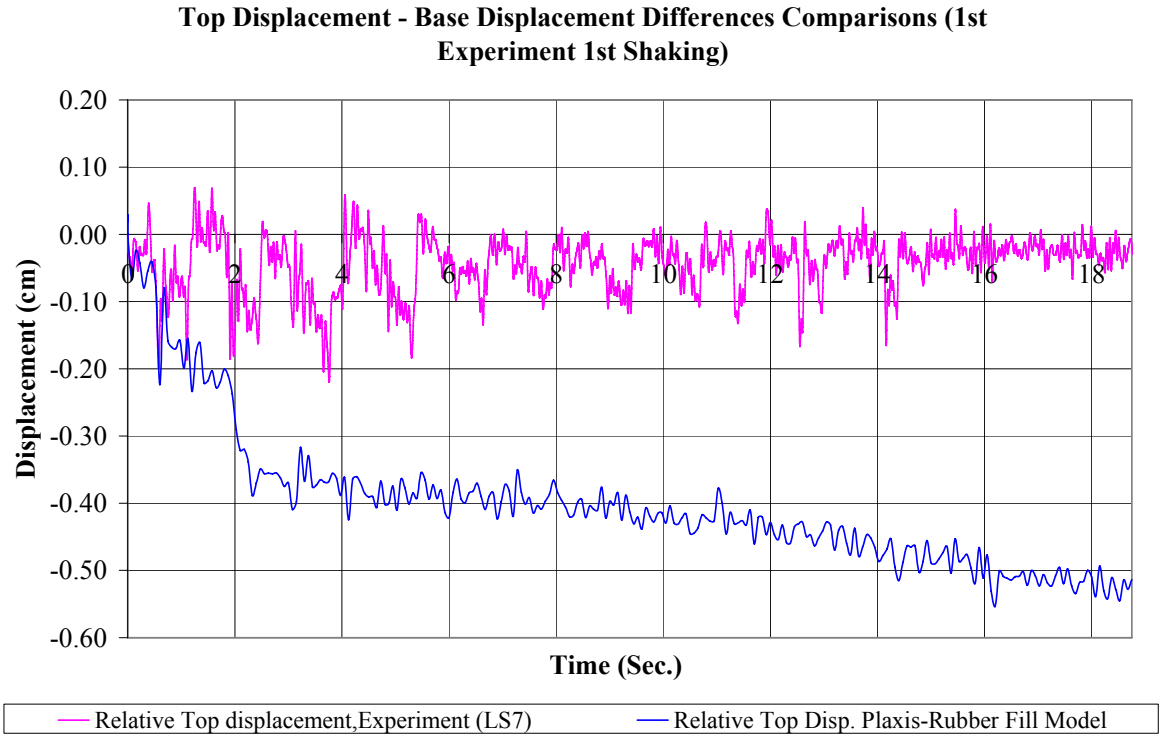

Figure 10.4. The top displacements (relative to base) measured by LS7 and Plaxis program in the 1st experiment 1st El-Centro earthquake motion

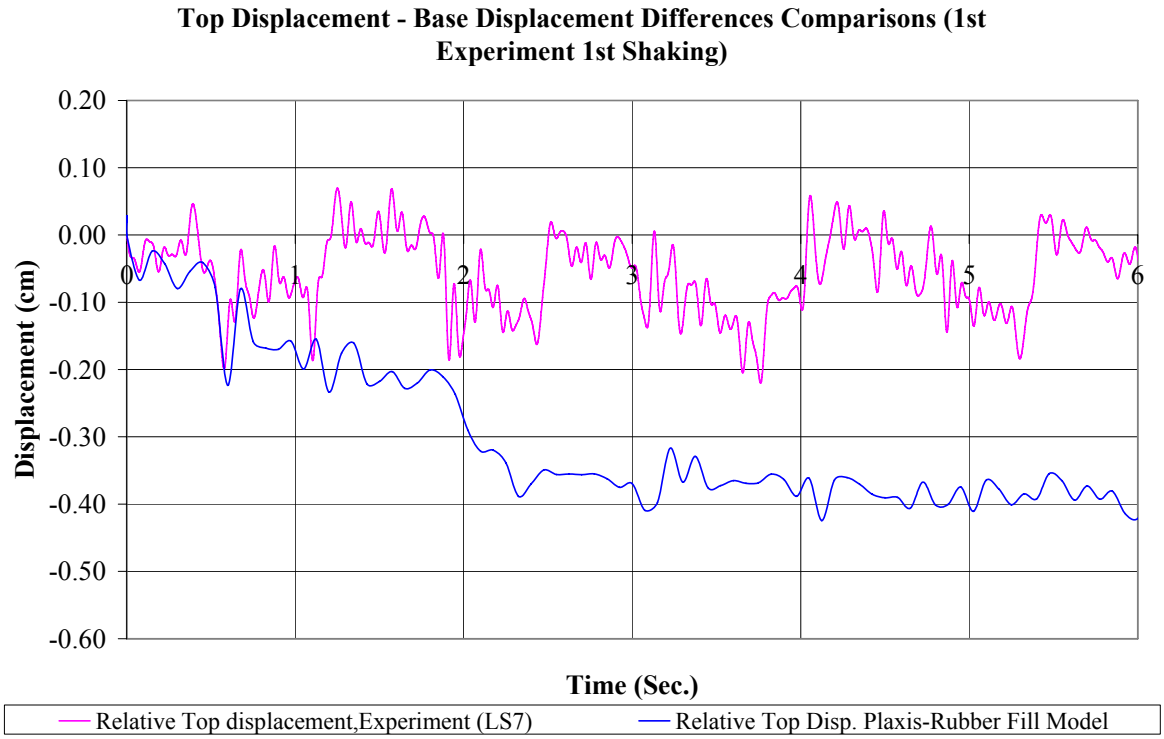

Figure 10.5. The top displacements (relative to base) measured by LS7 and Plaxis program in the 1st experiment 1st El-Centro earthquake motion (1st 6 sec.)

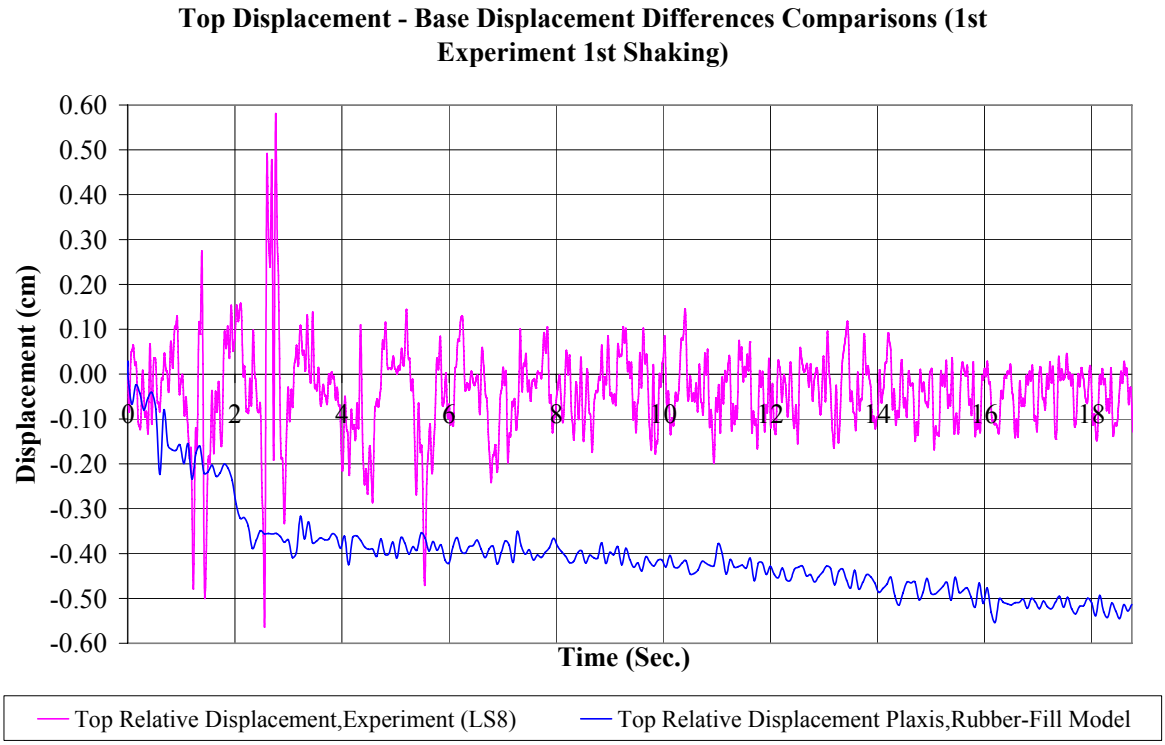

Figure 10.6. The top displacements (relative to base) measured by LS8 and Plaxis program in the 1st experiment 1st El-Centro earthquake motion

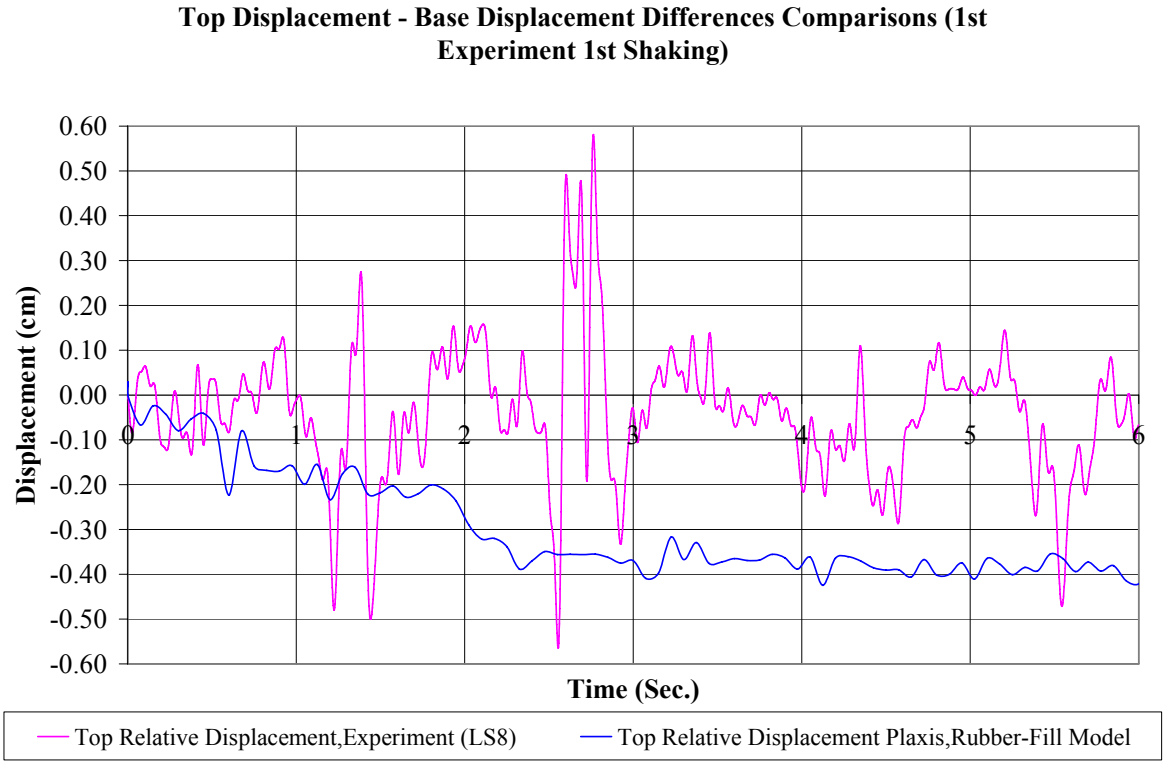

Figure 10.7. The top displacements (relative to base) measured by LS8 and Plaxis program in the 1st experiment 1st El-Centro earthquake motion (1st 6 sec.)

While Laser sensors measure almost no residual displacements on top of the wall at the end of the shaking, Plaxis v8.4 results show a residual relative displacement value of 5 mm at the top of the retaining wall. The relative displacement-time behavior measured by LS6 and LS7 resemble the behavior of numerical analyses results. However, LS8 show a stressed behavior in comparison with the other laser sensors, which is a possible indication that the laser ray hit to a non-smooth location of the modular block.

Presented in Figure 10.8 is the base displacement-time history record of the 1st El Centro Earthquake motion excitation during the 2nd experiment.

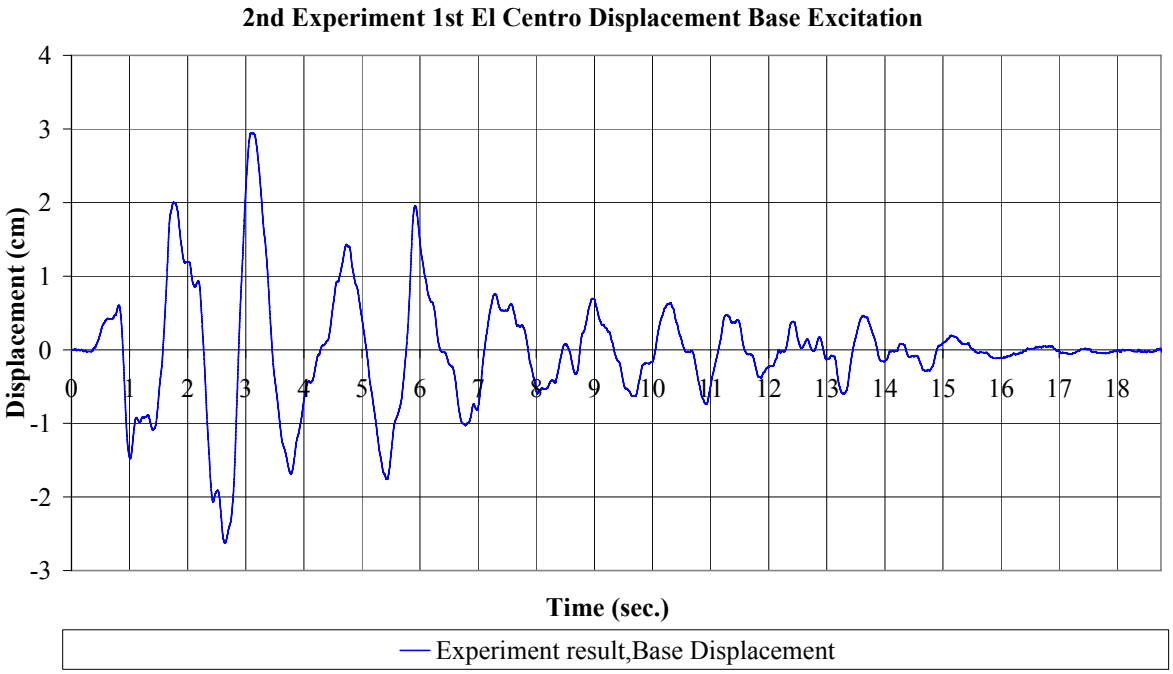

Figure 10.8. 2nd experiment 1st El-Centro shaking base excitation

In Figures 10.9 to 10.14, the comparisons of the 2nd experiments' results with the numerical analysis results can be seen. In these comparisons, the top relative displacements obtained from laser sensors LS6, LS7 and LS8, which correspond to right, middle and left points as shown in Figure 7.34 and the top relative displacements of the Plaxis program's rubber-filled back model were taken into consideration.

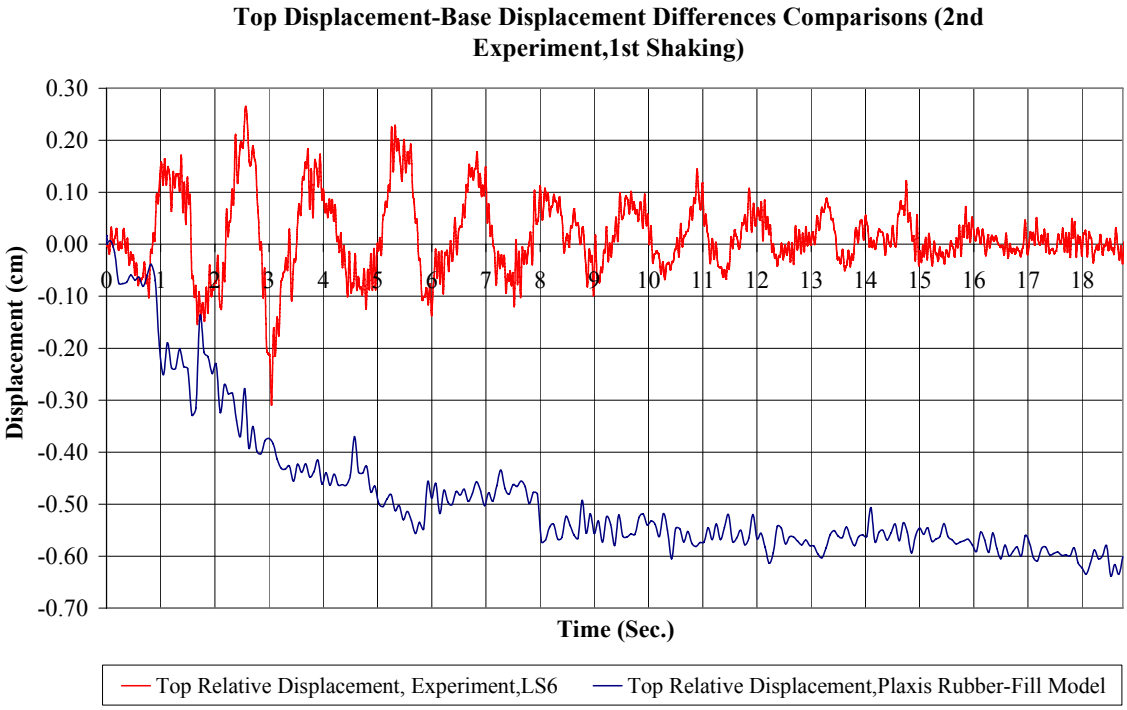

Figure 10.9. The top displacements (relative to base) measured by LS6 and Plaxis program in the 2nd experiment 1st El-Centro earthquake motion

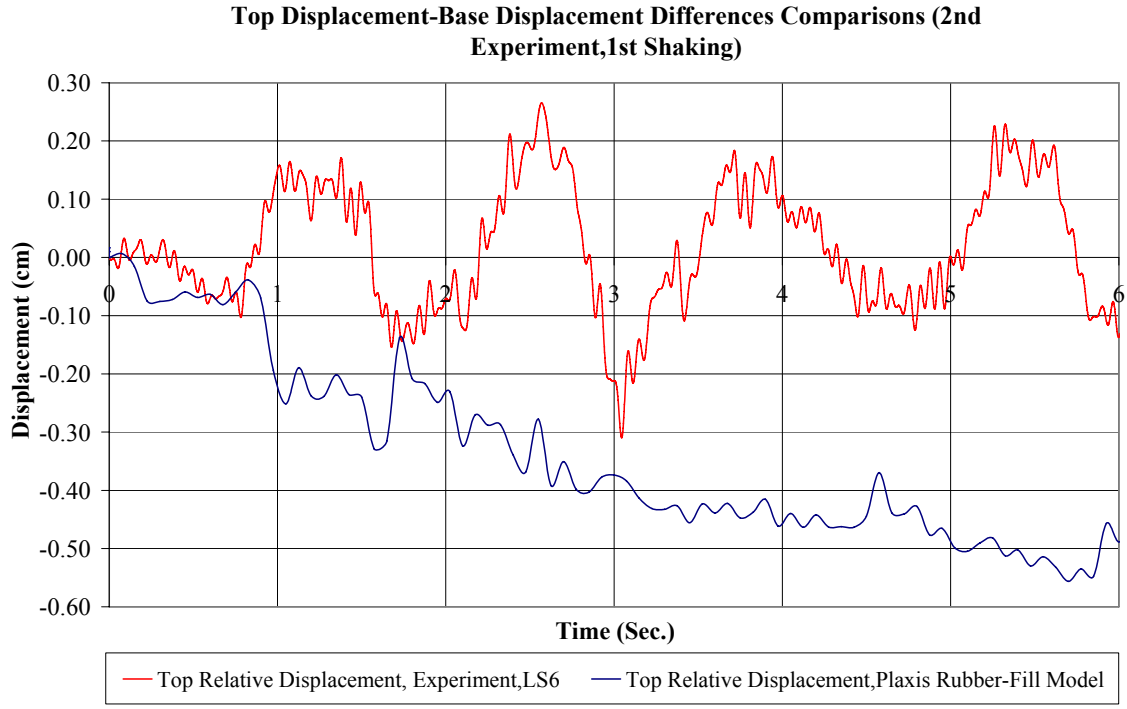

Figure 10.10. The top displacements (relative to base) measured by LS6 and Plaxis program in the 2nd experiment 1st El-Centro earthquake motion (1st 6 sec.)

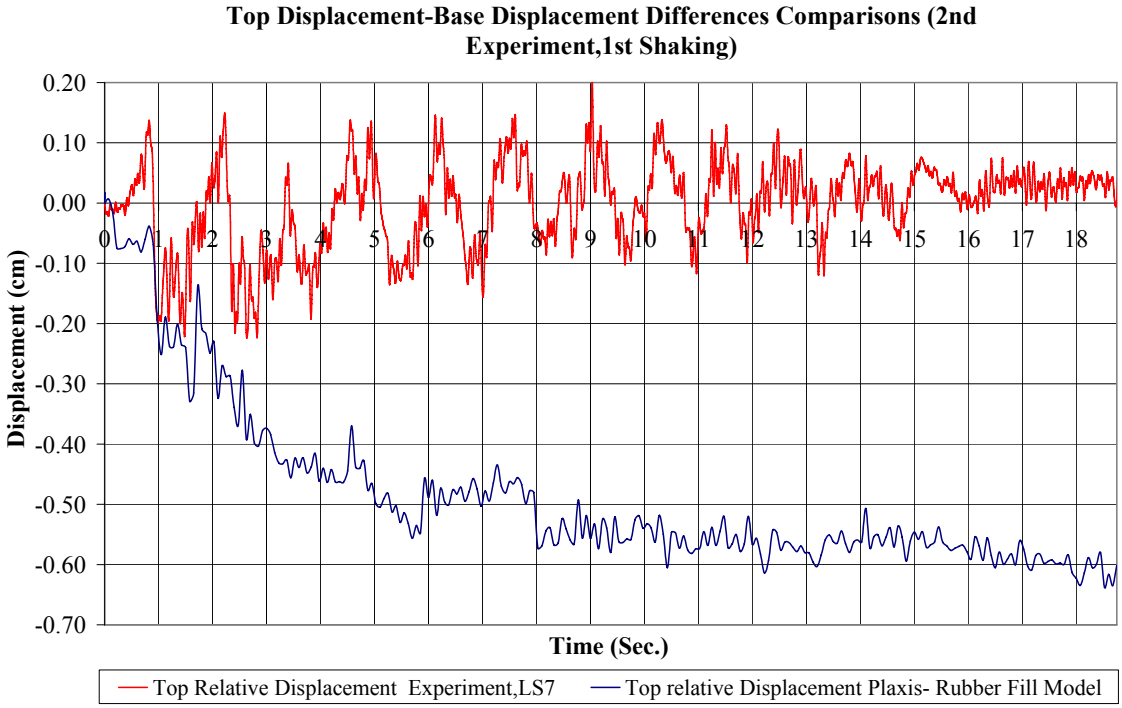

Figure 10.11. The top displacements (relative to base) measured by LS7 and Plaxis program in the 2nd experiment 1st El-Centro earthquake motion

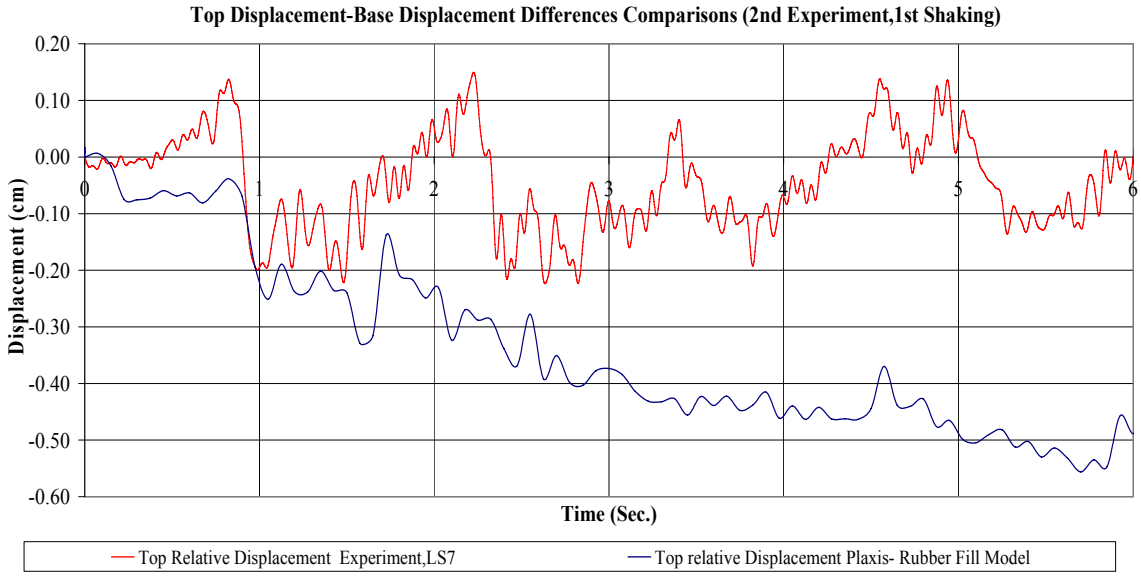

Figure 10.12. The top displacements (relative to base) measured by LS7 and Plaxis program in the 2nd experiment 1st El-Centro earthquake motion (1st 6 sec.)

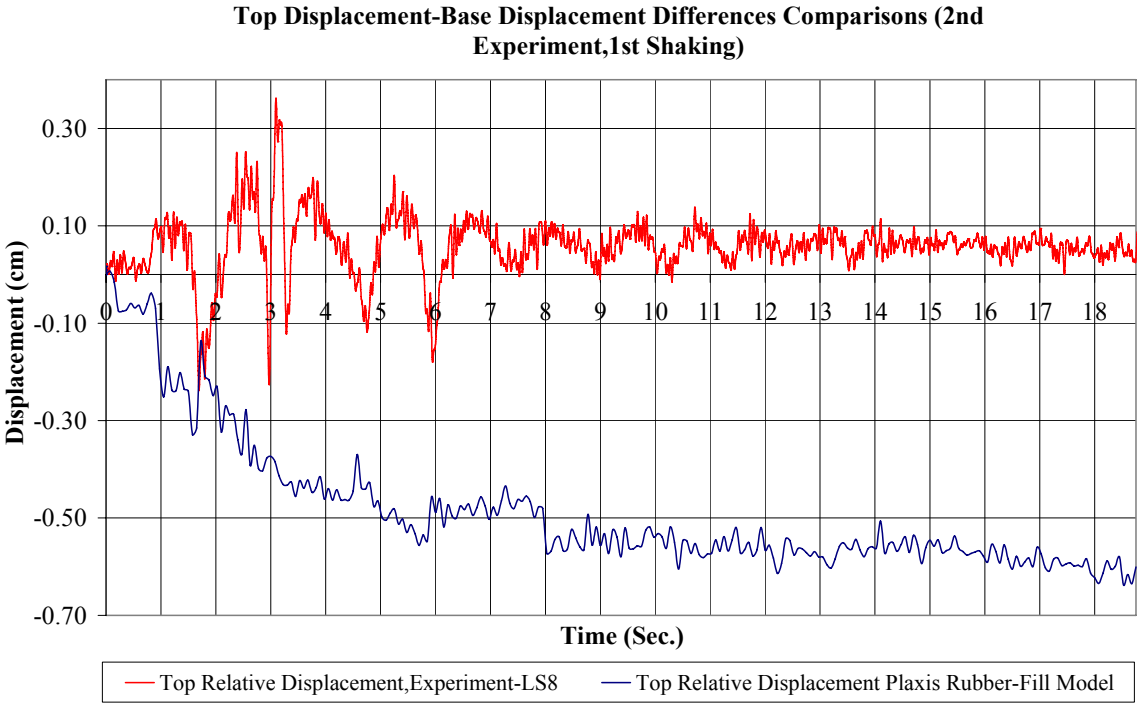

Figure 10.13. The top displacements (relative to base) measured by LS8 and Plaxis program in the 2nd experiment 1st El-Centro earthquake motion

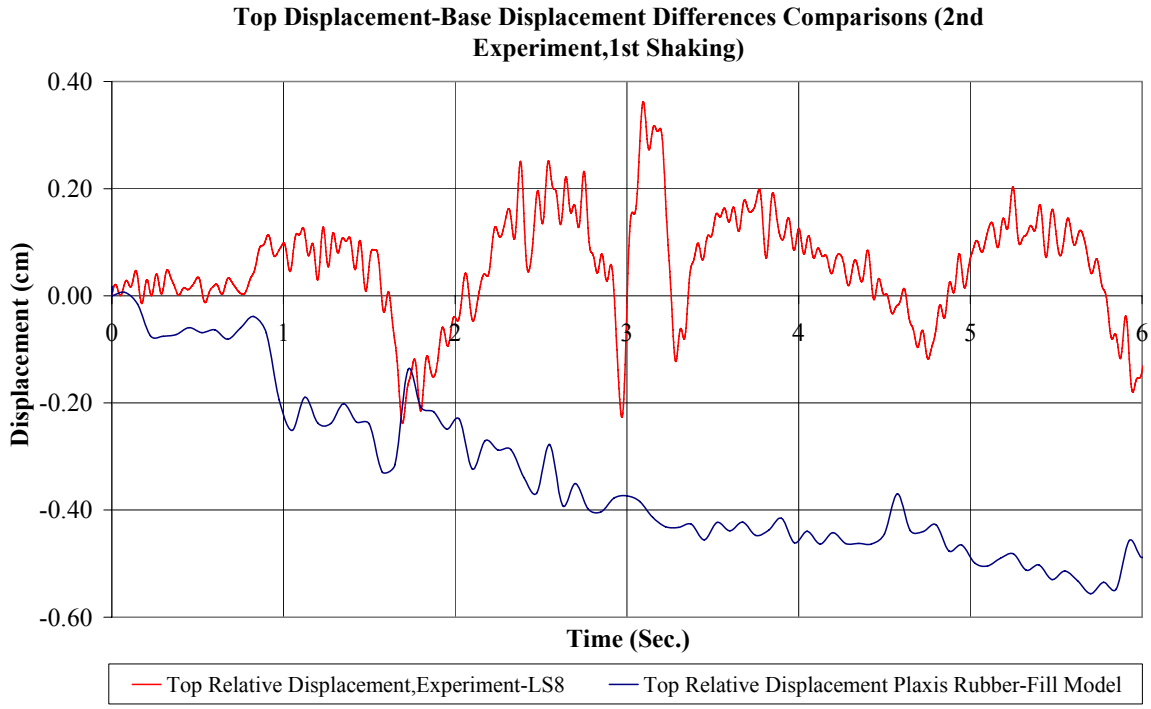

Figure 10.14. The top displacements (relative to base) measured by LS8 and Plaxis program in the 2nd experiment 1st El-Centro earthquake motion (1st 6 sec.)

While Laser sensors measure almost no residual displacements on top of the wall at the end of the shaking, Plaxis v8.4 results show a residual relative displacement value of 6 mm at the top of the retaining wall. The relative displacement-time behavior measured by LS7 best resembles the behavior of numerical analyses results.

Demonstrated in Figures 10.15 and 10.16 are the deformed shapes of the numerically simulated wall models.

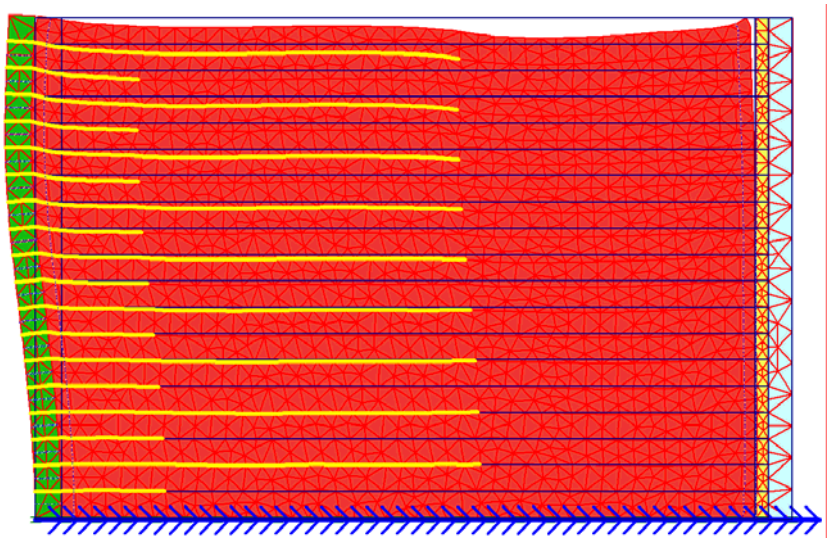

Figure 10.15. Deformed 1st numerical model at the end of the base excitation for L/H=0.9

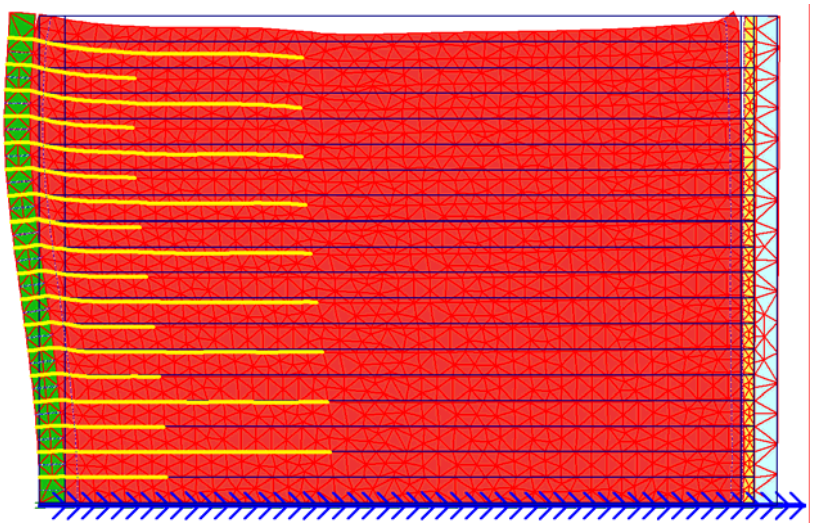

Figure 10.16. Deformed 2nd numerical model at the end of the base excitation for L/H=0.6

As an additional note, Plaxis v7.2 program, in which soil was modeled using Mohr-Coulomb model, calculated residual displacements at the top of the wall attaining to 7 mm and 12 mm for the 1st and 2nd experimental models, respectively.

11. GENERAL CONCLUSIONS

1. The fundamental frequency of the structure was determined based on Finite Element analyses and evaluation of acceleration-time history records to be 10 Hz and 12.5 Hz, respectively. These results demonstrate that the value obtained by FEM analysis was a very close estimation to the actual value. Taking into account the predominant frequency range of the El-Centro Earthquake record (0.5 Hz-2 Hz for the non-scaled and 0.71 Hz- 2.82 Hz for the scaled record), it is concluded that there is a significant difference between the natural frequency of the structure and the predominant frequency of the earthquake and because of this reason a resonant behavior of the structure wasn't observed. In addition to this, since the maximum acceleration of the time history record being 0.3g was far from causing plastic deformations in the structure the GRS-RW model behaved in a rigid manner.

2. The maximum amplification factor increased along the height towards the top of the structure both on the front wall and on top of the backfill. Additionally, after the successive shakings higher acceleration amplification factors were observed both on the front wall and on top of the backfill when considered with the previous shaking values. This is an indication of the compacting and stiffening effect of the earthquake loadings which was developed in the structure after the end of every shaking. By taking into account the observed little differences between the peak relative displacement plots of each shaking, it can be stated that during the shakings, while weaker soils acted like dampers to the wall, stronger soils amplified the accelerations in the structure.

3. As a general conclusion it can be stated that the GRS-RW, which was designed according to the methodologies in current design guidelines, performed very well under a moderately strong earthquake such as El-Centro. The GRS-RW models didn't suffer any trouble under external, internal and facing stability types of failure modes.

4. From the comparisons of the two experiment results, it can be concluded that, in the second experiment where shorter reinforcements were used, the geotextile members were exposed to larger dynamic tensile stresses than in the first experiment and deformed more. However, the dynamic tensile strains measured during the excitations in both experiments stayed well below the yield tensile strain of 11 per cent with the values reaching to 2.4 per cent at most.

5. By observing larger tensile stress values at level H = 40 cm (from the base of the wall) when compared to level H = 160 cm (from the base of the wall), it can be concluded that the dynamic load increment pressure distribution for internal stability analysis adopted in FHWA for the calculation of reinforcement loads is in accordance with the experimental results.

6. The maximum average tensile strains observed on the geotextile reinforcement develop on the regions near to the potential failure surface assumed by Rankine's theory. This is attributed to the high rigidness of the wall. Since shorter reinforcements were used in the 2nd experiment, shallower internal failure surfaces were observed when compared to the 1st experiment indicating that as the stiffness of the wall decreases internal failure surface flattens causing an increase in the volume of the sheared zone.

7. According to the Newmark's Displacement Method analyses, as the geotextile lengths decrease, the critical acceleration values (a_c) needed for the structure to undergo to residual displacements decrease as well. With the observation of a_c values between 0.6g and 0.73g for the 1st experiment and between 0.55g-0.78g for the 2nd experiment in different layers and in different failure modes it can be stated that an earthquake record such as El Centro earthquake could not induce permanent displacements in the structure.

8. The classical Modal Analysis Method used for linear systems with classical damping can be used for GRS-RWs as well. With the observation of the first two modes separately for the two test walls at certain time instances, it can be stated

that these are the most governing modes and superposition of these modes are adequate for dynamic design purposes under similar earthquakes such as El Centro.

9. While experiment results show almost no permanent displacements at the top of the wall, numerical analyses with the Plaxis v8.4 program calculate permanent displacements attaining to 5 and 6 mm at the top of the wall for the 1st and 2nd models, respectively. By taking into account these calculated small displacement values and close relative top displacement curves between the experimental and numerical analyses, it can be concluded that Plaxis v8.4's HSsmall model can better represent the behavior of GRS-RWs under dynamic loads by demonstrating hysteretic material damping than the basic Mohr-Coulomb model.

APPENDIX A: ACCELERATION-TIME HISTORY CURVES OF THE EL CENTRO EARTHQUAKE EXCITATIONS

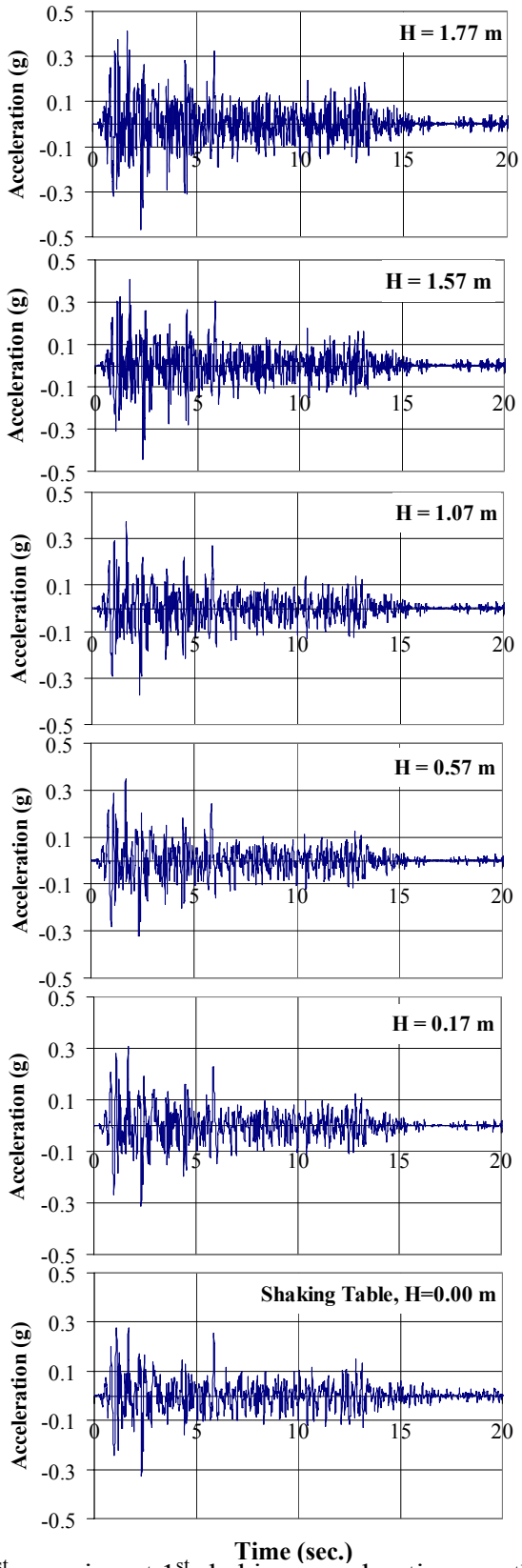

Figure A-1. 1st experiment 1st shaking, accelerations on the front wall

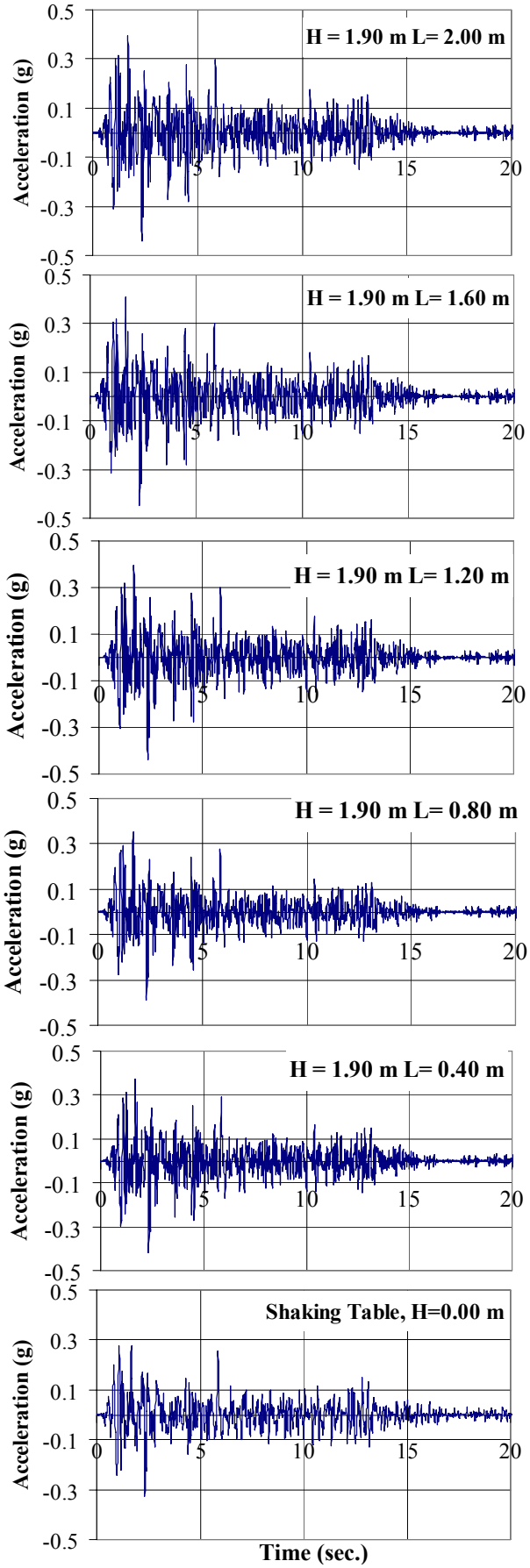

Figure A-2. 1st experiment 1st shaking, accelerations at the top of the backfill

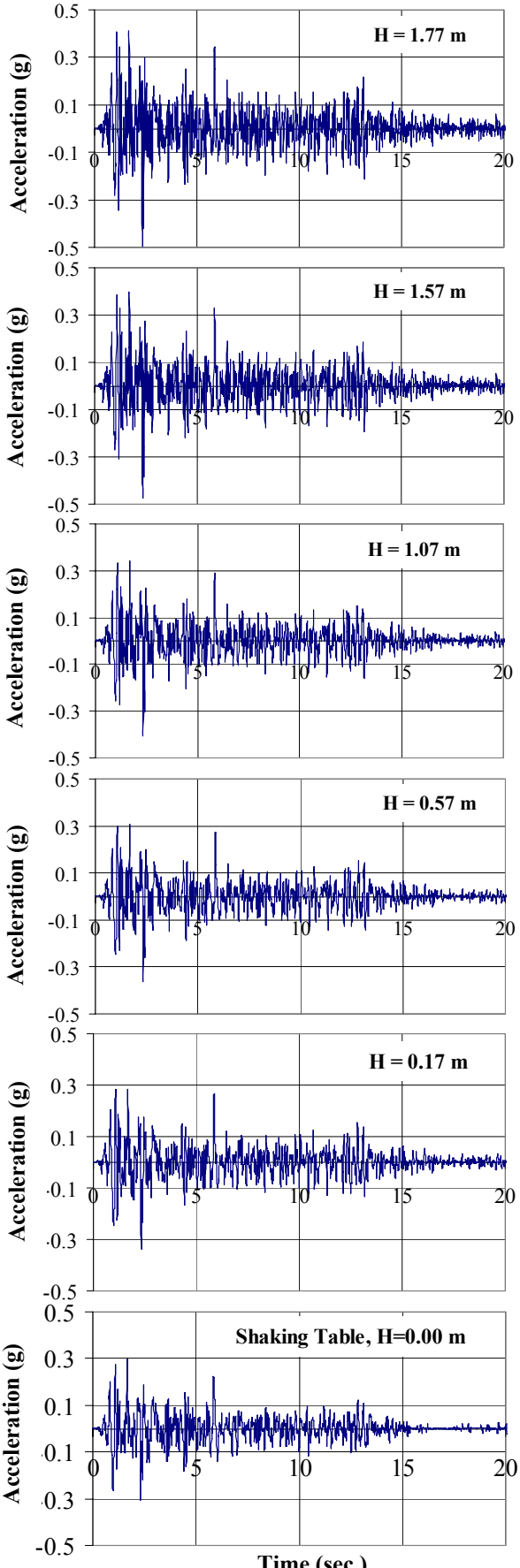

Figure A-3. 1st experiment 2nd shaking, accelerations on the front wall

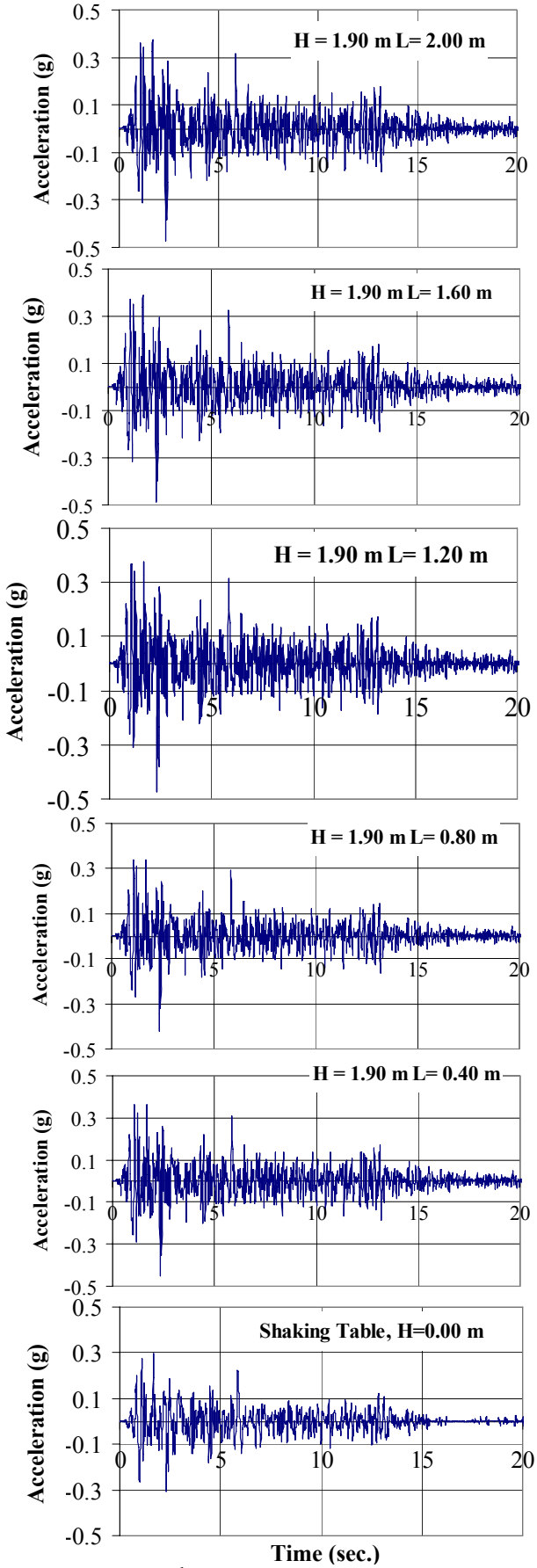

Figure A-4. 1st experiment 2nd shaking, accelerations at the top of the backfill

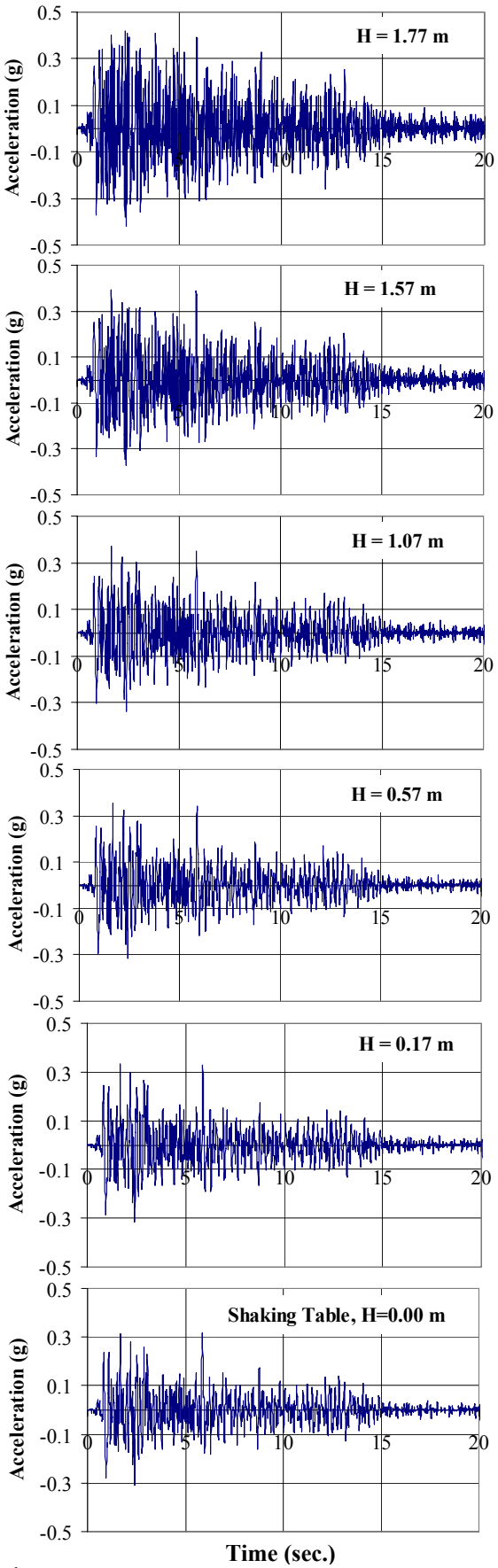

Figure A-5. 2nd experiment 1st shaking, accelerations on the front wall

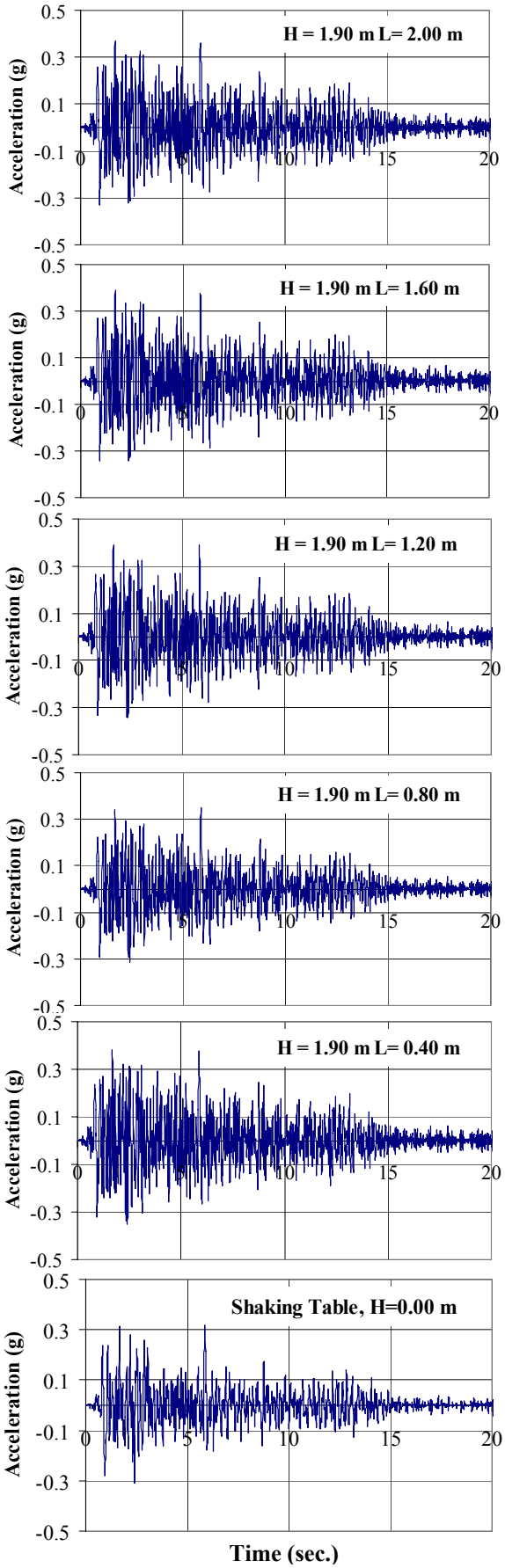

Figure A-6. 2nd experiment 1st shaking, accelerations on top of the backfill

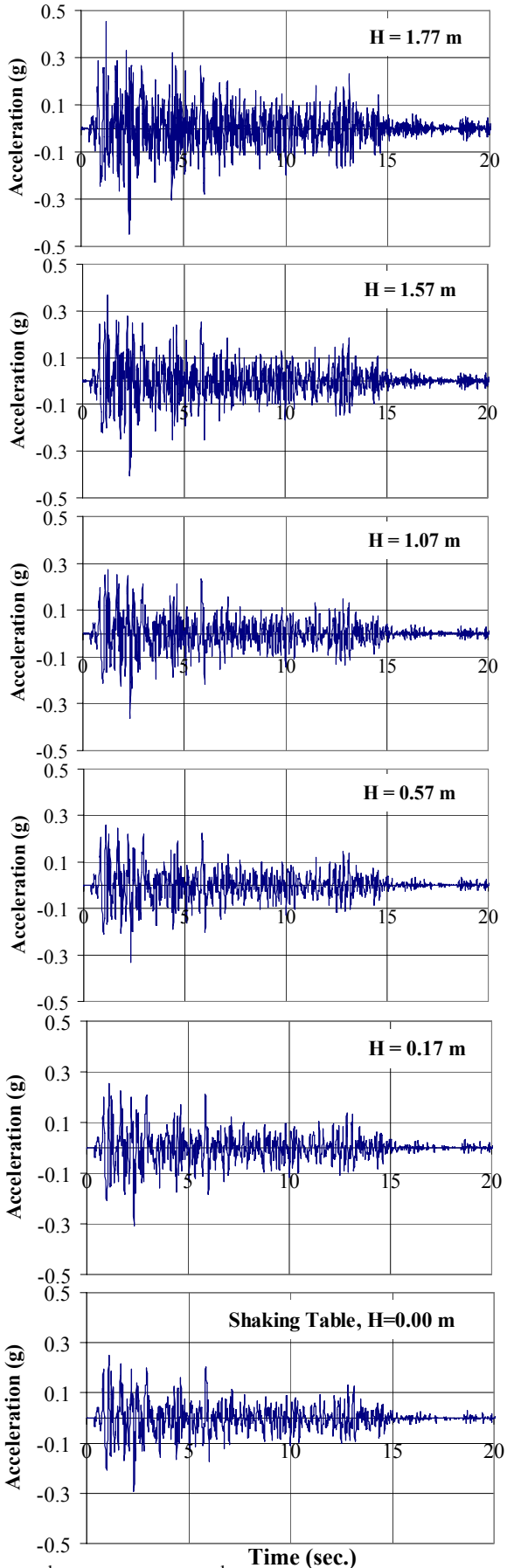

Figure A-7. 2nd experiment 2nd shaking, accelerations on the front wall

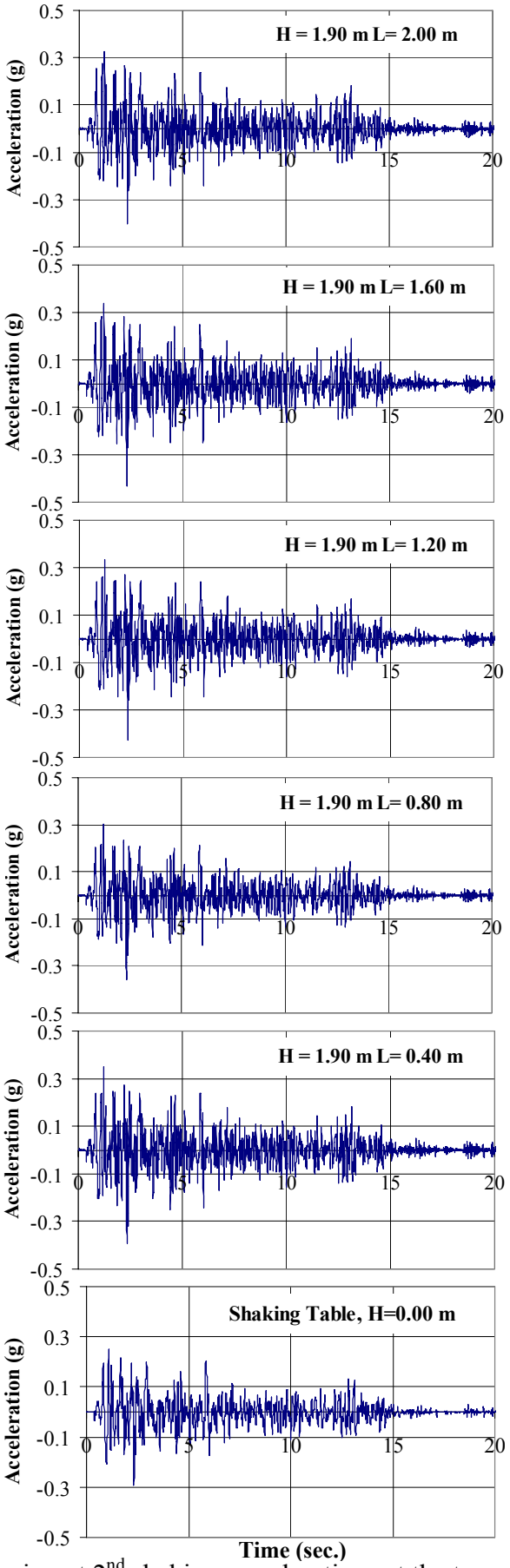

Figure A-8. 2nd experiment 2nd shaking, accelerations at the top of the backfill

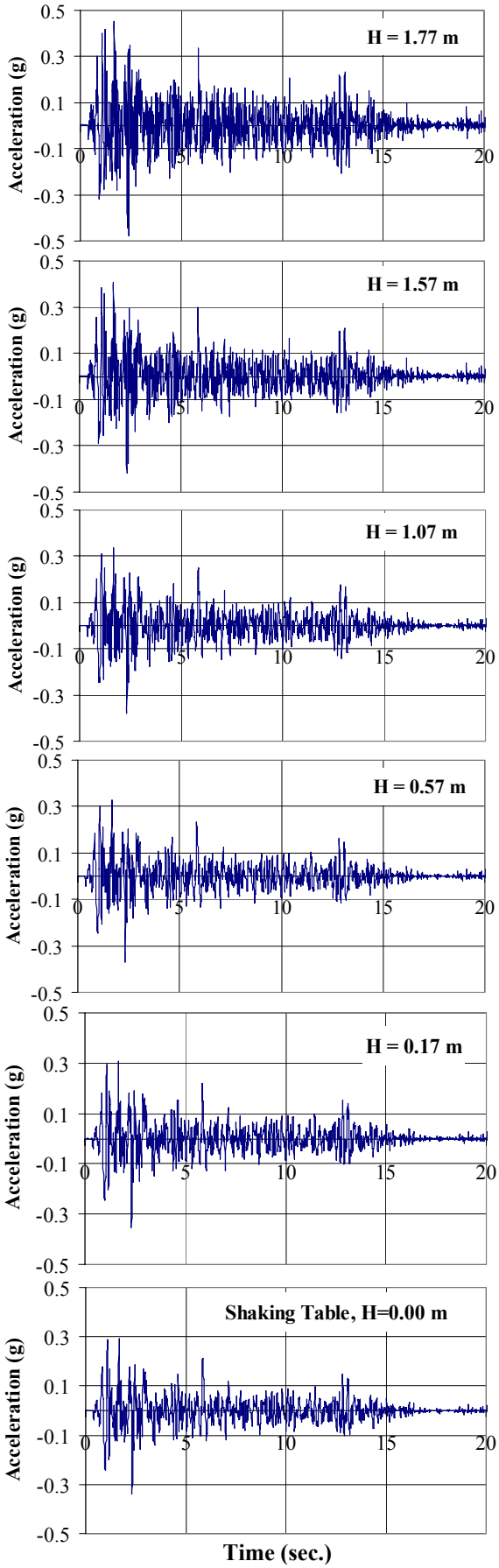

Figure A-9. 2nd experiment 3rd shaking, accelerations on the front wall

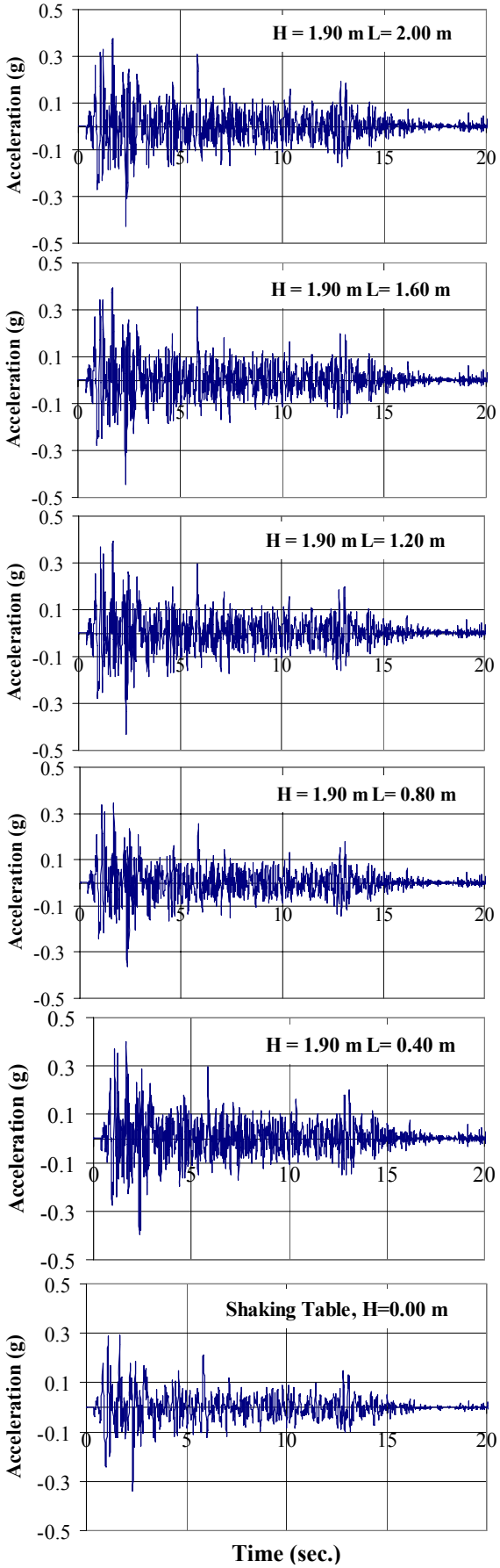

Figure A-10. 2nd experiment 3rd shaking, accelerations on top of the backfill

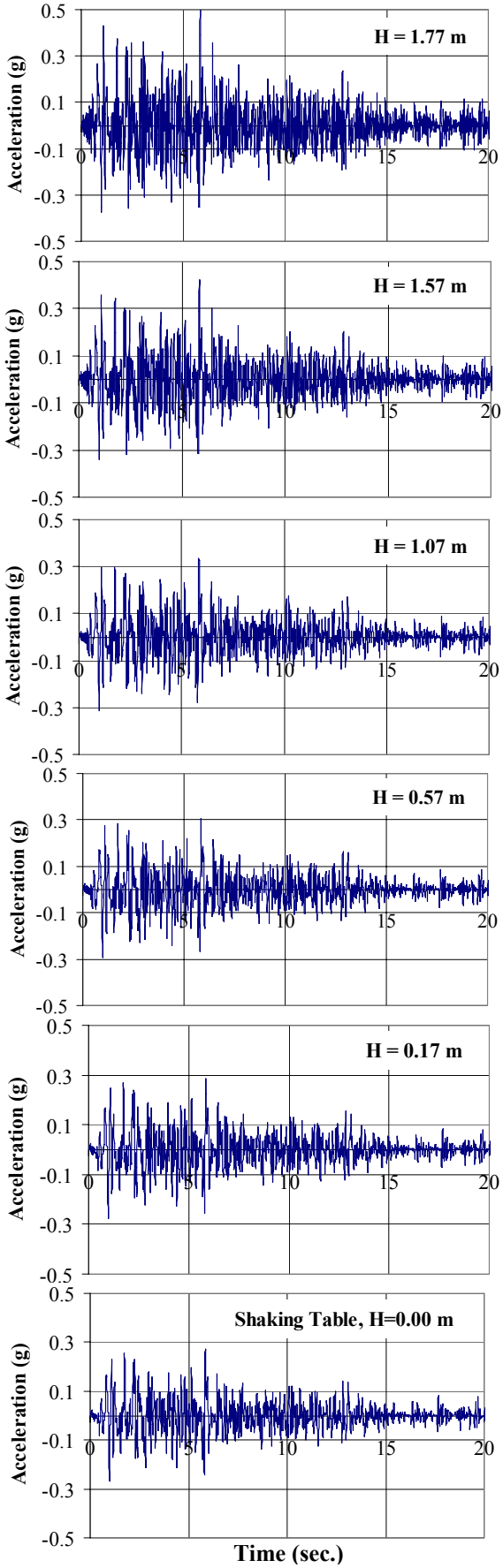

Figure A-11. 2nd experiment 4th shaking, accelerations on the front wall

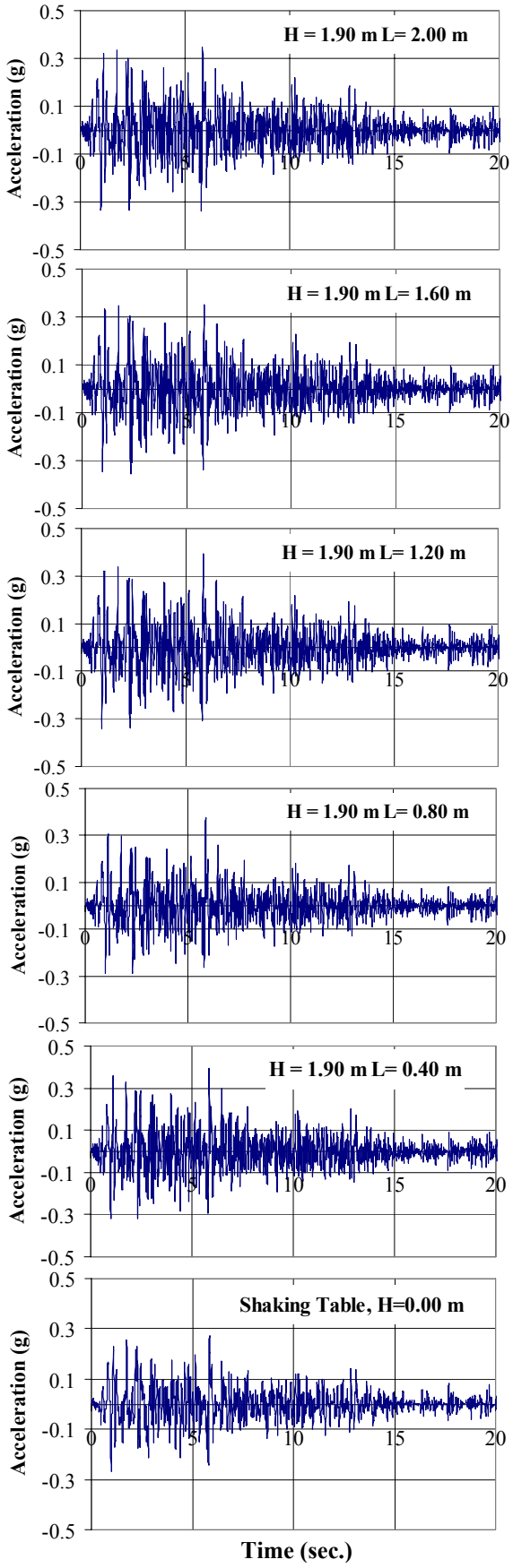

Figure A-12. 2nd experiment 4th shaking, accelerations on top of the backfill

REFERENCES

1. U.S. Department of Transportation, *FHWA Reinforced Soil Structures Volume I. Design and Construction Guidelines*, Volume I, FHWA, McLean, Virginia, November 1990.

2. Rimoldi, P., A. Ricciuti, and P. Recalcati, *Steep Reinforced Slopes*, 1994, http://www.tenax.net/geosynthetics/tech_doc.htm.

3. Jones C. J. F. P., *Earth Reinforcement and Soil Structures*, Butterworths Advanced Series in Geotechnical Engineering, London, 1985.

4. Bathurst, R. J., and M. C. Alfaro, "Review of Seismic Design, Analysis and Performance of Geosynthetic Reinforced Walls, Slopes and Embankments", *Earth Reinforcement, Ochiai, Yasufuku & Omine (eds)*, pp. 887-918, Balkema, Rotterdam, 2000.

5. Zornberg, J. G., N. Sitar and J. K. Mitchell, *Geotechnical Earthquake Engineering*, Prentice-Hall, New Jersey, 1996.

6. Goodings, D. J. and J. C. Santamarina, "Reinforced Earth and Adjacent Soils: Centrifuge Modeling Study", *Journal of Geotechnical Engineering*, ASCE Vol. 115, pp. 1021-1026, July 1989.

7. Porboha, A., D. Goodings, "Cohesive Soil Retaining Walls Reinforced With Geotextile", *Earth Reinforcement, Ochiai, Yasufuku & Omine (eds)*, pp. 463-468, Balkema, Rotterdam, 1996.

8. Zornberg, J. G., N. Sitar and J. K. Mitchell, "Performance of Geosynthetic Reinforced Slopes at Failure", *Journal of Geotechnical and Geoenvironmental Engineering*, ASCE Vol. 124, pp. 670-683, August 1998.

9. Bathurst, R. J. and K. Hatami, "Seismic Response Analysis of a Geosynthetic-Reinforced Soil Retaining Wall", *Geosynthetics International,* Vol. 5, Nos. 1-2, pp. 127-166, 1998.

10. Matsuo, O., T. Tsutsumi, K. Yokoyama and Y. Saito, "Shaking Table Tests and Analyses of Geosynthetic-Reinforced Soil Retaining Walls, *Geosynthetics International*, Vol. 5, Nos. 1-2, pp. 97-126, 1998.

11. El-Emam, M. M., R. J. Bathurst, K. Hatami and M.M. Mashhour, "Shaking Table and Numerical Modeling of Reinforced Soil Walls", *Landmarks in Earth Reinforcement, Ochiai, Yasufuku & Omine (eds)*, pp. 329-334, 2001.

12. Ling, H. I., Y. Mohri, D. Leshchinsky, C. Burke, K. Matsushima and H. Liu, "Large-Scale Shaking Table Tests on Modular-Block Reinforced Soil Retaining Walls", *Journal of Geotechnical and Geoenvironmental Engineering*, ASCE Vol. 131, No. 4, pp. 465-476, April 2005.

13. Ling, H. I., C. P. Cardany, L-X. Sun, H. Hashimoto, "Finite Element Study of a Geosynthetic-Reinforced Soil Retaining Wall With Concrete Block Facing", *Geosynthetics International,* Vol. 7, No. 2, pp. 137-162, 2000.

14. Ling, H. I., L. Huabei, V. N. Kaliakin and D. Leshchinsky, "Analyzing Dynamic Behavior of Geosynthetic-Reinforced Soil Retaining Walls", *Journal of Engineering Mechanics*, ASCE Vol. 130, No.8, pp. 911-920, August 2004.

15. State Of California Department Of Transportation Trenching and Shoring Manual, *Earth Pressure Theory and Application,* http://www.dot.ca.gov/hq/esc/construction/ manuals/ TrenchingandShoring/, 1990.

16. Ebeling, R. M. and E. E. Morrison, *The Seismic Design of Waterfront Retaining Structures*, (Technical report ; ITL-92-11 and Technical report NCEL TR-939) prepared for Department of the Army, US Army Corps of Engineers and Department of the Navy, Naval Civil Engineering Laboratory, 1992.

17. Bathurst, R. J., *Segmental Retaining Walls Seismic Design Manual*, National Concrete Masonry Association (NCMA), Herndon, Virginia, USA, 1998.

18. White, M., F., *Fluid Mechanics*, McGraw-Hill Inc., pp. 245-286, USA, 1986.

19. Santamarina, J. C., 1984, Effect of Adjacent Soils on Reinforced Soil Structures-Centrifuge Model Testing, M.S. Thesis, University of Maryland.

20. Jakrapiyanun, W., S. A. Ashford, Soil-Foundation-Structure-Interaction study using the Laminar Container using One-g Shake Table Testing, *The 16th ASCE Engineering Mechanics Conference Proceedings,* University of Washington, 2003.

21. Iai, S., and T. Sugano, "Soil-Structure Interaction Studies Through Shaking Table Tests", *Earthquake Geotechnical Engineering, Séco e Pinto (ed.)*, pp. 927-940, Balkema, Rotterdam, 1999.

22. Plaxis V8.4 Materials Manual, www.plaxis.nl/upload/productmanuals/V84-4_MaterialModels.pdf.

23. Seed, H. B., R. T. Wong, D. Leshchinsky, I. M. Idriss and K. Tokimatsu, "Moduli and Damping Factors for Dynamic Analyses of Cohesionless Soils", *Journal of Geotechnical Engineering*, ASCE Vol. 112, No. 11, pp. 1016-1032, November 1986.

24. Plaxis V8.4 Dynamics Manual, www.plaxis.nl/upload/productmanuals/V84-7_Dynamics.pdf.

25. Burke, C. B., 2004, *Full-Scale Shaking Table Tests and Finite Element Analysis of Reinforced Soil Retaining Walls*, Ph.D. Dissertation, Columbia University.

26. Bathurst, R. J., Z. Cai, M. Alfaro and M. Pelletier, "Seismic Design Issues for Geosynthetic Reinforced Segmental Retaining Walls", *Mechanically Stabilized Backfill*, Wu (editor), pp. 79-97, Balkema, Rotterdam, 1997.

27. Kadayıfçı, A., 2003, *Influence of Various Parameters on Seismic-Induced Permanent Displacement of Geosynthetic Reinforced Segmental Retaining Walls*, M.S. Thesis, Boğaziçi University.

28. Cai, Z. and R. J. Bathurst, "Seismic-induced Permanent Displacement of Geosynthetic-Reinforced Segmental Retaining Walls", *Canadian Geotechnical Journal*, Vol. 33, pp. 937-955, 1996.

29. Seed, H. B. and M. L. Silver, "Settlement of Dry Sands During Earthquakes", *Journal of Soil Mechanics & Foundation Divisions*, Vol. 98, pp. 381-397, 1972.

30. De Gennaro, V., J. Canou, J.C. Dupla, and N. Benahmed, "Influence of Loading Path on the Undrained Behaviour of a Medium Loose Sand", *Canadian Geotechnical Journal*, Vol. 41, pp. 166-180, February 2004.

31. Ling, H. I., H. Liu and Y. Mohri, "Parametric Studies on the Behavior of Reinforced Soil Retaining Walls under Earthquake Loading", *Journal of Engineering Mechanics*, Vol. 131, pp. 1056-1065, October 2005.

32. Hatami, K. and R. J. Bathurst, "Effect of Structural Design on Fundamental Frequency of Reinforced-Soil Retaining walls", *Soil Dynamics and Earthquake Engineering*, 19, pp. 137-157, 2000.

33. Carotti, A. and P. Rimoldi, "A Nonlinear Model for the Seismic Response Analysis of Geosynthetic-Reinforced Soil Structures", *Geosynthetics International,* Vol. 5, Nos. 1-2, pp. 167-201, 1998.